FZR-448

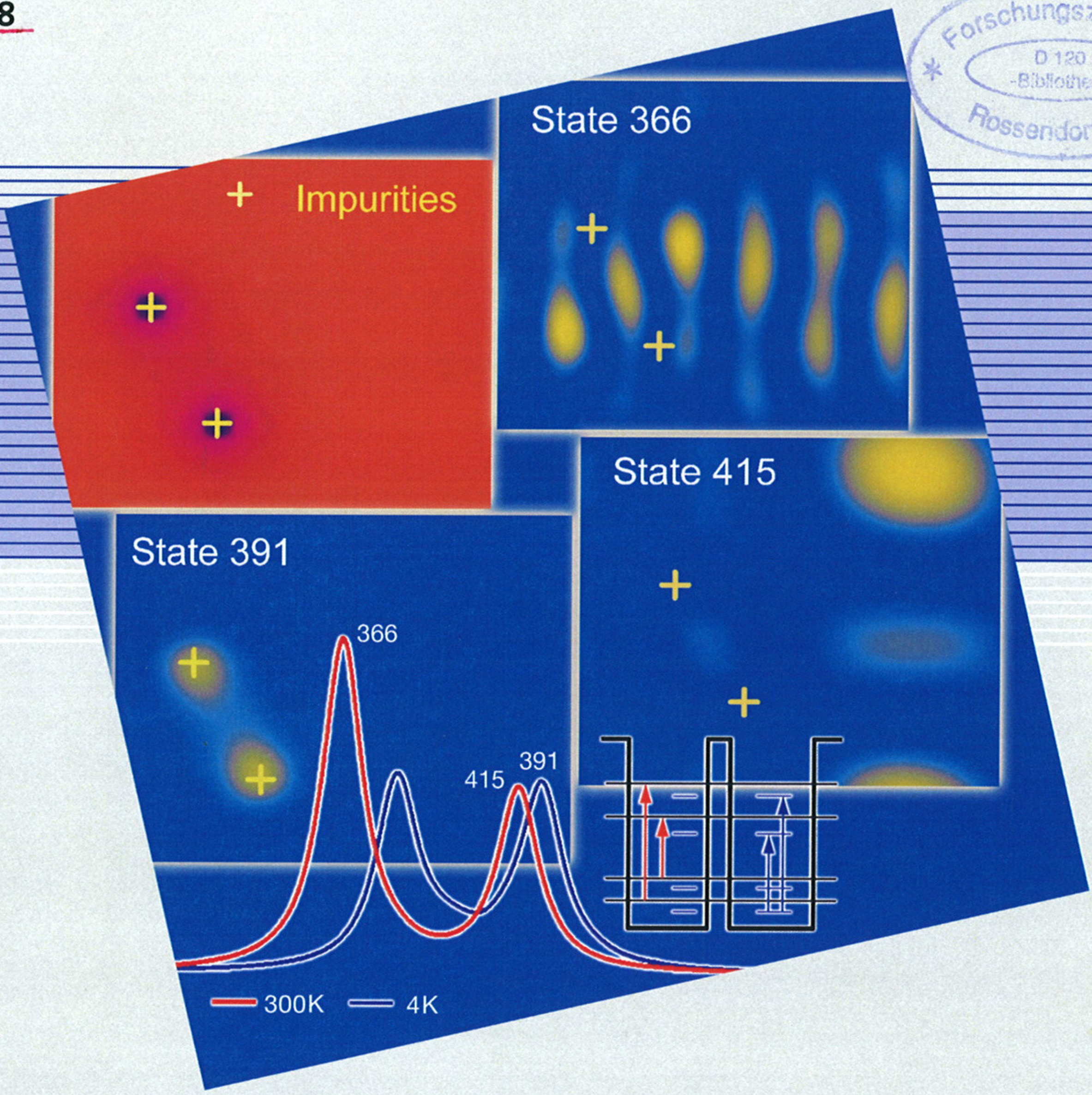

Wissenschaftlich-Technische Berichte
FZR-448 2006 · ISSN 1437-322X

Annual Report 2005

Institute of Ion Beam Physics and Materials Research

Forschungszentrum
Rossendorf

Wissenschaftlich-Technische Berichte
FZR – 448
2006

Annual Report 2005

Institute of Ion Beam Physics and Materials Research

Editors:

J. von Borany, V. Heera,
M. Helm, W. Möller

Forschungszentrum
Rossendorf

Cover Picture:

The graph in the lower part shows two mid-infrared absorption spectra of a GaAs/AlGaAs double quantum well structure, which exhibits intersubband transitions at higher temperature (red curve) and impurity transitions at lower temperature (blue curve). The quantum well potential (z-direction) with the transitions indicated by arrows is sketched besides. The upper square panel shows the position and the electrostatic potential of two random impurities, and the three blue panels show the calculated wavefunctions of the relevant final states in the xy plane (area 100 × 100 nm^2) and integrated over z. Clearly, state 391 is localized around the impurities, whereas 366 and 415 are extended states. The numbers of these final states are added to the corresponding peaks in the absorption spectra.

For details see contribution on p. 36.

Forschungszentrum Rossendorf e.V.
Institut für Ionenstrahlphysik und Materialforschung

Postfach 51 01 19
D-01314 Dresden
Bundesrepublik Deutschland

Direktoren	Prof. Dr. Wolfhard Möller	Prof. Dr. Manfred Helm
Telefon	+ 49 (3 51) 2 60 22 45	+ 49 (3 51) 2 60 22 60
Telefax	+ 49 (3 51) 2 60 32 85	+ 49 (3 51) 2 60 32 85
E-mail	w.moeller@fz-rossendorf.de	m.helm@fz-rossendorf.de

Internet http://www.fz-rossendorf.de/FWI

Preface by the Directors

The Institute of Ion Beam Physics and Materials Research (IIM) contributes to the "Structure of Matter" Research Program at the Forschungszentrum Rossendorf (FZR) with the fields "Ion-based Materials Research" and "Semiconductor Physics". It combines basic and applied research in the fields of ion beam applications to materials and semiconductor physics and technology, with more than 100 scientists, engineers, technicians, and PhD and diploma students. The institute operates a national and international ion beam center, which, in addition to its own scientific activities, offers services and transfers know-how on ion beam techniques to universities, other research institutes, and industry. It is involved in the scientific exploitation of the new experimental facilities at FZR, the infrared free-electron laser at the 40 MeV superconducting electron accelerator ELBE and the Dresden High Magnetic Field Laboratory (HLD).

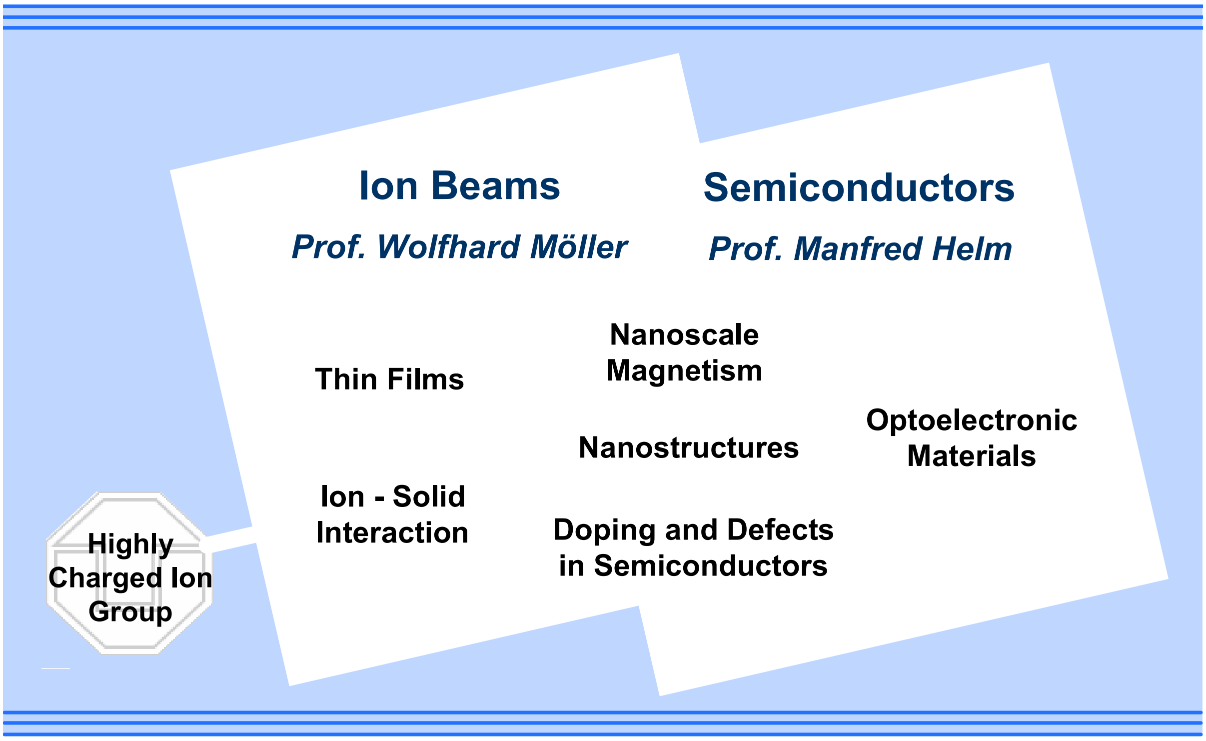

The diagram displays the 2005 R&D topics of the institute. A new topic, “Nanoscale Magnetism” has been initiated and is managed by PD Dr. Jürgen Fassbender, who also acts as the head of a new division "Nanofunctional Films". The research is focused on thin, nano-patterned magnetic layers as well as magnetic semiconductors, both synthesized or modified using ion beams. The topic “Optoelectronic Materials” is under the new guidance of PD Dr. Harald Schneider, who is also leading the ”Semiconductor Spectroscopy” division as a successor to Prof. Thomas Dekorsy. This group has taken care of the first external-user groups at the infrared free-electron laser FELBE.

In the present Annual Report, the IIM presents some selected scientific highlights of the past year together with a broader scientific and statistical overview. The scientific success is of course due to the efforts and dedication of all staff members, guests and students of the institute – sincere thanks to all of them! The institute would also like to thank all partners and friends from universities, industry, and research institutes around the world for good cooperations. Special thanks are due to the Executive Board of the Forschungszentrum Rossendorf, the Ministry of Science and Arts of the Free State of Saxony, the German Federal Ministry of Education and Research, and all other funding organizations for their support.

Prof. Wolfhard Möller　　Prof. Manfred Helm

Contents

Selected Reports

Short Contributions

Statistics

Selected Reports

Microstructure and Nonbasal-Plane Growth of Epitaxial MAX Phase Ti_2AlN Thin Films

M. Beckers, N. Schell, R.M.S. Martins, A. Mücklich, W. Möller and L. Hultman[1]

[1]*Thin Film Physics Division, Department of Physics, Chemistry and Biology (IFM),*
Linköping University, Linköping SE-581 83, Sweden

The $M_{n+1}AX_n$ phases [1] are a family of nanolaminated compounds, where M is a transition metal, A an A-group element and X is nitrogen and/or carbon. Their hexagonal structure consists of $[MX_6]$ octahedrons, interleaved by A-group element layers. In M_2AX_1 every third layer is constituted by A-group atoms, every fourth for M_3AX_2, every fifth for M_4AX_3. For the Ti-Al-N system Ti_2AlN [2] and Ti_4AlN_3 [3] have been reported. Here, the $[MX]_6$ slabs are identical with the structure of wear protective TiN. Since the M-X bonds are of strong covalent-ionic nature, the $M_{n+1}AX_n$ phases exhibit typical ceramic properties like high melting points and thermal stabilities [4]. On the other hand the M-A bonds are rather weak. Therefore, $M_{n+1}AX_n$ phases also exhibit metallic properties like good electrical-thermal conductivity [5]. Under force effect they deform by kink bands which yields high ductility and machinability. Due to this unique combination of properties, applications for $M_{n+1}AX_n$ phase are manifold, one of them being wear protective functional coatings for high temperature applications. The first $M_{n+1}AX_n$ phase thin films, in the Ti-S-C system, were deposited using magnetron sputtering [6]. $M_{n+1}AN_n$ phases are harder to obtain by sputter deposition, since the nitrogen has to be introduced via the gas phase. Hence, only very recently Joelsson *et al.* demonstrated the deposition of Ti_2AlN thin films [7]. They used reactive sputtering from a compound 2Ti:Al target, and deposited onto MgO(111) single-crystals at substrate temperatures of 830°C.

The present work reports on successful Ti_2AlN deposition by reactive cosputtering using elemental Ti and Al targets, at considerably lower substrate temperatures of 690°C studied by *in-situ* x-ray diffraction. The temperature was measured using a thermocouple clamped onto the substrate holder. MgO(111) wafers were used as substrates. The base pressure at the deposition temperature was $\sim 8 \times 10^{-5}$ Pa. Prior to the Ti_2AlN, a thin fcc $(Ti_{1-x}Al_x)N$ seed layer was deposited at Ar and N_2 fluxes of 2.76 and 1.38 sccm at a working pressure of 0.35 Pa. The Ti and Al magnetrons were set to 60 and 20 W, yielding a composition of $(Ti_{0.63}Al_{0.37})N$. For Ti_2AlN growth the deposition pressure was increased to 0.8 Pa at Ar and N_2 fluxes of 7.94 and 0.48 sccm, respectively. The Ti and Al magnetron powers were changed to 80 and 26 W.

The whole deposition chamber is mounted into the goniometer of the ROBL beamline at the European Synchrotron Radiation Facility (ESRF), and equipped with x-ray windows [8]. Monochromatized x-rays of 12.915 keV were employed to study the Ti_2AlN film growth *in-situ* in two different scattering geometries: (1) low angle specular reflectivity (XRR) either time-resolved at a fixed incidence angle, or scanned in coplanar scattering geometry for the determination of the film thickness; (2) large angle x-ray diffraction (XRD) in Bragg-Brentano geometry in order to determine the off-plane lattice parameter. The time resolved XRR signal can be used to observe changes in the surface morphology on an atomic scale, from which the growth mode of the developing film can be derived. The microstructure and texture of the final film was investigated using a combination of lab source pole figure measurements and cross-sectional transmission electron microscopy (XTEM). The final film composition was examined by Rutherford backscattering spectroscopy (RBS), using a 1.7 MeV He^+ beam.

Figure 1 shows time dependent XRR data for both the seed layer (a) and the Ti_2AlN $M_{n+1}AX_n$ phase layer (b) deposited onto MgO(111). Clear intensity oscillations are depicted for the seed layer. The oscillation amplitude does not diminish during deposition, hence a smooth layer-by-layer (step flow) growth onto MgO can be deduced, as expected from reported epitaxial growth of pure TiN onto MgO(111) [9]. XRR characterization during a deposition interruption yielded a layer thickness of 121 Å, corresponding to a low growth rate of 0.3 Å/s, further promoting the layer-by-layer growth. Each oscillation in the time dependent XRR can be attributed to one lattice constant of $(Ti_{0.63}Al_{0.37})N$, hence a perfect cube-on-cube heteroepitaxial relation $(Ti_{0.63}Al_{0.37})N\{100\}<100>$ // MgO $\{100\}<100>$ with only 0.74 % lattice mismatch between

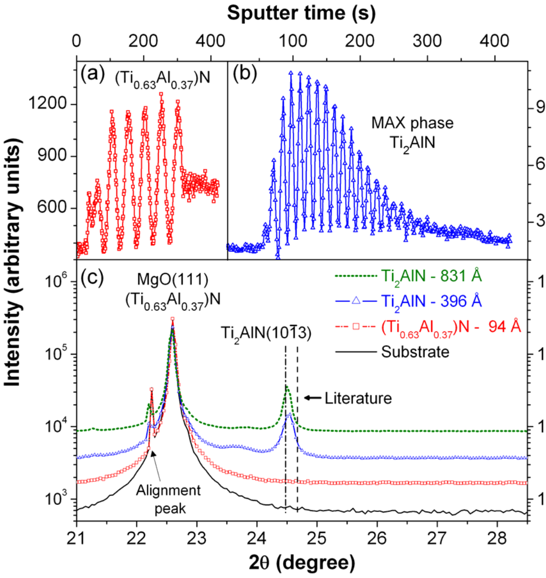

Fig. 1: Time dependent *in-situ* XRR of the fcc $(Ti_{0.63}Al_{0.37})N$ seed layer (a) and Ti_2AlN (b) on MgO(111). The oscillatory behaviour for the deposited seed layer as well as the Ti_2AlN are a fingerprint of layer-by-layer growth. The decreasing amplitudes of those oscillations reveal increasing roughness or island growth for Ti_2AlN. (b) The *in-situ* XRD data recorded after the deposition of the seed layer and two Ti_2AlN film deposition steps of approximately 400 Å each show only a $Ti_2AlN(10\bar{l})$ peak. The vertical dashed line represents literature data [10].

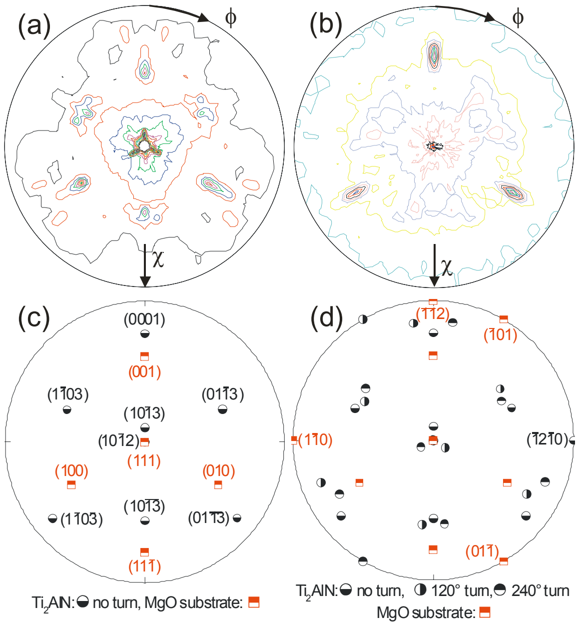

Fig. 2: Pole figures of MAX phase Ti_2AlN grown onto MgO(111), measured on the Bragg peaks $Ti_2AlN(10\bar{1}3)$ (a) and $Ti_2AlN(0002)$ (b). The stereographic projection (c) shows the theoretical poles of $Ti_2AlN\{10\bar{1}3\}$, $\{10\bar{1}2\}$, $\{0001\}$, $\{\bar{2}1\bar{1}0\}$ and $MgO\{111\}$, $\{1\bar{1}0\}$, $\{\bar{1}\bar{1}2\}$. The experimental pole figure can be obtained by turning the poles for 120° around the MgO[111] direction, as indicated by the symbols (d).

$(Ti_{0.63}Al_{0.37})N$ and (4.18 Å) MgO (4.211 Å) can be assumed. Figure 1(b) shows that even after interrupting the deposition process for about 1 h, the Ti_2AlN $M_{n+1}AX_n$ phase nucleation onto the seed layer again starts with a layer-by-layer mode. The oscillations are clearly visible for more than fifteen monolayers, however their exponential decay points to a pronounced kinetic roughening, i.e. a Stranski-Krastanov-like growth mode. The deposition rate of the Ti_2AlN MAX phase was determined to be 1.3 Å/s, explaining the smaller oscillation period compared to the seed layer.

The θ-2θ XRD scans are shown in Fig. 1(c). After deposition of the seed layer the intensity distribution remains undistinguishable due to the perfect epitaxial nature of the seed layer growth. In contrast, already after the first deposition of ~ 400 Å Ti_2AlN the $Ti_2AlN(10\bar{1}3)$ peak can clearly be identified as the only one resulting. It is so close to $Ti_2AlN(0006)$ that in early diffraction data the peaks were not separated [10], but due to the lack of other order $Ti_2AlN(000\ell)$ peaks a mix-up can be excluded. For later discussions it should be noted that the lattice spacing of the $Ti_2AlN(10\bar{1}3)$ peak is increased compared to the literature values as indicated by the dashed line.

Figure 2 shows the experimental pole figure for Ti_2AlN on MgO(111), recorded in the $Ti_2AlN(10\bar{1}3)$ Bragg peak. Due to the immediate vicinity of the $Ti_2AlN(0006)$ and MgO(111) as well as MgO(100) peaks, the pole figure comprises orientation distributions of all these four lattice planes. The θ-2θ scans of all cluster points within the experimental pole figure in Fig. 2(a) showed only substrate and $Ti_2AlN(10\bar{1}3)$ Bragg peaks, except for the ones at $\chi \sim 60°$. Here, a peak at $2\theta = 13°$ was observed, which is close to $Ti_2AlN(0002)$. The pole figure on that peak in Fig. 2(b) clearly shows three distinct cluster points at $\chi \sim 60°$ and $\phi = 0°$, 120° and 240°. Thus, the $Ti_2AlN(000\ell)$ basal planes are tilted ~60° away from the surface normal with threefold in-plane symmetry.

Figure 2(c) shows the stereographic projection of the Ti_2AlN [11] and MgO [10] lattice. Assuming single-crystal Ti_2AlN and MgO, the (111) substrate orientation leads to a central MgO(111) pole and three MgO{100} poles at a tilting angle $\chi = 54.7°$ and azimuth angles $\phi = 0°$, 120° and 240°. As seen in Fig. 2(b), close to the MgO(001) pole lies the $Ti_2AlN(000\ell)$ pole. As a consequence, the $Ti_2AlN(10\bar{1}3)$ pole does not lie in the center of the pole figure, but at $\chi = 9°$ and $\phi = 0°$. Accordingly, within the central position lies the $Ti_2AlN(10\bar{1}2)$ pole. Thus, one can denote $MgO(111) \,//\, Ti_2AlN(10\bar{1}2)$. Within Fig. 2(a), permutation of the first three Miller indices yields five additional $Ti_2AlN\{10\bar{1}3\}$ poles, positioned as indicated by the indices and the symbol (◒). Additionally, this figure must also be turned around by 120° and 240° due to the threefold symmetry of the $Ti_2AlN(0002)$ peak. This makes up for another fourteen [2 times (6+1)] cluster points. For clarity, the indexing of these collective points shown in Fig. 2(d) has been omitted. Each in-plane turn of 120° is indicated by the symbols (◑) and (◓). The picture obtained describes all the features of the experimental pole figures.

The azimuthal orientational relationship can be found by looking at the poles for $\chi = 90°$, where obviously the $MgO(1\bar{1}0)$ and $Ti_2AlN(\bar{1}2\bar{1}0)$ poles overlap. For the cubic MgO the corresponding direction is $[1\bar{1}0]$ and for the Ti_2AlN it is $[\bar{1}2\bar{1}0]$. Since there are three possible MgO<110> directions on the MgO(111) surface, the threefold in-plane symmetry of the Ti_2AlN can thus be described by the orientational relation $MgO\{111\}\langle 110\rangle \,//\, Ti_2AlN\{10\bar{1}2\}\langle\bar{1}2\bar{1}0\rangle$.

Figure 3(a) shows an XTEM micrograph from Ti_2AlN recorded along the MgO[112] zone axis. The layer is not single-crystalline, but exhibits equiaxed morphology with individual epitaxial grains corresponding to Fig. 2. Their sizes are in the dimension of the film thickness. Individual grains show strong diffraction contrast, which is due to the threefold in-plane symmetry described above. In accordance with time-resolved XRR the layer displays high surface roughness, caused by the tilted nonbasal–plane growth.

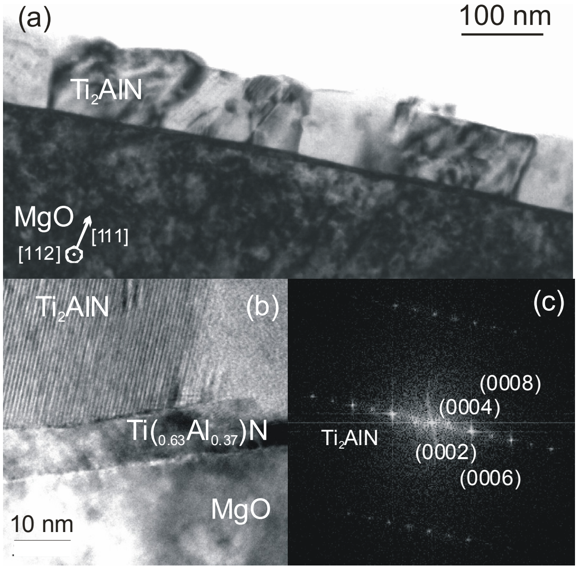

Fig. 3: XTEM micrographs of Ti_2AlN grown on MgO(111) along the MgO[112] zone axis. (a) shows the film morphology consisting of large crystal regions. (b) shows a high resolution micrograph at the interface with the typical MAX phase 2-1-1 layered structure. It is made up by the (000ℓ) planes as confirmed from the d-spacing calculation by Fast Fourier Transformation in (c).

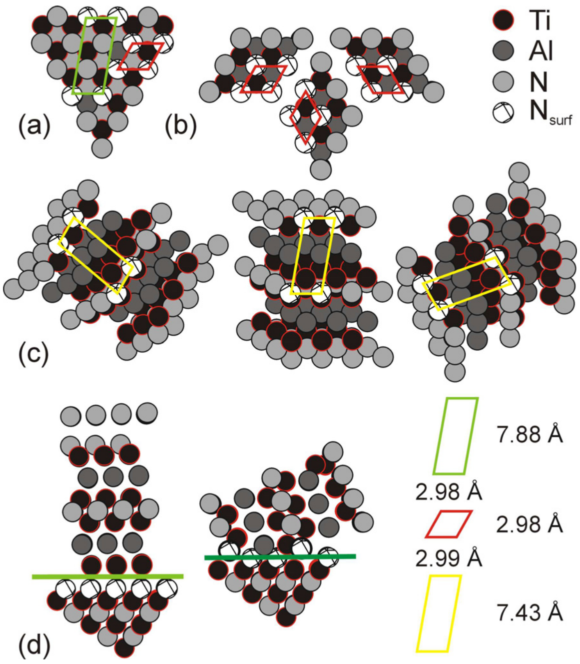

Fig. 4: Atomic model illustration of the different $(Ti_{0.63}Al_{0.37})N$ and Ti_2AlN crystallographic planes and directions together with the geometric reconstructions for the pseudomorphic fitting of Ti_2AlN onto $(Ti_{0.63}Al_{0.37})N(111)$. (a) shows the $(Ti_{0.63}Al_{0.37})N(111)$ surface and (b) the three different $Ti_2AlN\langle\bar{1}2\bar{1}0\rangle$ orientations of the $Ti_2AlN(0001)$ MAX phase basal-plane along the $(Ti_{0.63}Al_{0.37})N\langle 110\rangle$ directions. (c) shows the same threefold $Ti_2AlN\langle\bar{1}2\bar{1}0\rangle$ orientations for the $Ti_2AlN(10\bar{1}2)$ planes. (d) shows cross-sectional views of the $Ti_2AlN/(Ti_{0.63}Al_{0.37})N$ interface for basal-plane and nonbasal-plane growth.

Figure 3(b) shows the interface between one grains and the MgO substrate. The tilted Ti_2AlN basal-planes can be depicted from the layered 2-1-1 structure being typical for $M_{n+1}AX_n$ phases. The lattice plane spacing calculations by Fast Fourier Transformation confirm multiple $Ti_2AlN(000\ell)$ planes as shown in Fig. 3(c). The tilting angle of the basal planes is ~70°, in agreement with the pole figure measurements. Hence, each of the grains in Fig. 3(a) represents one possible in-plane orientation of the $Ti_2AlN(000\ell)$ plane.

To conclude, both pole figure and XTEM results show that the orientational relationship between the MgO and the Ti_2AlN is $MgO\{111\}\langle 110\rangle \,//\, Ti_2AlN\{10\bar{1}2\}\langle\bar{1}2\bar{1}0\rangle$. This is in contrast to the basal-plane growth of Ti_2AlN for high-temperature deposition conditions, with $MgO\{111\}\langle 110\rangle \,//\, Ti_2AlN\{0001\}\langle\bar{1}2\bar{1}0\rangle$ [7]. This basal-plane growth can be expected due to the low lattice mismatch of only 0.77% between the $Ti_2AlN(0001)$ and MgO(111) surfaces, as indicated in Figs. 4(a-d). During nucleation the $Ti_2AlN(0001)$ may arrange itself in three possible orientations along the MgO<110> directions. During coalescence, adjacent grains adjoin

(Fig. 4(b)), resulting in the reported single-crystal film morphology [7].

In our case the MgO(111) is parallel to the $Ti_2AlN(10\bar{1}2)$ plane, which is projected in Fig. 4(c). As indicated by the polygon on the surface nitrogen atoms constituting this plane, a low lattice mismatch of 0.77% along one MgO<110> direction is possible. However, single-crystalline epitaxial growth is prevented. First, an initial tilted nucleation with threefold in-plane orientation does *not* allow coalescence at increasing film thickness. This is in agreement with the polycrystalline equiaxed morphology observed in XTEM, and the pole figure results. Second, in the other MgO<110> directions the adaptation can only be achieved by taking also over next surface nitrogen atoms into account, as shown by the polygon in Fig. 4(a). Still, the reconstruction shows a quite large misfit of 7.88 Å to 7.43 Å, corresponding to 6%. Besides, the cross-sectional view in Fig. 4(d) demonstrates that the interface cannot be configured only by Ti-N bondings, as it would be the case for basal-plane grown $Ti_2AlN(0001)//MgO(111)$. In fact, a ternary Ti-Al-N atomic reconfiguration of more than nearest-neighbor-atoms is necessary.

This complicated strained interfacial bonding can be attributed to the following: When depositing on the $(Ti_{0.63}Al_{0.37})N$ seed layer, its (111) surface tends to be N-terminated [11]. Comparing with Fig. 4(d), this implies that the initial atomic layer of $Ti_2AlN(0001)$ has to consist purely of Ti atoms. However, the employed co-sputtering process provides an incoming flux of *both* Ti and Al atoms, so the initial elementary composition would need to be reconfigured. This reconfiguration will be hindered, since the $(Ti_{0.63}Al_{0.37})N(111)$ surface is one with a relatively high adatom bonding energy and thus low mobility [11]. Moreover, the comparably low substrate temperatures of only 690°C will aggravate this deficiency of adatom mobility. Hence, the texture evolution is kinetically prevented from achieving maximum thermodynamic stability, e.g. basal-plane orientation. A deposition on MgO substrates *without* a $(Ti_{0.63}Al_{0.37})N$ seed layer at 830°C [7] allows for the correct partitioning of the elements at the substrate-film interface. Decreasing the substrate temperature as in the present case causes different interfacial adaptation due to kinetical restrictions as described above.

In summary, Ti_2AlN single-phase thin films have been successfully deposited onto MgO(111) substrates at growth temperatures of 690°C. The growth process has been characterized by *in-situ* XRR and shows kinetic roughening of the developing films. The orientational relationship between MgO substrate and Ti_2AlN as derived by pole figure measurements is $MgO\{111\}<110> // Ti_2AlN\{10\bar{1}2\}<\bar{1}2\bar{1}0>$. This suggests a tilted, nonbasal-plane growth of the Ti_2AlN which leads to a non single-crystal morphology and rough, facetted surfaces as proven by XTEM. The nonbasal-plane growth can be explained in terms of insufficient adatom mobility during deposition leading to a kinetically restricted growth mode and to the observed tilted basal-plane growth.

Acknowledgments

We gratefully acknowledge technical assistance by U. Strauch during experiments and financial support from the Deutsche Forschungsgemeinschaft under contract SCHE 682.

The presented results have been recently published in a more detailed version as M. Beckers *et al.*, J. Appl. Phys. **99** (2006) 34902.

References

[1] M.W. Barsoum, Prog. Solid State Chem. **28** (2000) 201

[2] W. Jeitschko, H. Novotny, F. Benesovsky, Monatshefte der Chem. **94** (1963) 1198

[3] J.C. Schuster, J. Bauer, J. Solid State Chem. **53** (1984) 260

[4] F. Adibi, I. Petrov, L. Hultman, U. Wahlström, T. Shimizu, D. McIntyre, J. E. Greene, J. Appl. Phys. **69** (1991) 6437

[5] M.W. Barsoum, H.-I. Yoo, I.K. Polushina, V.Yu. Rud, T. El-Raghy, Phys. Rev. B **62** (2000) 10194

[6] J.-P. Palmquist, U. Jansson, T. Seppänen, P.O.Å. Persson, L. Hultman, P. Isberg, Appl. Phys. Lett. **81** (2002) 835

[7] T. Joelsson, A. Hörling, J. Birch, L. Hultman, Appl. Phys. Lett. **86** (2005) 111913

[8] W. Matz, N. Schell, W. Neumann, J. Bøttiger, J. Chevallier, Rev. Sci. Instrum. **72** (2001) 3344

[9] L. Hultman, D. Hesse, W.-A. Chiou, J. Mat. Res. **6** (1991) 1744

[10] M.Y. Gamarnik, M.W. Barsoum, T. El-Raghy, Powder Diffr. **15** (2000) 241

[11] D. Gall, S. Kodambaka, M. A. Wall, I. Petrov, J.E. Greene, J. Appl. Phys. **93** (2003) 9086

Fullerene-Like Arrangements in Carbon Nitride Thin Films Grown by Direct Ion Beam Sputtering

R. Gago, G. Abrasonis, A. Mücklich, W. Möller, Zs. Czigány[1] and G. Radnóczi[1]

[1]Research Institute for Technical Physics and Materials Science, Hungarian Academy of Sciences,
P.O. Box 49, H-1525 Budapest, Hungary

The theoretical work of Cohen and Liu [1] predicting the hypothetical β-C_3N_4 phase harder than diamond has motivated an intense research in carbon nitride (CN_x) materials during the last years. However, most of the attempts to synthesize this phase have resulted in amorphous graphitic structures and a limitation in the maximum nitrogen content incorporated to the films below 50 at.% [2]. Among these graphitic structures, an important finding is the evolution of fullerene-like (FL) features under certain growth conditions, consisting of bent and cross-linked nitrogen-containing graphite basal planes of nanoscale dimensions [3]. This atomic arrangement improves significantly the mechanical performance of the material, being compliant and tough at the same time, and making it a promising candidate for tribological applications [4]. The orientation, corrugation, folding, and cross-linking of the basal planes determines the actual physical properties of the graphitic solid, which exhibit a 3D superstructure that exploits the in-plane strength of sp^2 hybrids. These arrangements are not restricted to CN_x solids and have been found in other laminar materials [5]. As compared with pure C materials, the introduction of N reduces the energy barrier to induce curvature in the basal planes [6, 7].

So far, the production of well-structured FL-CN_x thin films has been only reported by reactive DC magnetron sputtering (dc-MS) while, recently, pulsed laser deposition (PLD) resulted also in partially structured films [8]. Low-energy (< 100 eV) ion bombardment and moderate substrate temperatures (400 – 800 K) have been shown to be essential for the synthesis of FL-CN_x thin films by dc-MS [9]. The required growth conditions are necessary to promote three-fold N bonding environments over N atoms in low-coordination sites (i.e. pyridine- and cyanogen-like environments) [10]. This indicates that three-fold N atoms, either in graphite-like or pyrrole-like environments, are the driving force for the insertion of curvature in graphitic basal planes. Moreover, a large fraction of this arrangement is necessary for the evolution of well-structured FL-CN_x. Therefore, FL-CN_x formation should be promoted by the suppression of the less-favourable bonding configurations as, in this case, low coordination sites.

Despite the successful synthesis of FL-CN_x, the growth mechanisms are still not fully understood. This is partially due to the limitation in the growth techniques yielding FL-CN_x. From previous results, it has been concluded that, in addition to the role of N atoms, C_xN_y ($x, y \leq 2$) species emitted from the sputtering target might contribute as film-forming species and imprint their structure on the evolving microstructure [11]. The relevance of C_xN_y precursors from the target has been supported by the lack of FL arrangements in CN_x films prepared by low-energy (~60 eV) N_2 ion beam assistance during e-beam evaporation of graphite [12].

Here, CN_x films are grown by direct N_2/Ar ion beam sputtering (IBS) of a graphite target to mimic the dc-MS process and, in this way, introduce single- and multi-atomic C_xN_y ($0 \leq x, y \leq 2$) species with hyperthermal energies (~1 – 10 eV) in the film-forming flux. CN_x films deposited in this way, exhibit fullerene-like features with standing graphitic basal planes but they are less structured as compared to FL-CN_x grown by dc-MS. The achievement and extension of these microstructural features is discussed in terms of the resulting bonding configurations, film-forming species and ion bombardment effects. The conclusions support the role of C_xN_y precursors for the microstructural evolution and the requirement of low-energy assistance to develop well-structured FL-CN_x.

Carbon (C) and CN_x thin films were grown by IBS of a 5” graphite target with N_2/Ar sputtering gas mixtures at moderate substrate temperatures (300, 423, 573 and 723 K) onto Si(100) and NaCl substrates. The ion beam was produced with a 3 cm Kaufman ion gun located ~11 cm away from the target. The ions impinged at an angle of 40° with respect to the target surface normal. The substrates were located facing the graphite target at a distance of ~30 cm. Before deposition, the substrates were cleaned for 10 min with 1 keV Ar^+ produced by an additional 5 cm Kaufman source facing the substrate. Further details about the growth method, composition and bonding structure of the films can be found in Ref. 13.

The microstructure was studied by high-resolution transmission electron microscopy (HRTEM). Plan-view specimens were obtained from samples grown on NaCl substrates by floating-off technique while cross-sectional specimens were made by gluing slices from samples grown on Si(100) followed by mechanical thinning, polishing and thinned to electron transparency by ion beam milling with 10 keV Ar^+ impinging at 4° with respect to the surface. In the final period of the milling process, the ion energy was decreased gradually to 250 eV to minimize surface amorphization [14, 15]. The investigations were made in a JEOL 3010 microscope operated at 300 kV and a resolution of 0.17 nm.

Figure 1 shows the HRTEM plan-view image of a CN_x sample grown by IBS at 573 K with a pure N_2 sputtering beam. Ordered domains of several nm in size consisting of straight and curved planes typical of FL arrangements can be seen. These features are better observed at the thinnest parts of the sample where high resolution imaging is possible and the influence of overlapping of projected features is minimized. Similar microstructure was observed in the films grown with other N_2/Ar mixtures and at 423 K and 723 K.

The presence of microstructure in the films produced by IBS can be further proven by cross-section HRTEM images. The images taken from C and CN_x films prepared at 723 K are shown in Fig. 2(a) and Fig. 2(b), respectively. The CN_x was produced with a N_2 content of 50% in the Ar/N_2 gas mixture. The image corresponding to the C film (Fig. 2(a)) shows a highly textured microstructure consisting of predominantly standing basal planes. The introduction of N (Fig. 2(b)) reduces the texture but promotes curvature in the basal planes. The preferential orientation of the basal planes was also observed in FL-CN_x grown by dc-MS [16]. The corrugation with N introduction is in agreement with the hypothesis that N is crucial for the evolution of heavily bent and frequently cross-linked basal planes at much lower energies as compared to pure C films.

The problem of projection artifacts for imaging the structural features can be partially overcome by considering selected area electron diffraction (SAED), since any overlapping does not affect the characteristic lattice spacing in the diffraction pattern [17]. In addition, the brightness and width of the diffraction pattern can be used to extract information on the degree of ordering. The corresponding SAED patterns are shown as insets in Fig. 2. They show diffuse features indicating the disordered structure of the film and corresponding to spacing of ~1.15, 1.95 and 3.5 Å (see labels in the inset of Fig. 2(c)). In the insets of panels (b) and (c) in Fig. 2, the dot diffraction pattern of the crystalline Si(100) substrate is also superimposed to indicate the relation of the texture of FL features to the substrate normal. The rings at ~1.15 and ~1.95 Å coincide with those observed for amorphous allotropes of C and CN_x films while the innermost ring at 3.5 Å match with the inter-plane separation of hexagonal basal planes in graphite (0002). The SAED images of Fig. 2 show a broad feature at 3.5 Å indicating the presence of defective graphitic basal planes. The appearance of a broad arc is due to the preferential orientation of the basal planes perpendicular to the surface normal. The SAED from plan-view images of well-structured FL-CN_x presents a similar diffuse pattern but with more distinguishable features and an additional ring at 1.75 Å [17]. The intensity of this ring correlates with that at 3.5 Å and, therefore, it is attributed to the inter-plane distance in graphite (0004). The presence and definition of the 3.5 and 1.75 Å rings have been correlated with the evolution of the FL structure, as signatures of the short/ medium range graphitic order [17]. In the case of IBS films, the characteristic 3.5 Å spacing shows similar structured films as those grown by dc-MS, but the diffuse ring at 1.75 Å is less defined. This feature is only observable in the SAED pattern in Fig. 2(c) as an arc (almost incorporated into the diffuse ring at 1.95 Å) and aligned to the arc at 3.5 Å. These observations indicate a smaller

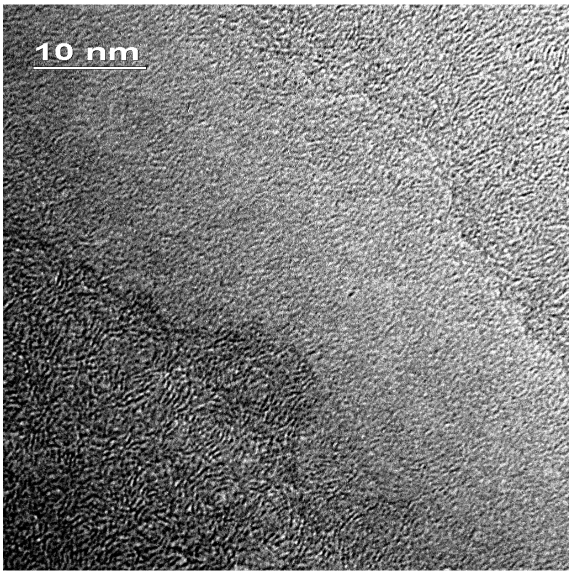

Fig. 1: Plan-view HRTEM image of a CNx film grown by IBS at 573 K with a pure N_2 sputtering beam.

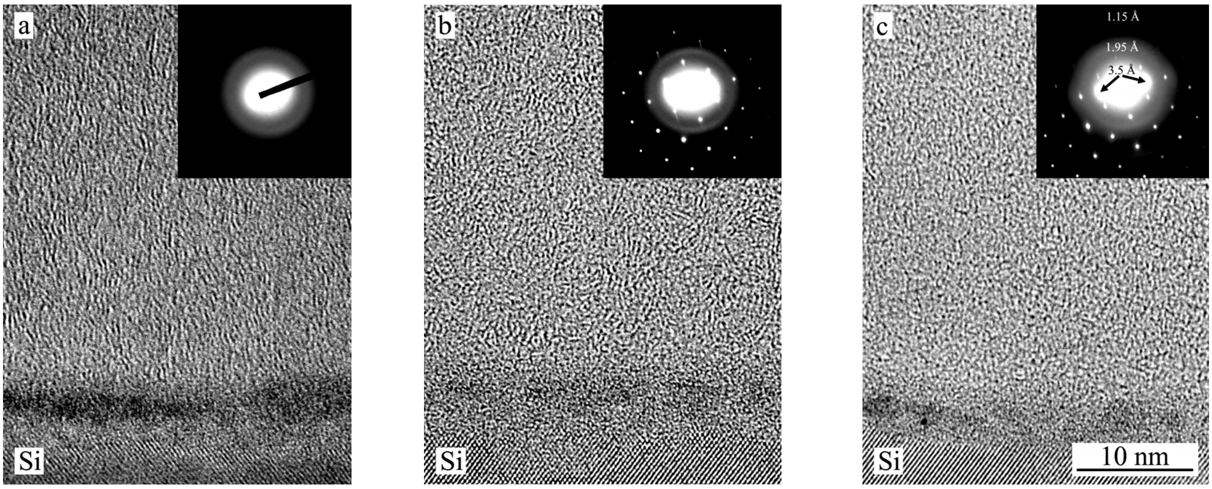

Fig. 2: Cross-section HRTEM images and SAED for (a) C and (b) CN_x (N_2/Ar ratio of 1 in the gas mixture) films grown by IBS at 723 K. Panel (c) shows a CN_x film grown by IBS (with a pure N_2 ion beam) at 723 K under concurrent 100 eV nitrogen ion assistance. The SAED patterns in panels (b) and (c) show the dot diffraction pattern of the Si(100) substrate superimposed to the pattern of the film (diffuse features).

degree of ordering or extension of the graphitic arrangements in IBS films as compared to their dc-MS counterparts. The latter conclusion can also be directly extracted from the comparison of the HRTEM images of Fig. 2 and those reported in Ref. 16.

The achievement of the FL microstructure in CN_x samples prepared by IBS indicates that, as expected, IBS mimics to some extent the growth by dc-MS. In this sense, significant amount of N (up to 20 at.%) can be incorporated in CN_x solid films by IBS of a graphite target, the main source of N coming from the nitridation of the target surface and the subsequent (chemical and physical) sputtering of atomic and molecular N-containing species. The N incorporation by IBS is slightly below the values reported by dc-MS (up to 25 at.%) due to the suppression of the concurrent N ion bombardment on the substrate surface from the plasma discharge. However, not only the similar composition is critical for achieving structured films but also the way that N atoms are incorporated in the C atomic network. The comparison in Ref. 13 of the bonding structure of CN_x films grown by IBS and dc-MS also yielded in both cases a significant participation of threefold nitrogen but a slightly higher relative content of cyanogen-like or nitrile bonding environments by IBS. The detrimental role of nitrile sites in FL arrangements is obvious since their terminating character hinders the further extension of graphene sheets, which could explain the lower degree of FL character in FL-CN_x films grown by IBS with respect to dc-MS.

The introduction of N_2 ion assistance (100 eV) during IBS was shown to induce a significant reduction of the relative content of nitrile bonding environments [13]. Therefore, the less structured films grown by IBS can be partially attributed to the lack of ion assistance during growth. The influence of ion bombardment during growth is very complex, but the IBS process itself can be considered as the deposition of energetic particles with hyperthermal energies in the range of 1 – 10 eV [18]. These energies are enough to introduce a significant amount of displacements on the surface of the growing film, as shown by the growth of dense a-C films [19]. In this way, the formation of FL microstructure can be understood as a temperature and ion induced clustering process under impingement of hyperthermal particles coming from the target (and from an assisting plasma or additional ion source) and site-selective incorporation of atomic and molecular N-containing species. When the degree of assisting ion bombardment is moderate (low ion energy or/and flux) it activates the surface reaction pathways through which N atoms located at low coordination number sites are preferentially removed or transformed into bonding environments with higher coordination number. However, when the degree of ion bombardment increases it can lead to amorphization [16] or complete re-sputtering [9] of the growing film. These assumptions are corroborated by the HRTEM image shown in Fig. 2 (c) obtained from a CN_x sample grown by IBS (100 % N_2 sputtering beam) and additional concurrent 100 eV nitrogen ion beam assistance, the assisting ions impinging at normal incidence with respect to the substrate surface. The image indicates that although some microstructure remains, the relatively high energy involved inhibits the evolution of extended FL domains. Lower energies could not be used due to experimental constraints but future experiments are in progress to reduce the energy of the assistance ions and, in this way, check the promotion of FL arrangements by ion assistance.

In conclusion, HRTEM images reveal the formation of FL-CN_x by IBS at moderate temperatures. This result supports the presence of C_xN_y species in the film-forming flux and low-energy ion bombardment as the main paths to induce the evolution of curved graphitic structures in CN_x solids. In addition, the formation of such structures is clearly related to the promotion of threefold N in hexagonal or pentagonal arrangements and a reduced participation of nitrile bonding environments.

Acknowledgements

This work has been carried out inside the IHP-Network "Synthesis, structure and properties of new fullerene-like materials" being supported by the EU contract no. HPRN-CT-2002-00209.

The presented results have been recently published as R. Gago *et al.*, Appl. Phys. Lett. **87** (2005) 071901.

References

[1] A.Y. Liu, M.L. Cohen, Science **245** (1989) 841

[2] C. Ronning, H. Feldermann, R. Merk, H. Hofsäss, P. Reinke, J.U. Thiele, Phys. Rev. B **58** (1998) 2207

[3] H. Sjöström, S. Stafström, M. Boman, J.E. Sundgren, Phys. Rev. Lett. **75** (1995) 1336

[4] L. Hultman, J. Neidhardt, N. Hellgren, H. Sjöström, J.-E. Sundgren, MRS Bulletin **28** (2003) 19

[5] I. Alexandrou, H.J. Scheibe, C.J. Kiely, A.J. Papworth, G.A.J. Amaratuga, B. Schultrich, Phys. Rev. B **60** (1999) 10903

[6] N. Lin, N. Hellgren, M.P. Johansson, L. Hultman, R. Erlandsson, J.-E. Sundgren, Phys. Rev. B **61** (2000) 4898

[7] S. Stafström, Appl. Phys. Lett. **77** (2000) 3941

[8] A.A. Voevodin, J.G. Jones, J.S. Zabinski, Zs. Czigány, L. Hultman, J. Appl. Phys. **92** (2002) 4980

[9] N. Hellgren, K. Macák, E. Broitman, M.P. Johansson, L. Hultman, J.-E. Sundgren, J. Appl. Phys. **88** (2000) 524

[10] R. Gago, I. Jiménez, J. Neidhardt, B. Abendroth, I. Caretti, L. Hultman, W. Möller, Phys. Rev. B **71** (2005) 125414

[11] J. Neidhardt, B. Abendroth, R. Gago, W. Möller, L. Hultman, J. Appl. Phys. **94** (2003) 7059

[12] R. Gago, J. Neidhardt, M. Vinnichenko, U. Kreissig, Zs. Czigány, A. Kolitsch, L. Hultman, W. Möller, Thin Solid Films **483** (2005) 89

[13] G. Abrasonis, R. Gago, I. Jiménez, U. Kreissig, A. Kolitsch, W. Möller, J. Appl. Phys. **98** (2005) 074907

[14] Á. Barna, B. Pécz, M. Menyhárd, Ultramicroscopy **70** (1998) 161

[15] Zs. Czigány, J. Neidhardt, I.F. Brunell, L. Hultman, Ultramicroscopy **94** (2002) 163

[16] J. Neidhardt, Zs. Czigány, I.F. Brunell, L. Hultman, J. Appl. Phys. **93** (2003) 3002

[17] J. Neidhardt, L. Hultman, Zs. Czigány, Carbon **42** (2004) 2734

[18] S.M. Rossnagel, J. Vac. Sci. Technol. A **7** (1989) 1025

[19] J.J. Cuomo, J.P. Doyle, J. Bruley, J.C. Liu, Appl. Phys. Lett. **58** (1991) 46

Fe Implanted Ferromagnetic ZnO

K. Potzger, S. Zhou, H. Reuther, A. Mücklich, F. Eichhorn, N. Schell,
W. Skorupa, M. Helm, J. Fassbender, T. Herrmannsdörfer[1] and T.P. Papageorgiou[1]
[1]Hochfeld-Magnetlabor Dresden, Forschungszentrum Rossendorf, P.O. Box 510119, 01314 Dresden

In the field of spintronics [1], diluted magnetic semiconductors (DMS) are worldwide under intense investigation. DMS are "conventional" semiconductors doped with transition metal (TM) or rare-earth ions which are diluted within the host matrix and ferromagnetically aligned via an indirect magnetic coupling [2-7]. The existence of DMS based on Mn doped p-type ZnO [2] and V, Ti, Fe, Co or Ni doped n-type ZnO [7] has been predicted by theory. However, currently only n-type conducting ZnO films or single crystals are available. Recent reviews of experimental work in the field, are given by S.J. Pearton *et al.* [8] and Ü. Özgür *et al.* [9]. Among other systems, n-type ZnO doped with Fe has been confirmed experimentally [10-12] to exhibit ferromagnetism at room temperature. In some cases, especially at high processing temperatures, unwanted secondary phases are formed inside the ZnO matrix, which are responsible for the ferromagnetic properties [11]. One way to overcome this problem is the use of ion beam doping at low temperatures and thus far from thermal equilibrium [12-14]. In any case, structural analysis methods with high sensitivity are necessary in order to exclude secondary phases.

In this report it will be shown that Fe-implantation into ZnO single crystals at a temperature of 623 K can lead to the formation of ferromagnetic α-Fe nanoparticles. On the other hand, Fe ions implanted at a temperature of 253 K are diluted within the ZnO host matrix and develop a ferromagnetic coupling.

Table 1: Implantation conditions for ^{57}Fe ions for the investigated samples (T_{imp} = implantation temperature, Φ = ion fluence). The implantation angle was set to 7° in order to avoid channeling effects. The calculated implantation profile thus has a Gaussian shape with a maximum atomic concentration ρ_{max} indicated. The sample identifiers refer to low/high fluence and low/high temperature.

Sample	Φ (cm^{-2})	ρ_{max} (%)	T_{imp} (K)
LFHT	4×10^{15}	0.5	623
HFHT	4×10^{16}	5	623
LFLT	4×10^{15}	0.5	253
HFLT	4×10^{16}	5	253

For this purpose we used commercially available, hydrothermally grown ZnO single crystals that have been Zn-face epi-polished by the supplier. These samples were implanted with ^{57}Fe ions at different temperatures and ion fluences (for a sample register and abbreviations see Table 1). The implantation energy of 180 keV yielded a projected range of $R_P = 79 \pm 33$ nm (TRIM code [15]). Prior to implantation, the virgin samples were characterized by X-ray diffraction (XRD, Siemens D5005), inductively coupled plasma mass spectrometry (ICPMS), and superconducting quantum interference device (SQUID, Quantum Design MPMS) magnetometry. It was found that the virgin crystals are perfectly single crystalline showing a contamination below 20 ppm for Cu, Ni and Fe and below 0.1 ppm for the other transition metals. Most important is the fact that even at low temperatures (5 K) all of the virgin samples behave purely diamagnetic upon magnetization reversal.

After implantation, the four samples (Table 1) were analyzed using SQUID magnetometry. It was found that only two of them, i.e. the HFHT and the LFLT samples exhibit a pronounced hysteresis loop upon magnetization reversal at $T = 5$ K (Table 2). After subtraction of the diamagnetic background, a saturation magnetization of $M_S = 0.30\ \mu_B$ ($M_S = 1.3\ \mu_B$) per implanted Fe ion and a coercivity of $H_C = 2.4 \times 10^4$ A m^{-1} ($H_C = 4.8 \times 10^3$ A m^{-1}) for the HFHT (LFLT) sample is determined. The hysteretic behavior remains also at $T = 300$ K (Fig. 1a, b). However, for the HFHT sample a more drastic decrease of M_S and H_C as compared to the LFLT sample is observed with increasing temperature (Table 2).

Table 2: Saturation magnetization M_S and coercivity H_C determined by SQUID magnetometry. The measurement temperatures are indicated.

Sample	M_S (μ_B per implanted Fe)		H_C (A m^{-1})	
	5 K	300 K	5 K	300 K
HFHT	0.30	0.17	2.4×10^4	2.4×10^3
LFLT	1.3	1.0	4.8×10^3	4.0×10^3

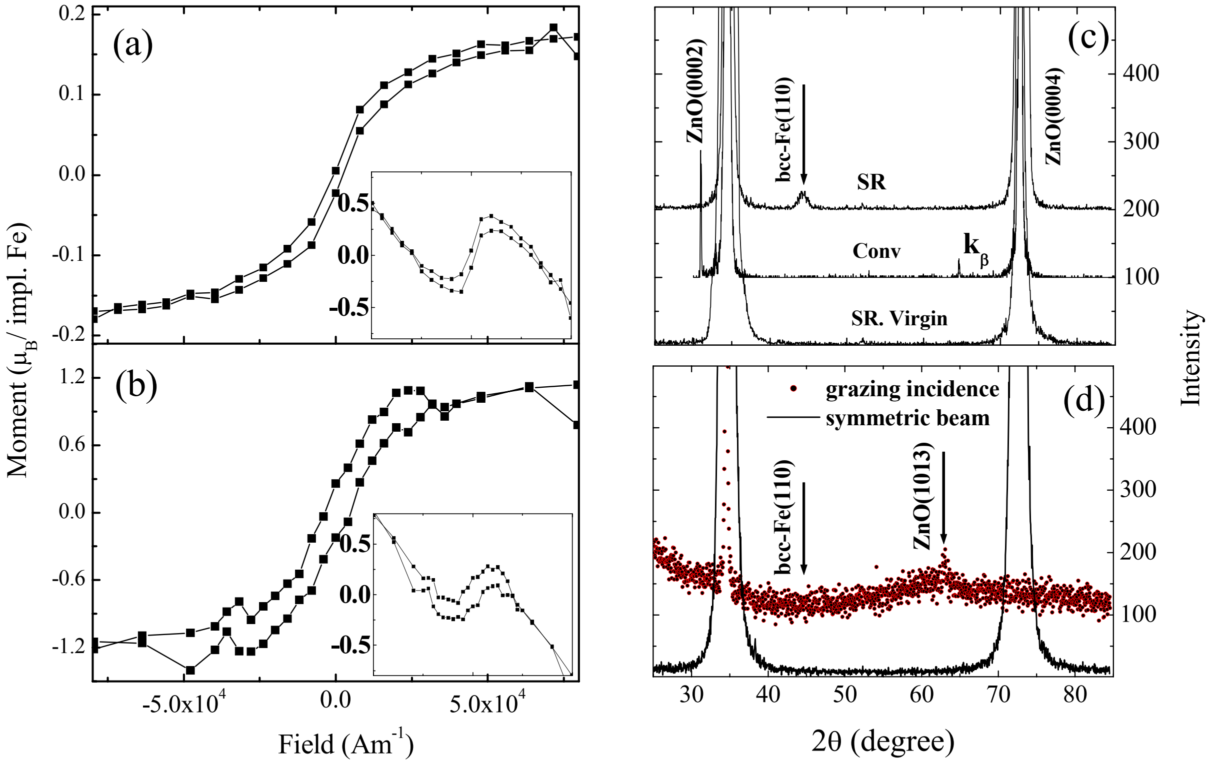

Fig. 1: Magnetization reversal recorded at 300 K using SQUID magnetometry for the HFHT (a), and the LFLT (b) sample. The inset shows the magnetization prior to background subtraction in $\mathrm{A\,m^{-1}}$ with respect to the substrate volume. The horizontal axes have the same scale. (c) Conventional (Conv.) and SR-XRD pattern (symmetric $2\theta/\omega$ scan) for the HFHT sample compared to a virgin sample. Small Fe nanoparticles can be detected only by SR-XRD. (d) SR-XRD pattern for the LFLT sample: no secondary phases are found by either a symmetric $2\theta/\omega$ scan or a grazing incidence scan.

In order to analyze the microscopic origin of the measured ferromagnetic properties of the HFHT- and LFLT-samples, synchrotron X-ray diffraction (SR-XRD) with monochromatic X-rays of 0.154 nm wavelength and room-temperature conversion electron Mössbauer spectroscopy (CEMS) were used for all samples. In contrast to conventional XRD, the much higher X-ray intensity in SR-XRD allows one to detect also small amounts of very tiny nanoparticles. Fig. 1c shows a symmetric $2\theta/\omega$ scan for the HFHT sample. Sharp, high intensity peaks from bulk ZnO are visible at $2\theta \sim 34.4°$ and $2\theta \sim 72.6°$. At $2\theta \sim 44.5°$, a rather broad and low intensity peak originating from α-Fe(110) with a theoretical Bragg angle of $2\theta = 44.66°$ occurs. The nanoparticle size is estimated to be around 8 nm using the Scherrer formula [16]. Apart from α-Fe, no other phases are detected. In order to support these findings by real space methods, cross-sectional transmission electron microscopy (TEM, Philips CM 300) has been performed. The nanoparticles could be identified indirectly due to a Moiré-pattern with a visible diameter of about 6 – 12 nm (Fig. 2, inset) at a distance of only 50 nm from the surface. Concordantly, the maximum iron concentration was found at $R_{EDX} = 51 \pm 38$ nm by means of energy-dispersive X-ray microanalysis (EDX). In CEMS, only the HFHT sample exhibits a fraction of ^{57}Fe probe nuclei, that show a clear magnetic hyperfine splitting (sextet) corresponding to a magnetic hyperfine field of $B_{HF} = 30.5$ T (Fig. 2) which is - due to size effects - slightly smaller than the known value of metallic α-Fe ($B_{HF} = 33.0$ T). This fraction covers 12.5% of the ^{57}Fe nuclei absorbing the incident γ-radiation. Its isomer shift (*IS*) of 0.06 mm/s with respect to α-Fe doubtlessly represents metallic Fe^0. The remaining Fe in the HFHT sample exhibits ionic charge states showing no ferromagnetic hyperfine splitting. The interpretation of these fractions is, in part, rather difficult. The best fit has been obtained using one singlet representing a Fe^{3+}-state reported already elsewhere [17] and two quadrupole-split lines representing Fe^{2+} states (Fig. 2). The absence of a quadrupole splitting (*QS*) of Fe^{3+} excludes $\mathrm{ZnFe_2O_4}$-precipitates since there is always an electric field gradient present at the octahedral sites [18, 19]. $\mathrm{Fe_3O_4}$ usually does not show a quadrupole splitting in the Fe^{2+} states [17] and can thus also be excluded indirectly. These conclusions are consistent with those obtained from SR-XRD.

The interpretation of the origin of the ferromagnetic properties of the HFHT sample is thus straightforward: During implantation metallic Fe-nanoparticles are formed. This is due to higher migration of Fe at the elevated temperature as compared to the HFLT and LFLT samples. Moreover, the required diffusion length for nanoparticle formation is much shorter at the higher fluence as compared to the LFHT sample (Table 1). The superparamagnetic limit of Fe nanoparticles is described by the relaxation time

$$\tau = \tau_0 \exp[\frac{E_A V}{k_B T}],$$

where E_A is the anisotropy energy density (5×10^4 J/m^3 for Fe), V is the particle volume and k_B is the Boltzmann constant. τ_0 amounts to $\sim 10^{-9}$ s [20]. Thus at $T = 5$ K and a measurement time of ~ 100 s which is typical for SQUID magnetometry the critical nanoparticle diameter for superparamagnetic behavior results to 4 nm. From the above discussed structural analysis we know that all nanoparticles diameters are larger than this value and should intrinsically behave like ferromagnetic α-Fe bulk material. Taking into account the fraction of 12.5 % of metallic Fe found by CEMS and a magnetic moment of 0.30 μ_B per implanted Fe ion, a value of $M_S = 2.4$ μ_B per Fe atom within the metallic nanoparticles is determined in agreement with the known value for bulk Fe of 2.2 μ_B. The slight overestimation probably results from the fact that the CEMS spectrum contains also a small fraction resulting from superparamagnetic Fe nanoparticles which could not be resolved in CEMS. At 300 K, the hysteresis loop obtained by SQUID magnetometry exhibits a distinct decrease of M_S down to 0.17 μ_B per implanted Fe ion, and of H_C down to 2.4×10^3 A m^{-1} compared to the measurement at 5 K (Table 2). Both effects result from the size distribution of the Fe-nanoparticles, since with increasing temperature also larger nanoparticles become superparamagnetic or approach to the superparamagnetic limit.

In contrast to the other three samples, a long-time CEMS spectrum (500 hours) recorded for the LFLT sample ($T_{imp} = 253$ K, $\Phi = 4 \times 10^{15}$ cm^{-2}) exhibits only a single line corresponding to a Fe^{3+} state. Thus the majority of the detected ions are ferric but nonmagnetic similar to the results for Fe doped SnO$_2$ [5]. A decision about the existence of a ferromagnetic sextet could not be provided along with CEMS due to the small counting rate resulting from the low fluence implanted and the lower uniformity of the Fe lattice sites as compared to the samples implanted at 623 K. However, for the LFHT, HFLT and especially the ferromagnetic LFLT sample no secondary phases have been found using SR-XRD (Fig. 1d) and no metallic Fe^0 states have been detected using CEMS.

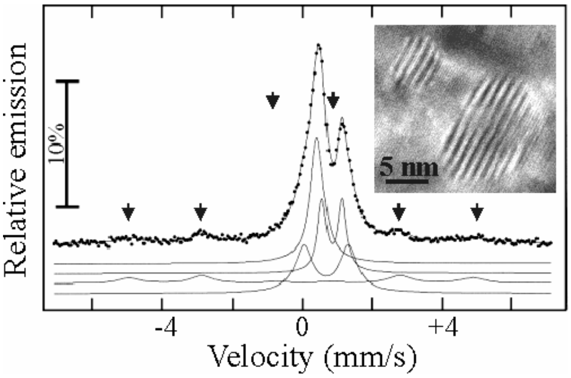

Fig. 2: CEMS of the HFHT sample recorded at 300 K. The fit curves represent (from top to bottom) a single emission line corresponding to a Fe^{3+} state ($IS = 0.53$ mm/s with respect to α-Fe), a quadrupole split emission line ($QS = 0.6$ mm/s) corresponding to a Fe^{2+} state ($IS = 0.69$ mm/s), a sextet line resulting from a magnetic hyperfine splitting of a metallic Fe^0 state ($IS = 0.06$ mm/s) and a strongly quadrupole split line ($QS = 1.3$ mm/s) of a Fe^{2+} state ($IS = 0.78$ mm/s). The inset shows Moiré contrasts measured using TEM that can be associated with small metallic Fe nanoparticles corresponding to the CEMS results. The arrows indicate the sextet.

Consequently, the implanted Fe-ions are diluted within the ZnO host matrix. Thus - in sharp contrast to the HFHT sample - the ferromagnetic behavior of the LFLT sample (Fig. 1b) results from an indirect exchange interaction between diluted Fe ions similar to the one reported in Ref. 5 for the case of Fe doped SnO$_2$. Surprisingly the ferromagnetic behavior occurs at much lower Fe concentrations than that reported in Ref. 5 or predicted by theory. In the case of diluted Fe^{3+} (5 μ_B per ion), 28 % and in the case of diluted Fe^{2+} (6 μ_B per ion), 23 % of the implanted ions would contribute to the ferromagnetic interaction. The minimal Fe-Fe distance for the LFLT sample can be estimated to be 1.3 nm. Considering the different implantation temperatures and fluences affecting the diffusion behavior and the ion induced damage in the four investigated samples, a crude explanation of their behavior with respect to the formation of a DMS can be provided: An implantation temperature of 623 K causes a broadening of the Fe implantation profile. Hence, a ferromagnetic state of the Fe ions that are diluted within the LFHT sample cannot be established due to the low local Fe concentration. Within the LFLT sample however, the implantation profile is sharper and therefore the local Fe concentration is large enough to form a room-temperature DMS. For the lack of a DMS state within the high fluence implanted samples this argumentation does not hold because the total amount of implanted Fe ions was 10 times larger than for the LFHT sample, but with many associated defects. Thus these defects introduced during implantation must play a key role for the DMS formation. Rutherford backscattering (RBS) analysis shows that the damage level for both high fluence implanted samples are similar, i.e. $\chi_{min}\sim 65\,\%$ [21], while the damage level for the LFLT sample is much lower ($\chi_{min} = 30\,\%$, χ_{min} of the virgin samples: 3 %). Such defects affect the transport properties of ZnO [22] and thus the path of ferromagnetic coupling.

In summary, 180 keV Fe implanted ZnO single crystals can develop ferromagnetic properties that are either caused by α-Fe nanoparticles or an indirect coupling of the Fe ions in a DMS system, depending on the details of ion fluence and implantation temperature. Detailed structural analysis is required to rule out secondary phases.

The presented results have been recently published as K. Potzger *et al.*, Appl. Phys. Lett. **88** (2006) 052508.

References

[1] S.A. Wolf, D.D. Awschalom, R.A. Buhrman, J.M. Daughton, S. von Molnár, M.L. Roukes, A.Y. Chtchelkanova, D.M. Treger, Science **294** (2001)1488

[2] T. Dietl, H. Ohno, F. Matsukura, J. Cibert, D. Ferrand, Science **287** (2000) 1019

[3] V. Barzykin, Phys. Rev. B **71** (2005) 155203

[4] D.J. Priour, E.H. Hwang, S. Das Sarma, Phys. Rev. Lett. **92** (2004) 117201

[5] J.M.D. Coey, A.P. Douvalis, C.B. Fitzgerald, M. Venkatesan, Appl. Phys. Lett. **84** (2004) 1332

[6] J.M.D. Coey, M. Venkatesan, C.B. Fitzgerald, Nat. Mater. **4** (2005) 173

[7] K. Sato, H. Katayama-Yoshida, Semicond. Sci. Tech. **17** (2002) 367

[8] S.J. Pearton, D.P. Norton, K. Ip, Y.W. Heo, T. Steiner, J. Vac. Sci. Technol. B **22** (2004) 932

[9] Ü. Özgür, Ya.I. Alivov, C. Liu, A. Teke, M.A. Reshchikov, S. Doğan, V. Avrutin, S.-J. Cho, H. Morkoç, J. Appl. Phys. **98** (2005) 041301

[10] M. Venkatesan, C.B. Fitzgerald, J.G. Lunney, J.M.D. Coey, Phys. Rev. Lett. **93** (2004) 177206

[11] J.H. Shim, T. Hwang, S. Lee, J.H. Park, S.-J. Han, Y.H. Jeong, Appl. Phys. Lett. **86** (2005) 082503

[12] A.Y. Polyakov, A.V. Govorkov, N.B. Smirnov, N.V. Pashkova, S.J. Pearton, K. Ip, R.M. Frazier, C.R. Abernathy, D.P. Norton, J.M. Zavada, R.G. Wilson, Mat. Sci. Semicon. Proc. **7** (2004) 77

[13] E. Rita, U. Wahl, J.G. Correia, E. Alves, J.C. Soares, Appl. Phys. Lett. **85** (2004) 4899

[14] D.P. Norton, M.E. Overberg, S.J. Pearton, K. Pruessner, J.D. Budai, L.A. Boatner, M.F. Chisholm, S.J. Lee, Z.G. Khim, Y.D. Park, R.G. Wilson, Appl. Phys. Lett. **83** (2003) 5488

[15] J. Ziegler, J. Biersack, U. Littmark, The Stopping and Range of Ions in Matter, Pergamon Press, New York, 1985, SRIM 2000 code, www.srim.org

[16] B.D. Cullity, Elements of X-ray Diffraction, Reading, MA: Addison-Wesley, 1978, p. 102

[17] E. Murad, Phys. Chem. Miner. **23** (1996) 248

[18] H.B. Mathur, A.P.B. Sinha, C.M. Yagnik, Indian J. Pure Ap. Phy. **5** (1967) 155

[19] B.J. Evans, S.S. Hafner, H.P. Weber, J. Chem. Phys. **55** (1971) 5282

[20] R. Waser, Nanoelectronics and Information Technology, Wiley-CH, Weinheim, 2003, p. 624

[21] χ_{min} is the channeling minimum yield in RBS/C, which is the ratio of the backscattering yield when the impinging beam is aligned parallel to a crystallographic axis to that for a random beam incidence. Therefore, an amorphous sample shows a χ_{min} of 100 %, while a perfect single crystal corresponds to a χ_{min} of 1-2 %.

[22] S.O. Kucheyev, C. Jagadish, J.S. Williams, P.N.K. Deenapanray, M. Yano, K. Koike, S. Sasa, M. Inoue, K. Ogata, J. Appl. Phys. **93** (2003) 2972

A Transient Electrical Model of Charging for Ge Nanocrystal Containing Gate Oxides with DRAM-Like Behavior

V. Beyer, J. von Borany and A. Mücklich

Since the mid 90s the multidot memory has been of major interest in the research activities of emerging non-volatile memory devices [1, 2]. This memory concept is based on a layer of well separated Si or Ge nanocrystals (NCs) embedded in the transistor gate oxide substituting the floating gate of classical Flash-memory devices. Among various techniques for NCs fabrication [3] ion-beam synthesis (IBS) has been established as a versatile method to produce a high density (> 10^{12} cm^{-2}) of small (< 3 nm) Ge or Si NCs in thin gate oxides [4, 5]. Multidot memories likewise promise short programming / write times (t_{prog} < 1 µs), low operating voltages (|V_{prog}| n 10 V) as well as high endurance (10^9 cycles) with preferably long data retention [1, 6, 7].

In this paper, the write performance of Ge NCs containing gate oxides is investigated by means of MOS (metal-oxide-semiconductor) capacitors. It has been shown that under specific preparation conditions a self-organized, δ-like layer of Ge NCs close to the Si/SiO$_2$ interface (IF) is formed during IBS in thin SiO$_2$ films [8, 9]. For this case, where the charge transfer occurs in the direct tunneling (DT) regime, charging by holes (instead of electrons) offers the advantage of enhanced data retention due to the higher tunneling barrier ϕ_b [10]. Thus, we studied the time dependence of hole charging under substrate accumulation conditions. The evaluation is based on capacitance-voltage (*C-V*) measurements of MOS capacitors which restrict the programming time to $t_{prog} \geq 3$ ms. To predict the write performance with respect to memory applications for much shorter times (t_{prog} ~ µs), this experimental study will be accompanied by simulations using a physical / electrical model of the device structure.

The MOS capacitors were prepared as follows: ^{74}Ge$^+$-ions (12 keV, 5×10^{15} cm^{-2}) were implanted at room temperature in a 20 nm thick thermally grown gate oxide on <100> p-type Si (ρ ~ 10 Ω cm). After a standard cleaning step in H$_2$O$_2$ / H$_2$SO$_4$, rapid thermal annealing (RTA) was carried out at 950°C for 30 s in Ar to recover the damaged oxide and to form the Ge NCs. Afterwards, metal dots (A = 0.1 mm^2) were fabricated by Al-sputtering, photolithographic patterning and a 400°C, 15 min furnace anneal in N$_2$.

The Ge profile and the corresponding NC-distribution in the gate oxide were characterized by Rutherford backscattering spectrometry (RBS) and transmission electron microscopy (TEM), respectively. The RBS measurements were obtained by 1.7 MeV He$^+$ ions at a scattering angle of 170° and an incident angle of 70° to improve the depth resolution. The TEM analysis was carried out on a Philips CM300 microscope operating at 300 kV. The *C-V* characteristics of the MOS capacitors were measured by a Keithley 590 CV analyzer at 100 kHz using a programmable external voltage source (Keithley 237). The measurement sequence is shown in Fig. 1.

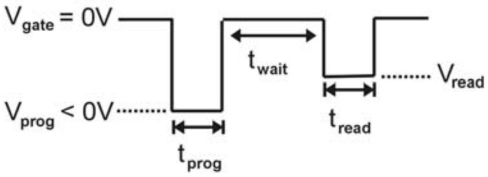

Fig. 1: Sequence of the applied voltage pulses to investigate the programming characteristic of MOS capacitors.

The MOS devices were charged by negative square voltage pulses ($-3\text{ V} \geq V_{prog} \geq -8\text{ V}$) with durations of $3\text{ ms} \leq t_{prog} \leq 30$ s. After 1 ms at the reference potential of 0 V, a read pulse was applied with $|V_{read}| < |V_{prog}|$ for $t_{read} = t_{prog}$ while the *C-V* data $C(V_{read})$ are recorded. V_{read} is adjusted in such a way that at the beginning of the read-cycle $C(V_{read})$ is about $C_{FB}(V_{FB,0})$ which avoids any influence of the reading process itself on the NCs charge state after programming. C_{FB} denotes the flatband capacitance and $V_{FB,0}$ the flatband voltage of the initial (uncharged) MOS capacitor. Thus, the flatband voltage shift - as a measure of the stored charge - is easily obtained as $\Delta V_{FB} = V_{read} - V_{FB,0}$. Profiting by a short data retention (~ s) and the high endurance this procedure was repeated for each data point (V_{prog}, t_{prog}).

To enable a calculation of the charging characteristics $\Delta V_{FB} = f(V_{prog}, t_{prog})$, at first the size, density, and the position of the NCs had to be defined as input parameters for the transient model. Thus, the Ge profile and the corresponding NC distribution in the gate oxide were investigated by RBS and TEM, respectively. After annealing a

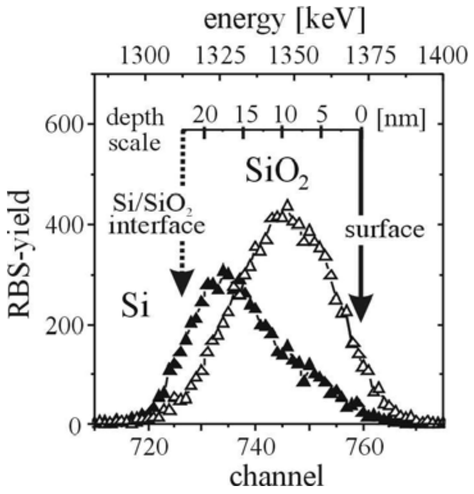

Fig. 2: Ge distribution after ion-implantation (△) and annealing (▲) as measured by RBS. After annealing the major part (~ 1.3×10^{15} cm^{-2}) of the remaining Ge is located in a close vicinity to the Si/SiO$_2$-IF.

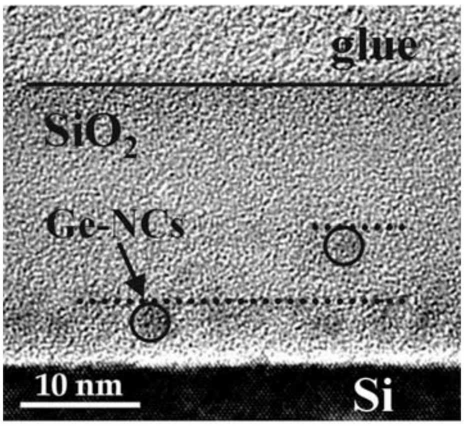

Fig. 3: Cross-sectional bright-field TEM-micrograph of the Ge implanted oxide after annealing. Primarily due to their very small size the Ge NCs are detected only by Z-contrast imaging.

significant redistribution of the initial (as-implanted) Ge profile towards the Si/SiO$_2$-IF is obtained from RBS in Fig. 2. A layer of separated Ge NCs forms in the oxide close to the IF as confirmed from TEM imaging (cf. Fig. 3). For the near-interface NCs a mean size of $d_{nc} \approx 2$ nm and a density of $N_{nc} \sim 1 \times 10^{12}$ cm^{-2} as a lower limit can be deduced. For a total oxide thickness of ~23 nm the tunneling oxide thickness varies between ~1 and 2.5 nm. An upper limit of the NC density of $N_{nc} \sim 7 \times 10^{12}$ cm^{-2} can be deduced from RBS if the amount of near-interface Ge (1.3×10^{15} cm^{-2}) contributes completely to equal sized NCs of 2 nm diameter.

Based on a floating-gate-like approach [11, 12] (see Fig. 4) this structure is modeled as an oxide containing a narrow distribution of equal-sized Ge NCs. The NCs are considered as an assembly of separated storage nodes with capacitances towards the substrate and gate electrode C_{tox} and C_{cox} representing the tunnel-(TOX) and the control-(COX) oxide, respectively.

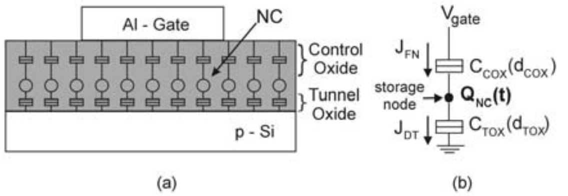

Fig. 4: (a) Structure model of a NCs containing MOS diode. (b) Equivalent circuit for one NC as a floating storage node (schematics derived after Ref. 13).

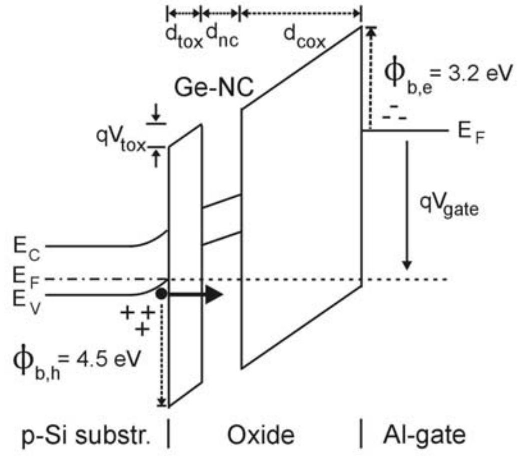

Fig. 5: Schematic band diagram of a MOS structure with a Al-gate and a Ge-NCs containing gate-oxide for a negative gate-voltage.

For negative programming voltages (V_{prog}) holes are transferred by a direct tunneling (DT) process from the accumulated p-Si substrate towards the Ge NCs (see a schematic band diagram in Fig. 5). V_{prog} is limited to low electric fields ($E_{ox} < 4$ MV/cm) to exclude Fowler-Nordheim (FN) injection of electrons or holes. Thus, the total current density simplifies to DT of holes $J_{DT,h}$ (see Refs. 14, 15)

$$J_{DT,h} = \frac{q^3 (m_0 / m_{ox,h})}{8\pi h \phi_{b,h}} E_{tox}^2 \Theta_{tox} \qquad (1)$$

where the transmission probability Θ_{tox} for holes through the tunnel-oxide is given for a parabolic dispersion relation in the Wentzel-Kramers-Brillouin (WKB) approximation by [14, 16]

$$\Theta_{tox} = \exp\left(- \frac{8\pi \sqrt{2 m_{ox,h}} \left(\phi_{b,h}^{3/2} - \left(\phi_{b,h} - |qV_{tox}| \right)^{3/2} \right)}{3hq|E_{tox}|} \right) \qquad (2)$$

Here, h denotes Planck's constant, q the elementary charge, m_0 the free electron mass, V_{tox} and

$E_{tox} = V_{tox}/d_{tox}$ are the voltage drop and the electric field across TOX, respectively. The tunneling barrier of holes $\phi_{b,h}$ and the effective mass for holes in the oxide $m_{ox,h}$ were set to $\phi_{b,h} = 4.5$ eV and $m_{ox,h} = 0.32\, m_0$ as assumed for hole valence band tunneling in a semi-empirical approach by Lee and Hu [16]. As the effective charge density Q_{nc} according to the whole capacitor surface is implicitly given by the integral over J_{DT} [12], the time dependent (transient) charging process of the NCs is calculated iteratively as

$$Q_{nc}(t_{i+1}) = Q_{nc}(t_i) + R_{nc} J_{DT}(V_{tox}, Q_{nc}(t_i))\Delta t\,. \quad (3)$$

where $R_{nc} = (\pi/4)\, d_{nc}^2\, N_{nc}$ presents the relative part of the capacitor area covered by Ge NCs. Equation (3) holds for small time increments Δt, hence the potentials within the gate oxide do not change significantly between the time steps t_i and t_{i+1}. The voltage drop across the tunneling oxide V_{tox} depends on the coupling factor k, the NCs charge Q_{nc} and the reduced applied gate voltage V'_{gate} according to [12, 17]

$$V_{tox}(t_i) = k\left(V'_{gate}(t_i) + \frac{Q_{nc}(t_i)}{\varepsilon_{ox} / d_{cox}} \right) \quad (4)$$

$$\text{with} \quad k = \frac{d_{tox}}{d_{tox} + (\varepsilon_{ox}/\varepsilon_{nc}) d_{nc} + d_{cox}} \quad (5)$$

To the benefit of simplified equations the charge is centered at the interface between the NCs and the control-oxide as usually presumed for floating-gate devices [12]. Correspondingly $\Delta V_{FB}(t)$ can be calculated using $Q_{nc}(t)$ from Eq. (3) by

$$\Delta V_{FB}(t_i) = -Q_{nc}(t_i) d_{cox} / \varepsilon_{ox}\,. \quad (6)$$

From the physical point of view, the NCs are characterized by their size d_{nc}, the dielectric permittivity $\varepsilon_{nc} \bullet \varepsilon_{Ge}$, the density N_{nc} and their position with respect to the Si/SiO$_2$-IF, i.e. d_{tox}. The latter one has the strongest influence on the charging properties. Due to the statistic processes of ion beam mixing at the Si/SiO$_2$-IF, phase separation and Ge redistribution during IBS, the spatial distribution of NCs is characterized by a variable distance of the NCs to the Si-substrate, i.e. each d_{tox} corresponds to a number of NCs with different values of $Q_{nc}(t)$ and J_{DT}. In the calculation this effect has been taken into account using a normalized Gaussian distribution of d_{ox} with a spread of σ.

Based on the structural parameters and the described theoretical model the programming characteristics $\Delta V_{FB} = f(V'_{gate}, \sigma, t)$ have been calculated and compared with experimental data, i.e. $\Delta V_{FB} = f(V_{prog}, t_{prog})$ (Fig. 6). For the simulations $d_{nc} = 2$ nm and $N_{nc} = 3 \times 10^{12}$ cm^{-2} have been used which leads to $R_{nc} \approx 10$ %. For these values a V_{FB}-shift of -7 V corresponds to ~ 2.5 holes per NC at an average. Assuming a fixed d_{tox} without any spread (i.e. $\sigma = 0$ nm) the simulations result in programming characteristics with a significant stronger slope (dotted lines) compared to the measured data points in a semi-log plot (see Fig. 6(a)). For increasing σ the slope becomes weaker as presented for $d_{tox} = 2.5$ nm in Fig. 6(a) (straight lines). A fit of the measured data leads to a value of $d_{tox} = 1.6$ nm with $\sigma = 0.5$ nm in reasonable agreement with the TEM results, which holds for all programming voltages (Fig. 6(b)). The charging saturates for $t_{prog} > 10$ s at $\Delta V_{FB,max} = V'_{gate}$. As in the calculation both $V_{FB,0}$ and the substrate surface potential ψ_S are neglected as constant terms, the difference V_{prog} - $\Delta V_{FB,max} \bullet -0.8$ V $\approx V_{FB,0}$ corresponds mainly to the work-function difference ϕ_{MS} between the Al-gate and the p-Si substrate. The simulations reveal that programming times of $t_{prog} < 1$ µs for $|\Delta V_{FB}|\ .\ 1$ V can be achieved with low programming voltages for a structure with

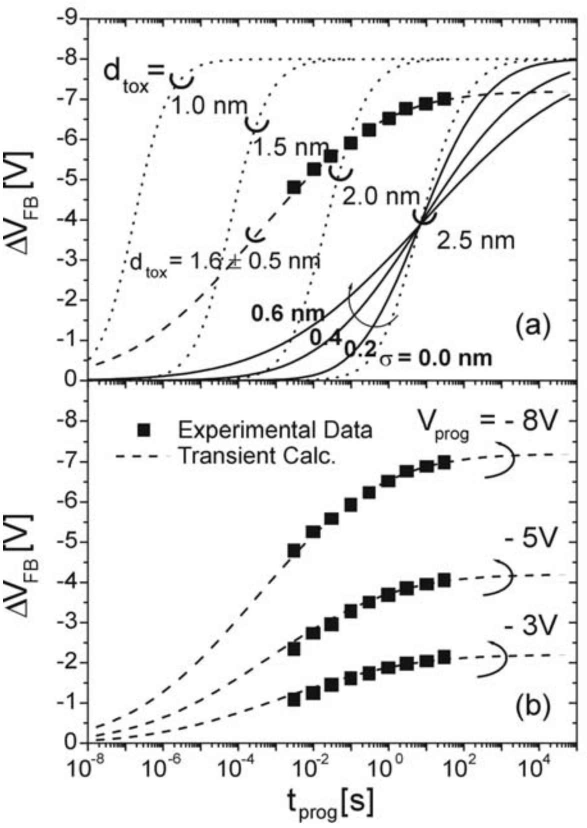

Fig. 6: (a) Comparison of the measured flatband voltage shift ΔV_{FB} ($V_{prog} = -8$ V) with the programming characteristics simulated for different spatial distributions of the Ge NCs: (i) 1.0 nm ≤ d_{tox} ≤ 2.5 nm const., i.e. $\sigma = 0$ nm (dotted lines), and (ii) $d_{tox} = 2.5$ nm with 0.2 nm ≤ σ ≤ 0.6 nm (straight lines). The dashed line indicates the best fit of the experimental result with $d_{tox} = (1.6 \pm 0.5)$ nm and $V'_{gate} = -7.2$ V. (b) The calculated distribution of d_{tox} holds for a series of transient programming characteristics with different programming voltages V_{prog} (V'_{gate}/V_{prog} is -7.2 V / -8 V, -4.2 V/ -5 V, and -2.2 V/ -3 V).

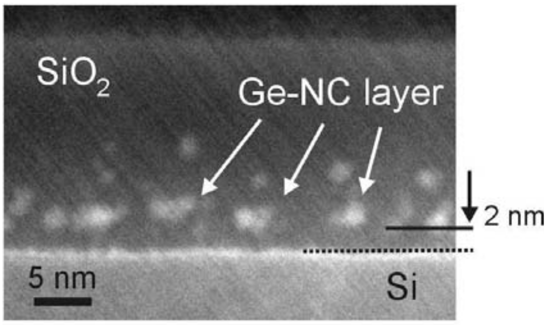

Fig. 7: HAADF STEM imaging of the NCs containing oxide. The Ge NCs are marked by the bright spots.

near-interface Ge NCs embedded in thin gate oxides. As due to the small distance of the NCs to the Si-substrate the charge holds just for seconds or minutes, this device shows more DRAM-like than non-volatile behavior.

Moreover, the high sensitivity of ΔV_{FB} to the value of d_{tox} (cf. Fig. 6(a)) allows an extraction of structural parameters of the NCs layer in the oxide by fitting the experimental measured charge characteristics. In particular the distribution of the NCs with respect to their distance to the Si/SiO$_2$-IF can be precisely determined. Recently, the results of the transient calculations presented in this paper were clearly confirmed by dark-field imaging in the scanning mode of TEM (STEM), see Fig. 7. Using a high-angle annular dark-field (HAADF) detector, a significantly improved Z-contrast of the Ge NCs is obtained compared to conventional bright-field imaging. From Fig. 7, the size of the NCs next to the Si/SiO$_2$-IF can be determined to $d_{nc} \approx 2$ nm and the tunneling distance to $d_{tox} - 1.5 \text{ nm} \leq 2$ nm at an average which is in an excellent agreement to $d_{tox} = (1.6 \pm 0.5)$ nm as deduced from the calculation.

In summary, a transient model of charging of gate oxides containing a NC layer close to the Si/SiO$_2$-IF has been developed. The close agreement between the calculated write characteristics and the experimental data clearly confirms the validity of the floating-gate like approach with DT as the dominant charge transfer process. The investigated structures enable short programming times and low operating voltages offering promising options for new multidot memory devices. In addition, the simulation of the experimental write characteristics allows to determine precisely the position of embedded storage nodes (here the Ge NCs) with respect to the Si/SiO$_2$-IF which is a crucial physical parameter for the charge storage behavior of the memory.

Acknowledgements

The work was performed in cooperation with Infineon Technologies Dresden and supported by the "Bundesministerium für Bildung und Forschung" of Germany. Special thanks to R. Grötzschel (FZR) and M. Klimiankou (Forschungszentrum Karlsruhe) for the RBS and HAADF STEM investigations, respectively.

References

[1] 2003 edition of the ITRS, http://public.itrs.net

[2] S. Tiwari, F. Rana, H. Hanafi, *et al.*, Appl. Phys. Lett. **68** (1996) 1377

[3] J. DeBlauwe, IEEE Trans. Nanotechnology **1** (2002) 72

[4] J. von Borany, T. Gebel, K.-H. Stegemann, *et al.*, Solid State Electron. **46** (2002) 1729

[5] C. Bonafos, M. Carrada, N. Cherkashin, *et al.*, J. Appl. Phys. **95** (2004) 5696

[6] S. Tiwari, J. Wahl, H. Silva, J. Welser, Appl. Phys. A **71** (2000) 403

[7] H. Hanafi, S. Tiwari, I. Khan, IEEE Trans. Electron Devices **43** (1996) 1553

[8] H. Heinig, T. Müller, B. Schmidt, *et al.*, Appl. Phys. A **77** (2003) 17

[9] V. Beyer, J. von Borany, in Materials for Information Technologies, ed. by E. Zschech, H. Mikolajick, Springer Verlag Berlin, 2005

[10] K. Han, I. Kim, H. Shin, IEEE Trans. Electron Devices **48** (2001) 874

[11] B. DeSalvo, G. Ghibaudo, G. Pananakakis, *et al.*, IEEE Trans. Electron Devices **48** (2001) 1789

[12] G. Groeseneken, H. Maes, J. VanHoudt, J. Witters, Basics of nonvolatile semiconductor memory devices, in NVSM Technology Piscataway, NJ: IEEE Press, 1998, chap. 1

[13] H. Wang, N. Takahashi, H. Majima, *et al.*, Jap. J. Appl. Phys. Part 1 **40** (2001) 2038

[14] K.F. Schuegraf, C. Hu, IEEE Trans. Electron Devices **41** (1994) 761

[15] Z.A. Weinberg, J. Appl. Phys. **53** (1982) 5052

[16] W.-C. Lee, C. Hu, IEEE Trans. Electron Devices **48** (2001) 1366

[17] B. DeSalvo, G. Ghibaudo, P. Luthereau, *et al.*, Solid-State Electron. **45** (2001) 1513

Light Emission and Charge Trapping in Er Doped Silicon Dioxide Films Containing Silicon Nanocrystals

A. Nazarov[1], J.M. Sun, I.N. Osiyuk[1], I.P. Tjagulskii[1], V.S. Lysenko[1], W. Skorupa,
R.A. Yankov and T. Gebel[2]

[1]*Institute of Semiconductor Physics, National Academy of Sciences of Ukraine*
Prospekt Nauki 45, 03028 Kyiv, Ukraine

[2]*nanoparc GmbH, Bautzner Landstrasse 45, D-01454 Dresden – Rossendorf, Germany*

Er implanted SiO_2 films have recently attracted considerable interest due to the possibility of making EL devices that operate at a wavelength of 1.54 µm, i.e. within the range of optical transparency of quartz optical fibers [1, 2]. The fabrication of such light emitting devices is fully compatible with Si based integrated circuit (IC) technology, thus permitting their integration into advanced Si ICs. Critical issues of the device performance are the relatively low emission efficiencies and the low currents that can be passed through the dielectric. It has been shown in a number of studies that the introduction of Si nanocrystals into Er-doped SiO_2 enables the intensity of the PL at 1.54 µm to be largely increased [3-5] while causing concurrently a somewhat reduced EL intensity [6]. However, the mechanism of attenuation of the Er associated EL at 1.54 µm after introducing Si nanoclusters into the SiO_2 matrix has not been elucidated. The present work provides new insights into the relationship between light emission efficiency and charge trapping in Er doped SiO_2 containing Si nanoclusters. The influence of the Si nanocluster density on both the capture of charge carriers at traps associated with the presence of Er and the resulting PL and EL at 1.54 µm is examined for the first time.

Si wafers with a 200 nm thick thermally grown SiO_2 film were used in the study. The depth profiles of the implanted Si^+ and Er^+ ions were calculated using TRIM 98 as a first approximation. Si^+ ions were implanted at two implantation energies of 35 and 80 keV, which generated a fairly flat-topped profile of 1.1 to 15 at.% excess silicon atoms over a depth region of 65 to 150 nm. After annealing at 1100°C in an N_2 ambient for 1 h necessary to form Si nanocrystals, Er^+ ions were implanted at 280 keV with a dose of 1×10^{15} cm^{-2} in such a way as to position the peak of their distribution about the central part of the Si clusters profile. Finally, the samples were annealed at 850°C in an ambient of N_2 for 30 min to reduce the amount of the implantation induced damage and activate the implanted Er^{3+} centers. The top electrodes were 100 nm indium-tin-oxide (ITO) layers patterned into circular dots with a diameter of 0.05 to 1.00 mm.

The formation of Si nanoclusters and Er^{3+} centers were monitored by PL measurements over the wavelength range of 600 to 900 nm and at 1535 nm using the 532 nm line of a Nd:YAG laser and the 633 nm line of a He-Ne laser with a power of 5 mW as the excitation sources, respectively. Measurements of the EL and charge trapping were carried out in a high field, constant current injection regime. Charge traps were studied over a wide range of cross sections using three levels of injected constant current density, namely 1×10^{-7}, 2×10^{-5} and 5×10^{-4} A cm^{-2}, with the last value of the current density being typical of the regime of EL excitation. During the current injection, negative (or positive) charges were trapped within the oxide layer, which caused a decrease (or increase) in the electric field distribution at the Si/SiO_2 interface. In order to maintain a constant current injection, one needs to shift the applied voltage as the trapped charges change. Charge trapping processes were studied under conditions of electron injection from the Si substrate into the oxide by measuring the shift of the applied voltage with the injected charge Q_{inj}. The absolute value of the net trapped charge was calibrated using the shift of the flat band voltage, ΔV_{FB}, extracted from the high frequency (1 MHz) capacitance-voltage (C-V) characteristics after injecting an electron charge of 1×10^{13} e/cm^2.

Figure 1(a) shows EL spectra measured over the wavelength range of 1450 to 1650 nm in Er implanted structures containing Si nanocrystals of different density. The peak at 1535 nm, which is characteristic of the intra-transition of the electron in the Er^{+3} ion from the excited $^4I_{15/2}$ state to the ground state, is clearly seen. A broad PL peak centered at 700 nm was observed as a result of the introduction into the oxide of an excess of Si atoms above 3 at.%. The position of the PL peak

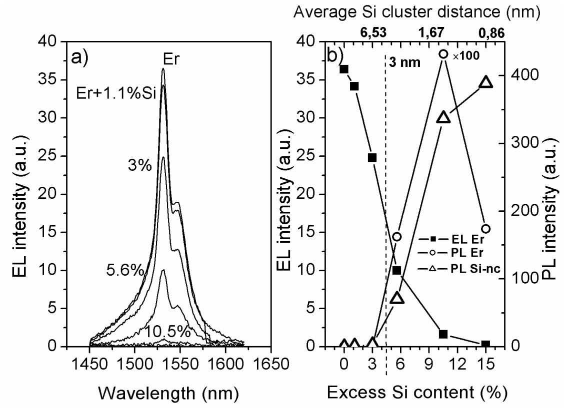

Fig. 1: (a) Electroluminescence (EL) spectra of the ITO-SiO_2-Si structures with SiO_2 containing Si nanoclusters and Er; (b) PL and EL intensity at 1535 nm wavelength and PL intensity at 707 nm wavelength in dependence on excess Si content.

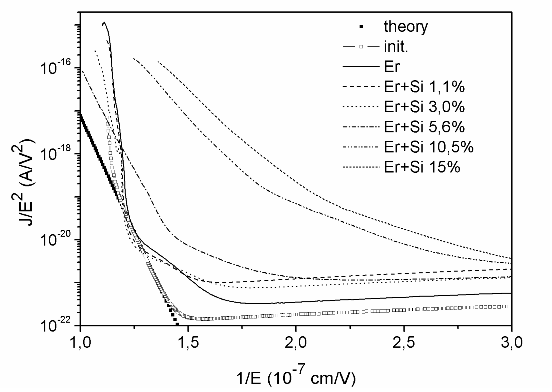

Fig. 2: Injected current density divided by the square of the electric field versus the reciprocal electric field in the ITO-Si-rich SiO_2:Er-Si MOS structure with different excess Si concentrations.

did not change with increasing Si concentration and corresponds to the formation of Si nanoclusters with a mean size of about 3 nm [7]. The relative PL intensity of the emission peak of the Si nanocrystals and the peak at 1535 nm due to the presence of Er^{3+} ions are shown in Fig. 1(b). One can see that the increase in Si nanocluster density results in an increased PL intensity of the infrared peak from Er^{3+}. A maximum value is observed at the excess Si content of 10 at.% . In contrast, the EL intensity at 1535 nm is strongly quenched at such an excess silicon concentration. It should be noted that the intensity of the infrared EL diminishes strongly with decreasing the average distance between the silicon clusters below the mean free path of the hot electrons (or heat up distance), which equals to approximately 3 nm [8]. Our calculations show that for Si nanoclusters with a mean size of 3 nm, the average distance between the nanoclusters becomes smaller than 3 nm for an excess Si content of more than 5 at.% (see Fig. 1(b)). Thus the average energy of the electrons will decrease with increasing the fraction of direct tunneling among the silicon nanoclusters.

It should also be noted that in our case EL from Si nanoclusters has not been observed at the currents and voltages used, up to the breakdown of the dielectric. This can serve as evidence of the ineffective excitation of the Si nanoclusters by the high energy injected electrons. Due to the inefficient excitation of silicon nanoclusters, the EL from the Er centers can not be efficiently excited through the strong energy transfer from the excited silicon clusters to the Er centers compared with the PL excitation processes.

The current density, J, versus inverse electric field, E, was plotted in Fowler-Nordheim (FN) coordinates ($ln(J/E^2)-1/E$) for different values of the excess Si content as shown in Fig. 2. The characteristics so obtained reveal that up to a 3 at.% excess Si content the current injection through the dielectric can be described by the Fowler-Nordheim electron tunneling mechanism [9]. For a higher concentration of the excess Si atoms of 5.6 at.%, the effective potential barrier for FN tunneling decreases from 3.15 to 2.90 eV. This points to the influence of trapping on the electron tunneling through the triangular potential barrier from Si to the SiO_2 conduction band, the so-called trap-assisted tunneling mechanism [10]. At a higher excess Si content the transition from FN tunneling to direct tunneling between silicon clusters can be clearly seen (Fig. 2).

The dependence of the trapped charge on the injected electron charge is shown in Fig. 3. The starting unimplanted oxide exhibits practically no charge trapping following electron injection at a charge density of 10^{13} e/cm². After the same amount of injection the Er^+ implanted sample shows considerable positive charge trapping. This indicates the presence of hole traps with a giant cross-section ($\sigma_{h0} > 10^{-13}$ cm²) in the Er-implanted oxide. The subsequent introduction into the Er-implanted oxide of Si nanoclusters results in additional electron trapping and points towards the formation of negative charge traps with a giant cross-section ($\sigma_{e0} > 10^{-13}$ cm²). Furthermore, an increase in the Si nanoclusters density up to 15% is accompanied by an increased magnitude of the trapped negative charges (see inset to Fig. 3).

Computer data processing of the $C_{OX}\Delta V_{CC}$ vs. Q_{inj} curves was done on the basis of the model for the first order charge carrier trapping [11, 12]:

$$Q^i_t = Q^i_{t\,max} [1 - exp(-\sigma_i Q_{inj})] ,$$

where Q^i_t and $Q^i_{t\,max}$ are respectively the trapped and the maximal trapped charge at the i^{th} trap, and σ_i is the cross-section of the i^{th} trap. The most

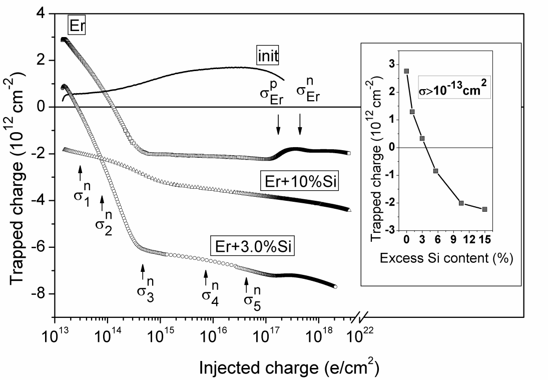

Fig. 3: Net trapped charge calculated from the change in voltage applied to the ITO-SiO_2-Si structure in a constant current regime as a function of injection charge from the Si substrate, for Er and Si implanted SiO_2. Inset: Charge on the traps with capture cross-section of more than 10^{-13} cm^2 as a function of excess Si content.

important findings may be summarized as follows. The starting structure exhibits only hole traps with cross-sections $\sigma_{h1} \approx 6.2 \times 10^{-15}$ cm^2, $\sigma_{h2} \approx 1.2 \times 10^{-15}$ cm^2 and $\sigma_{h3} \approx 4.7 \times 10^{-17}$ cm^2. The implantation of Er, apart from hole traps of a giant cross-section ($> 10^{-13}$ cm^2), introduces into the oxide an appreciable concentration of electron traps of a large cross-section $\sigma_{e1} \approx 7.0 \times 10^{-14}$ cm^2 and $\sigma_{e2} \approx 7.0 \times 10^{-15}$ cm^2 as well as a specific pair of electron and hole traps with similar cross-sections $\sigma_e^{Er} \approx 3.0 \times 10^{-18}$ cm^2 and $\sigma_h^{Er} \approx 6.0 \times 10^{-18}$ cm^2, respectively. The additional implantation of Si, resulting in the formation of Si nanoclusters, apart from creating electron traps of a giant cross-section, increases too the concentration of electron traps with the following cross-sections: $\sigma_{e1} \approx 7 \times 10^{-14}$ cm^2, $\sigma_{e2} \approx 7 \times 10^{-15}$ cm^2 and $\sigma_{e3} \approx 1.5 \times 10^{-15}$ cm^2. However, as the concentration of the extra Si exceeds 5.6 at.%, the capture of electrons at these traps shows a dramatic decrease (see Fig. 3). For excess Si concentrations above 3 at.%, there is also a considerable reduction in the charge trapping at the electron/hole trap pair of a small cross-section ($\sim 10^{-18}$ cm^2) that is formed following the implantation of Er.

Thus, it is believed that large Er inclusions, which trap effectively positive charge, create in their vicinity defects that can capture electrons. The introduction of Si nanocrystals into the matrix enhances the process of electron trapping at these crystallites as well as in the presumably disordered surroundings, which may lead to Coulomb scattering of the injected electrons and attenuation of their interaction with the Er centers around them. Since the excitation of the Er through the excitation of the Si clusters is not efficient in the EL process, we suggest that Er excitation is mainly due to direct impact excitation of hot electrons [13], which are accelerated by the high electric field in the SiO_2 conduction band after FN tunnelling injection from the Si substrate. The scattering of hot electrons by both the charged defects and the Si nanoclusters results in a reduction of the average energy and the average impact excitation cross section of the Er centres around the negatively charged nanoclusters. Increasing the Si nanocrystal density (for concentrations of the excess Si larger than 5 at.%) alters the conductance from FN tunnelling to direct tunnelling through silicon clusters. The tunnelling electrons have insufficient energy to excite Er centres, which subsequently reduces the EL efficiency.

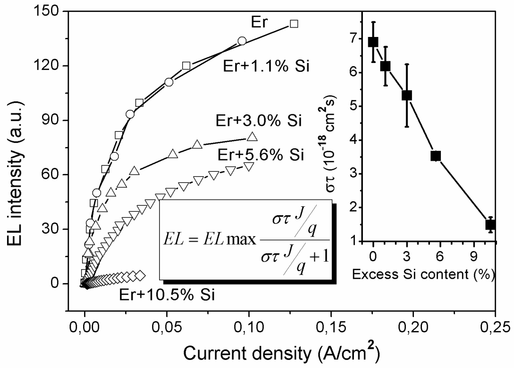

Fig. 4: EL intensity vs. current density for an ITO-Si-rich SiO_2:Er-Si MOS structure for different concentrations of the excess Si atoms. Inset: The $\sigma\tau$ as a function of excess Si content calculated from the data presented in Fig. 4 using the expression $EL=EL_{max}\ \sigma\tau J/(\sigma\tau J+1)$, where the τ is the overall lifetime of the Er, and σ is the excitation cross-section of the Er centers.

The defect influence on the product of the effective electron life time *(τ)* and the effective cross-section of excitation *(σ)* can be estimated from the dependence of the EL intensity on current density [6] in Fig. 4. As can be seen from the inset to Fig. 4, the value $\sigma\tau$ decreases about seven times with increasing excess Si content from 1.1 to 15 at.%. In a study [3] of the dependence of the Er luminescence decay time on the excess Si concentration from 2.4 to 11 at.% after annealing at the same temperature of 1100°C, the lifetime of the Er-induced PL was found to decrease only by a factor of about 2 (from 4.4 to 2.1 ms). This means that the excitation cross section of Er was reduced by a factor of more than 3 in the EL excitation by introducing Si clusters with an excess Si content of up to 15 at.%.

Such different behavior of the PL and EL depending on the Si nanocrystals density is associated primarily with the different nature of the excitation in the vicinity of the Er^{3+} ion. In the PL excitation process, the excitation of Er occurs via naturally charged exciton relaxation created in the Si nanoclusters, which does not alter significantly the electric field around the Si nanocrystals. In the EL excitation process, electrons trapped at the Si nanoclusters act repulsively to the hot electrons for excitation of both of the nanoclusters and the Er centers in the surroundings. This could be one of the reasons for the insufficient excitation of both the EL from nanoclusters and the Er centers with introducing discrete Si clusters. The larger the number of the Si nanocrystals surrounding an Er inclusion, the more efficient screening of the electric field among the clusters occurs, which is essential for the heating of electrons. Consequently, in considering the excitation of Er ions by electrons passing through an amorphous SiO_2 layer, one should take into account their interaction with the defect environment of the Er inclusions.

In conclusion, it has been found that the introduction of Si nanocrystals results in the creation of negative charge traps of a giant cross-section, which can scatter efficiently "hot" electrons. Higher concentrations of the Si nanoclusters alter the mechanism of current passage through the dielectric. In this case, electrons are most likely transported in the SiO_2 via Si nanocluster mediated tunnelling, and therefore they interact very little with the Er inclusions.

The presented results have been recently published as A. Nazarov *et al.*, Appl. Phys. Lett. **86** (2005) 151914.

References

[1] L. Pavesi, J. Phys.: Condens. Matter **15** (2003) R1169

[2] M. Sopinskyy, V. Khomchenko, Current Opinion in Solid State and Materials Sci. **7** (2003) 97

[3] M. Fujii, K. Imakita, K. Watanabe, S. Hayashi, J. Appl. Phys. **95** (2004) 272

[4] K. Watanabe, M. Fujii, S. Hagashi, J. Appl. Phys. **90** (2001) 4761

[5] A.J. Kenyon, C.E. Chryssou, C.W. Pitt, T. Shimizu-Iwayama, D.E. Hole, N. Sharma, C.J. Humphreys, J. Appl. Phys. **91** (2002) 367

[6] M.E. Castagna, S. Coffa, M. Monaco, L. Caristia, A. Messina, R. Mangano, C. Bongiono, Physica E **16** (2003) 547

[7] B. Garrido, M. Lopez, C. Garcia, A. Perez-Rodriduez, J.R. Morante, C. Bonafos, M. Carrada, A. Claverie, J. Appl. Phys. **91** (2002) 798

[8] D.J. DiMaria, T.N. Theis, J.R. Kirtley, F.L. Pesavento, D.W. Dong; S.D. Brorson, J. Appl. Phys. **57** (1985) 1214

[9] Z.A. Weinberg, J. Appl. Phys. **53** (1982) 5052

[10] S. Fleischer, P.T. Lai, Y.C. Cheng, J. Appl. Phys. **72** (1992) 5711

[11] V.V. Afanas'ev, V.K. Adamchuk, Prog. Surf. Sci. **47** (1994) 301

[12] A.N. Nazarov, T. Gebel, L. Rebohle, W. Skorupa, I.N. Osiyuk, V.S. Lysenko, J. Appl. Phys. **94** (2003) 4440

[13] Y.S. Han, S.Y. Seo, J.H. Shin, Appl. Phys. Lett. **79** (2001) 178

Multiple Implantations into Si: Influence of the Implantation Sequence on Ion Range Profiles

M. Posselt, M. Mäder, A. Lebedev and R. Grötzschel

Advanced silicon technology uses successive implantations of p- and/or n-dopants without any intermediate annealing steps. A characteristic example is the engineering of the regions of source, drain, extension and halo (cf. [1-3] and references therein). The sequence of the implantations may have a significant influence on the final distribution of dopants and radiation damage. In particular, it affects the as-implanted profiles of dopants, if in one or more implantation steps the direction of ion incidence is close to a major crystallographic axis of the silicon substrate. For example, the extension implantation is often performed perpendicularly to the wafer surface, i.e., nearly parallel to the [001] channel. The defect production in previous implantations steps influences the shape of dopant and damage distributions in a subsequent channeling implantation step, since these defects may lead to increased dechanneling. This work reports on investigations of the influence of the implantation sequence on the shape of as-implanted depth profiles of dopants. The experimental results are discussed qualitatively and can be reproduced quantitatively by atomistic computer simulations.

Two examples of consecutive implantations into the [001] channel direction were considered: (i) 35 keV B followed by 50 keV As (sequence 1) and (ii) 50 keV As followed by 35 keV B (sequence 2). The implanted fluences are given in the figures shown below. The p-type (001) Si samples were cleaned in hydrofluoric acid (HF) before the implantation. Prior to implantation, the alignment of the ion beam into the [001] direction was performed by the standard procedure employed in Channeling Rutherford Backscattering Spectrometry (RBS/C) [4]. The implantations were carried out at room temperature. The B and As depth profiles were measured by Secondary Ion Mass Spectrometry (SIMS) at Evans East (East Windsor, NJ, USA) using a PHI Quadrupole SIMS instrument. The B and As detection limits were 10^{15} and 10^{14} cm^{-3}, respectively. The accuracy of the depth calibration was 5%. Furthermore, RBS/C analysis was performed in order to determine the as-implanted damage.

The SIMS data obtained for sequence 1 are shown by the thick lines in Figs. 1 (a) and (b). For comparison, the As profiles in samples without B pre-implantation are depicted in Fig. 1 (c). The results clearly demonstrate that the defects formed by the B implantation (5.6×10^{15} cm^{-2}) cause a significant dechanneling of the subsequently implanted As ions. This reduces the penetration depth of As considerably. Due to the relatively low fluences of the As implantations, the dechanneling of the As ions is mainly caused by the defects produced by the B implantation, and the damage buildup during the As implantation plays only a minor role. This is confirmed by the observation that for the three fluences considered the shape of the As depth distributions is similar. Furthermore, the comparison between the shape of the boron profile obtained at the low fluence of 2.3×10^{13} cm^{-2} with that for 5.6×10^{15} cm^{-2} shows that with increasing boron fluence the implanted boron ions are more and more dechanneled. This means that at a boron fluence of 5.6×10^{15} cm^{-2} a certain amount of defects is formed. The SIMS data for sequence 2 are depicted in Figs. 2 (a) and (b). The boron profile in a sample pre-implanted with an As fluence of 1.1×10^{13} cm^{-2} is very similar to the profile in a sample without As pre-implantation (cf. Fig. 1 (a)). For the higher arsenic fluences, the defects formed during the As implantation lead to an increased dechanneling of the subsequently implanted B ions. The damage profiles obtained by RBS/C measurements (Fig. 2 (d)) show that defect accumulation occurs during both the arsenic and the boron implantations. At the highest As and B fluences, the maximum damage level approaches the amorphization threshold. The comparison with RBS/C data obtained after As implantation leads to the conclusion that the subsequent B implantation does not significantly increase the disorder within the region of the defects formed by the As implantation.

The measured B and As depth distributions were simulated using the Crystal-TRIM program. It treats the penetration of ions into the target by a sequence of binary collisions with target atoms in the closest environment of the ion trajectory. Since many details of the Crystal-TRIM code have been provided in previous papers [5-8], the following description is limited to the values of certain parameters and to the models for damage buildup and

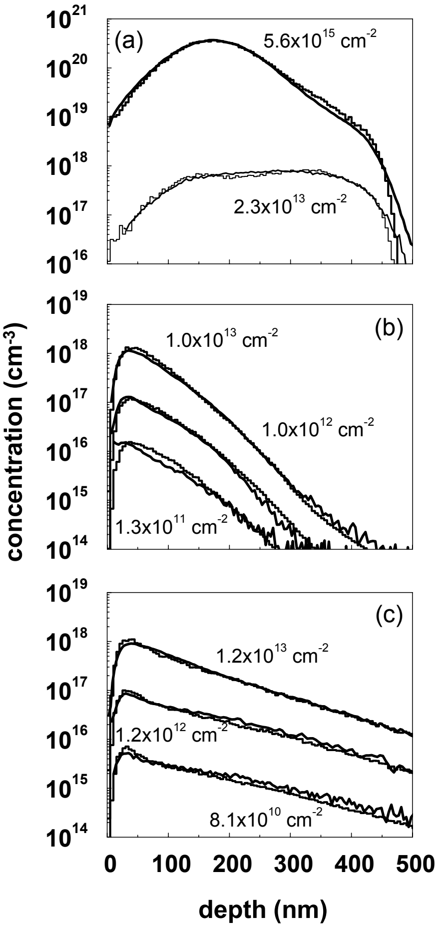

Fig. 1: Implantation sequence 1: 35 keV B (5.6×10^{15} cm^{-2}) followed by 50 keV As (1.3×10^{11}, 1.0×10^{12}, 1.0×10^{13} cm^{-2}). In (a) and (b) the thick lines show the B and As depth distributions measured by SIMS, respectively. The B profile in (a) was determined after the first implantation step. For comparison, the measured As depth profiles in samples without B pre-implantation are also given (c). In (a) the thin line shows SIMS data obtained after B implantation at 2.3×10^{13} cm^{-2}. The histograms depict the results of computer simulations.

dynamic annealing. The thickness of the native oxide layer on the (001) Si sample was set to 0.5 nm, i.e., smaller than the default value of 1.5 nm. This assumption is justified due to the HF cleaning procedure before the implantation. The parameters C_λ and C_{el} used in the model for the electronic energy loss of an incident ion in a collision with a target atom [5] have the following values: $C_\lambda = 1.01$, $C_{el} = 1.1$ for B and $C_\lambda = 0.9$, $C_{el} = 1.57$ for As. The first parameter is employed to calculate the electronic energy loss averaged over all impact parameters, using the ZBL electronic stopping cross-section [9]. The second parameter describes the impact-parameter dependence of the electronic energy loss in a modified Oen-Robinson model [10].

The Crystal-TRIM code simulates only the ballistic processes during ion bombardment, but not the subsequent relaxation processes which are responsible for the formation of the as-implanted defect structure. Therefore, a phenomenological description is used to treat the influence of defect production on the trajectories of the implanted ions [7, 8]. It is based on results of molecular dynamics simulations and on experimental investigations. The fundamental quantities of the model are the nuclear energy deposition per target atom E_n^A and the probability p_d that the implanted ion collides with an atom of a damaged region. The first quantity can be determined exactly by the consideration of the ballistic processes. It increases monotonically throughout the implantation since each implanted ion contributes to the nuclear energy deposition. The second quantity describes the damage level in the target and depends on E_n^A, the ion species, the target temperature and the incident ion flux. E_n^A and p_d are local quantities, i.e., their values may vary in dependence on the considered volume element of the target. The collision of the ion with atoms in a damaged region is treated in the same manner as projectile-target collisions in an amorphous target. This is a simplifying assumption about the nature of the defects formed during ion implantation. Molecular dynamics simulations showed that the as-implanted defect structure depends on the ion mass [11, 12]. The implantation of heavy ions leads to dense collision cascades. Therefore, after the fast relaxation of the ballistic disorder a considerable number of complex defects may be formed. Some of them are small amorphous regions or amorphous pockets, as assumed in the simplified damage model. On the other hand, light ion implantation with a comparable local nuclear energy deposition per atom yields a smaller percentage of complex defects since the collision cascades are more dilute. Temperature and ion flux influence the dynamic annealing during the ion bombardment [13, 7, 8]. The phenomenological description used in Crystal-TRIM considers two simple but extreme cases: (i) the damage buildup and (ii) the dynamic annealing (cf. [7], equations (1) and (2)). In both cases, for low values of E_n^A the damage probability p_d grows linearly with E_n^A. In the damage buildup model the local region is amorphized ($p_d = 1$), if p_d exceeds the threshold p_t ($p_t \leq 1$). If dynamic annealing prevails, the local damage saturates at a constant level p_S ($p_S \leq 1$) when p_d exceeds p_S. The model parameters, i.e., the parameter C_a which characterizes the linear increase, and the threshold p_t or p_S, depend on the ion species, the target temperature and the ion flux. In the present work the damage accumulation model is applied to simulate the As implantation ($C_a = 10.67$ meV^{-1}, $p_t = 0.12$), whereas the dynamic annealing model is used for the B implantation ($C_a = 1.6$ meV^{-1},

$p_S = 0.01$). These assumptions are consistent with the results of experimental investigations that show that at room temperature the defect formation by heavy ions, such as As, is dominated by the damage buildup, whereas for light ions, such as B, the dynamic annealing prevails [13, 14]. Figures 1 (a), 1 (c), and 2 (a) illustrate that Crystal-TRIM simulations with the above damage models are able to reproduce the SIMS profiles very well. Note that the damage models for B and As contain only two model parameters that are independent of ion fluence and energy.

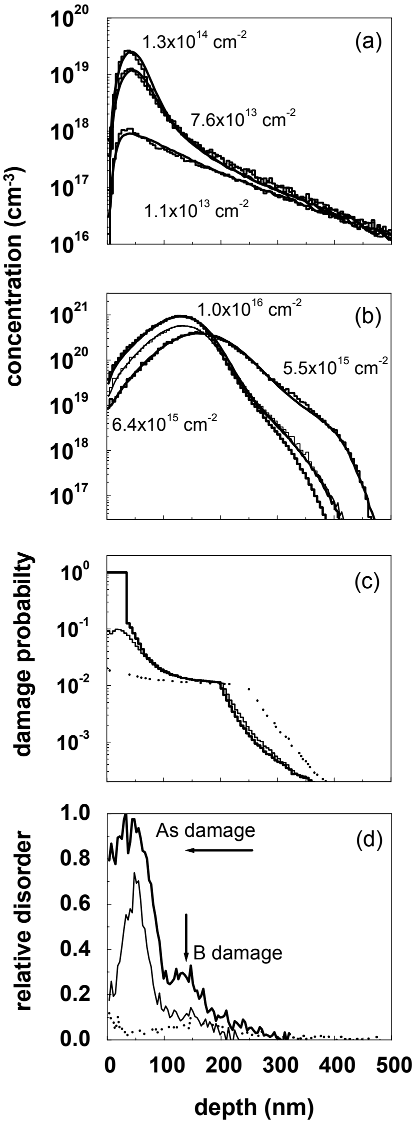

Fig. 2: Implantation sequence 2: 50 keV As (a) followed by 35 keV B (b). Three cases are shown: $1.0 \times 10^{16}\,\mathrm{cm}^{-2}$ B after $1.3 \times 10^{14}\,\mathrm{cm}^{-2}$ As, $6.4 \times 10^{15}\,\mathrm{cm}^{-2}$ B after $7.6 \times 10^{13}\,\mathrm{cm}^{-2}$ As, and $5.5 \times 10^{15}\,\mathrm{cm}^{-2}$ B after $1.1 \times 10^{13}\,\mathrm{cm}^{-2}$ As. The As profiles in (a) were measured after the first implantation step. Continuous lines and histograms depict SIMS data and results of computer simulations, respectively. For the three cases given above, the thick, the thin and the dotted lines show the depth dependence of the damage probability (c) and the depth profiles of the relative disorder which was determined by RBS/C (d).

In this work the phenomenological description of defect formation within the framework of the Crystal-TRIM code is extended to multiple implantations with different ion species. It is assumed that, during a certain implantation step *i*, a given damage model (damage buildup or dynamic annealing) is used to determine the partial damage probability p_d^i as a function of the nuclear energy deposition E_n^{iA} within this step. The total damage probability is determined by the sum of the damage probabilities p_d^{jE} obtained at the end of all previous implantation steps *j* and p_d^i. If this sum exceeds 1, it is reset to 1. For example, in the second step of sequence 1, the total damage probability is the sum of the value obtained at the end of the B implantation and the partial damage probability during the As implantation. In both implantation steps, the partial damage probabilities are determined in the same manner as in the case of single B or As implantations. Figures 1 (b) and 2 (b) demonstrate that the ion range distributions in multiple implantations can be simulated very well using the extended damage model. It should be emphasized that the model is tested under conditions where the shape of the range profiles is most sensitive to dechanneling by defects, i.e., for two consecutive channeling implantations at different fluences. The good agreement with the SIMS data indicates that the partial damage probability obtained at the end of a certain implantation step is a unique characteristic of the damage formed in this step, and that this quantity can be employed to determine its contribution to the dechanneling of the ions implanted in subsequent steps. Consequently, the extended model should be generally applicable to multiple implantations with different ions species. The depth dependence of the damage probability at the end of the implantation sequence 2 is given in Fig. 2 (c). The comparison with Fig. 2 (d) shows that the damage probability has a similar dependence on depth as the relative disorder. The depth distribution of the relative disorder is somewhat shallower than that of the damage probability. This may be due to the overestimation of the stopping cross-section for channeled He in the analysis of the RBS/C spectra, i.e., in the transformation of the energy to the depth scale. The absolute values for the damage probability and the relative disorder differ considerably. This is not surprising since the data shown in Fig. 2 (d) were simply obtained by normalizing to the random yield without any detailed considerations regarding the nature of the defects which cause the dechanneling of the He ions [15]. On the other hand, the damage probability (Fig. 2 (c)) was calculated in the framework of the phenomenological model described above, which uses the simplified assumption that the as-implanted defect structure consists of amorphous pockets. These defects have a strong influence on the ion trajectories so that a small damage probability suffices to cause significant dechanneling.

Acknowledgements

The authors thank Dr. M.S. Denker (Evans East) for the SIMS analysis and for valuable comments.

The present results have been recently published as M. Posselt *et al.*, Appl. Phys. Lett. **87** (2005) 043109.

References

[1] P.M. Zeitzoff, in: Semiconductor Fabtech, 10th Edition, Henley Publishing, London, 1999, p. 275

[2] T. Ghani, K. Mistry, P. Packan, M. Armstrong, S. Thompson, S. Tyagi, M. Bohr, Symp. VLSI Tech. Dig., 2001, p. 17

[3] D. Onimatsu, K. Shibahara, in: Extended Abstracts, Int. Conf. on Solid State Devices and Materials, Tokyo, 2001, p. 184

[4] W.-K. Chu, J.W. Mayer, M.-A. Nicolet, Backscattering Spectrometry, Academic Press, New York, 1978

[5] M. Posselt, Radiat. Eff. Defects Solids **130/131** (1994) 87

[6] M. Posselt, B. Schmidt, C.S. Murthy, T. Feudel, K. Suzuki, J. Electrochem. Soc. **144** (1997) 1495

[7] M. Posselt, L. Bischoff, J. Teichert, Appl. Phys. Lett. **79** (2001) 1444

[8] M. Posselt, L. Bischoff, J. Teichert, A. Ster, J. Appl. Phys. **93** (2003) 1004

[9] J.F. Ziegler, J.P. Biersack, U. Littmark, The Stopping and Range of Ions in Solids, Pergamon Press, New York, 1985

[10] O.S. Oen, M.T. Robinson, Nucl. Instr. Meth. **132** (1976) 647

[11] M.-J. Caturla, T. Diaz de la Rubia, L.A. Marques, G.H. Gilmer, Phys. Rev. **B 54** (1996) 16683

[12] M. Posselt, Mater. Res. Soc. Symp. Proc. **647** (2001), O2.1.1

[13] R.D. Goldberg, J.S. Williams, R.G. Elliman, Nucl. Instr. Meth. B **106** (1995) 242

[14] F.F. Morehead, Jr., B.L. Crowder, Radiat. Eff. **6** (1970) 27

[15] J.R. Tesmer, M. Nastasi, J.C. Barbour, C.J. Maggiore, J.W. Mayer (Editors), Handbook of Modern Ion Beam Material Analysis, Materials Research Society, Pittsburgh, 1995

Homogenization of the Melting Depth in SiC on Si Structures during Flash Lamp Irradiation

M. Voelskow, W. Skorupa, M. Smith[1] and R. McMahon[1]

[1]Department of Engineering, University of Cambridge
Trumpington Street, Cambridge CB2 1PZ, United Kingdom

The current technology for growing 3C-SiC films epitaxially on Si-substrates is based on chemical vapor deposition (CVD) at 1350°C. The control of defects in the initial stages of deposition is crucial for the ultimate quality of the 3C-SiC layer. However, due to the relatively high misfit of 21 % between the lattice parameters of Si and 3C-SiC, the defect density in the SiC layer is very high (~ 10^{12} cm^{-2}). For the successful application of epitaxially grown 3C-SiC films in microelectronics technology a significant reduction of the defect density is necessary.

The irradiation of thin silicon carbide layers on silicon substrates with intense light pulses from lasers or flash lamps can give a marked improvement in the layer properties [1]. Transient melting of the silicon immediately beneath the SiC/Si interface allows the SiC layer, which is highly stressed after growth, to relax. However, in pulsed melting of monocrystalline materials, the liquid-solid interface is facetted, as observed in initial studies of flash lamp annealing by Heinig *et al.* [2]. Melting and regrowth therefore lead to pronounced surface relief, as shown in Fig. 1(a), making the substrates unsuitable for further processing.

This contribution reports a method of controlling the melt depth, thereby suppressing faceted melting and excessive surface roughness, overcoming a major limitation of liquid phase processes. The approach involves implanting enough carbon into the silicon substrate below the SiC layer to create a layer with an elevated melting temperature to act as a "melt stop."

The melt process then takes place as shown in Fig. 1(b). Although initial melting below the SiC is faceted, increasing the pulse energy causes the molten regions to join to produce a continuous molten zone up to the melt stop. After the pulse is over and the sample starts to cool down, the implanted layer acts as a seed for the recrystallization of the molten silicon layer. Therefore it is necessary to ensure that the implantation temperature is high enough to avoid excessive damage to the crystalline structure of this region.

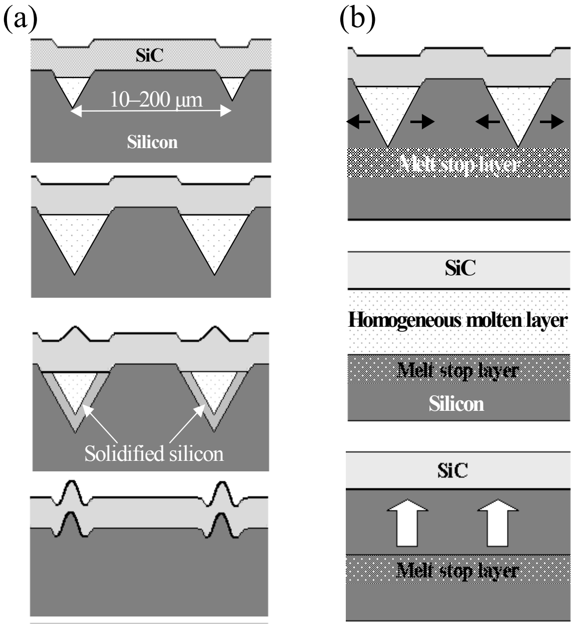

Fig. 1: Schematic representation of the melting and re-solidification behavior during the flash lamp annealing on a thin SiC-on-Silicon wafer for (a) non-implanted sample and (b) implanted (with melt stop) sample.

The effect of the melt stop technique was initially investigated using plain silicon wafers. From previous experiments, regarding the flash lamp heating of silicon, the degree of surface roughness is more pronounced on a free silicon surface than on a surface covered with silicon carbide. After the determination of the optimal implantation and annealing conditions for minimizing the surface roughness for pure silicon samples, a melt stop layer was implanted into a SiC/Si structure well behind the interface. For this purpose, 18-nm-thick 3C-SiC films were grown epitaxially on Si-substrates by CVD at 1350°C. Subsequently a high dose (3×10^{17} cm^{-2}) of carbon ions was implanted at an energy of 200 keV through the SiC film into the bulk silicon to a defined depth behind the Si/SiC interface. To limit the damage in the SiC top layer the implantation was carried out at a temperature of 600°C. The profile calculation using the TRIM computer code [3] predicts a carbon rich melt stop layer with a thickness of about 200 nm and a maximum carbon

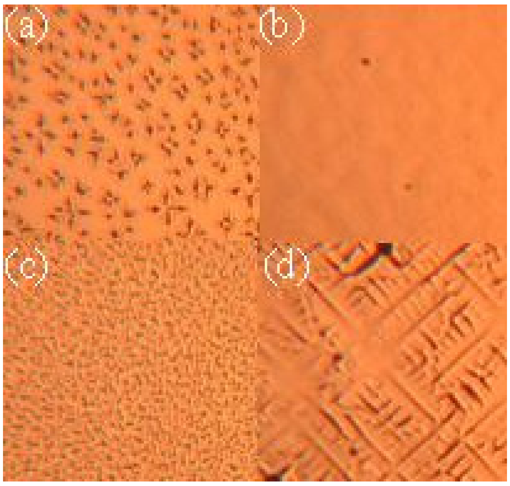

Fig. 2: Optical microscope observations for melt stop in a SiC on Si sample. Each figure represents a 0.5 mm square. (a) 2.9 kV (onset of melting). Simulations predict onset of melting will occur at 2.95 kV. (b) 3.4 kV (uniform melting of silicon). Simulation predicts melting of about 60 nm. Melting increases slowly as temperature is rising, 66°C above melt temperature (c) 3.5 kV (onset of melting of silicon below the implanted profile). Simulation predicts melting of bulk silicon at 3.52 kV. Temperature is now over 100°C above the melting point of silicon. (d) 3.1 kV (non-implanted sample). Deep melting is already occurring in the substrate.

concentration of 30 at.% at a depth 500 nm. The implanted zone has a predominantly crystalline structure containing 3C-SiC precipitates having a mean diameter of 4 nm.

Inspection of the silicon-carbon phase diagram [4] shows that the addition of just a small percentage of carbon to silicon leads to an significant increase of the silicon melting temperature. For example, the admixture of 10 % carbon to silicon results in a melting temperature of approximately 2000°C. Consequently, the carbon implanted intermediate layer should represent an effective barrier to the deep facetted melting of silicon.

For the pulse heating the Rossendorf flash apparatus [5] has been used. The pulse time, used for the experiments was 3 ms and the preheating temperature was 850°C. All samples were flashed under argon atmosphere.

In Fig. 2 optical micrographs of the carbon implanted samples, which were flashed at different energies, are shown in comparison with a non implanted sample. At a relatively low flash voltage of 2.9 kV, melting of the surface is incomplete, resulting in a mosaic of melted and un-melted parts. Increasing the flash voltage to 3.4 kV causes the regions to coalesce, forming a continuous molten surface layer above the melt barrier. For this case a very low surface roughness is obtained.

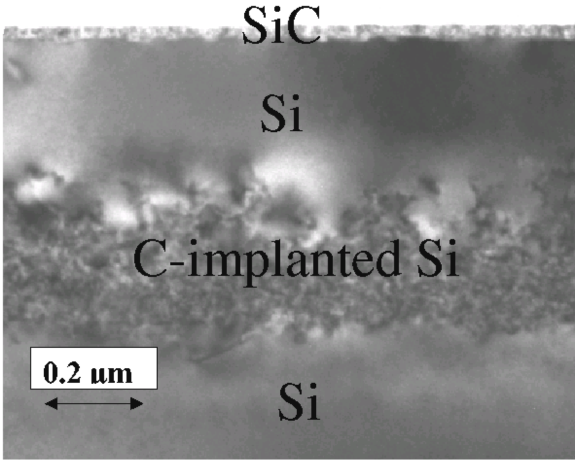

Fig. 3: XTEM of a flash lamp annealed SiC on silicon sample, with a carbon implanted layer.

If the flash energy is increased to 3.5 kV, bulk melting starts behind the carbon melt barrier, resulting in a very rough surface after recrystallization. In comparison to the carbon implanted sample, the non implanted surface shows a rough surface at any energy above 3.1 kV, with the degree of roughness increases with increasing flash energy or rather with increasing melting depth.The pulse energies (voltages) corresponding to the onset of melting below the SiC layer and the threshold for deep melting into the silicon substrate have been calculated using a model for the flash lamp process [1], modified to incorporate the dependence on melting temperature arising from the carbon implantation. The comparison made in Fig. 2 shows the model and experimental work are consistent.

In Fig. 3 a cross-sectional transmission electron microscopy (XTEM) micrograph of a flashed SiC/Si structure is shown. The flash voltage was 3.3 kV, sufficient to ensure melting up to the melt stop. The thin silicon carbide layer on top of a mostly defect free upper silicon substrate layer is clearly visible, whereas the region between 400 and 600 nm is characterized by the occurrence of a high concentration of small silicon carbide precipitates having their origin in the high dose of implanted carbon ions. The effective suppression of facetted melting is confirmed by the absence of surface morphology. Consequently, the wafer surface remains flat regardless of the molten silicon interface layer. Lateral mass transport due to capillary waves [6], a consequence of the 10 % difference in density of solid and liquid silicon, may occur, but a melt stop layer significantly reduces the height of the hillocks by limiting the volume of liquid silicon.

The use of a melt stop gives an additional benefit in that effective annealing can be achieved over a range of process conditions (approximately 3.0 - 3.5 kV), increasing the tolerance to lateral inhomogeneities in energy density, variations in energy from flash to flash and differences in wafer structure.

Apart from its application for the improvement of heteroepitaxial silicon carbide on silicon structures there should be a potential of the melt stop technique for semiconductor doping too. Using a melt stop layer beneath an initial ion implanted dopant profile it should be possible to get after the flash lamp melting, depending on the segregation coefficient of the implanted species, either a rectangular profile (high segregation coefficient) or a very sharp dopant peak near the surface (low segregation coefficient). Moreover, the melt stop technique is equally applicable to laser induced melting, opening the way for the wider application of liquid phase processes.

Acknowledgements

This work was supported by the EU, project No GRD 1-2001- 40466. Moreover, we do gratefully acknowledge the support of the European FLASiC consortium and, especially, the kind support of W. Anwand, D. Panknin, A. Mücklich and T. Schumann, all at FZ Rossendorf.

The presented results have been recently published as M. Voelskow *et al.*, Appl. Phys. Lett. **87** (2005) 241901.

References

[1] M. Smith, R. McMahon, M. Voelskow, W. Skorupa, Appl. Phys. Lett. **96** (2004) 4883

[2] K.-H. Heinig, M. Voelskow, J. Matthaei, Proceedings of the International Conference on Energy Pulse and Particle Beam Modification of Materials, Dresden, 1984

[3] J.F. Ziegler, J.P. Biersack, U. Littmark, The Stopping and Ranges of Ions in Solids, New York, Pergamon, 1985, Vol. 1

[4] E.A. Brandes, G.B. Brook, Smithells Metals Reference Book, 7th ed., Butterworth-Heinemann, Oxford, 1998, p. 11

[5] W. Anwand, W. Skorupa, L. Rebohle, T. Trautmann, S. Tamme, T. Grass, International Topical Workshop on Heteroepitaxy of 3C-SiC on Silicon and its Application to Sensor Devices, Krippen, Germany, 2005

[6] D.K. Fork, G.B. Anderson, J.B. Boyce, R.I. Johnson, P. Mei, Appl. Phys. Lett. **68** (1996) 2138

Resonant Impurity Bands in Semiconductor Superlattices

D. Stehr, C. Metzner[1], M. Helm, T. Roch[2] and G. Strasser[2]
[1]Institut für Technische Physik I, Universität Erlangen, Erwin-Rommel-Str. 1
D - 91058 Erlangen, Germany
[2]Institut für Festkörperelektronik, TU Wien, Floragasse 7, 1040 Wien, Austria

Semiconductor superlattices, consisting of a periodic sequence of thin layers of different semiconductors, can serve as a model system for a wealth of phenomena in solid state physics. The artificial periodicity in one dimension (the growth direction of the epitaxial layer) allows one to create tailored band structures with so called minibands and minigaps, which are much narrower than the bands (and gaps) in natural bulk crystals. Such structures have enabled researchers the first observation of phenomena like Bloch oscillations and Wannier-Stark ladders [1].

A fundamental problem in semiconductor physics is the existence of localized states in addition to extended band states, which are unavoidable due to disorder and doping, and give rise to a metal insulator transition as a function of doping density [2]. In an effective mass framework, the limit of low doping and zero compensation is equivalent to a system of isolated hydrogen atoms, resulting in the well known shallow impurity levels located below the conduction band. At higher doping densities, impurity bands are formed due to the interaction between doping atoms and eventually the impurity band develops into a band tail of localized states. The metal-insulator transition (MIT) usually occurs while the Fermi energy is located in the impurity band [3]. In a slightly metallic semiconductor, the MIT can be induced by a magnetic field, which leads to stronger confinement of the wave functions and thus to localization [4].

Confining an impurity in a quantum well (QW) has two prime effects: (1) The binding energy is increased from one effective Rydberg (Ry*) in three dimensions up to four Ry* in the ideally two dimensional case [5]. For a realistic QW the value is somewhere in between [6]. (2) Due to the reduced symmetry of the problem, the degeneracy of the hydrogenic states is reduced. If still the terminology of the 3D hydrogen atom is used, the $2p_z$ (or $2p_0$, where $m = 0$ is the magnetic quantum number) state is split of from the $2p_{xy}$ levels and becomes a resonant state lying just below the second ($n = 2$) quantum well subband [7, 8]. In fact, this $2p_0$ level becomes the ground state of a new 2D hydrogenic series associated with the $n = 2$ subband. The exact correspondence between 3D and 2D hydrogenic states has been discussed in Ref. 9. The $2p_0$ level has been observed in Raman scattering [10] and infrared spectroscopy [11]; in particular, the $1s$ - $2p_0$ transition can be regarded as an impurity shifted intersubband transition, slightly higher in energy than the latter. In semiconductor superlattices, the $1s$ - $2p_0$ transition has been very clearly revealed [12], since due to the finite miniband width it is spectrally separated from the van Hove singularities in the inter-miniband absorption spectra; recently it has also been observed in the infrared absorption of isolated quantum wells [13].

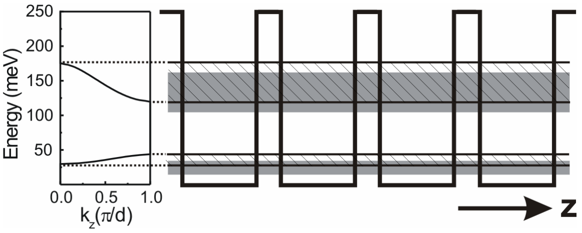

Fig. 1: Schematic of a superlattice with minibands (hatched) and impurity bands (shaded area), slightly lower in energy than the minibands (see later in the text).

In this Letter we show that this picture has to be modified. We numerically calculate the energy levels of a finite quantum well system with impurities and follow the evolution from a double quantum well to a superlattice (see Fig. 1). We show that each subband level has its associated impurity level (series) attached, and in the limit of a superlattice, also the impurity levels lie dense and form a resonant impurity band, energetically overlapping the associated miniband. Energy levels and wavefunctions are not easily experimentally accessible in a direct manner, therefore we are calculating the infrared absorption as an observable quantity, which is compared to experimental absorption spectra. Apart from the amazing agreement we are able to explain some hitherto not understood observations in the regime of the magnetically induced metal insulator transition [14], leading to a reinterpretation of existing data.

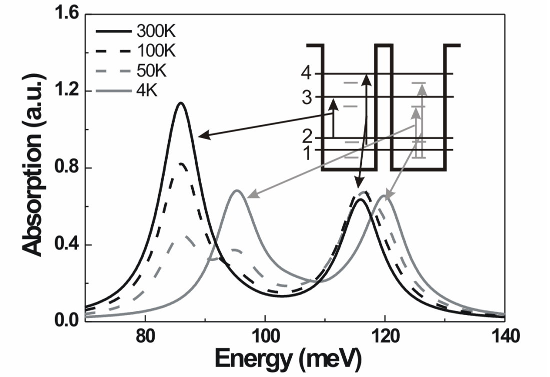

Fig. 2: Calculated infrared absorption spectra of a double quantum well for different temperatures as indicated. A sketch of the structure is shown in the inset with the relevant transitions.

Previous calculations of impurity levels in quantum wells were often based on variational approaches [4, 5, 7, 11], and mostly low-lying levels have been investigated. Yet already in 1984 Priester *et al.* [7] showed that each 2D subband has an impurity band associated with it. Serre *et al.* [15] performed calculations of the density of states (DOS) in a multiple-scattering approach, later on also used in [16] for δ-doped layers. Other works include low-lying states in a double QW [17] and a fully numerical investigation of the DOS in a 2D system with random impurities [18].

For our calculation we start from a fully three dimensional Hamiltonian which contains the z-dependent quantum well potential on the basis of the effective mass approximation, the Coulomb potential of impurities at a certain location z_0, but randomly distributed in the xy-plane, and the Hartree potential of the electrons in z-direction. Electron-electron interaction is neglected in this study. In this framework we solve the Schrödinger equation for N coupled quantum wells ($N = 1..20$) numerically exact on a square of $100 \times 100\ \mathrm{nm}^2$ with periodic boundary conditions in xy direction. Putting one impurity into this square corresponds to a density of $n = 1 \times 10^{10}\ \mathrm{cm}^{-2}$. The method follows closely the one published in Ref. 19. Thus there are no *a priori* assumptions concerning the impurity states, like they are contained in any variational ansatz (which has been the main tool in the past to calculate shallow impurity levels in quantum wells [4, 5, 7, 11]. Typically the calculation results in several hundred to thousands of energy levels. We calculate the optical transition matrix elements between all of them and use these together with the correct occupation via Fermi-Dirac statistics to calculate the absorption coefficient (with radiation polarized along the growth direction z). As a result we get, for the first time to our knowledge, a QW or superlattice infrared absorption spectrum which treats subbands and impurity states on the same footing. In addition, we average the spectra over several impurity configurations and convolve them with a Lorentzian of width 4 meV. The latter accounts for homogeneous broadening and removes all fine structure resulting from the finiteness (discreteness) of the system. We are also able to identify the energy level pairs which give the strongest contribution to the absorption spectra.

Table 1: List of the strongest transitions at $T = 4$ K (upper) and $T = 300$ K (lower). Listed are the initial (i) and final (j) states of each transition, their respective oscillator strengths, f_{ij}, and energies, ε_{ij}. The transition in last line at $T = 300$ K is the strongest around 116 meV, but totally the 23rd strongest. The wave functions of the bold states are plotted in Fig. 3.

4 K

$i \to j$	f_{ij}	ε_{ij} (meV)
1 → 272	0.35	94.5
0 → 275	0.31	96.1
0 → **391**	0.28	119.6
1 → 392	0.27	120.6
0 → 6	0.16	9.2

300 K

$i \to j$	f_{ij}	ε_{ij} (meV)
17 → 286	0.022	85.95
33 → 307	0.020	85.94
…	…	…
…	…	…
10 → **415**	0.012	115.85

We start by discussing a symmetric double quantum well. Its energy levels are grouped into doublets (Fig. 2, inset), split by the thin tunneling barrier. Note that these states can be regarded as precursors to the miniband edges in a superlattice. Figure 2 shows the results of such a calculation for a GaAs/Al$_{0.3}$Ga$_{0.7}$As double quantum well with a doping density of $n = 1 \times 10^{10}\ \mathrm{cm}^{-2}$ in each QW (thickness of each well 9 nm, barrier thickness 2.5 nm) at temperatures 4, 50, 100, and 300 K [20]. Let us start with the high-temperature spectra. Two absorption peaks are observed at 86 and 116 meV, corresponding to the 2 → 3 and 1 → 4 intersubband transitions, respectively (but note that, strictly, the subband index is not a good number in the presence of impurities). The former one occurs because the $n = 2$ state is thermally occupied at 300 K. The relative peak heights reflect the larger oscillator strength for the 2 → 3 compared to the 1 → 4 transition. The 1 → 3 and 2 → 4 transitions are parity forbidden in a symmetric structure. At low temperature the 2 → 3 peak disappears due to thermal depopulation of the

$n = 2$ subband; instead a peak at 95 meV appears, which can be identified as the transition between the $1s$ impurity ground state and the $m = 0$ resonant impurity state associated with the $n = 3$ subband. Note that these spectra are already reminiscent of experimental superlattice spectra (e.g., Ref. 12), where the $1 \rightarrow 4$ transition would correspond to the singularity at the mini-Brillouin zone center (at $k_z = 0$) and the $2 \rightarrow 3$ transition at its edge (at $k_z = \pi / d$, where d is the superlattice period).

Let us now analyze the behavior of the high-energy peak around 116 meV. As the temperature is lowered, it shifts to slightly higher energy (to 120 meV). In our model, this shift is not related to a variation of band parameters or many-body effects; hence, it must be related to single particle energies. In fact, a closer inspection shows that at low temperature this peak can be identified with the transition from the impurity ground state to the $m = 0$ state associated with the $n = 4$ level; i.e., it is the ''impurity shifted'' $1 \rightarrow 4$ transition. This assignment can be proven by looking at the wave functions in the xy plane. At first we identify the energy levels that give the major contribution to the absorption spectrum, and, in particular, to the 116 – 120 meV peak, at high and low temperatures. Table 1 lists the transitions between the calculated quantum states in order of descending strength. At $T = 4$ K there are just four strong transitions, from the impurity ground states in the two QWs ($i = 0,1$) to the excited impurity state associated with the $n = 3$ and 4 subbands, respectively [21].

The fifth-strongest transition is one in the far infrared, related to the $2p_0$ state near the $n = 2$ subband (not shown or further discussed here for simplicity). The squared modulus of the xy wave function of the state $j = 391$ (integrated over the z coordinate) is plotted in Fig. 3 (left panel). This is clearly a state that is strongly localized around the position of the impurity ions. Note that at 4 K the Fermi energy lies between the impurity ground state and the first subband; i.e., only impurity states are occupied. At $T = 300$ K the situation is completely different. There is a large number of transitions that contribute to the observed peaks, none of them with oscillator strength greater than 0.022. Looking at one of these final states ($j = 415$, the strongest one with transition energy around 116 meV, right panel of Fig. 3), it is clear that this is an extended state. The maxima and minima of the probability distribution are related to the impurity potentials, the involved k values, and the periodic boundary conditions. The initial state $i = 10$ is, of course, also extended. Thus we have shown that the high-energy peaks at 120 and 116 meV have an entirely different origin; namely, they originate from impurity and miniband states, respectively. While this - a resonant impurity state associated with the $n = 4$ subband - may not be surprising for itself, it bears consequences for the situation in a superlattice, where it would correspond to a resonant impurity state associated with the *upper edge* of the second miniband [22].

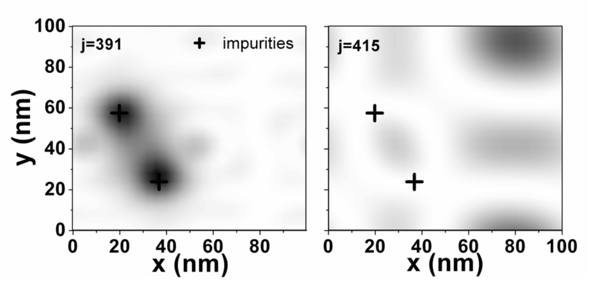

Fig. 3: Contour plot of the squared moduli of the states $j = 391$ and 415 in the xy plane (integrated over the z coordinate). The positions of the impurities (one in each QW) are indicated by crosses.

As a good approximation for a superlattice, we performed the calculation for 20 coupled quantum wells (the same parameters as above, i.e., well width 9 nm, barrier thickness 2.5 nm). The impurities are distributed over 1 nm of the QW center with a density of $n = 1 \times 10^{10}$ cm^{-2} per QW (the binding energy varies negligibly over this 1 nm range and is very close to the bulk value).

The calculated absorption spectra for different temperatures are shown in Fig. 4. For high temperatures the spectrum consists of a strong low-energy peak and a weaker one at higher energy. These are, according to well established interpretation [12], related to the van Hove singularities of the interminiband absorption at the edge ($k_z = \pi / d$) and the center ($k_z = 0$) of the mini-Brillouin zone, respectively (see Fig. 1). Upon lowering the temperature, the low-energy peak disappears due to thermal depopulation of the first

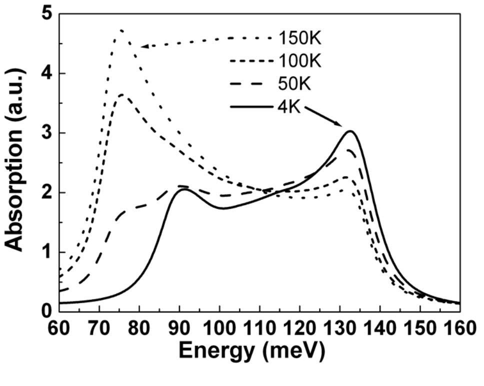

Fig. 4: Calculated infrared absorption spectra of a superlattice for different temperatures as indicated.

miniband. What remains is a peak at 90 meV, which has previously been assigned to an impurity transition [12]. This interpretation remains valid by performing a similar analysis as for the double QW.

Let us now turn to the higher energy peak at 133 meV. As stated above, at high temperature this corresponds to the interminiband transition at $k_z = 0$. At low temperature, however, where it simply appears to become stronger, both the comparison with the double QW and the analysis of the wave functions [23] show that this is again an impurity transition, namely, from the ground state to the impurity state associated with the upper edge of the second miniband. In fact, the whole spectrum (from 90 to 133 meV) at $T = 4$ K is due to impurity transitions, and reflects a band of resonant states, partly overlapping the second miniband (see Fig. 1; these states are de facto localized, yet strictly they are resonant states that can decay into the continuum). Note that this is not an impurity band in the usual meaning (arising from interacting impurity ions), but results from the large number of QWs, just like the miniband. Hence, it cannot be decided by simply looking at the experimental spectrum whether the 133 meV peak is a miniband or an impurity transition. The calculation shows that the Fermi energy at $T = 4$ K lies slightly below the bottom of the first miniband. Thus clearly, the appearance of this peak is *not* an indicator for the Fermi energy lying in the first miniband, as has been falsely assumed in the past [14]. Also, this peak will *not* disappear, when a metallic sample is driven into an insulating state via a strong magnetic field - a fact that has been observed but not understood in the past [14].

In order to demonstrate the validity of the present calculation, we have measured the interminiband absorption in a $GaAs/Al_{0.3}Ga_{0.7}As$ superlattice (well width 9 nm, barrier width 2.5 nm, 300 periods), doped with $n = 2 \times 10^{10}$ cm^{-2} in the center of each QW (corresponding to a bulk density of $n = 1.7 \times 10^{16}$ cm^{-3}). The sample has been prepared in a multiple-total-reflection waveguide geometry and the absorption spectra (measured in a Fourier-transform spectrometer) are obtained by normalizing the *p*-polarized signal by the *s*-polarized one. The result is displayed in Fig. 5 for different temperatures. Comparison with the theoretical spectra in Fig. 4 shows an amazing agreement of the line shapes and their temperature dependence. Low-temperature magnetotransport shows a marginally metallic behavior, with a MIT being induced by magnetic fields above 4 T. This behavior is consistent with an impurity-band metal, where the Fermi energy at low temperature lies in the impurity band [24].

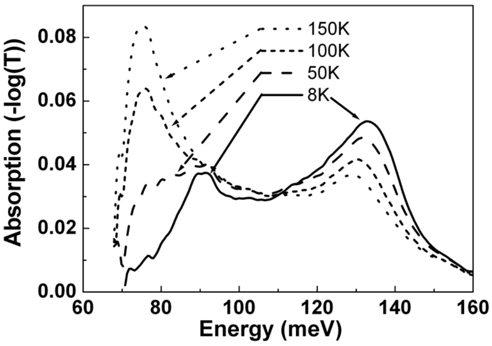

Fig. 5: Experimental infrared absorption spectrum of a $GaAs/Al_{0.3}Ga_{0.7}As$ superlattice with 9 nm well width and 2.5 nm barrier thickness. The cutoff at 70 meV is due to the detector employed in the measurement.

In summary, we have presented a theory that is able to describe the infrared optical properties of a superlattice treating the superlattice potential and the random impurity potential in a unified framework. The occurrence of impurity bands in the continuum has been demonstrated, explaining experimentally observed spectra. By including electron-electron interaction and/or a magnetic field in the calculation, it should be possible in the future to study the metal-insulator transition as a function of doping density or induced by a magnetic field.

The presented results have been recently published as D. Stehr *et al.*, Phys. Rev. Lett. **95** (2005) 257401.

References

[1] K. Leo, High-Field Transport in Semiconductor Superlattices; Springer, New York, 2003

[2] See, e.g., Localization and Interaction in Disordered Metals and Semiconductors, edited by D. M. Finlayson, Institute of Physics Publications, Bristol, U.K., 1986

[3] D. Romero *et al.*, Phys. Rev. B **42** (1990) 3179

[4] M.C. Maliepaard *et al.*, Phys. Rev. Lett. **61** (1988) 369

[5] G. Bastard, Phys. Rev. B **24** (1981) 4714; C. Mailhiot, Y.-C. Chang, T.C. McGill, Phys. Rev. B **26** (1982) 4449

[6] In addition, the binding energy becomes dependent on the location with respect to the growth direction *z*.

[7] C. Priester, G. Allan, M. Lannoo, Phys. Rev. B **29** (1984) 3408

[8] R.L. Greene, K.K. Bajaj, Phys. Rev. B **31** (1985) 4006

[9] J.P. Cheng, B.D. McCombe, Phys. Rev. B **42** (1990) 7626

[10] T.A. Perry *et al.*, Phys. Rev. Lett. **54** (1985) 2623

[11] M. Helm *et al.*, Phys. Rev. B **43** (1991) 13 983

[12] M. Helm *et al.*, Phys. Rev. B **48** (1993) 1601, M. Helm, Semicond. Sci. Technol. **10** (1995) 557

[13] M. Carras *et al.*, Phys. Rev. B **70** (2004) 233310

[14] W. Hilber *et al.*, Phys. Rev. B **53** (1996) 6919, M. Helm *et al.* (unpublished)

[15] J. Serre, A. Ghazali, A. Gold, Phys. Rev. B **39** (1989) 8499

[16] J. Kortus, J. Monecke, Phys. Rev. B **49** (1994) 17 216

[17] S.T. Yen, Phys. Rev. B **68** (2003) 165331

[18] M. Hofmann, M. Bockstedte, O. Pankratov, Phys. Rev. B **64** (2001) 245321

[19] C. Metzner, M. Hofmann, G.H. Döhler, Phys. Rev. B **58** (1998) 7188

[20] Note that our calculation also yields the low-energy spectra (<10 meV) due to impurity and intersubband transitions near the first doublet. They are not shown here since we concentrate on the comparison to midinfrared absorption experiments.

[21] Note the different level numbering: n counts the few subbands due to the z confinement, whereas i counts the levels of the full 3D calculation.

[22] In a completely different context localized states near the upper miniband edge have been predicted; see H. A. Fertig, S. Das Sarma, Phys. Rev. B **42** (1990) 1448

[23] We suppress any detailed discussion as for the double QW, due to the large number of energy levels involved here.

[24] S. Liu *et al.*, Phys. Rev. B **45** (1992) 1155

High-Intensity Terahertz Radiation from a Microstructured Large-Area Photoconductor

A. Dreyhaupt, S. Winnerl, T. Dekorsy and M. Helm

The development of new terahertz (THz) sources is of great importance for a large variety of scientific and technological applications. For the generation of THz waves with fs pulses several emitter concepts have been employed like optical rectification [1], phase-matched difference-frequency mixing [2], surface field THz emitters [3], photoconductive switches [4, 5], or biased pin-diodes [6]. Several attempts have been made to increase the THz emission efficiency by employing photoconductors with laterally structured emitter electrodes [7, 8]. The driving forces for further developments of impulsive THz emitters are applications which require a large bandwidth and/or high THz electric field amplitudes. The performance of THz emitters based on photoconductors (PC) is limited by several conditions. In order to achieve a high bandwidth the electric field applied to the PC should be high in the 100 kV/cm range, i.e., close to the breakdown voltage of the PC. On the other hand the optically excited area should be large to prevent local heating of the PC with the exciting laser pulses which would have a detrimental effect on the carrier mobility and thus decrease the bandwidth. Therefore the solution of using pin-diodes has advantages over lateral electrical contacts to the PC, since in a pin-diode high electric fields exist in the whole area of the diode. Yet the acceleration of carriers in a pin-diode is perpendicular to the surface which results in a bad outcoupling efficiency of the dipole radiation with the main intensity being emitted parallel to the surface. Hence the acceleration of carriers in the plane of the PC would be favorable. However, large lateral electric fields applied over large areas, i.e., large electrode spacing, require pulsed high voltage sources in the kV range which one tries to avoid because of the electronic interference with sensitive electronic equipment in the laboratory [9]. Another limitation of PC emitters with lateral carrier excitation is the emission of the radiation via coupling to a microstructured dipole antenna, which typically exhibits a narrower bandwidth than the intrinsic carrier acceleration in the PC.

Here we investigate the THz radiation from photoconductive metal-semiconductor-metal (MSM) structures modified in a way to achieve unidirectional carrier acceleration on a large active area for high excitation powers. The emission is based on the intrinsic acceleration of carriers in the PC and hence does not require a narrow-band antenna. High electric fields of the order of 100 kV/cm are achieved by convenient dc voltages of about 50 V applied to the MSM structure, which eliminates the need for pulsed high power voltage supplies. This approach provides a broadband high-power THz emitter.

A schematic of the THz emitter is shown in Fig. 1. Two interdigitated finger electrodes are processed by optical lithography on the surface of a semi-insulating GaAs wafer. The finger electrode width and spacing are 5 µm. Semi-insulating GaAs is an appropriate substrate because of its high carrier mobility and the high breakdown field. The electrode metallization consists of 5 nm Cr and 200 nm Au. An opaque further metallization of Cr–Au covers every second finger electrode spacing. The second metallization is isolated from the first by a polyimide layer (PMDA-ODA, Kapton) of about 2 µm or a sputtered SiO_x layer of 560 nm thickness. When the finger electrodes are biased, the electric-field direction is reversed between successive fingers. Owing to the opaque second gold metallization on top of the finger electrodes optical excitation takes place only in substrate areas which exhibit the same field direction. Under optical excitation charge carriers are accelerated unidirectionally over the whole excited area. The THz radiation emitted through

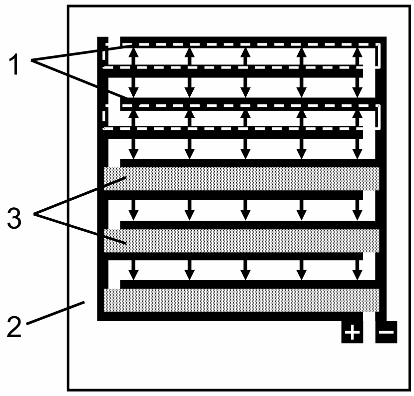

Fig. 1: Schematic sketch of the THz emitting MSM structure; (1) interdigitated finger electrodes, (2) SI GaAs substrate, (3) opaque metallization shadowing one electric field direction. The electric field direction is indicated by arrows.

the substrate interferes constructively in the far field. This technique follows a similar approach of Yoneda *et al.* [10]. They use a diamond based interdigitated electrode structure excited with a high-power Kr*F laser. The excitation in uniform field regions is achieved by the spatial modulation of the illuminating laser amplitude by a binary mask.

The setup for the detection of the THz waves is based on conventional electro-optical sensing [11, 12]. A mode-locked Ti:sapphire oscillator generates 50 fs pulses at a wavelength of 800 nm and a repetition rate of 78 MHz. This beam is used to pump the room temperature operated THz emitter under normal incidence. The charge carriers are excited with an average power of max. 200 mW focused on a spot of about 80 µm. This corresponds to an excitation density of 1.7×10^{18} cm^{-3}. It should be noted that in the present device less than 20 % of the incident radiation is absorbed in the PC due to 75 % coverage of the surface with metallization and the reflectivity of the PC. This value can be increased by using an asymmetric MSM finger structure minimizing the shadowed region between the electrodes and an antireflection coating. The THz emitter is biased with a 50 kHz square wave voltage. The THz wave trains emitted through the substrate are focused with off-axis parabolic mirrors on the detection system. A small fraction of the pump beam is split off, passed through an optical delay stage and realigned with the THz waves by a tin doped indium oxide (ITO) coated mirror [13]. A 230 µm thick ZnTe(110) crystal is used for the electro-optical detection of the THz field amplitude. The THz field induced change of the probe beam polarization is measured with a polarizing beam splitter and two photodiodes. The difference signal of the photodiodes is recorded by a lock-in amplifier locked to the modulation frequency of the THz emitter bias. The emitter design allows for modulation frequencies up to some MHz. The modulation frequency chosen here is well above from the amplitude noise of the pump laser. The duty cycle of the bias voltage was varied between 3.5 % and 50 %.

Figure 2(a) shows the THz electric fields emitted at different acceleration fields. They are compared to the emission of a device without the second metallization layer biased at 20 kV/cm. The THz field value was calculated from the relative intensity change of the probe beam at the detectors as described by Planken *et al.* [14].

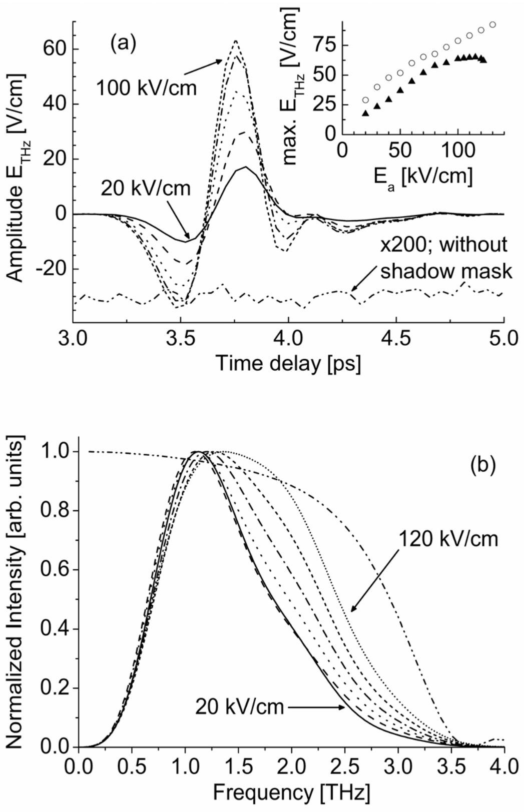

Fig. 2: (a) Time domain THz waveform for different acceleration fields of 20 kV/cm (solid line), 40 kV/cm (dashed line), 60 kV/cm (dotted line), 80 kV/cm (dashed–dotted line), and 100 kV/cm (short dashed line) at a duty cycle of 15 % and an excitation density of 8.6×10^{17} cm^{-3}. The dashed double-dotted line represents the essentially vanishing THz emission of a device without the second metallization at 20 kV/cm and 50 % duty cycle, magnified by a factor of 200 and shifted vertically. The inset shows the maximum absolute THz field at different acceleration fields with 3.5 % (circles) and 15 % (triangles) duty cycle. (b) Power spectra calculated from the time domain THz electric field of (a), normalized to unity. The additional short dotted line corresponds to an acceleration field of 120 kV/cm and the dashed double dotted line represents the calculated response of the ZnTe analyzer crystal.

The THz field amplitude increases linearly with rising acceleration field as shown in the inset of Fig. 2. This increase is based on the faster carrier acceleration in higher electric fields. At a bias-voltage duty cycle of 15 % the slope of the THz amplitude versus the acceleration field becomes sublinear above 80 kV/cm. This sublinearity vanishes using 3.5 % duty cycle of the acceleration field. Higher duty cycles increase the substrate temperature because of the higher average power dissipation by the photocurrent and the associated reduction of the mobility. A maximum THz field of 85 V/cm is reached at an acceleration field of 130 kV/cm with a duty cycle of 3.5 %. This THz field amplitude is comparable to the value achieved by Zhao *et al.* [8] using a cooled semilarge aperture emitter operated at 400 V. However, the maximum signal to noise ratio is provided by a duty cycle of 50 %.

The dashed double dotted line in Fig. 2(a) represents the THz emission of a device without the second metallization at an acceleration field of 20 kV/cm, magnified by a factor of 200 and shifted vertically. No THz field amplitude could be measured there. This is expected due to the alternating direction of the photocurrent within the alternating electric field between the electrodes. Hence in the far field the interference of the THz radiation is destructive.

To explain the observed waveforms and their field dependence the photocarrier dynamics have to be considered [5, 6, 15, 16]. In the limit of a dipole radiation approximation, the field amplitude of the emitted radiation in the far field is proportional to the time derivative of the transient photocurrent. The main cycle sets in with a small negative peak followed by a higher positive peak continued with a few smaller cycles. The main positive peak corresponds to the strong onset of the photocurrent due to the acceleration of carriers in the bias field of the electrodes. The subsequent negative peak is attributed to a decrease of the photocurrent by carrier deceleration. This peak increases relative to the main peak with increasing acceleration field owing to faster scattering into low mobility conduction band side valleys. At high excitation densities this negative peak is influenced by carrier-carrier scattering and screening of the acceleration field as discussed below. The preceding negative peak before the main peak is assigned to pulse reshaping by the frequency dependent THz focus of the detection system [15, 17].

The normalized power spectra shown in Fig. 2(b) are calculated from the time domain data of Fig. 2(a) via a numeric Fourier transformation. These spectra extend from 0.5 to 3 THz. The high-frequency cut-off is detection limited owing to signal cancellation based on the difference of the phase velocity of the THz wave trains and the group velocity of the probe beam in the thick ZnTe crystal. The spectral peak frequency shifts from 1.1 to 1.5 THz upon increasing the acceleration field from 20 to 120 kV/cm and is connected to the carrier dynamics discussed above. The high-frequency characteristics (> 3 THz) of the emitter has to be explored with a thinner detection crystal [12] and shorter excitation and probe pulses.

In order to investigate the dependence of the THz emission on the excitation density we performed experiments at fixed acceleration fields. Figure 3(a) shows the THz amplitude recorded at 20 kV/cm. The inset of Fig. 3(a) compares the maximum THz field amplitude at acceleration fields of 20 kV/cm and 120 kV/cm. The THz field amplitude increases linearly in the excitation-density range investigated here due to the linear increase in photocurrent. The waveform exhibits a second negative peak which increases its amplitude with increasing excitation density relative to the main peak. This effect is attributed to stronger screening of the acceleration field, which provides a faster surge of the photocurrent at high carrier densities [15]. This argumentation is supported by the corresponding spectra in the frequency domain. Figure 3(b) shows the frequency spectra calculated from the time domain data of (a). At low excitation densities the spectra show a narrow peak at about 750 GHz followed by a broader shoulder. This shape is transformed to a broad characteristic at a center frequency of 1.6 THz at high excitation densities.

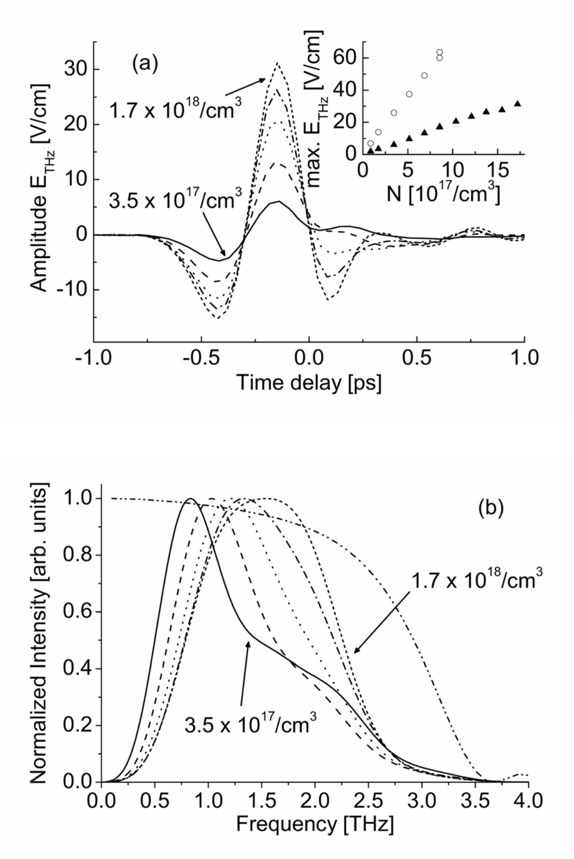

Fig. 3: (a) Normalized time domain THz waveform at $E_a = 20$ kV/cm and a duty cycle of 15 % for different excitation densities of 3.5×10^{17} cm^{-3} (solid line), 6.9×10^{17} cm^{-3} (dashed line), 1.0×10^{18} cm^{-3} (dotted line), 1.4×10^{18} cm^{-3} (dashed-dotted line), and 1.7×10^{18} cm^{-3} (short dashed line). The inset shows the maximum absolute THz field at different excitation densities for $E_a = 20$ kV/cm (triangles) and 120 kV/cm (circles). (b) Power spectra calculated from the time domain THz electric field of (a), normalized to unity. The dashed double dotted line shows the calculated response of the ZnTe analyzer crystal.

We like to note the high potential to further increase the THz field of our device. Our concept is scalable towards larger emitting areas from presently approximately 5000 μm^2 to some mm^2 and even cm^2 which can be excited with amplified laser pulses. This in principle would enhance the emitted THz amplitude by orders of magnitude. Such a system could have comparable performance to optical rectification or difference frequency mixing [2] and would open the pathway to nonlinear THz spectroscopy in many interesting systems. In addition such an emitter would be suitable for generation of continuous wave THz radiation by mixing two laser lines in a PC [18]. This approach has often been limited by the power dissipation in a small excited area.

In conclusion, we have demonstrated the generation of high-intensity THz radiation based on a transient photocurrent in a large-area emitter with a novel electrode design in conjunction with selective shadowing of the optical excitation. This device overcomes disadvantages inherent to emitters using photoconductive antennas and large aperture emitters using two electrodes. In contrast to the latter the proposed device structure enables the exploitation of a large emitting area while keeping the bias field at large values. The high acceleration field which can be obtained in our concept makes the use of low-temperature grown GaAs favorable.

Acknowledgements

We acknowledge the preparation of the polyimide isolation layer by M. Guenther, and the support in sample preparation and helpful discussions by H. Felsmann and B. Schmidt.

The presented results have been recently published as A. Dreyhaupt *et al.*, Appl. Phys. Lett. **86** (2005) 121114.

References

[1] X.-C. Zhang, Y. Jin, X.F. Ma, Appl. Phys. Lett. **61** (1992) 2764

[2] K. Reimann, R.P. Smith, A.M. Weiner, T. Elsaesser, M. Woerner, Opt. Lett. **28** (2003) 471

[3] X.-C. Zhang, D.H. Auston, J. Appl. Phys. **71** (1992) 326

[4] D. Grischkowsky, S. Keiding, M.V. Exter, C. Fattinger, J. Opt. Soc. Am. B **7** (1990) 2006

[5] For a review, see J. Shan, T.F. Heinz, in Ultrafast Dynamical Processes in Semiconductors, edited by K.-T. Tsen, Springer-Verlag, Berlin, 2004, pp. 1–56

[6] L. Xu, X.-C. Zhang, D.H. Auston, B. Jalali, Appl. Phys. Lett. **59** (1991) 3357

[7] S.R. Andrews, A. Armitage, P.G. Huggard, A. Hussain, Phys. Med. Biol. **47** (2002) 37053710

[8] G. Zhao, R.N. Schouten, N. van der Valk, W.T. Wenckebach, P.C.M. Planken, Rev. Sci. Instrum. **73** (2002) 1715

[9] P.K. Benicewicz, J.P. Roberts, A.J. Taylor, J. Opt. Soc. Am. B **11** (1994) 2533

[10] H. Yoneda, K. Tokuyama, K. Ueda, H. Yamamoto, K. Baba, Appl. Opt. **46** (2001) 6733

[11] Q. Wu, X.-C. Zhang, Appl. Phys. Lett. **68** (1996) 1604

[12] A. Leitenstorfer, S. Hunsche, J. Shah, M.C. Nuss, W.H. Knox, Appl. Phys. Lett. **74** (1999) 1516

[13] T. Bauer, J.S. Kolb, T. Löffler, E. Mohler, H.G. Roskos, U.C. Pernisz, J. Appl. Phys. **92** (2002) 2210

[14] P.C.M. Planken, H.-K. Nienhuys, H.J. Bakker, T. Wenckebach, J. Opt. Soc. Am. B **18** (2001) 313

[15] P.U. Jepsen, R.H. Jacobsen, S.R. Keiding, J. Opt. Soc. Am. B **13** (1996) 2424

[16] T.-A. Liu, M. Tani, C.-L. Pan, J. Appl. Phys. **93** (2003) 2996

[17] C. Fattinger, D. Grischkowsky, Appl. Phys. Lett. **54** (1989) 490

[18] E.R. Brown, K.A. McIntosh, K.B. Nichols, C.L. Dennis, Appl. Phys. Lett. **66** (1995) 285

Short Contributions

Ion-Solid Interaction

D. Kost
S. Facsko
R. Hellhammer[1]

Electron spectroscopy on HCIs-interaction with Cu, Si, and SiO_2

Double differential secondary electron spectra were evaluated in dependence of the kinetic energy and the charge state of incoming highly-charged ions (HCIs). For Cu and Si surfaces a quadratic increase of the reemitted energy with increasing charge state up to Ar^{7+} is observed. For Ar^{8+} and Ar^{9+} the increase is steeper due to the contribution of the projectile LMM Auger electrons. The reemitted energy amounts to between 15% and 20% of the total potential energy of the incoming ion, almost independent of the ion charge state. For SiO_2 layers on Si, quasi-static surface charging of some 10 V is observed, which increases at increasing oxide thickness, so that the contribution of low-energy electrons to the reemission of potential energy is suppressed. Therefore, energy reemission is negligible for charge states up to Ar^{7+}. For Ar^{9+}, the reemitted energy increases to 12% of the total potential energy due to the LMM Auger electron contribution. At decreasing kinetic energy for Ar^{9+}, the electron yield and the reemitted energy increase slightly with decreasing projectile energy.

Collaboration:[1]Hahn-Meitner-Institute, Berlin, Germany

A. Keller
S. Facsko
J. Grenzer
O. Plantevin[1,2]
D. Carbone[1]
T.H. Metzger[1]
R. Gago[3]

In-situ x-ray diffraction of GaSb nanopatterned by normal incidence sputter erosion

Low-energy ion erosion of surfaces can lead to the formation of self-organized structures in the range from 10 to 100 nm. Periodic ripple patterns and hexagonally ordered dot arrays can be achieved for oblique and normal incidence, respectively. The evolution of dot patterns on GaSb(001) under normal incidence sputtering at ion energies from 100 to 1000 eV was investigated *in-situ* using grazing incidence small angle x-ray scattering (GISAXS) and grazing incidence diffraction (GID) at the beamline ID01 at the ESRF. With GISAXS the morphology and the correlation of the dots is analysed, while in GID information about the crystalline structure (i.e. strain) is achieved. Three time regimes are identified as smoothing at the beginning of sputtering, followed by pattern formation, and increase of lateral order at high ion fluences.

Collaboration: [1]ID01-Anomalous Scattering Beamline, ESRF, France, [2]Centre de Spectrométrie Nucléaire et de Spectrométrie de Masse, France, [3]Centro de Micro-Análisis de Materiales, Universidad Autónoma de Madrid, Spain

S. Roßbach
A. Keller
S. Facsko

Ion induced ripple formation on Si surfaces at grazing angles

The surface morphology induced by ion beam erosion of Si has been studied for incidence angles of 50–70° to the surface normal at different ion energies and ion fluences. In a window from 60 to 70° regular ripple patterns oriented perpendicular to the ion beam are formed. At smaller incidence angles the surface remains flat, whereas at 75° irregular structures appear which are assigned to processes governed by shadowing effects. The wavelength of the ripple patterns depends on the ion energy and varies from 20 nm at 240 eV to 60 nm at 1 keV. With ion fluence the periodicity also increases in contrast to the Bradley-Harper model which predicts a constant wavelength. From theory a critical angle is expected around 60° where the orientation of the ripple structures should change from perpendicular at smaller angles to parallel at higher angles. In contrast, two ripple modes are present at all incidence angles where ripples appear. A detailed analysis of the power spectra density reveals two periodic features in the patterns. The ripples with the small periodicity are periodically modulated with a wavelength of 100 nm, oriented parallel to the ion beam. Simulations with an extended continuum equation model show qualitative agreement with these findings.

Investigation of the ripple structure in Si by x-ray scattering techniques

S. Grigorian[1]
J. Grenzer
S. Hazra[2]
T.K. Chini[2]
U. Pietsch[1]

The morphology of Ar$^+$ ion beam induced ripples on Si was studied. The formation of ripple structures on the sample surface is evident from AFM, while its formation in the buried crystalline region below an amorphous top layer is evident from grazing incidence diffraction (GID) studies. The GID technique reveals that these periodically modulated wave-like buried crystalline features become highly regular and strongly correlated at Ar ion beam energies between 60 keV and 100 keV. The vertical density profile obtained from the analysis of vineyard profiles shows that the density in the upper top part of ripples is strongly decreased. Particularly, we measured the degree of amorphization of the top layer as a function of irradiation dose using grazing incidence amorphous scattering (GIAS). Two broad peaks indicating short-range ordering of amorphous material changing with the penetration depth of the probing x-ray wave suggest a model of dose-dependent amorphization. The strong damage of crystalline structure starting at low doses (5×10^{16} cm^{-2}) before it becomes complete amorphous and mostly uniform at high doses of irradiation ($>5 \times 10^{17}$ cm^{-2}).

Collaboration: [1]Institute of Physics, University of Siegen, Germany, [2]Surface Physics Division, Saha Institute of Nuclear Physics, Kolkata, India

Proton microprobe analysis of normal and osteoporosisaffected compact bone

L. Harangus[1]
A. Iordan[1]
E.A. Preoteasa[1]
D. Grambole
R. Grötzschel
F. Herrmann
C. Neelmeijer
S. Gomez[2]
A. Mihul[3]
C. lonescu-Tirgoviste[4]
D. Gutu[4]

In osteoporosis, the altered metabolism of Ca and trace elements leading to low bone density is not fully understood. Therefore PIXE, PIGE and proton backscattering (PBS) were applied complementary to analyse the outer layer of femur and tibia from normal and experimental diabetes-affected rats, tibia from humans with osteoporosis-complicated diabetes, clinically sound human femoral neck and normal bovine metacarp. Measurements were carried out at the Rossendorf nuclear microprobe with a 3.1 MeV proton microbeam focused to a spot of about 3 μm.

Hydroxylapatite (HA), CaF$_2$, NaCl and pyrite were used as reference materials. Concentrations were determined from PIXE spectra by GUPIX calculations. In all bones, a P/Ca ratio of 0.32 – 0.39 was found, below the 0.46 value of HA. PBS suggests a fraction of Ca as carbonate in addition to HA. Most elements of the second main group were detected: Mg by PIGE and PBS, and Ca as well as Sr and Ba by PIXE. Other divalent ion-forming trace metals detected by PIXE are Cr, Mn, Fe, Ni, Cu and Zn from the transition element groups, and Pb. Only normal bones contained Cr, Mn and Cu. The concentration of Ca, Fe, Ni and Zn varies strongly even in the same bone, while the Sr concentration shows only small variations. Ca maps exhibit spatially well-defined patterns of bands. Diabetic rat bones show Ca depleted regions near the surface, giving a hint for next studies of osteoporosis affected bones.

Collaboration: [1]National Institute for Physics and Nuclear Engineering, Bucharest, Romania, [2]Faculty of Medicine, University of Cadiz, Spain, [3]Faculty of Physics, University of Bucharest, Romania; [4]Nicolae Paulescu Institute of Diabetes Research, Bucharest, Romania

The Becin hoard – silver coins of the Ottoman Empire

M. Mäder[1]
M. Schreiner[1]
E. Bidaud[1]
W. Zich[1]
K. Uhlir[1]
D. Grambole
F. Herrmann
M. Alram[2]

In summer 2000 a spectacular hoard of silver coins was excavated at the medieval site Becin, next to Ephesos. This trove, which includes about 60.000 coins with a total weight of about 30 kg, represents the largest finding of coins ever made in Turkey. The main part of the coins covers almost all mint places recorded for the Ottoman Empire and all rulers of the second half of the 16th century up to the beginning of the 17th century. Thus, the numismatic evaluation and the material analysis of the coins will provide a general insight in the monetary and economic history of the Ottoman Empire during that period. Samples could be taken from a limited number of coins in order to prepare cross-sections. Afterwards, complementary measurements were carried out using photon, electron as well as proton beams. Silver and copper as major constituents of the coins could be determined quantitatively by all of the three analytical techniques (XRF, SEM/EDX, PIXE). The calculated concentration values are comparable within the measurement uncertainties. PIXE measurements enable to characterize also the trace elements, like Au, Pb and Bi. Additionally, the proton microprobe allows an elemental mapping to illustrate the spatial distribution of the constituents. Initial results including only few analyzed coins show already different groups concerning their chemical composition. Thus, composition analysis of the major elements proved to be suitable to study the development of the debasement of the silver coins in the Ottoman Empire.

Collaboration: [1]Institute of Science and Technology in Art, Academy of Fine Arts, Vienna, Austria, [2]Coincabinet, Museum of Fine Arts, Vienna, Austria

A. Turos[1,2]
A.M. Abdul-Kader[1,2]
D. Grambole
J. Jagielski[1,2]
A. Piątkowska[1]

The effects of ion bombardment of ultra-high molecular weight polyethylene

Medical grade ultra-high molecular weight polyethylene (UHMWPE) due to its mechanical strength and toleration by the human body it is very often applied as material for implants. Since UHMWPE is rather fragile upon dynamic load ion bombardment was applied to improve its tribological properties. UHMWPE samples were irradiated with 130 keV He ions to the fluences ranging from 1×10^{14} to 2×10^{16} cm^{-2}. Hydrogen profiling was performed using the nuclear reaction ^{1}H(^{15}N,$\alpha\gamma$)^{12}C. Important hydrogen release was observed with increasing ion dose and was correlated with the linear energy transfer (LET). Bombardment with light ions, like H or He, producing primarily ionization and little displacements promotes crosslinking. Tribological tests on ion bombarded polyethylene clearly demonstrated that in spite of observed dehydrogenation of surface layers important increase of hardness and lower brittleness can be attained.

Collaboration: [1]Institute of Electronic Materials Technology, Warsaw, Poland, [2]Soltan Institute of Nuclear Studies, Świerk/Otwock, Poland

L. Salavcova[1]
A. Mackova[2]
U. Kreißig

Annealing effects of proton-exchanged optical waveguides in Er-doped lithium niobate

The chemical composition and optical properties of proton-exchanged, Er-doped $LiNbO_3$ were studied in dependence on the annealing conditions. After different annealing treatments the composition of exchanged layers were determined by neutron depth profiling (NDP), He-ERDA and heavy-ion ERDA. The concentration of OH-groups was measured by infrared absorption spectroscopy. The aim of heat treatment is to reduce the concentration of OH-groups, which effect undesirably the lifetime of excited states of erbium, while maintaining the increase of the refractive index at the interface, defining the waveguiding properties. These were measured by mode spectroscopy at 632.8 nm. During the annealing the hydrogen within the exchanged layer moves deeper into the substrate and the crystallographic phase of the exchanged layer changes towards the desired α-phase. The lowest amounts of OH-groups were found at highest annealing temperatures. At 400°C the hydrogen concentration decreased to 25% and the waveguiding properties are sufficient, whereas at temperatures above 400°C a degradation of the waveguiding properties has been observed.

Collaboration: [1]Institute of Chemical Technology Prague, Prague, Czech Republic, [2]Czech Academy of Sciences, Rez/Prague, Czech Republic

Thin Films

Growth modes of undoped ZnO thin films by reactive pulsed magnetron sputtering

M. Vinnichenko
A. Rogozin
N. Shevchenko
L. Vazquez[1]
A. Kolitsch
W. Möller

The growth modes of ZnO thin films on amorphous SiO_2/Si and single crystalline $Al_2O_3(0001)$ substrates are investigated. The films are characterized by XRD, AFM, and spectroscopic ellipsometry (SE). On amorphous substrates at $T_S > 500$°C, films with high (0001) texture are formed, with AFM scaling analysis suggesting competitive unstable 3D growth with shadowing effects. As confirmed by XRD φ-scans, deposition on chemically cleaned Al_2O_3 (0001) substrates results in the formation of epitaxial ZnO layers in a wide range of deposition parameters, with two types of domains, one of them being rotated by 30° relative to the dominating orientation. An additional oxygen plasma cleaning of the substrate allows to form single-domain epitaxial films. Under optimized conditions, these films remain epitaxial for a wide range of oxygen partial pressures (1.4×10^{-4}- 3.4×10^{-3} mbar) at a substrate temperature of 550°C. The largest grain size of approximately 100 nm and the best (0001) texture of ZnO are formed at oxygen partial pressure of 1×10^{-3} mbar with a minimum FWHM of the XRD rocking curve of 0.366°. In this case, AFM shows surface morphology patterns characteristic for 2D growth. SE indicates the absence of grading of the optical constants across the film, and a significantly lower optical absorption compared to films grown without oxygen plasma pretreatment.

Collaboration: [1]Instituto de Ciencia de Materiales de Madrid, Consejo Superior de Investigaciones Cientificas, Madrid, Spain

Indium tin oxide thin film annealing by electric current

A. Rogozin
N. Shevchenko
M. Vinnichenko
A. Kolitsch
W. Möller

As a new method of indium tin oxide (ITO) annealing in vacuum, direct electric current (DC) flow through the film is explored. ITO films of about 170 nm thickness were produced by reactive pulsed magnetron sputtering. During annealing at constant electric power, the film resistance, free electron density, and structure evolution were monitored *in-situ*. Compared to conventional isothermal annealing, the current annealing is more efficient with a noticeable reduction of the thermal budget and a decrease of the kinetic exponent of crystallization. Electrical inhomogeneities of the film, which produce locally overheated regions, are discussed as potential reason for the acceleration of the crystallization process. However, the DC annealing requires electrical contacts to the film. An advanced contactless method of annealing by microwave induced current has been developed which provides a fast amorphous-to-crystalline transformation of ITO films with a significant decrease of their resistivity.

Nitrogen incorporation in carbon nitride films produced by direct and dual ion-beam sputtering

G. Abrasonis
R. Gago[1]
I. Jimenez[2]
U. Kreissig
A. Kolitsch
W. Möller

Carbon and carbon nitride (CN_x) films were grown on Si(100) substrates by direct ion-beam sputtering (IBS) of a carbon target at different substrate temperatures (RT – 450°C) and Ar/N_2 sputtering gas mixtures. Additionally, the effect of concurrent nitrogen (N) ion assistance during the growth of CN_x films by IBS was investigated. The samples were analyzed by ERDA and XANES. The ERDA results showed that significant nitrogen amount (up to 20 at.%) was incorporated in the films, without any other nitrogen source but the N_2-containing sputtering gas. The N atomic fraction in the films is proportional to the N_2 content in the sputtering beam and no saturation limit is reached under the present working conditions. The film areal density decreases at increasing growth temperature, with a correlation between the C and N losses. The XANES results indicate that N atoms are efficiently incorporated into the carbon network and can be found in different bonding environments, such as pyridine-like, nitrile-like, graphite-like, and embedded N_2 molecules. The contribution of molecular and pyridine-like nitrogen decreases when the temperature increases while the contribution of N in the nitrile-like configurations increases. The N ion assistance results in the significant increase of the N content in the film but it induces a further reduction of the deposited material. Additionally, the assisting ions inhibited the formation of the nitrile-like configurations while promoting N environments in graphite-like positions. The N incorporation and release mechanisms and dominance of a certain N chemical environment is influenced by the type of N precursors and the hyperthermal particle induced atomic displacements and bond breaking on the surface of the growing film.

Collaboration: [1]Centro de Micro-Análisis de Materiales, Universidad Autónoma de Madrid, Spain, [2]Instituto de Ciencia y Tecnología de Polímeros, Consejo Superior de Investigaciones Científicas, Madrid, Spain

M. Berndt
M. Vinnichenko
U. Kreißig
G. Abrasonis
A. Kolitsch
W. Möller

Growth of carbon and carbon nitride thin films by low-energy N_2/Ar ion assisted evaporation of C_{60}

The growth of C and CN_x films by evaporation of C_{60} fullerene and simultaneous low-energy (~ 150 eV) N/Ar ion bombardment has been investigated. The films have been grown at different ion to molecule arrival ratios I_{Ion}/I_{Mol} (4 – 10) and substrate temperatures (RT – 300°C). The film areal density and composition has been obtained from ERDA, their thickness from spectroscopic ellipsometry, and their chemical bonding structure from Raman spectroscopy. Raman spectra of the films grown without ion assistance show similar features as the Raman spectrum of the C_{60} precursor powder. N or Ar ion assistance in the present energy range results in decomposition of C_{60} in the films independent of I_{Ion}/I_{Mol}. The N and Ar atomic ratios in the films (16 – 27 at.% for N and 2 – 4 at.% for Ar) are proportional to I_{Ion}/I_{Mol} and no saturation limit has been obtained for the used experimental conditions. The amount of deposited material decreases with increasing I_{Ion}/I_{Mol} for a given substrate temperature for both type of ions. Ion assistance also results in a densification of the films.

Collaboration: NanoMaterials Ltd., Israel

R.M.S. Martins
N. Schell
M. Beckers
R.J.C. Silva[1]
F.M. Braz Fernandes[1]

Effect of a TiN buffer layer on the growth of NiTi sputtered thin films

Shape Memory Alloy (SMA) NiTi thin films have attracted much interest as functional materials. However, there are still important issues unresolved like texture development and its control. Near-equiatomic NiTi films of ~ 800 nm were fabricated on SiO_2/Si(100) substrates by co-sputtering from Ni/Ti and Ti targets in a process chamber installed in the HUBER goniometer at ROBL. *In-situ* XRD analysis during the growth of these films was applied to investigate the influence of a TiN buffer layer grown prior to the deposition of the NiTi films. TiN acts not only as a diffusion barrier, but may also induce different crystallographic orientations of the NiTi film on top. A (111) textured TiN layer of about 200 nm thickness induces the preferential growth of (110) planes of the NiTi B2 phase already from the beginning of the deposition. Using a thin non-textured TiN buffer layer (d < 80 nm), the diffraction peak B2(110) also appears from the beginning but much less intense. In this case, the B2(211) was additionally detected with comparable intensity to the B2(110). These results confirm the possibility to launch a certain crystallographic orientation of NiTi thin films by a TiN buffer layer, which has a strong influence on the extent of the strain recovery.

Collaboration: [1]CENIMAT, Campus da FCT/UNL, Monte de Caparica, Portugal

N. Shevchenko
H. Reuther
E. Richter

Surface structure and properties of ion implanted NiTi alloy

Shape memory and superelastic NiTi alloy is a promising material for biomedical applications, provided the release Ni ions into the biological environments can be sufficiently reduced. Oxygen plasma immersion ion implantation at an ion energy of 20 keV, an ion fluence of $10^{17} – 10^{18}$ cm^{-2}, and substrate temperatures below 250°C results in the formation of a transparent rutile TiO_2 surface layer with a Ni content down to below 1 at.%. Concurrently, the underlying alloy is enriched with Ni. Phases of Ni_4Ti_3 and Ni_3Ti are also found in addition to NiTi. The oxide layer thickness as well as the surface roughness are controlled by the balance of reactive ion-induced diffusion and ion sputtering. The nickel depleted TiO_2 layer serves as a barrier to corrosion and out-diffusion of Ni ions. Biocompatibility tests show a largely superior in vitro blood compatibility of the oxygen ion implanted NiTi surfaces compared to untreated materials.

Supported by
Boston Scientific
SCIMED

J. Rosen[1]
S. Mraz[1]
U. Kreissig
D. Music[1]
J.M. Schneider[1]

Effect of ion energy on structure and composition of cathodic arc deposited alumina (Al_2O_3) thin films

The effect of energy supplied to the growing alumina film on the composition and structure has been investigated by varying substrate temperature and substrate bias potential. The constitution and composition were studied by XRD and ERDA, respectively. Increasing the substrate bias potential from −50 to −100 V caused the amorphous or weakly crystalline films to evolve into stoichiometric, crystalline films with a mixture of the α- and γ-phase above 700°C, and γ-phase dominated films at temperatures as low as 200°C. All films had a grain size of < 10 nm. In order to correlate phase formation with synthesis conditions, the plasma chemistry and ion energy distributions were measured at synthesis conditions. These results indicate that for a substrate bias potential of −50 V ion energies in excess of 100 eV are attained, both from a high energy tail and the accelerated ions with a charge state > 1. These results are of importance for an increased understanding of the evolution of film composition and microstructure, also providing a pathway to γ-alumina growth at temperatures as low as 200°C.

Collaboration: [1]Materials Chemistry, RWTH Aachen, Germany

J.M. Andersson[1]
E. Wallin[1]
U. Helmersson[1]
U. Kreissig
E.P. Münger[1]

Phase control of Al_2O_3 thin films grown at low temperatures

Alumina (Al_2O_3) thin films are widely used as wear-resistant or diffusion barrier coatings. Usually the hard and thermally stable α-phase is required. Low-temperature growth (500°C) of α-Al_2O_3 thin films by reactive magnetron sputtering was achieved for the first time. The films were grown onto Cr_2O_3 nucleation layers and the effects of the total and O_2 partial pressures were investigated. At 0.33 Pa total pressure and ≥ 16 mPa O_2 partial pressure α-Al_2O_3 films formed, while at lower O_2 pressure or higher total pressure (0.67 Pa) values only the α-phase was detected in the films. Heavy-ion ERDA measurements reveal that all films were stoichiometric. These results showed that the phase content of the films could be controlled by controlling the energy of the depositing species. The effect of residual water vapour (~ 10^{-4} Pa) on the films was also studied, showing no change in phase content and no incorporated H (< 0.1 at.%). Overall, these results are of fundamental importance for the further development of low-temperature grown Al_2O_3 films.

Collaboration: [1]Linköping University, Linköping, Sweden

E. Alves[1]
A.R. Ramos[1]
N.P. Barradas[1]
U. Kreißig

Studies of compositional and structural changes in ZrO_xN_y films depending on growth conditions

The presence of oxygen in transition metal nitrides allows the tailoring of film properties between those of metallic nitrides and the correspondent ionic

L. Rebouta[2]
F. Vaz[2]

oxides. Changing the oxide/nitride ratio gives the possibility to tune the bandgap, bandwidth, crystallographic order and hence the properties of the films. The work focuses on the analysis of ZrO_xN_y thin films, the composition evolution with changing growth conditions and its relation to the structural and morphological properties of the films. The films were prepared by rf reactive magnetron sputtering, using different reactive gas flows. Composition and structure were measured combining IBA and XRD techniques. The depth profiles of nitrogen and oxygen have been obtained by ERDA. Results showed that the oxygen fraction in the films increases with gas flow, reaching a value of $x \sim 0.33$ for a reactive gas flow mixture of 6.25 sccm. During growth mixed zirconium nitride and oxide phases form. Furthermore, the deposition rate correlates with the oxygen content variations, showing a continuous decrease with reactive gas flow.

Collaboration: [1]Nuclear and Technological Institute, Sacavem, Portugal; [2]University of Minho, Guimaraes, Portugal

R. Yankov
A. Donchev[1]
M. Schütze[1]
E. Richter

Efficient oxidation protection of γ-TiAl alloys by ion implantation of halogens

For the development of a commercially viable process for enhancing the high-temperature (> 700°C) oxidation resistance of γ-TiAl alloys, exploratory beamline co-implantation studies have been performed using $F^+ + B^+$, $F^+ + C^+$, $F^+ + N^+$, $F^+ + Y^+$, $(SiF)^+$, and $Cl + Y^+$ ions with overlapping implantation profiles at a mean depth of 100 nm. Oxidation tests at 900°C in synthetic air demonstrated a lowest mass gain after 100 h for $(SiF)^+$ implant followed by $F^+ + B^+$, $F^+ + C^+$ and $F^+ + N^+$ implants. Initial efforts using PIII of Cl from an 80 % Ar / 20 % Cl plasma have focused on the optimization of the process. Highest oxidation resistance has been achieved with 106 pulses at a bias voltage of 30 kV, a frequency of 250 Hz, and an RF power of 350 W. Increasing the power to 1000 W leads to appreciable deterioration of the oxidation behavior. The optimized PIII of Cl produces largely improved oxidation resistance similar to that achieved by beamline implantation of Cl. In order to ease practical handling, dichlormethane (CH_2Cl_2) has been used as an alternative precursor gas, with an even slightly increased oxidation resistance compared to the Ar/Cl processing. This may be explained by the combined effect of Cl and C as a microalloying element. The oxidation time for the CH_2Cl_2- treated samples has been extended to 1000 h, and excellent oxidation resistance has been retained throughout the test.

Supported by AiF

Collaboration: [1]Karl-Winnacker-Institute of the DECHEMA e.V., Frankfurt/Main, Germany

N. Özkucur[1]
E. Richter
C. Wetzel[2]
F. Hollstein[2]
R.H.W. Funk[1]
T.K. Monsees[1]

Enhanced biocompatibility of human endothelial cells on ion-beam-treated polyurethane surfaces

To improve the biocompatibility of polyurethane (PUR) in blood-contacted devices, PUR surfaces were modified by ion irradiation using C, O, N, or Ar ions with energies of 0.3 – 50 keV and doses of $10^{13} – 10^{15}$ ions/cm^2. Adhesion, proliferation and cytotoxicity of human umbilical vein endothelial cells (HUVEC) were compared to unmodified control surfaces (uPUR). Ion irradiation strongly influences surface topography and free energy as demonstrated by AFM and contact angle measurement, respectively. The surface roughness is lowest at medium ion energies and increases at elevated ion dose. The largest contact angles result from medium ion energies. A triple immunostaining for actin cytoskeleton, vinculin (as a marker of focal contacts) and nuclei (DAPI), was employed for adhesion studies. The apoptosis rates were calculated by counting fragmented nuclei. WST-1 assay was used for analysis of cell proliferation. A strong improvement in endothelial cell adhesion and proliferation on ion implanted surfaces was observed. Intensive cell spreading and most focal contacts were found on O- and N-implanted surfaces, followed by Ar-implanted, or N- and O-plasma treated implants. In contrast, C-implanted surfaces display low adhesion and a higher apoptosis rate. Ion energy has a stronger effect on cell numbers (24 h) and cell proliferation (5 d) than ion dose.

Collaboration: [1]Institute of Anatomy, TU Dresden, Germany, [2]Techno-Coat Oberflächentechnik GmbH, Zittau, Germany

A. Bentzen[1,3]
A. Ulyashin[2]
A. Suphellen[3]
E. Sauar[1]
D. Grambole
D.N. Wright[3]
E.S. Marstein[3]
B.G. Svensson[2]
A. Holt[3]

Surface passivation of silicon solar cells by a-Si/Si_3N_4 dual layers

Surface passivation of silicon by a dual structure consisting of a hydrogenated amorphous silicon (a-Si) thin film capped by a Si_3N_4 anti-reflection layer, both layers deposited by plasma enhanced chemical vapour deposition, was investigated. The results show that a synergetic effect on the surface passivation properties is obtained from such a dual structure. Moreover, the surface passivation can be significantly enhanced after a short anneal for temperatures up to about 500°C, whereas anneals at higher temperatures result in degradation of the passivation properties. From NRA of the as-deposited and annealed structures, the enhanced surface passivation experienced after annealing is indicated to be due to hydrogen release from the structure towards the Si substrate, possibly followed by a redistribution of hydrogen and subsequent passivation of Si dangling bonds in the sub-interface region.

Collaboration: [1]Renewable Energy Corp. AS, Høvik, Norway, [2]Center for Material Science and Nanotechnology, University of Oslo, Norway, [3]Section for Renewable Energy, Institute for Energy Technology, Kjeller, Norway

M. Kutzer[1]
F. Allenstein[1]
G. Beddies[1]
R. Grötzschel
H.-J. Hinneberg[1]
S. Mantl[2]

Ohmic contacts on Si(001) by selenium modification of metal/semiconductor-interface

The deposition of about one monolayer (ML) of Se onto Si(001) leads to the restoration of surface geometry and consequently to an electronic and chemical surface passivation. In particular, it is possible to realise metal-contacts with negative Schottky barriers on Se-passivated n-type Si(001). We studied the deposition of Se on n-type Si(001) after various surface preparation steps to find conditions for self-limited growth of only 1 ML. The depositions were performed in a MBE system in ultrahigh vacuum (UHV). Selenium was evaporated by using two different source materials: $SnSe_2$ and WSe_2. The surface retention of Se atoms, that means the remaining Se areal density and as well as that of contaminations were measured *ex-situ* by RBS with He ions. It could be shown that Se only sticks to “clean”, silicon terminated Si(001) surfaces, achieved by growing a Si buffer layer of 80 nm or by etching-off the native SiO_2 in UHV a chemical reaction of impinging Si at 700°C which reduces SiO_2 to volatile SiO. Due to the low binding energy of Se at Si the Se desorption during the exposition to atmosphere and later during the RBS measurement cannot be avoided and therefore samples had to be enhanced with a metallic cap layer that disables the Se loss. Using the compound $SnSe_2$ as source material a contamination of the Se coverage with Sn at the level of about 1 at.% was unavoidable. In the case of WSe_2 the W contamination in the passivation layer is below the RBS detection limit of $< 10^{11}$ atoms/cm^2.

Collaboration: [1]TU Chemnitz, Germany [2]Forschungszentrum Jülich, Germany

Nanoscale Magnetism

J. Fassbender
J. McCord[1]

Control of saturation magnetization, anisotropy and damping due to Ni implantation in thin $Ni_{81}Fe_{19}$ layers

The static and dynamic magnetic properties of 20 nm thick $Ni_{81}Fe_{19}$ films implanted with Ni-ions have been investigated as a function of the ion fluence up to 1×10^{16} cm^{-2} (~5 at.%). The implantation has been performed at 30 keV. The maximum of the projected ion range is located in the center of the ferromagnetic layer for a rather homogeneous ion distribution throughout the film. With increasing ion fluence the saturation magnetization and the effective magnetic anisotropies (static and dynamic) are reduced. However, the effective magnetic damping is drastically enhanced for higher ion fluences. This increase can be explained mainly by the drop in saturation magnetization in connection with structural changes. In addition ion implantation in an applied magnetic field allows the setting of the uniaxial anisotropy direction irrespective of the initial orientation.

Collaboration: [1]Leibniz Institute of Solid State and Materials Research Dresden, Germany

J. Fassbender
J. von Borany
A. Mücklich
K. Potzger
W. Möller
J. McCord[1]
L. Schultz[1]
R. Mattheis[2]

Structural and magnetic modifications in Cr implanted permalloy

The static and dynamic magnetic properties, especially the magnetic damping behavior, have been investigated as a function of saturation magnetization in thin $Ni_{81}F_{19}$ (permalloy) films. Ion implantation doping with Cr in the percentage regime has been used to effectively reduce the Curie temperature and thus the saturation magnetization at room temperature. In order to understand the magnetic modifications the changes in stoichiometry but also the ion induced structural changes have been addressed. As a function of fluence first an improvement of the (111) fiber texture, then a lattice expansion and finally a partial amorphization of the interface near region of the permalloy layer is found. The region of amorphization can be understood quantitatively by simulation of the concentration profiles as a function of depth in combination with irradiation induced damage formation. The magnetic properties change correspondingly. For increasing Cr doping a drop in saturation magnetization and a decrease of the uniaxial magnetic anisotropy is observed. For a fluence of 0.8×10^{16} Cr/cm^2 (~4 at.%) the magnetic damping parameter α increases by a factor of 7. This strong increase is mainly caused by the reduction of the saturation magnetization and a change of the sample crystallinity.

Collaboration: [1]Leibniz Institute of Solid State and Materials Research Dresden, Germany, [2]Institute for Physical High Technology Jena, Germany

V. Cantelli
J. v. Borany
J. Grenzer
J. Fassbender
R. Kaltofen[1]
J. Schumann[1]

Influence of He ion irradiation on thin NiMn/$Ni_{81}F_{19}$ exchange bias films

Magnetron sputtered film stacks of 5 nm Ta/50(15) nm NiMn/20 nm $Ni_{81}Fe_{19}$/5 nm Ta deposited at SiO_2/Si substrates were subsequently irradiated with He^+ ions (30 keV, $1 \times 10^{15} - 3 \times 10^{16}$ cm^{-2}, RT or 250°C). The transition from the paramagnetic NiMn phase (fcc) to the chemically ordered, antiferromagnetic tetragonal $L1_0$ phase during annealing (100 – 500°C, Vacuum) was studied by *in-situ* XRD using synchrotron radiation. A small $L1_0$ fraction (< 15%) is already available after deposition. The transformation to a dominating $L1_0$ ordered NiMn film (long-range order parameter $S > 0.5$) takes place between 300 – 400°C irrespective of the irradiation. This is consistent with magnetization reversal measurements of the corresponding permalloy layers. Annealing at elevated temperatures ($T_A > 400$°C) leads to a loss of $L1_0$ ordering due to a complete intermixing of the NiMn and the permalloy films. The benefit of low-fluence ion irradiation (1×10^{15} cm^{-2}) is a reduction of the mosaicity for both the NiMn and the permalloy film, and a smoothening of internal interfaces.

M.C. Weber[1]
H. Nembach[1]
B. Hillebrands[1]
J. Fassbender

All-optical probe of precessional magnetization dynamics in exchange biased $Ni_{81}Fe_{19}$/FeMn bilayers

An internal anisotropy pulse field is launched by an 8.3 ps short laser excitation, which triggers precessional magnetization dynamics of a polycrystalline $Ni_{81}Fe_{19}$ / FeMn exchange bias system on a picosecond timescale. Due to the excitation the exchange coupling across the interface between the ferromagnetic and the antiferromagnetic layer is reduced, leading to a fast reduction of the exchange bias field and to a dramatic increase of the zero-field susceptibility. The fast optical unpinning is followed by a slower recovery of the interfacial exchange coupling dominated by spin-lattice and heat flow relaxation with a time constant of the order of 160 ps. The measured picosecond time evolution of the exchange decoupling and restoration is interpreted as an anisotropy pulse field giving rise to fast precessional magnetization dynamics of the ferromagnetic layer. The strength of the internal pulse field and even the initial magnetization deflection direction from the equilibrium orientation can be controlled by the absorbed photons. The dependence of the effective Gilbert damping on both small and large angle precessional motion was studied, yielding that both cases can be modeled with reasonable accuracy within the Landau-Lifshitz and Gilbert framework.

supported by DFG

Collaboration: [1]Department of Physics, TU Kaiserslautern, Germany

K. Küpper
L. Bischoff
J. Fassbender
K.W. Chou[1]
B. van Waeyenberge[1]
H. Stoll[1]
G. Schütz[1]
T. Tyliszczak[2]
I. Neudecker[3]
C.H. Back[3]

Suppression of vortex core motion by means of focused ion beams

Recently, vortex-core driven magnetization dynamics has become a hot topic. The gyrotropic motion of the vortex core is found to be in the sub-GHz regime and thus easily accessible with high-resolution synchrotron-based time-resolved transmission x-ray microscopy (TR-TXM) techniques. In order to investigate the influence of artificial magnetic defects positioned within the vortex structure on the magnetization dynamics and the potential switching between individual defects focused ion beam milling has been employed. The understanding and control of these mechanisms is of utmost scientific and technological relevance. A series of circular and square shaped permalloy ($Ni_{81}Fe_{19}$) microstructures have been investigated, which exhibit a nanoscopic hole at different positions. The gyrotropic motion of the vortex core is excited by means of a microwave sine-excitation with different excitation amplitudes. The magnetization dynamics is sensed by TR-TXM. It is found that a defect located far away from the vortex core has almost no influence on the magnetization dynamics. However, a point defect located in the centre of the structure suppresses the gyrotropic motion of the vortex core completely.

Collaboration: [1]Max-Planck Institute for Metal Research, Stuttgart, Germany, [2]Advanced Light Source, Lawrence Berkeley National Laboratory, Berkeley, USA, [3]Institute for Experimental and Applied Physics, University of Regensburg, Germany

M.C. Weber[1]
H. Nembach[1]
B. Hillebrands[1]
M.J. Carey[2]
J. Fassbender

Real-time evidence of two-magnon scattering in exchange coupled bilayers

Coherent spin waves in exchange biased bilayers have been excited by ultrafast photomodulation of the exchange bias anisotropy. Photoinduced precession in CoFe / IrMn samples with different IrMn thickness, thus, different exchange bias fields, has been studied in real-time by time-resolved Kerr-effect. The extracted effective damping parameter is proportional to the square of the exchange bias field. Two-magnon scattering of the coherent precession of the ferromagnetic layer at local interfacial fluctuations of the exchange bias field can account for the observed increase. Hence, there is time-domain evidence of two-magnon damping involved in the relaxation of photoexcited spins.

Collaboration: [1]Department of Physics, TU Kaiserslautern, Germany, [2]Hitachi Global Storage Technologies, San Jose, USA

supported by
DFG

K. Küpper
L. Bischoff
R. Mattheis[1]
P. Fischer[2]
J. Fassbender

Magnetic domains and magnetization reversal of ion-induced magnetically patterned RKKY-coupled $Ni_{81}Fe_{19}/Ru/Co_{90}Fe_{10}$ films

Pure magnetic patterning by means of ion beam irradiation of magnetic thin films and multilayers result often from a post deposition local modification of the interface structure with only minor effects on the film topography. In this study a 60 keV fine focused Co ion beam was used to change the coupling in a $Ni_{81}Fe_{19}/Ru/Co_{90}Fe_{10}$ structure from antiferromagnetic to ferromagnetic on a micron scale. Thereby an artificial structure with locally varying interlayer exchange coupling and therefore magnetization alignment is produced. High-resolution full-field x-ray microscopy is used to determine the magnetic domain configuration during the magnetization reversal process locally and layer resolved due to the element specific contrast in circular x-ray dichroism. In the magnetically patterned structure there is in addition to the locally varying interlayer exchange coupling across the Ru layer also the direct exchange coupling within each ferromagnetic layer present. Therefore the magnetization reversal behaviour of the irradiated stripes is largely influenced by the surrounding magnetic film.

Collaboration: [1]Institute for Physical High Technology Jena, Germany, [2]Center for X-Ray Optics, Lawrence Berkeley National Laboratory, Berkeley, USA

M.O. Liedke
K. Potzger
A.H. Bothmer
B. Hillebrands[1]
M. Rickart[2]
P.P. Freitas[2]
J. Fassbender

Domain structure during magnetization reversal of PtMn/CoFe exchange bias micro patterned lines

The magnetic domain configuration and the magnetization reversal behaviour of micropatterned exchange bias elements were investigated by means of magnetic force microscopy. In addition to the unidirectional anisotropy the shape anisotropy determines the overall magnetization reversal behaviour. In order to modify the ratio between both anisotropy contributions the exchange bias field strength was reduced by means of 5 keV He^+ ion irradiation. For the as-prepared samples a mono-domain magnetization state with the magnetization direction aligned along the exchange bias field direction was found regardless of the element shape. After irradiation the unidirectional anisotropy contribution is reduced and hence the previously homogeneous magnetization state brakes up into small domains with 360° domain walls in between. The appearance of these domain walls, which was mainly observed for the descending branch of the magnetization reversal, is found to depend strongly on the structure width and orientation.

Collaboration: [1]Department of Physics, TU Kaiserslautern, Germany, [2]INESC MN, Lisbon, Portugal

Supported by
EU

P. Candeloro[1]
S. Blomeier[1]
P.A. Beck[1]
H. Schultheiß[1]
H.T. Nembach[1]
B. Hillebrands[1]
M.O. Liedke
J. Fassbender
B. Reuscher[2]

Evidence of lateral coupling in exchange bias double layers with lateral modulation of the exchange bias field

Magnetic properties of a $Ni_{81}Fe_{19}$/FeMn exchange bias bilayer were modified on the micron and submicron scale by ion irradiation, without significant changes in the sample topography. The resulting magnetic patterns were investigated by MOKE and MFM. The hysteresis loops measured by MOKE reveal that the magnetization reversal is not proceeding independently in irradiated and non-irradiated areas. This magnetic coupling is confirmed by MFM measurements, which clearly show that magnetic domains in irradiated and non-irradiated elements are mutually influencing each other during the reversal process.

Collaboration: [1]Department of Physics, TU Kaiserslautern, Germany, [2]Institut für Oberflächen- und Schichtanalytik (IFOS), Kaiserslautern, Germany

supported by
EU

Ferromagnetic Gd-implanted ZnO single crystals

K. Potzger
S. Zhou
F. Eichhorn
F. Herrmann
M. Helm
W. Skorupa
J. Fassbender
T. Herrmannsdörfer[1]
A. Bianchi[1]

In order to introduce ferromagnetic properties, ZnO single crystals have been implanted with Gd ions at 180 keV ion energy and two different fluences. Magnetization reversal hysteresis loops have been recorded for as-implanted as well as annealed samples using a SQUID magnetometer. For a fluence of 5×10^{15} ions/cm^2, post implantation annealing leads to an increase of the saturation moment up to 1.8 μ_B/Gd at exactly 300 K, thus excluding Gd, ZnGd or Gd_2O_3 secondary phases to be the origin of the observed ferromagnetism.

Collaboration: [1]Dresden High Magnetic Field Laboratory, Forschungszentrum Rossendorf, Germany

Structure and ferromagnetism of Mn^+ ion-implanted ZnO thin films on sapphire

G. Brauer
W. Anwand
W. Skorupa
H. Schmidt[1]
M. Diaconu[1]
M. Lorenz[1]
M. Grundmann[1]

Slow positron implantation spectroscopy (SPIS), based on the generation, implantation and subsequent annihilation of mono-energetic positrons in a sample, has been used to study depth dependent vacancy-type damage in three ZnO films grown by PLD on c-plane sapphire. Doping was achieved by implantation of 250 keV Mn^+ ions at 300°C with three different fluences - 10^{16}, 3×10^{16}, and 6×10^{16} cm^{-2}, and subsequent thermal annealing in air. The evolution of the open volume damage, its depth distribution, and the magnetic behaviour was investigated by SPIS and MFM. No indication of magnetic domain formation was found in any of the three films after implantation and the first annealing at 500°C, whereas after the second annealing at 750°C the two samples having the higher fluence showed stripe-like magnetic domains.

Collaboration: [1]Institut für Experimentelle Physik II, Universität Leipzig, Germany

Mn-silicide nanoparticles formed in Si using ion implantation

S. Zhou
K. Potzger
A. Mücklich
R. Grötzschel
B. Schmidt
F. Eichhorn
W. Skorupa
J. Fassbender

300 keV Mn^+ ions were implanted into Si with a fluence of 1×10^{15} cm^{-2}, 1×10^{16} cm^{-2}, 5×10^{16} cm^{-2}, respectively. The samples were annealed at 800°C in N_2 ambient for 5 min by rapid thermal annealing method. RBS/C, TEM and XRD were applied for structural characterization. It was found that this annealing is not sufficient to remove the implantation damage. Moreover no evidence is found for Mn substituting Si sites. Mn_xSi_y nanoparticles were formed after annealing. The control of these effects is essential for the design of Si-based diluted magnetic semiconductors.

Magnetic and structural properties of ^{57}Fe implanted GaN

G. Talut
H. Reuther
F. Eichhorn
K. Potzger
S. Zhou

In order to investigate the possibility to create and stabilize a DMS (diluted magnetic semiconductor) behaviour in the (Ga,Fe)N-system, p-doped GaN was implanted with $^{57}Fe^+$ ions (200 keV, $1 - 16 \times 10^{16}$ cm^{-2}) at 350°C and subsequently annealed between 700 and 900°C in N_2-flux for 5 min. CEMS measurements of the as-implanted samples ($1 - 16 \times 10^{16}$ cm^{-2}) show a magnetic hyperfine field of $B_{hf} = 10$ T which cannot only be attributed to α-Fe ($B_{hf} = 33$ T). However, annealing of the high-fluence implanted samples ($\geq 6 \times 10^{16}$ cm^{-2}) result in the formation of fiber-textured α-Fe-clusters with 5 and 15 nm size after 700 and 900°C annealing, respectively. For the highest Fe-doped sample (16×10^{16} cm^{-2}) annealed at 900°C, AES reveals a dispersion of the Fe-implantation profile due to radiation-enhanced diffusion and the existence of Fe-rich regions which reflects the formation of Fe clusters. Zero-field-cooled / field-cooled SQUID measurements of the sample implanted with 1×10^{16} cm^{-2} and annealed at 850°C show a Curie-temperature of 250 – 270°C, which is associated with the DMS. However it also indicates the presence of superparamagnetic Fe-clusters with a blocking temperature of 40 K. No other crystalline phases like iron-nitrides were found by XRD.

Supported by
DFG

Magnetic properties of ion implanted diamond and graphite

V. Heera
R. Höhne[1]
P. Esquinazi[1]

Recent experimental and theoretical studies suggest the existence of intrinsic ferromagnetism in carbon structures with predominant sp^2-bonds like highly oriented pyrolytic graphite (HOPG) and fullerene polymers. In contrast, ferromagnetism in diamond with sp^3 bonds has never been observed. It is speculated that the magnetism in the carbon phases is caused by special lattice defects and not, as sometimes suggested, by magnetic impurities. In order to elucidate the role of lattice defects, nonmagnetic and magnetic impurities in different carbon phases, a series of implantation experiments was carried out. Diamond and HOPG samples were implanted with F^+ and Fe^+. Defect-rich surface layers with impurity concentrations from 50 to 500 ppm extending to a depth of about 2 µm were produced by multiple energy implantation in the MeV range. The magnetic properties were measured with a SQUID magnetometer. Preliminary results show that the weak ferromagnetism of the unimplanted HOPG is not markedly influenced after implantation of iron or fluorine. The paramagnetic part of the magnetization of HOPG and diamond clearly increases by ion implantation mainly due to the enhancement of disorder. No ferromagnetism was detected in the diamond samples.

Collaboration: [1]University of Leipzig, Germany

Ion beam synthesis of Fe nanoparticles in MgO and yttria stabilized zirconia (YSZ)

K. Potzger
H. Reuther
S. Zhou
A. Mücklich
R. Grötzschel
F. Eichhorn
M.O. Liedke
J. Fassbender
H. Lichte[1]
A. Lenk[1]

In order to synthesize embedded Fe nanoparticles MgO(001) and YSZ(001), single crystals have been implanted with Fe^+ ions at different temperatures and ion energies of 100 keV and 110 keV respectively. Using a fixed ion fluence of $6\times10^{16}\,\mathrm{cm}^{-2}$, γ-Fe nanoparticles are formed inside the MgO substrate up to a temperature of 1073 K. In contrast, ferromagnetic α-Fe nanoparticles are formed inside YSZ at elevated temperatures with an efficiency of 100 % at an implantation temperature of 1273 K. Their ferromagnetic behaviour is reflected by a magnetic hyperfine field of 330 kOe and a hysteretic magnetization reversal. Electron holography measurements have been carried out in order to visualize the stray field of the particles.

Collaboration: [1]Triebenberg Laboratory for High-Resolution Electron Microscopy, TU Dresden, Germany

Influence of energetic atoms on the $L1_0$ ordering of FePt films fabricated by magnetron sputtering

V. Cantelli
J. von Borany
J. Fassbender
N. Schell
S. Zhou

The $L1_0$-ordering of stoichiometric FePt films (30 – 120 nm) deposited on SiO_2/Si substrates by dc magnetron sputtering from elemental targets has been studied. A low deposition rate (0.6 Å/s) and Ar pressure (0.3 Pa) was used. The kinetics of $A1\rightarrow L1_0$ transition and ordering in FePt films have been investigated by *in-situ* XRD at the Synchrotron beamline ROBL at ESRF. The transition has been obtained at relatively low temperatures of (300 ± 20)°C leading to almost complete $L1_0$ ordered films with an ordering parameter $S > 0.8$. No remarkable differences are obtained by combining deposition at room temperature and post-deposition annealing or deposition at the annealing temperature except of slightly variations in the grain size. An additional ion irradiation with He^+ (50 keV, $1\times10^{15} - 3\times10^{16}\,\mathrm{cm}^{-2}$) does not influence the transition temperature and the degree of ordering. Calculations reveal that for our experimental conditions there is no thermalization of the sputtered target atoms and the reflected Ar neutrals, thus a considerable fraction of atoms meet the substrate with energies exceeding the displacement threshold. This corresponds to the formations of point defects already during deposition which support the $L1_0$ ordering if they get mobile at temperatures >250°C.

K.-H. Heinig

Even-odd effect of anisotropy transfer from a stack of metal films to the $L1_0$ superstructure

Atomic collisions in solids are often associated with the concept of disorder. However, recently we demonstrated that irradiation may induce chemical order in intermetallic alloys, where significant structural $L1_0$ order of alternating (001)Fe and (001)Pt atomic layers in almost fcc-type FePt was obtained and controlled in FePt by postgrowth He ion irradiation well below the ordering temperature. Now, the irradiation-assisted $L1_0$ phase formation from a stack of several atomic layers thick Fe and Pt films was studied by kinetic Monte-Carlo simulations. An unexpected even-odd effect in the anisotropy of the final $L1_0$ phase was discovered: Whereas stacks of films consisting of an even number of atomic (001) layers show no preferred c-axis selection of the final structure, stacks of films consisting of an odd number of atomic (001) layers may show an almost perfect c-axis alignment perpendicular to the substrate. This very selective $L1_0$ phase formation has been understood by the peculiarity of the reaction pathway in a stack of films: The $L1_0$ FePt phase forms from Fe and Pt via the two $L1_2$ phases (Fe_3Pt, $FePt_3$), where the $L1_2$ unit cells fit commensurably or incommensurably in a single film of one metal. Thus, during the formation of the $L1_0$ superstructure from the two $L1_2$ phases, the anisotropy of the Fe/Pt interface will be either transferred to a single $L1_0$ variant or will be lost completely. This evolution of anisotropy of layered systems is very important for the synthesis of new magnetic recording films.

M.O. Liedke
S. Rossbach
S. Facsko
J. Fassbender

Exchange bias on rippled substrates

Monoatomic steps at the interfaces between a ferromagnetic and an antiferromagnetic layer give rise to uncompensated spins which are the origin of the exchange bias phenomenon. Such steps have been generated by substrate surface patterning by means of Ar^+ ion erosion. Depending on the primary energy and the angle of incidence, a rippled surface with a well defined periodicity (~20 – 100 nm) and peak-to-valley height (~2 – 5 nm) has been created. On top of this surface, an exchange bias system consisting of 5 nm $Ni_{81}Fe_{19}$ coupled to 10 nm $Fe_{50}Mn_{50}$ has been prepared by MBE. The interface corrugation remains throughout the layer stack. By means of a field annealing cycle the exchange bias direction has been initialized either along or perpendicular to the ripple direction, which causes to align the uniaxial and unidirectional anisotropy contributions either parallel or perpendicular to each other. The magnetization reversal behaviour has been investigated by means of MOKE. For both cases the magnetic easy- and hard-axes remained identical as the uniaxial anisotropy contribution is much larger than the unidirectional one. However, exchange bias initialization along or perpendicular to the ripple direction shifts the magnetization reversal loop of the easy-axis or hard-axis, respectively. A complete angular dependence of the magnetization reversal behaviour has been investigated for both cases and compared to simulations based on a Stoner-Wohlfarth coherent rotation model. A good agreement between experimental data and simulations is found.

Nanostructures

L. Röntzsch
K.-H. Heinig
B. Schmidt
A. Mücklich
W. Möller
J. Thomas[1]
T. Gemming[1]

Direct evidence of self-aligned Si nanocrystals formed by ion irradiation of Si/SiO$_2$ interfaces by energy-filtered TEM

Recently it has been proven that thin SiO$_2$ layers placed between the Si substrate and a poly-Si top layer become an efficient charge storage medium for non-volatile memory applications by Si$^+$ ion irradiation and subsequent annealing. It has been predicted by atomistic computer simulations that δ-layers of tiny Si nanocrystals (NCs) are formed by this technique. So far these NCs could neither be imaged by TEM nor unambiguously identified by any other analytical method. For the first time, we deliver direct evidence of Si NC δ-layers in SiO$_2$ by energy-filtered TEM. We found ≤ 3 nm sized Si NCs at the ion-irradiated ($E_{Si} = 50$ keV, $\Phi_{Si} = 7 \times 10^{15}$ cm^{-2}) and annealed ($T = 1050$°C, $t = 120$ s) Si/SiO$_2$ interfaces of a MOS-like "50 nm Si / 15nm SiO$_2$ / Si substrate" structure. The position and shape of the NC δ-layers are in good agreement with the predictions of former atomistic computer simulations.

Collaboration: [1]Leibniz Institute for Solid State and Materials Research Dresden, Germany

L. Röntzsch
K.-H. Heinig

Atomistic simulations on the focused-ion-beam-based synthesis of functional 1D nanostructures

Nanowires (NWs) play an important role as basic components of electronic and photonic devices. Atomistic computer simulations on focused ion beam (FIB) implantation and subsequent phase separation during thermal annealing were performed. The systematic investigations are aimed at optimum reaction pathways for CMOS-compatible fabrication of metal silicide and semiconductor nanowires. On realistic time and length scales, the simulation of the whole process was divided into two steps: (i) the spatio-temporal evolution of FIB implantation profiles was calculated by a new computer code including dynamical target changes, local ion erosion etc, (ii) post-implantation annealing causes NW formation, which is modelled by kinetic Monte Carlo simulations. It is demonstrated that the evolution of the FIB implantation profile proceeds in three stages: (i) phase separation by nucleation and growth, (ii) NW formation by coalescence of nanoclusters, (iii) NW surface smoothening. Likewise, functional structures for nanoelectronic and photonic devices including several NWs, like T- or X-junctions, are obtained by crossing different FIB traces.

Supported by
DFG

L. Röntzsch
K.-H. Heinig

Search for reaction pathways of a CMOS-compatible channel fabrication for nanofluidic devices

Nanofluidic devices are going to play an important role in miniaturization, automation and parallelization of chemical, biological, or medical systems. For "lab-on-a-chip" devices, CMOS compatibility is desired. We discovered a potential reaction pathway for a nonconventional, however, CMOS-compatible fabrication method of nanofluidic channels and channel networks. Starting from the "silicon-on-nothing" technique developed by a Japanese group (T. Sato *et al.*, Jap. J. Appl. Phys. **43** (2003) 12), we predict, by kinetic Monte-Carlo simulations, nanochannel formation in (001)Si from appropriate trench ensembles. During a thermal treatment, thin trenches decouple quickly from the wafer surface forming buried voids. In a self-organizing manner, neighbouring voids coalesce and, thus, form a buried channel. Thick trenches are more stable. They remain open at the wafer surface and, therefore, may act as vertical supply and drain pipes for buried channels. The simulations predict also the formation of elementary nanochannel networks such as T- or X-like junctions, H-filters, as well as buried toroidal voids.

Supported by
DFG

L. Röntzsch
K.-H. Heinig

Size and position control of chains or arrays of nanoparticles by thermocapillarity

Surface free energy minimization, driven by capillary forces, may lead to morphological changes of wires, i.e. their decay into a droplet chain (Rayleigh instability). At nanoscale dimensions, capillary-driven self-organization processes are subject to increasing fluctuation with decreasing size, thus preventing the formation of long-range ordered regular structures. Here, a novel method to fabricate size- and position controlled chains of nanoparticles is examined by means of kinetic Monte Carlo simulations. The method rests on the temperature dependence of surface tension – the origin of thermocapillarity. Uncompensated forces occur due to surface temperature gradients. It is found that surface tension gradients trigger the biased migration of atoms from hot to cold regions. We predict that the regularity of nanoparticle chains formed during the self-organized disintegration of nanowires can be considerably improved by an external periodic temperature profile along the nanowires. Strong external temperature fields control the nanowire decay, however, weak ones have to be commensurable with the Rayleigh wavelength to produce long rang order.

Supported by DFG

T.W.H. Oates
A. Mücklich

Controlling the growth of Ag nanoparticles in polymer matrices using spectroscopic ellipsometry

Controlled growth of metal nanoparticles in a polymer matrix is of technical interest for catalytic, biosensor and optoelectronic applications. Monitoring of PVD nanoparticle growth using *in-situ* spectroscopic ellipsometry (SE) has been performed. Ag nanoparticle growth is performed in an RF magnetron sputter facility equipped with *in-situ* SE and sample stage heating capabilities. High resolution TEM imaging of the nanoparticles shows almost spherical single-crystal particles. Major advances have been made in modelling of the SE data utilising collective electron oscillations in the form of plasmon-polariton resonances. Information concerning the particle size and nucleation processes can be extracted by considering the mean free path of the electrons in the nanoparticles. For incorporation of the nanoparticles in polymer matrices, dual magnetron sputtering is utilised for the production of metal nanoparticle/polymer composite films by both alternate and co-sputtering and the process monitored with *in-situ* FTIR and SE. A second approach investigates the growth of nanoparticles by reduction of metallic ions in a polymer. Thermal degradation of an organometallic precursor dispersed in polystyrene is shown to produce silver particles of the order of 6 nm radius, a process which is recorded in real-time by SE. Plasmon- polariton resonances in the particles allow the real time growth of the particles to be followed in the range of 2 to 10 nm in radius.

Supported by EU (MC-IIF)

C. Akhmadaliev
B. Schmidt
L. Bischoff

Investigation of FIB assisted $CoSi_2$ nanowire and nanochain growth in crystalline silicon

The ion beam synthesis of $CoSi_2$ nanowires (NW) by writing stoichiometric FIB implantation and subsequent annealing has been studied. Si(111) and Si(100) samples were implanted at a sample temperature of 450°C or at room temperature (RT). The implantation dose for heated and non-heated samples was in the range of $(0.5 – 2) \times 10^{17}$ cm^{-2} and $(0.1 – 1.0) \times 10^{16}$ cm^{-2}, respectively. The line scan direction of the FIB was aligned under 0°, 15°, 30° and 45° relative to the <110> crystal direction. The heated samples were subsequently annealed in a two step process: 600°C for 60 min and 1000°C for 30 min in dry N_2. Stable $CoSi_2$ nanowires with diameter down to 10 – 50 nm and up to 5 µm length were achieved when the FIB trace was precisely aligned along <110>-direction. In the case of a misaligned FIB trace the nanowires are not stable and decay into chains of CoSi$_2$ nanoparticles. This behaviour is consistent with 3D kinetic Monte-Carlo-simulations of phase separation, coalescence and decay of NWs. FIB implantation at RT leads to local defect formation and produces nucleation (strain) centers. After implantation the sample back side was additionally coated with 10 nm Co. During subsequent annealing (heating, quenching) a Co super-saturation through the sample was achieved. Self-aligned wire growth starting at the nucleation centers and along <110> directions was observed in Si(100) and Si(111) substrate materials. Further efforts are focused on increasing of reproducibility of nanowire growth and the fabrication of nanodevices.

Supported by
DFG

L. Bischoff
C. Akhmadaliev
S. Facsko
A. Keller

Surface structures induced by sputtering of Si and Ge with a FIB

Self-organized periodic structures with submicron periodicity are known to be formed by a broad ion beam. They can be arranged as ripple patterns at off-normal ion incidence and as hexagonal patterns at normal incidence. We have studied the pattern formation induced by a scanned focused ion beam (FIB) on Si and Ge surfaces as a function of ion species, ion current, ion dose, and incidence angle. While high currents of about 1 nA lead to strongly structured surfaces, low currents of some ten pA seem to result in a flattening of the surface at nearly the same total current densities of the order of A cm^{-2}. At off-normal angles of incidence the appearance of ripple patterns with periodicities around 1 μm similar to the ripples produced by broad beams are observed. However, at normal incidence of the FIB new complex structures starting from the edges of the scanned area are formed which are not observed during broad beam ion irradiation. A great advantage of the FIB is its ability for *in-situ* imaging of secondary electrons during pattern formation. The *in-situ* analysis of the dynamical behavior of the surface morphology gives a new access to distinguish between the different models for the pattern formation.

C. Akhmadaliev
L. Bischoff
B. Schmidt
V. Luchnikov[1]
M. Stamm[1]

Focused ion beam milling of polymer bi-layers for fabrication of self-rolled micro- and nanotubes

The formation of micro- and nanotubes from scrollable polymer bi-films deposited on an Al sacrifice layer on a silicon substrate was studied. The dimensions and the position of the rolled-up tubes were controlled by FIB-milling of H- and U-like structures of different shape in the polymer films. The FIB has several advantages compared to the application of other techniques, like mechanical cutting or lithography, due to a better spatial resolution and the direct structuring of materials independent of the composition. First the silicon substrate was covered with an Al layer. Then the polymer bi-layer was deposited by means of spin-coating starting with a film of poly-4-vinyl pyridine from a chloroform solution followed by a polystyrene film from a toluene solution. The FIB pattered samples were etched in alkaline water or in acid solution in order to remove the Al layer which enables the polymer bi-layer to roll-up into tubes. The diameter is a function of the polymer thickness whereas for a 50 nm thick bi-layer tubes with a diameter of about 0.8 – 1 μm were obtained.

Collaboration: [1]Leibniz-Institute for Polymer Research Dresden, Germany

Supported by
DFG

J. Grenzer
L. Bischoff
M. Posselt
U. Pietsch[1]

X-ray grazing incidence investigations of focused ion beam implantation pattern at Si and GaAs surfaces

2D arrays of circular dots have been fabricated on GaAs(001) and Si(001) substrates using a Ga$^+$ FIB implantation with a spot size of about 50 nm (normal incidence, 25 keV, 10^{14} cm^{-2} per dot). The 2D-lattice structures had a period of 250×250 nm^2 covering a total area of 0.2 mm^2. The influence of the implanted ions on the host lattice has been investigated by means of grazing incidence diffraction (GID) performed at the ESRF-beamlines ID10 and ID1. The low-dose implantation creates point defects (interstitials and vacancies) below the surface in both substrates. In Si substrates a 2D periodical strain field is generated which is clearly obtained in the GID pattern. For the GaAs substrate we found a more complex scattering pattern depending on the in-plane orientation of the 2D dot array with respect to the crystallographic orientation of the GaAs crystal. A significantly enhanced scattering contrast is obtained if the implantation is performed with a twist of 14° towards the [110] direction. The reason for the experimentally obtained difference in the scattering pattern between FIB implanted Si and GaAs is still under discussion, but clearly associated with the crystalline structure of the substrate.

Collaboration: [1]Institute of Physics, University of Siegen, Germany

Etch rate retardation of Ga^+ ion beam irradiated silicon

B. Schmidt
S. Oswald[1]
L. Bischoff

Surface chemistry during wet chemical etching in alkaline KOH solution and dry etching in SF_6/O_2 plasma of high-dose Ga^+ implanted Si has been investigated by means of SIMS and XPS. During wet chemical etching in a KOH/H_2O solution a thin layer of GaO_x of < 1 nm thickness is formed, which has been investigated in more detail by angle-resolved XPS. In the case of dry reactive ion etching (RIE) the surface chemistry is quite different. In this case a more enhanced oxidation of Ga takes place due to the high reactivity of atomic oxygen from the SF_6/O_2 plasma. SIMS results show that during RIE a Ga-rich surface layer forms, and therefore an enhanced Ga oxidation takes place, leading to a thicker GaO_x layer compared to wet chemical treatment. XPS depth profiling reveals a stoichiometry of almost completely oxidized Ga (Ga_2O_3) layer free from Si with a thickness of about 5 – 10 nm. The etch rate lowering in Ga^+ as-implanted silicon is ascribed to the formation of gallium oxide at the Si surface during the etch processes.

Collaboration: [1]Institute of Solid State and Materials Research Dresden, Germany

Influence of sputtering conditions and electron energy on XPS depth profiling of Ge in SiO_2

S. Oswald[1]
B. Schmidt
K.-H. Heinig

Ge nanocluster formation in SiO_2 is of growing interest for new electronic applications. Ion beam synthesis using Ge implantation connected with thermal annealing is one possible preparation method of such clusters. In addition to investigations of electrical and structural changes during the cluster formation process we also studied chemical changes in the samples using XPS. This was done with low-energy noble gas ion sputtering for depth profiling. Binding state information can be obtained from the XPS data by means of factor analysis in combination with other structural investigations. However, mixed bonding states probably created by ion beam damage during sputter erosion dominate the results. It is shown that, by changing the experimental conditions (ion beam impact depth during sputtering, electron information depth during XPS measurement) these mixed states are influenced in an appropriate manner. It is concluded that useful chemical information on the behaviour of the implanted Ge can be derived despite of the ion beam damage.

Collaboration: [1]Institute of Solid State and Materials Research Dresden, Germany

Shallow pn-junctions for piezoresistive cantilevers

M. Zier
B. Schmidt

Piezoresistive ultra thin p-type silicon layers can serve as compact, highly sensitive bending sensors in AFM cantilevers. Such piezoresistors for use in cantilever arrays have been fabricated using ion implantation of 1 keV B^+ ions. To reduce channeling and therefore the pn-junction depth, the substrate was pre-amorphised by irradiation with 30 or 60 keV Ge^+ ions. To remove the radiation damage and for electrically activation of boron, RTA for 10 to 60 s at 1000°C was employed. In parallel computer simulations of the ion implantation and annealing were carried out using the Crystal-TRIM and TESIM codes. TEM cross-section images showed an excellent agreement of the thickness of the amorphised layer with Crystal-TRIM simulations. SIMS measurements for the B^+ implanted and annealed samples agreed very well with TESIM simulations. For electrical characterization, test structures were fabricated to measure the sheet and contact resistances, the pn-junction breakdown and the leakage current, so that they can be optimised very quickly. The resistor layer meets the desired sheet resistance of around 300 Ω/□ and the junctions provide an excellent reverse bias insulation with a high breakdown voltage (> 150 V) and a low leakage current ($< 10^{-7}$ A). Further research using point defect engineering to create ultra-shallow junctions is currently pursued.

Supported by EU

Doping and Defects of Semiconductors

W. Vandervorst[1]
T. Janssens[2]
B. Brijs[2]
R. Delhougne[2]
R. Loo[2]
M. Caymax[2]
B.J. Pawlak[3]
M. Posselt

Athermal germanium migration in strained silicon layers during junction formation with solid-phase epitaxial regrowth

The Ge depth profile within a system consisting of a thin strained Si layer on top of a strain-relaxed SiGe buffer was monitored after the preamorphization step (without any anneal) and after the solid-phase epitaxial regrowth (SPER) process. The SIMS data show a drastic Ge redistribution if during the preamorphization a considerable amount of nuclear energy deposition occurs near the Si–SiGe interface. Therefore, the change of the Ge depth distribution is athermal and directly related to the atomic displacements in the collision cascades of the impinging ions. Atomistic simulations using the TRIDYN code confirm that ballistic mixing can be indeed considered as the dominant mechanism for the Ge redistribution. The calculated Ge depth profiles agree very well with measured data. Thermal anneals at the SPER temperatures, prior to or after the preamorphization implant, do not affect significantly the Ge distribution since the thermal diffusivity of Ge is relatively low.

Collaboration: [1]IMEC and KU Leuven, Belgium, [2]IMEC Leuven, Belgium, [3]Philips Research Leuven, Belgium

M. Posselt
F. Gao[1]
D. Zwicker

Migration of di- and tri-interstitials in silicon

A comprehensive study on the migration of di- and tri-interstitials in Si was performed using classical molecular dynamics simulations with the Stillinger-Weber potential. For temperatures between 800 and 1600 K the defect diffusivity, the self-diffusion coefficient per defect and the corresponding effective migration barriers were calculated. Compared to the mono-interstitial, the di-interstitial migrates faster, whereas the tri-interstitial diffuses slower. The mobility of the di- and the mono-interstitial is higher than the mobility of the lattice atoms during the diffusion of these defects. On the other hand, the tri-interstitial mobility is lower than the corresponding atomic mobility. The migration mechanism of the di-interstitial shows a pronounced dependence on the temperature. At low temperature a high mobility on zig-zag-like lines along a <110> axis within a {110} plane is found, whereas the change between equivalent <110> directions or equivalent {110} planes occurs seldom and requires a long time. At high temperature a frequent change between equivalent {110} planes is observed. During the diffusion within {110} planes the di-interstitial moves like a wave packet so that the atomic mobility is lower than that of the defect. On the other hand, the change between equivalent {110} migration planes is characterized by frequent atomic rearrangements. The visual analysis of the tri-interstitial diffusion reveals complex migration mechanisms and a high atomic mobility. The present results have implications for the explanation of experimental data on defect evolution and migration.

Collaboration: [1]Pacific Northwest National Laboratory, Richland, USA

H. Geßner
M. Posselt

Atomistic study of intrinsic defects in germanium

A number of parametrizations of the Stillinger-Weber (SW) interatomic potential and one of the Tersoff potential were evaluated with respect to their accuracy in describing the structure and energetics as well as the migration of point defects in Ge. For the SW parameter sets of W. Yu *et al.* and K. Nordlund *et al.* the structure and energetics of the vacancy and of the most stable self-interstitial configuration agree reasonably well with the ab-initio results from the literature. Furthermore, for these parametrizations, the contribution of vacancies to self-diffusion is found to be significantly higher than that of self-interstitials, in agreement with experimental data. However, the calculated activation energy for self-diffusion in Ge (2.2 eV) is smaller than the measured value (3.1 eV). Therefore, the accuracy of those interatomic potentials found to be most suitable in the present study is still not sufficient for a quantitative description of point defect properties in Ge.

S. Prucnal[1]
J.M. Sun
A. Nazarov[2]
I.P. Tjagulskii[2]
I.N. Osiyuk[2]
W. Skorupa

Correlation between defect-related electroluminescence (EL) and charge trapping in Gd-implanted SiO_2 layers

When amorphous silica is bombarded with energetic ions, various types of defects are created as consequence of ion-solid interaction (oxygen deficient centres: ODC, non-bridging oxygen hole centres: NBOHC, E'-centres, etc.). MOS structures with Gd implanted SiO_2 exhibit strong ultraviolet EL at 316 nm from Gd^{3+} ions. The intensity of the luminescent peaks from ODC at 460 nm (2.7 eV), NBOHC at 650 nm (1.9 eV) and defect centres with emission at 600 nm (2.07 eV) changes with Gd concentration. Charge trapping in Gd implanted SiO_2 layers was induced using constant current electron injection to study the EL intensity in dependence on the applied voltage change. The process of electron trap generation during high field carrier injection results in an increase of the EL from NBOHC, whereas the initial increase of the luminescence from ODCs (460 nm) appears in the same injected charge range where positive charge is trapped. Direct correlation between electron trapping and the quenching of the EL at 600 and 460 nm was observed with variation of the implanted Gd concentration.

Collaboration: [1]Maria Curie-Sklodowska University, Lublin, Poland, [2]Institute of Semiconductor Physics, Kiev, Ukraine

J.M. Sun
S. Prucnal[1]
H. Reuther
W. Skorupa

Point defects and electrical stability of SiO_2:Gd layers due to potassium and fluorine atoms

MOS light emitting diodes (MOSLEDs) containing Gd exhibit strong ultraviolet electroluminescence (EL) at 316 nm from Gd^{3+} and luminescence enhancement from defects at 465 nm, 520 nm and 650 nm corresponding to ODCs, E'-centres and NBOHCs (see contribution above), respectively. The elimination of such defects is very important from the viewpoint of electrical stability of MOSLEDs. The creation and transformation of point defects in bulk SiO_2:Gd containing fluorine and potassium atoms and their influence on optical and electrical stability of MOSLEDs during constant current injection was investigated. Additional implantation of fluorine into the SiO_2:Gd layer leads to a decrease of the number of defects together with an increasing efficiency of 316 nm Gd^{3+} EL. Mobile positive potassium ions can recombine with the negative charges trapped by the RE centres or in their vicinity. In contrast to that potassium doped SiO_2:Gd layers cause a distinct decrease of the EL quenching of the UV light, but a fourfold increased operation time in comparison with the samples containing only Gd or Gd + F ions.

Collaboration: [1]Maria Curie-Sklodowska University, Lublin, Poland

S. Prucnal[1]
J.M. Sun
W. Anwand
W. Skorupa

Flash-lamp processing in the ms-range for MOS-based light emitting diodes

Conventional annealing processes as furnace annealing (FA) and rapid thermal annealing (RTA) were compared to the more advanced technique of flash-lamp annealing (FLA) regarding the EL efficiency, electrical stability, defect formation and rare-earth nanocluster (RE-NC) creation in MOS-based light emitting diodes (MOSLEDs) with Gd and Tb implanted SiO_2 layers. The samples were annealed at different temperature/time regimes (800 to 1000°C, 40 min for FA, 1000°C to 1200°C, 6 s for RTA and 1100°C to 1200°C, 20 ms for FLA). The formation and distribution of RE-NCs in silica were investigated using a combination of RBS and XTEM. We observed strong correlation between the EL efficiency, the NCs sizes and the employed annealing techniques for both Gd and Tb implanted oxides. The increase of the annealing temperature and time leads to an inrease of the RE-NC size and a decrease of the EL efficiency. The mean size of the RE-NC diameter changed from 2 nm for 900°C up to 15 nm for 1100°C in the case of FA, while the high-temperature FLA (1200°C for 20 ms) causes the formation of NCs with an average diameter below 2 nm. Therefore, FLA has a clear advantage among other annealing techniques (FA and RTA) with respect to stable and efficient light emitters such as MOSLEDs devices.

Collaboration: [1]Maria Curie-Sklodowska University, Lublin, Poland

Crystallization of amorphous Si films by flash-lamp annealing

D. Panknin
M. Voelskow
W. Skorupa
B. Pecz[1]
L. Dobos[1]
C. Lioutas[2]
N. Vouroutzis[2]

The crystallization of amorphous silicon films deposited on glass using the flash-lamp annealing (FLA) process was realized and studied. The duration of the flash is 20 ms, about two orders of magnitude shorter than the standard rapid thermal annealing process. The a-Si films deposited on Corning glass were irradiated with different energy densities and crystallized exhibiting grains with a mean size up to 6 μm. These grains are almost free of in-grain defects. In this process amorphous silicon can be crystallized both by solid phase crystallization (SPC) and in the super lateral growth (SLG) regime. As in the case of laser processing, both regimes of SPC for low energy densities, as well as SLG for high energy densities appear during the FLA process. In order to reduce the strain due to the thermal gradient, the samples were preheated from the backside. The ability of the FLA process to eliminate the in-grain defects in already crystallized poly-Si films at 600°C is also demonstrated.

Collaboration: [1]Research Institute of Technical Physics and Material Science, Budapest, Hungary, [2]University of Thessaloniki, Greece

Modelling of flash-lamp-induced crystallization of a-Si thin films on glass

M. Smith[1]
R. McMahon[1]
M. Voelskow
D. Panknin
W. Skorupa

Thin polycrystalline Si films are attractive for the fabrication of active-matrix liquid crystal displays. The use of flash-lamp annealing to crystallize amorphous silicon (a-Si) layers on glass substrates as a low-cost manufacturing route shows a lot of promise. In this process, amorphous silicon can be crystallized both by solid phase crystallization (SPC) and in the super lateral growth (SLG) regime. A thermal model was developed, which incorporates the phase transitions during annealing The model comprises three parts. The first part is the thermal model, which computes the temperature profiles in the wafer from the energy absorbed from flash lamp pulse, taking into account any internal phase transitions. The second part is the optical model, which calculates how the flash lamp irradiation is absorbed into the wafer and transformed into heat energy. The final part of the model is the incorporation of the kinetics of the phase transitions, which include solid-liquid transitions as well as solid-phase crystallization. We have shown that predictions from the model are in good agreement with experimental observations. In addition, the model is a valuable aid to optimise the process conditions.

Collaboration: [1]University of Cambridge, UK

Characterization of 6H-SiC surfaces after ion implantation and annealing using positron annihilation spectroscopy and AFM

G. Brauer
W. Anwand
W. Skorupa
S. Brandstetter[1]
C. Teichert[1]

Systematic slow positron implantation spectroscopy (SPIS) and AFM studies of various 6H-SiC samples were performed to clarify the role of conductivity type, crystal quality, ion implantation (B^+, Al^+, N^+), and annealing (1650°C) in the formation of continuous long furrows running in one direction across the wafer surface. It is found that the observed changes in surface morphology are primarily the result of step bunching during thermal activation and thus occur regardless of conductivity type, crystal quality, and type of ion implantation. On terraces separating the step bunches, stripe-like islands with a discrete height in the nanometer range have been observed which may have some link with the type of ion implantation. SPIS results clearly indicate the formation of vacancy clusters in n-type material which are connected with the mobility of nitrogen in the samples at elevated temperatures. It is found that defect profiling by SPIS is not influenced by the changes in surface morphology observed due to annealing.

Collaboration: [1]Institut für Physik, Montanuniversität Leoben, Austria

C.C. Ling[1]
X.D. Chen[1]
G. Brauer
W. Anwand
W. Skorupa
H.Y. Wang[1,2]
H.M. Weng[2]

Deep-level defects in n-type 6H silicon carbide induced by He implantation

Defects in He^+ implanted n-type 6H–SiC samples have been studied with deep-level transient spectroscopy. A deep-level defect was identified by an intensity with a logarithmical dependence on the filling pulse width, which is characteristic of dislocation defects. Combined with information extracted from positron-annihilation spectroscopic measurements, this defect was associated with the defect vacancy bound to a dislocation. Defect levels at 0.38 / 0.44 eV (E1 / E2), 0.50, 0.53, and 0.64 / 0.75 eV (Z1 / Z2) were also induced by He implantation. Annealing studies on these samples were also performed and the results were compared with those obtained from electron- (0.3 and 1.7 MeV) and neutron-irradiated n-type 6H–SiC samples. The E1 / E2 and the Z1 / Z2 signals found in the He-implanted samples are more thermally stable than those found in the electron-irradiated or the neutron-irradiated samples.

Collaboration: [1]Dept. of Physics, University of Hong Kong, PR China, [2]Dept. of Modern Physics, University of Science and Technology of China, Hefei, PR China

R. Kögler
A. Peeva
A. Mücklich
F. Eichhorn
W. Skorupa
A. Kuznetsov[1]
J. Christensen[1]
B.G. Svensson[1]

Excess vacancies generated by high-energy ion implantation in SiGe

High-energy ion implantation into Si creates damage consisting of an interstitial-dominated region (excess interstitials) at the mean projected ion range, R_P, and a vacancy-dominated region around $R_P/2$ (excess vacancies). This damage distribution is caused by the ion impulse conservation during implantation and by the effective local vacancy-interstitial defect recombination in Si. Important features of the damage can be calculated by binary collision models. In the case of ion implantation into SiGe the theory predicts a decrease of excess vacancy generation with increasing Ge fraction. However, the experimental investigations show a significantly enhanced content of excess vacancies for ion implantation in SiGe compared to the implantation under equal conditions into Si. The main contribution to the high excess vacancy concentration in SiGe results from the less effectively working vacancy-interstitial defect recombination in SiGe in comparison to Si. A consequence of this result is that well established models for implantation damage generation and annealing in Si, like the +1 model, have to be reconsidered in the case of ion implantation into SiGe.

Collaboration: [1]University of Oslo, Norway

R. Kögler
A. Mücklich
F. Eichhorn
M. Posselt
H. Reuther
T. Schumann
I. Skorupa
W. Skorupa

Compound formation in the ternary system Pr-Si-O by ion beam synthesis

The compound formation in the ternary system Pr-Si-O initiated by ion beam synthesis in Si and in silicon-on-insulator (SOI) substrate was investigated. The oxygen content was varied by additional O ion implantation and by thermal oxidation. Compounds were studied after annealing by TEM, XRD, AES, SIMS, and spreading resistance profiling (SRP). For an annealing temperature of 1100°C Pr silicate grains were predominantly detected. The

J.S. Christensen[1]

most frequently observed silicate compounds are $Pr_{9.33}Si_6O_{26}$ and $Pr_2Si_2O_7$. Pr silicide ($PrSi_2$, PrSi) was detected for lower annealing temperatures such as 900°C and also to a minor fraction after high annealing temperatures. Surprisingly PrSi was also found in SiO_2. Pr oxide (Pr_2O_3), the promising compound for high-k dielectrics, could not be clearly detected. If it is formed at all, then only to a minor fraction. The obtained results can be explained by the simple consideration that the reordering energy in the Si matrix related to the compound formation should must be minimized.

Collaboration: [1]Dept. of Physics, Centre for Material Science and Nanotechnology, University of Oslo, Norway

H. Weishart
V. Heera
W. Skorupa
C. Dubois[1]

Nitrogen impurities in high-fluence Si-implanted diamond

The extent of unintended coimplantation with nitrogen of diamond implanted with $5.5 \times 10^{17}\,cm^{-2}$ of Si was investigated. The diamond samples were implanted using ^{28}Si. Since the nitrogen molecule $^{14}N_2$ has the same mass, nitrogen from the residual gas in the chamber will also be implanted. In order to reduce radiation-induced damage and to enhance formation of the new SiC phase the implantation was performed at an elevated temperature of 900°C. Subsequently, the sample was annealed for 10 min at 1500°C in an rf-heated furnace. For SIMS analysis the nitrogen signal was calibrated using a reference sample that was implanted with a nitrogen fluence of 3×10^{14} ions/cm^2 yielding a maximum N atomic concentration of 0.05 at.%. Because of the high Si concentration in diamond the SIMS Si-signal can not be calibrated by a reference sample. According to the SIMS analysis an unintended co-implantation of the diamond with nitrogen in the order of 10% of the Si fluence occurred. Thus the Si-implanted diamond layer exhibits a very high N-concentration up to $3 \times 10^{21}\,cm^{-3}$ in the maximum of the ion distribution.

Collaboration: [1]INSA, LPM Bat502, Villeurbanne, France

H. Weishart
V. Heera
W. Skorupa

n-type conductivity in high-fluence Si-implanted diamond

Experiments regarding the electrical properties of Si-implanted natural IIa-type diamond were continued. The range of implantation temperatures was extended to 760 and 1100°C. Fluences between 4.5 to $6.2 \times 10^{17}\,Si^+/cm^2$ were applied. These implantation parameters yield a 0.2 μm thick buried layer of epitaxially aligned SiC nanocrystallites. Raman spectroscopy shows that the generation of a small fraction of graphitic sp^2-bonds of up to 15% in the diamond host matrix occurs. Hall measurements were done in the temperature range between 110 and 820 K. All samples show a thermally stable, high n-type conductivity with electron concentrations of more than $10^{20}\,cm^{-3}$. The origin of this exceptionally high electron concentration may be attributed to unintentional co-implantation with nitrogen. Both, conductivity as well as electron concentration increase with the amount of graphitic sp^2-bonds in the diamond. Our revised model for explanation of this behavior assumes that electrons primarily originate from nitrogen donors in the SiC nanocrystals. The electron transport mainly occurs across the low-resistivity SiC nanograins. Defect levels within the forbidden gap in the diamond help the electrons to jump between the SiC grains. The more defects (sp^2-bonds) in the diamond the higher the conductivity. Defect levels in the diamond additionally supply charge carriers at temperatures above room temperature.

Optoelectronic Materials

F. Peter
S. Winnerl
A. Dreyhaupt
M. Helm

Profile of a photoconductive THz Emitter excited by an amplified femtosecond Ti:Sapphire laser

A large-area photoconductive THz emitter consisting of two metallization layers on a semiconductor, which are electrically insulated from each other has been investigated. The first metallization produces a periodic metal-semiconductor-metal (MSM) structure on the semiconductor for applying an electric field, whereas the second metallization shadows the optical excitation in every second period of the MSM structure. In this way, the photoexcited carriers are unidirectionally accelerated in the device, thus giving rise to constructive interference of the emitted electromagnetic fields. The THz emitter is excited by unfocused fs optical pulses from a Ti:Sapphire amplifier with an average power of 60 mW at a 1 kHz repetition rate. We analyse the spatial profile of the THz radiation from such an emitter. The resulting THz beam has a bandwidth from 0.1 THz to 4 THz and a field amplitude of up to 6 kV/cm (at 30 V bias). The THz pulse energy as determined from our experiments was 500 pJ with a measured THz spot size of 5 mm. The focussed THz spot was mapped out and analyzed with respect to the frequency. A strong increase of the beam diameter with decreasing frequency was found. Comparing the achieved THz intensities with those obtained by optical rectification in ZnTe, our photoconductive shadow emitter gives rise to higher peak-to-peak field amplitude at comparable excitation power. Our new emitter design, in combination with amplified laser systems is likely to enable new applications in THz spectroscopy and imaging.

S. Friebel
S. Winnerl
W. Seidel
H. Schneider
M. Helm

Extraction of single FELBE radiation pulses using a laser-activated plasma switch

In order to decrease the average radiation power of the Rossendorf free-electron laser (FEL) FELBE, as required for certain experiments, the FEL repetition rate should be reduced from 13 MHz to 1 kHz. To this end, plasma switching of FEL radiation pulses was demonstrated. The plasma switch is based on the principle of photo-induced reflectivity induced by an optically excited electron-hole plasma. Germanium serves as semiconductor material for the switch. The semiconductor was illuminated by a Ti:Sapphire laser ($\lambda = 800$ nm, $\tau < 100$ fs), which generates an electron-hole plasma on the front surface of the semiconductor. The generation of sufficient plasma density leads to a variation of the optical semiconductor properties for the infrared FEL radiation. The time-resolved measurement of the reflectivity yields a rise time of about 7 ps and an exponential decay with a time constant of 110 ps. For the highest value of the Ti:Sapphire laser fluence (1.75 mJ/cm^2), a reflectivity of Ge for FEL radiation ($\lambda = 9.2$ μm) of 85 % was achieved. We thus succeeded to extract single FEL radiation pulses out of the 13 MHz pulse train, indicating that this plasma switch is most suitable for the Rossendorf FEL. Further examinations will concentrate on achieving similar results using a Nd:YAG laser amplifier ($\lambda = 1064$ nm, $\tau < 16$ ps) for excitation of the Ge-based plasma switch.

M.P. Semtsiv[1]
M. Ziegler[1]
S. Dressler[1]
W.T. Masselink[1]
N. Georgiev
T. Dekorsy[2]
M. Helm

Strain-compensated AlAs/(In,Ga)As quantum well structures for short wavelength intersubband absorption and laser emission

Intersubband transitions in strain-compensated AlAs/(In,Ga)As heterostructures, demonstrating both absorption and quantum-cascade laser emission at short wavelengths, have been investigated. Optimizing the layer structure and growth, including managing the internal strain and designing around indirect valleys, we achieved absorption peaks at wavelengths as short as 1.7 μm in fully strain-compensated AlAs/(In,Ga)As structures, with significant oscillator strength extending out to 1.55 µm. Quantum cascade lasers based on similar heterojunctions have been realized. They exhibited laser emission as short as 3.7 µm, with low-temperature threshold current densities of 860 A/cm^2 in pulsed mode and output power as high as 6 W per facet (12 W total). This excellent performance is achieved because of the very large Gamma-valley conduction band discontinuity, allowing large intersubband energy differences. Furthermore, the design inhibits carrier loss from the upper lasing state into the continuum even at elevated operating temperatures, resulting in room-temperature operation, where the power is still 240 mW. The temperature coefficient T_0 is 119 K. The 30-period structure exhibits an external differential efficiency of 13 % (40 % per period) at low temperatures and a maximum wall-plug efficiency of 24 %. The lasing transition takes place from several upper states to several lower states, resulting in a relatively broad (300 cm^{-1}) gain spectrum and could allow the design to be used in external tuning configurations.

Collaboration: [1]Dept of Physics, Humboldt University, Berlin, Germany, [2]Dept. of Physics, University of Konstanz, Germany

C.V.B. Tribuzy
S. Ohser
S. Winnerl
H. Schneider
M. Helm
J. Neuhaus[1]
T. Dekorsy[1]
K. Biermann[2]
H. Künzel[2]
M.P. Semtsiv[3]
W.T. Masselink[3]

Intersubband relaxation dynamics in narrow InGaAs/AlAsSb and InGaAs/AlAs quantum well structures using pump-probe spectroscopy

Intersubband transitions in semiconductor quantum wells (QWs) can be employed for various mid-infrared optoelectronic devices. Presently there is strong interest to extend the available wavelength range into the near infrared, by using materials with a large conduction band offset. To achieve such short wavelengths thin QWs are required, where the first excited state inside the QW may lie higher than some state related to indirect valleys. Examples for such material systems are strained InGaAs/AlAs or lattice matched InGaAs/AlAsSb, both grown on InP. We have studied the intersubband relaxation dynamics in multiple QWs of both material systems by femtosecond pump-probe measurements using an optical parametric oscillator. By the transient transmission as a function of the pump-probe delay we observe that some long living states can be present in our systems. This can be caused by transfer of electrons to X- or L-states in the QWs or the barriers. We have studied samples with different QW thickness, containing doping impurities localized either inside the QW or in the barriers, and compared them to simulations based on rate equations.

Supported by Humboldt Foundation

Collaboration: [1]Dept. of Physics, University of Konstanz, Germany, [2]Fraunhofer Heinrich-Hertz Institut für Nachrichtentechnik (HHI), Berlin, Germany, [3]Dept. of Physics, Humboldt University, Berlin, Germany

D. Stehr
S. Winnerl
T. Dekorsy[1]
M. Helm
T. Roch[2]
G. Strasser[2]

Pump-probe spectroscopy of interminiband relaxation and electron cooling in doped superlattices

The picosecond dynamics of electrons in a doped GaAs/Al$_{0.3}$Ga$_{0.7}$As superlattice have been investigated by pump-probe experiments using the infrared free-electron laser FELBE at Rossendorf. At short delay times the pump-probe signal shows a fast bleaching of the interminiband absorption followed by relaxation and thermalization within a few ps. At larger delays, a slow component of the pump-probe signal is observed, which can be assigned to carrier cooling. The cooling time shows a strong dependence on the intensity of the pump pulse and the lattice temperature, ranging from 6 ps at 75 K up to 50 ps at 5 K. In addition, the cooling is observed to lead to a positive or negative transmission change, resulting from the temperature dependence of the linear absorption spectrum at the respective wavelength. In this respect, the linear absorption measurements of the sample and the pump-probe signal are perfectly consistent. We show that, in contrast to quantum wells, the superlattice provides a unique picosecond thermometer for the electron temperature based on the dependence of the absorption on the electron distribution function.

Collaboration: [1]Dept. of Physics, University of Konstanz, Germany, [2]Institut für Festkörperelektronik, TU Wien, Austria

M. Wagner
D. Stehr
S. Winnerl
M. Helm

Broad-band THz radiation from optical rectification in GaSe for pump-probe-experiments with the FEL

We have built up a broad-band THz-radiation source for time-dependent optical-pump and THz-probe experiments. Our THz source is based on phase-matched optical rectification in thin GaSe crystals driven by 10 fs laser pulses. With different emitters we are able to generate radiation in a broad spectral range between 12 THz (detector cut-off) and 50 THz with a FWHM of 16 THz by adjusting the phase-matching angle. THz pulses as short as 45 fs can thus be generated and we can achieve a time-averaged THz power of 250 nW out of a near-infrared 120 mW beam. Our experimental arrangement allows us to switch between linear THz-autocorrelation measurements with two pulses from the same emitter and THz cross-correlation with two pulses from different emitters. These setups have been used to characterize the THz-pulses and to perform interband-pump / intersubband-probe measurements, respectively. The functionality was demonstrated by comparing absorption spectra of a multiple-quantum-well (MQW) sample and a superlattice, as obtained by an infrared spectrometer, with the Fourier-transform of the THz autocorrelation measurement. The setup is ready to be used with the FEL or another synchronized laser for spectrally resolved pump-probe experiments. In some first experiments of this kind, we have studied the lifetime of photo-excited carriers in a MQW using a Ti:Sapphire laser that has been successfully synchronized to the THz-radiation source.

H.-J. Fitting[1]
R. Salh[1]
T. Barfels[1]
B. Schmidt

Multimodal luminescence spectra of ion-implanted silica

Thermally oxidized SiO_2 layers have been implanted by oxygen and sulfur ions up to an atomic dopant fraction of about 4 at.%. The cathodoluminescence spectra of these ion implanted layers show, besides the characteristic bands, an identical sharp and intense multimodal structure in the green up to near IR region. The energy step differences of the luminescence sublevels in average amount to 120 meV and indicate vibronic transitions in terms of a configuration coordinate potential model. The most probable candidate for these spectra are O_2 interstitial molecules, as we could demonstrate by respective configuration coordinate data. These assumptions are in contrast to photonic crystal models for the multimodal spectra as well as to models of quantum size effects, both discussed recently in literature.

Collaboration: [1]Department of Physics, University of Rostock, Germany

J. Potfajova
J.M. Sun
B. Schmidt
T. Dekorsy
W. Skorupa
M. Helm

Fabrication of efficient Si based light emitting diodes with resonant cavities

Resonant-cavity light-emitting diodes (RCLED) on a silicon-on-insulator (SOI) substrates present a promising path towards more efficient Si based optical devices. The pn-diodes were fabricated using standard silicon technology and boron implantation into n-Si. Forward biased highly boron doped pn-junctions are known to show efficient room-temperature luminescence at a wavelength of 1150 nm, This electroluminescence (EL) is also observed in the present 5 µm thick SOI layers, however modulated by characteristic thickness fringes. The thickness of the top Si layer was reduced down to 1300 nm by anisotropic etching, which is an optimum in order to obtain a 4λ microcavity with a sharp EL peak at the wavelength of 1150 nm. The desired thickness was measured by FTIR spectroscopy. The back-side etching process of the SOI wafer down to the buried SiO_2 layer as an etch-stop was also optimized. For fabrication of an effective RCLED, a resonator will be fabricated by deposition of Si/SiO_2 distributed Bragg reflectors both on the top and the rear side of the pn-diode.

J.M. Sun
W. Skorupa
T. Dekorsy
M. Helm
L. Rebohle[1]
T. Gebel[1]

Modulation of the 1535 nm photoluminescence from Er-doped Si-rich silicon dioxide by field-induced quenching

Field-induced quenching of the intense photoluminescence at 1535 nm was observed from Si-rich SiO_2:Er thin films prepared by Er^+ and Si^+ co-implantation. The quenching effect was strongly enhanced by increasing the density of Si nanoclusters (NCs) at an electric field above 5 MV/cm. A modulation ratio of 0.37 was obtained at an electric field of 9 MV/cm for a 200 nm Er-doped Si-rich layer containing 0.24% of Er atoms and 10% excess Si NCs. The mechanism of the field-induced quenching of the photoluminescence was studied by simultaneously measuring the light intensity from NCs and Er^{3+} ions, the injection current and the electric field. The quenching mechanism could be attributed to the field induced separation of the excitons created in the Si NCs and tunneling of carriers between the Er ions and Si NCs. This strong field-induced quenching effect will be useful for controlling the optical gain in Si-rich SiO_2:Er waveguide amplifiers, but also for the small size optical modulator in silicon photonics.

Collaboration: [1]nanoparc GmbH, Dresden, Germany

J. M. Sun
S. Prucnal[1]
W. Skorupa
M. Helm
L. Rebohle[2]
T. Gebel[2]

Efficient blue electroluminescence from metal-oxide-semiconductor light emitting devices with Ce and Gd co-implanted SiO_2 layers

Ultraviolet and blue electroluminescence (EL) was observed from Gd and Ce co-implanted indium-tin oxide / SiO_2:(Gd, Ce) / Si metal-oxide-semiconductor light emitting devices (MOSLEDs). The UV emission peak at 316 nm and the broad blue emission at around 440 nm are ascribed to electronic transitions from $^6P_{7/2}$ to $^8S_{7/2}$ of Gd^{3+} centers and 5d-4f transitions of Ce^{3+}, respectively, both excited by hot electrons. A decrease of the EL decay time and the impact cross-section of Gd^{3+} was observed with co-implanted Ce. As a consequence, the strong energy transfer from Gd^{3+} to Ce^{3+} centers leads to a five-fold increase of the blue EL from Ce^{3+} centers in silicon MOSLEDs.

Collaboration: [1]Maria Curie-Sklodowska University, Lublin, Poland, [2]nanoparc GmbH, Dresden, Germany

S. Prucnal[1]
X.Q. Cheng
J.M. Sun
R. Kögler
W. Skorupa

Optical and microstructural properties of SiO_2 layers containing Er, Ge and Si atoms

Photoluminescence (PL) properties of 500 nm thick SiO_2 layers containing combined Ge+Si and Er+Si implants have been studied. The double-beam implantations of Ge+Si and Er+Si were performed both sequentially and simultaneously. After implantation, the samples were annealed at temperatures ranging from 700 to 1100°C, in order to obtain Si and Ge nanoclusters (NCs) and remove the point defects induced by ion implantation. A weak near-UV luminescence peak at 315 nm, a strong blue band at 400 nm and a near-infrared 780 nm band were observed from samples implanted by Ge and Si atoms. The SiO_2 layers containing Er and Si-NCs exhibit a strong infrared PL peak at 1.54 μm. The enhancement of the this PL peak with increasing Si nanocluster concentration suggests an energy transfer from Si-NCs to Er^{3+} ions in the SiO_2 matrix. It should be noted that the simultaneous implantation creates more defects in the matrix than the sequential one. Moreover, diffusion of Ge towards the Si/SiO_2 interface during the annealing process is suppressed by silicon ions additionally introduced into SiO_2.

Supported by Humboldt Foundation

Collaboration: [1]Maria Curie-Sklodowska University, Lublin, Poland

Others

J. Grenzer
A. Zen[1]
D. Neher[1]
S. Grigorian[2]
U. Pietsch[2]
U. Asawapirom[3]
S. Janietz[3]
U. Scherf[4]

Effect of molecular weight on the structure and crystallinity of poly (3-hexylthiophene)

The carrier mobility of field-effect transistors made from regioregular poly (3-hexylthiophene) (P3HT) increases strongly with the molecular weight. Using complementary techniques (differential scanning calorimetry, XRD), the structural properties of P3HT has been studied as a function of the molecular weight. For powder samples, all weight fractions possess a rather broad molecular weight distribution. The measurements reveal a strong decrease of the crystallization temperature and, most important, a significant decrease of the degree of crystallinity with decreasing molecular weight. In order to study the structure of P3HT thin films (thickness several 10 nm) in lateral and vertical directions, X-ray grazing incidence diffraction and reflectivity measurements were utilized. These methods show that thin layers of the low molecular weight fraction consist of well-defined crystalline domains embedded in a disordered matrix. Thus we propose that the transport properties of layers prepared from fractions of P3HT with different molecular weight is largely determined by the crystallinity of the samples and not by the perfection of the packing of the chains in the individual crystallites.

Collaboration: [1]Institute of Physics, University of Potsdam, Germany, [2]Institute of Physics, University of Siegen, Germany, [3]Macromolecular Chemistry, University of Wuppertal, Germany, [4]Fraunhofer Institute for Applied Polymer Research, Gol, Germany

R.I. Grynszpan[1,2]
N. Baclet[3]
A. Darque[3]
J.L. Flament[4]
F. Zielinski[4]
W. Anwand
G. Brauer

Positron and deuteron depth profiling in ^{3}He implanted Electrum-like alloy

In spite of previous extensive studies, the He behavior in metals still remains an issue in microelectronics as well as in nuclear technology. A gold-silver solid solution ($Au_{60}Ag_{40}$: synthetic gold-rich electrum) was chosen as a relevant model to study helium irradiation of heavy metals. After $^3He^+$ ion implantation at an energy ranging from 4.2 to 5.6 MeV, NRA based on the $^3He(d,p)^4He$ reaction, was performed in order to study the thermal diffusion of He atoms. At room temperature, NRA data reveal that a single Gaussian can fit the He-distribution, which remains unchanged after annealing at temperatures below 0.45 of the melting point. Slow positron implantation spectroscopy, used to monitor the fluence dependence of induced defects unveils a positron trapping saturation, which occurs for He contents of the order of 50 – 100 appm, whereas concentrations larger than 500 appm seem to favor an increase in the *S*-parameter of Doppler broadening. Moreover, at high temperature, NRA results clearly show that He long range diffusion occurs, though, without following a simple Fick law.

Collaboration: [1]Lab. de Chimie Métallurgique des Terres Rares, ISCSA, Thiais, France, [2]Positive Leptons Spectroscopy Cell, DGA/CEP/CGN/LOT, Dept. of Defense, Arcueil, France, [3]CEA/VA/DRMN/SEMP, Is-sur-Tille, France, [4]CEA/DIF/DPTA/SP2A, Bruyères-le-Châtel, France

R.I. Grynszpan[1,2,3]
S. Saudé[1,2,3]
L. Mazerolles[3]
G. Brauer
W. Anwand

Positron depth profiling in ion-implanted zirconia stabilized with trivalent cations

Slow positron implantation spectroscopy has been performed on a series of $(ZrO_2)_{1-x}$ $(M_2O_3)_x$ solid solutions, either stabilized in the cubic phase (with M: Y, Dy or Er and x = 0.095, 0.16 or 0.16, respectively) or in the tetragonal metastable phase (M: Y and x = 0.03). Stabilization induces native oxygen-vacancy complexes, which lead to saturation trapping of positrons in the cubic crystals, regardless of the cation type. The positron diffusion length in the tetragonal phase ($L_+ \approx 60$ nm, vs. ≈ 2.5 nm in the cubic phase) suggests that Y atoms segregate around antiphase boundaries formed in the lattice. Implantations of helium and oxygen ions induce new defects, more trapping effective than the native defects. However, their production rate and temperature stability seem primarily dependent on the crystal structure, hence on the concentration of trivalent cations, irrespective of their chemical nature.

Collaboration: [1]SERAM & SINUMEF, Ecole Nationale Supérieure d'Arts et Métiers, Paris, France, [2]DGA/CEP/CGN/LOT, Dept. of Defense, Arcueil, France, [3]ISCSA, IFR-CNRS-1780, Thiais, France

Equipment

M. Friedrich
W. Bürger
A. Reichel
S. Turuc

Operation and development of the electrostatic accelerators

The ***2 MV VdG*** accelerator has been used exclusively for RBS analysis. The rf ion source has been equipped with a ceramic discharge bottle. This modification results in higher beam currents with improved stability. A modernized energy stabilizing system has been installed.

The ***5 MV Tandem*** has been applied for ion beam analysis, high-energy implantation and detector development. After rupture of the charging belt (CIGO / Italy) after 1700 operation hours a new belt (Wennerlund / Sweden) was installed. After reducing the self-charging effect at the inner belt side by an additional discharge needle line inside the terminal the belt has given satisfying stability of the terminal voltage. The energy and beam position stability has been improved by a new control strategy on the base of predictive compensation of terminal voltage disturbances (see separate report).

The ***3 MV Tandetron*** has been applied mainly for high-energy implantation and ion beam analysis. At the second He ion source a commercial Rb charge exchange canal (NEC / USA) has been installed.

In 2005 the total operating hours of the high-energy accelerators were 1681 h (2 MV VdG), 1673 h (5 MV Tandem) and 1670 h (3 MV Tandetron). The available beam times of the 5 MV Tandem and of the 3 MV Tandetron were reduced due to a three-week inspection of the pressure vessels by the technical supervising authorities.

W. Bürger
H. Lange

Predictive compensation of terminal voltage disturbances at Van de Graaff belt generators

The precision of controlling the acceleration voltage (AV) of Van de Graaff (VdG) accelerators directly by the charging current is strongly limited by the dead time of the charge transfer in the belt generator from ground potential to the accelerator terminal. A major source of instabilities are imperfections of the charging belt, which accordingly lead to a periodic ripple. In a novel approach, this periodicity allows to estimate the development and to counteract ahead of time. For this purpose, the control chain from the input of the charging current generator up to the reaction of the AV has been precisely identified, and a real-time predictive algorithm has been developed. Accordingly, a control strategy was implemented in a microcontroller RENESAS SH2/7047. Based on a measurement of the transfer function of the charging system, estimates of few spectral lines of the AV disturbance are continuously calculated by a sliding short time signal transformation into the Fourier frequency domain. For the spectral lines, compensation signals are estimated, retransformed to the time domain and added to the charging current controller input. In this way, the belt-rotation related ripple of the two VdG accelerators was decreased by a factor of 5 – 10, and the total effective ripple by a factor of 3 – 4. The relative AV fluctuation reaches a level well below $\Delta U/U < 10^{-4}$, which is not attainable by conventional methods.

R. Heller
D. Kost
G. Zschornack[1]
S. Facsko

Characteristics of the highly charged ion beam from the Dresden EBIT source

The Rossendorf Two Beam Facility offers both an ECR ion source for low to medium ionic charge states and the Dresden room-temperature electron beam ion trap (EBIT) for highest charge states. In order to optimise the highly charged ion output, the ion extraction from the EBIT was studied. At the 1st faraday cup directly after the extraction optics total ion currents up to 2 µA were determined. The charge state distribution analysis of the ion beam revealed the formation and extraction of charge states up to Ar^{18+} as well as charge states up to Xe^{44+}. For the first time the so called “leaky mode” of the EBIT source was studied to more detail, which delivers a continuous beam in contrast to the usual pulsed operation. It could be demonstrated that continuous beams even of high charge states (e.g. Ar^{17+} and Xe^{21+}) can be produced. The transmission of the ion beam through the beamline has been determined to be nearly 100 %. For guiding the EBIT beam into the target chamber, the remaining magnetization of the ECR source magnet was suppressed by additional constant-current windings.

Collaboration: [1]Institute for Applied Physics, TU Dresden, Germany

D. Kost
F. Röder

Plasma potential of the ECR ion source of the dual-beam highly-charged ion facility

At the dual-beam facility, highly charged ions are decelerated down to kinetic energies of some 10 eV times charge state. In this low energy range the plasma potential of the ion source renders an important contribution to the total kinetic energy. For its measurement, a single Langmuir probe was constructed and adapted to the ECR ion source. The results were found in good agreement with measurements of the total kinetic ion energy using a retarding field arrangement. Main source parameters influencing the plasma potential are the microwave (MW) power and the gas pressure. The plasma potential increases monotonically from 10 V to 25 V with MW power from 40 to 240 W and with gas pressure in the range of 10^{-6} to 6×10^{-5} mbar. However, a hysteretic behaviour is observed in the pressure range of 3×10^{-6} to 10^{-5} mbar. Avoiding this regime, the plasma potential is nearly constant with (10 ± 2) V in the low-pressure range of 10^{-6} to 3×10^{-6} mbar, and with (27 ± 3) V above 10^{-5} mbar.

S. Winnerl
D. Stehr
W. Seidel
H. Schneider
M. Helm
K. Unterrainer[1]
F.F. Schrey[1]
B.A. Carpenter[2]
E.A. Zibik[2]
J. Cockburn[2]
L.R. Wilson[2]
S. Schneider[3]
J. Seidel[3]
S. Grafström[3]
L.M. Eng[3]

supported by EU

Cooperation with and support of external user groups at FELBE

Partially supported by an "integrated infrastructure initiative" funded by the European Union, the free-electron laser facility FELBE was made available to external user groups for the first time. Interesting initial experiments have been conducted in cooperation with scientists from Rossendorf. These users included groups from Vienna and from Sheffield, who performed infrared pump / probe measurements on InGaAs/GaAs quantum dots, and a group from TU Dresden, who developed an infrared scattering scanning optical near-field microscope. In addition to interesting scientific interactions, these experiments also provided an important opportunity to gain experience with this service-oriented operation mode of FELBE, which represents an important step towards our goal of creating a major scientific impact within Europe through this facility.

Collaboration: [1]Institut für Festkörperelektronik, TU Wien, Austria, [2]University of Sheffield, Dept. of Physics and Astronomy, UK,[3]Institute of Applied Physics, TU Dresden, Germany

N. Schell
F. Eichhorn
A. Bjeoumikhov[1]
H. Prinz[2]
C. Ollinger[3]

Parabolic capillary optics with less than 50 µm focus and large focal distance for synchrotron radiation scattering

In cooperation with the Institute for Scientific Instruments, Berlin, a unique parabolic focussing optics for the general purpose materials research station at the ROssendorf BeamLine, ROBL-CRG at ESRF, was developed and commissioned. The measured gain between 8 – 12 keV was > 1000, the focal spot <40 µm at a focal length of 235 mm (8 keV) and 244 mm (11.5 keV), respectively, which allows the use of special sample environments around the focus spot. The low divergence of < 0.15° especially permits the *in-situ* characterization of stress states in copper dual inlaid interconnect micro-structures as well as the measurement of far-field diffraction patterns of planar wave-guides. For the positioning of selected regions of the sample with respect to the X-ray spot a CCD camera system is used. Corresponding first test results showed the advantages of this parabolic focusing optics in comparison to the standard beam geometry using apertures for decreasing the X-ray spot size.

Supported by AMD

Collaboration: [1]Institute for Scientific Instruments, Berlin, Germany, [2]AMD Saxony, Dresden, Germany, [3]Institute for X-ray Physics, University of Göttingen, Germany

N. Schell
J. von Borany
J. Hauser
M. Beckers

Installation and test of a new magnetron sputter deposition chamber equipped with an additional ion gun for *in-situ* synchrotron radiation scattering experiments

A new process chamber for the *in-situ* study of film growth and modification during magnetron sputter deposition by synchrotron XRD and XRR was developed and commissioned. The chamber is sealed with four Be-windows allowing scattering access of –2° up to +50° off-plane and –2.9° up to +65° in-plane, respectively. The chamber fits into the standard six-circle HUBER diffractometer of the ROssendorf BeamLine (ROBL) at ESRF. Two comercial miniature magnetrons with additional gas inlets allow for the deposition of compound films and multilayers. Substrate heating up to 1000°C and substrate biasing is possible. An additional ion gun up to 6 keV and 10 µA allows post-deposition ion irradiation or energetic ion bombardment during sputter deposition. The performance of the chamber was tested during the high-temperature deposition of MAX phase Ti_2AlN films.

J. Grenzer
F. Eichhorn

New universal high-resolution diffractometer

Since December 2005 a new high-resolution four circle diffractometer (XRD-3003 PTR from GE Inspection Technologies) in an unique configuration is operating at IIM. The device is optimized for small sample sizes using a beam of $2 \times 2\text{mm}^2$. This is realized by a standard sealed tube in combination with a 2D collimating mirror resulting in an almost parallel beam in two dimensions. The system can be equally used for standard coplanar high resolution and reflectivity measurements as well as for non-coplanar measurements using grazing incidence and exit geometries. Without any monochromator a photon flux of 5×10^7 /s within a beam diameter of 500 µm and a beam divergence of about 1 mrad in both directions is obtained. Depending on the investigated sample the (angular and spectral) resolution of the setup can be changed accordingly by using a four-bounced monochromator Ge(220) and a triple-axis analyzer for the highest resolution possible or a multilayer analyzer for intermediated experimental resolutions.

O. Drachenko
S. Winnerl
H. Schneider
M. Helm

Rapid-scan THz spectroscopy for application in pulsed magnetic fields

The pulsed high-magnetic-field laboratory (HLD) at FZR will enable many exciting experiments in solid state physics. Among others, THz spectroscopy is an important technique to investigate material properties in high magnetic fields. However, state-of-the-art time-domain THz spectroscopy is not fast enough to be performed within a millisecond magnetic-field pulse, mainly because mechanical delay lines are used for temporally scanning the THz wave. Therefore we build up a system based on asynchronous optical sampling (ASOPS). This approach uses two exciting femtosecond laser sources with slightly different repetition rates (F and F+D) to gate the emitter and detector of the THz spectrometer (which will be installed in the magnet). The lasers produce two pulses with a time delay linearly ramped in time between zero and 1/F. Since the scan rate of the time delay is fixed by the beat frequency D, ASOPS does not require any mechanical delay stage, so that the THz transient field can be recorded much faster (>kHz). To this end a novel twin-laser system has been installed in the high magnetic field laboratory and successfully characterized, followed now by the set up of the THz spectrometer.

Development of new alloy LMIS for FIB applications

L. Bischoff
W. Pilz
C. Akhmadaliev
C.J. Aidinis[1]
T. Ganetsos[2]

Two new types of alloy liquid metal ion sources (LMIS) for the application in the IMSA-Orsay Physics FIB system were developed, tested and analysed concerning their *I-V* characteristics, mass spectra, energy spread of certain ion species and their temperature behavior. An electrochemical sharpened 250 µm tungsten wire tip was wetted with a $Mn_{45}Ge_{54}Si_1$ alloy (T_{melt} = 720°C) and welded on a heating filament. Ion beams of single isotopic Mn^{1+} (dominating in the beam) and Mn^{2+} could be clearly separated. Mn is a promising element for doping or modification of electrical, mechanical, optical or magnetic properties of II-VI semiconductors. Secondly a $Ga_{38}Bi_{62}$ (T_{melt} = 222°C) alloy LMIS was prepared on a mechanically treated Ta emitter. This $Ga_{38}Bi_{62}$ LMIS allows one to dope, i.e. Si with acceptors (Ga) as well as with shallow donors (Bi) using the same ion source. The relatively high vapor pressure of Mn and Bi at higher temperatures requires the operation of the source close to T_{melt} to obtain a long source life time.

Collaboration: [1]Department of Physics, University of Athens, Greece, [2]TEI of Lamia, Greece

Glossary

AES	Auger Electron Spectroscopy
AFM	Atomic Force Microscopy
CEMS	Conversion Electron Mössbauer Spectroscopy
CMOS	Complementary MOS
CVD	Chemical Vapour Deposition
EFTEM	Energy Filtered Transmission Electron Microscopy
EL	Electroluminescence
EDX	Energy Dispersive X-ray Analysis
ERDA	Elastic Recoil Detection Analysis
ESRF	European Synchrotron Radiation Facility, Grenoble
FEL	Free Electron Laser
FIB	Focused Ion Beam
FLA / P	Flash Lamp Annealing / Processing
FTIR	Fourier Transform Infrared Spectroscopy
GIXRD	Gracing Incidence X-ray Diffraction
HRTEM	High-Resolution Transmission Electron Microscopy
IBAD	Ion Beam Assisted Deposition
ITO	Indium-Tin Oxide
LMIS	Liquid Metal Ion Source
MBE	Molecular Beam Epitaxy
MFM	Magnetic Force Microscopy
MOKE	Magneto-Optic Kerr Microscopy
MOS	Metal-Oxide-Semiconductor
MOSFET	Metal-Oxide-Semiconductor Field Effect Transistor
NRA	Nuclear Reaction Analysis
PIGE	Proton-Induced Gamma-Ray Emission
PIII	Plasma Immersion Ion Implantation
PIXE	Proton-Induces X-ray Emission
PLD	Pulse Laser Deposition
PVD	Physical Vapour Deposition
ROBL	Rossendorf Synchrotron Beamline (at the ESRF)
RBS	Rutherford Backscattering Spectroscopy
RBS/C	Rutherford Backscattering Spectroscopy under Channelling Conditions
RT	Room Temperature
RTA	Rapid Thermal Annealing

SAD	Selected Area Diffraction
SEM	Scanning Electron Microscopy
SIMS	Secondary Ion Mass Spectrometry
SPIS	Slow Positron Implantation Spectroscopy
STM	Scanning Tunnel Microscope
TEM	Transmission Electron Microscopy
XANES	X-ray Absorption Near Edge Spectroscopy
XPS	X-ray Photoelectron Spectroscopy
XRD	X-ray Diffraction
XRF	X-Ray Fluorescence Analysis
XRR	X-ray Reflectivity
XTEM	Cross-Sectional Transmission Electron Microscopy

Supporting Institutions

AiF	Arbeitsgemeinschaft Industrieller Forschungsvereinigungen e.V.
AvH	Alexander-von-Humboldt Stiftung
BMBF	Bundesministerium für Bildung und Forschung
BMWA	Bundesministerium für Wirtschaft und Arbeit
DAAD	Deutscher Akademischer Austauschdienst
DFG	Deutsche Forschungsgemeinschaft
EU	European Union
MPG	Max-Planck-Gesellschaft
SMWK	Sächsisches Staatsministerium für Wissenschaft und Kunst
SMWA	Sächsisches Staatsministerium für Wirtschaft und Arbeit
WTZ	BMBF-Programm der „Wissenschaftlich-Technischen Zusammenarbeit“

Statistics

Book Chapters

Beyer, V., Borany, J. von
Ion-beam synthesis of nanocrystals for multidot memory structures
in: Materials for Information Technology – Devices, Interconnects and Packaging; Series: Engineering Materials and Processes (Eds. E.Zschech, C. Whelan, T. Mikolajick), Springer-Verlag, Berlin, 2005, ISBN: 1-85233-941-1, pp. 139 – 147

Neelmeijer, C., Mäder, M.
Endangered glass objects identified by ion beam analysis
in: Cultural Heritage Conservation and Environmental Impact Assessment by Non-Destructive Testing and Micro-Analysis (Eds. R. Van Grieken, K. Janssens), A.A. Balkema Publishers, Taylor & Francis Group, London, 2005, pp. 211 – 222

Publications in Refereed Journals

Ion-Solid-Interaction

Abdul-Kader, A.M., Turos, A., Grambole, D., Jagielski, J., Piatkowska, A., Madi, N.K., Al-Maadeed, M.
Compositional transformations in ion-implanted polymers
Nucl. Instr. Meth. B **240** (2005) 152

Bracht, H., Staskunaite, R., Haller, E.E., Fielitz, P., Borchardt, G., Grambole, D.
Silicon diffusion in sol-gel derived isotopically enriched silica glasses
J. Appl. Phys. **97** (2005) 046107

Constantinescu, B., Bugoi, R., Cojocaru, V., Voiculescu, D., Grambole, D., Herrmann, F., Ceccato, D.
Romanian ancient gold objects provenance studies using micro-beam methods: the case of Pietroasa hoard
Nucl. Instr. Meth. B **231** (2005) 541

Mackova, A., Grötzschel, R., Nekvindova, P., Spirkova, J., Svorcik, V., Zemek, J.
Analysis of PF surfaces and interfaces using nuclear analytical methods
Acta Phys. Slovaca **55** (2005) 323

Mackova, A., Spirkova, J., Nekvindova, P., Salavcova, L., Grötzschel, R., Eichhorn, F.
Comparison of crystal lattice changes caused by APE treatment of Er: $LiNbO_3$ and by localised Er doping into $LiNbO_3$ obtained by RBS-channeling and XRD analysis
Nucl. Instr. Meth. B **240** (2005) 391

Mäder, M., Jembrih-Simbürger, D., Neelmeijer, C., Schreiner, M.
IBA of iridescent Art Nouveau glass - comparative studies
Nucl. Instr. Meth. B **239** (2005)107

Posselt, M., Mäder, M., Lebedev, A., Grötzschel, R.
Multiple implantations into Si: influence of the implantation sequence on ion range profiles
Appl. Phys. Lett. **87** (2005) 043109

Rosén, D., Katardjiev, I., Berg, S., Möller, W.
TRIDYN simulation of target poisoning in reactive sputtering
Nucl. Instr. Meth. B **228** (2005) 193

Salavcova, L., Spirkova, J., Capek, P., Novotna, M., Vacik, J., Mackova, A., Kreißig, U.
Effect of the annealing process on active properties of proton-exchanged optical waveguides in erbium-doped lithium niobate
Ceramics - Silikaty **49** (2005) 86

Thin Films

Abd El-Rahman, A.M., Negm, N.Z., Prokert, F., El-Hossary, F.M., Richter, E., Möller, W.
Depth-related microstructure of rf plasma nitrocarburized austenitic stainless steel
Surf. Coat. Technol. **191** (2005) 140

Abd El-Rahman, A.M., El-Hossary, F.M., Prokert, F., Negm, N.Z., Schell, N., Richter, E., Möller, W.
In-situ stability study of nitrocarburized 304 stainless steel during heating
Surf. Coat. Technol. **200** (2005) 602

Abrasonis, G., Riviere, J.P., Templier, C., Pranevicius, L., Barradas, N.P.
Flux effect on the ion-beam nitriding of austenitic stainless-steel AISI 304L
J. Appl. Phys. **97** (2005) 124906

Abrasonis, G., Gago, R., Jimenez, I., Kreißig, U., Kolitsch, A., Möller, W.
Nitrogen incorporation in carbon nitride films produced by direct and dual ion-beam sputtering
J. Appl. Phys. **98** (2005) 074907

Allenstein, F., Budzinski, L., Hirsch, D., Mogilatenko, A., Beddies, G., Grötzschel, R., Hinneberg, H.
Influence of Al on the growth of $NiSi_2$ on Si(001)
Microelectron. Eng. **82** (2005) 474

Almtoft, K.P., Bøttiger, J., Chevallier, J., Schell, N., Martins, R.M.S.
Influence of the substrate bias on the size and thermal stability of grains in magnetron-sputtered nanocrystalline Ag films
J. Mat. Res. **20** (2005) 1071

Andreasen, K.P., Bøttiger, J., Chevallier, J., Schell, N.
Real time in-situ diagnostics of PVD growth using synchrotron radiation
Surf. Coat. Technol. **200** (2005) 1

Beckers, M., Schell, N., Martins, R.M.S., Mücklich, A., Möller, W.
In-situ x-ray diffraction studies concerning the influence of Al concentration on the texture development during sputter deposition of Ti-Al-N thin films
J. Vac. Sci. Technol. A **23** (2005) 1384

Beckers, M., Schell, N., Martins, R.M.S., Mücklich, A., Möller, W.
The influence of the growth rate on the preferred orientation of magnetron sputtered Ti-Al-N thin films studied by in-situ x-ray diffraction
J. Appl. Phys. **98** (2005) 44901
ESRF Newsletter **42** (2005) 20

Belov, A.Y., Jäger, H.-U.
Relaxation kinetics in amorphous carbon films: an insight from atomic scale simulation
Thin Solid Films **482** (2005) 74

Belov, A.Y., Jäger, H.-U.
Formation and evolution of sp^2 clusters in amorphous carbon networks as predicted by molecular dynamics annealing simulations
Diam. Rel. Mat. **14** (2005) 1014

Bohne, Y., Shevchenko, N., Prokert, F., Borany, J. von, Rauschenbach, B., Möller, W.
In-situ characterization of phase formation during high-energy oxygen ion implantation in molybdenum
Nucl. Instr. Meth. B **240** (2005) 157

Casiraghi, C., Piazza, F., Ferrari, A. C., Grambole, D., Robertson, J.
Bonding in hydrogenated diamond-like carbon by Raman spectroscopy
Diam. Rel. Mat. **14** (2005) 1098

Dittmar, K., Engelmann, H.-J., Peikert, M., Wieser, E., Borany, J. von
Investigation of ultrathin tantalum based diffusion barrier films using AES and TEM
Appl. Surf. Sci. **252** (2005) 185

Foerster, C.E., Fitz, T., Dekorsy, T., Prokert, F., Kreißig, U., Mücklich, A., Richter, E., Möller, W.
Carbon ion implantation in pure aluminium at low fluences
Surf. Coat. Technol. **192** (2005) 317

Gago, R., Abrasonis, G., Mücklich, A., Möller, W., Czigany, Z., Radnoczi, G.
Fullerene-like arrangements in carbon nitride thin films grown by direct ion beam sputtering
Appl. Phys. Lett. **87** (2005) 071901

Gago, R., Neidhardt, J., Vinnichenko, M., Kreißig, U., Czigány, Z., Kolitsch, A., Hultman, L., Möller, W.
Synthesis of carbon nitride thin films by low-energy ion beam assisted evaporation: on the mechanisms for fullerene-like microstructure formation
Thin Solid Films **483** (2005) 89

Gago, R., Jiménez, I., Neidhardt, J., Abendroth, B., Caretti, I., Hultman, L., Möller, W.
Correlation between bonding structure and microstructure in fullerene-like carbon nitride thin films
Phys. Rev. B **72** (2005) 115414

Gago, R., Vinnichenko, M., Jäger, H.-U., Belov, A.Yu., Jiménez, I., Huang, N., Sun, H., Maitz, M.F.
Evolution of sp^2 networks with substrate temperature in amorphous carbon films: experiment and theory
Phys. Rev. B **72** (2005) 014120

Gomes, G.F., Ueda, M., Reuther, H., Richter, E., Beloto, A.F.
Nitrogen recoil chromium implantation into SAE 1020 steel by means of ion beam or plasma immersion ion implantation
Surf. Coat. Technol. **196** (2005) 275

Gomes, G.F., Ueda, M., Beloto, A., Reuther, H., Richter, E.
Chromium enrichment of AISI 304 stainless steel surface after nitrogen ion recoil bombardment of chromium film
Nucl. Instr. Meth. B **240** (2005) 194

Gorbunov, A., Levin, A.A., Meyer, D.C., Bischoff, L., Eckert, D., Köhler, B., Mertig, M., Weissbach, T., Wieser, E., Pompe, W.
Correlation of structural and physical properties of metastable Fe-Cr phases
Crystal Res. Technol. **40** (2005) 106

Ignatova, V.A., Möller, W., Conard, T., Vandervorst, W., Gijbels, R.
Interpretation of TOF-SIMS depth profiles from ultrashallow high-K dielectric stacks assisted by hybrid collisional computer simulation
Appl. Phys. A **81** (2005) 71

Mändl, S., Fritzsche, B., Manova, D., Hirsch, D., Neumann, H., Richter, E., Rauschenbach, B.
Wear reduction in AISI 630 matensitic stainless steel after energetic nitrogen ion implantation
Surf. Coat. Technol. **195** (2005) 258

Mändl, S., Manova, D., Neumann, H., Pham, M.T., Richter, E., Rauschenbach, B.
Correlation between PIII nitriding parameters and corrosion behaviour of austenitic stainless steels
Surf. Coat. Technol. **200** (2005) 104

Maitz, M.F., Poon, R.W.Y., Liu, X.Y., Pham, M.T., Chu, P.K.
Bioactivity of titanium following sodium plasma immersion ion implantation and deposition
Biomat. **26** (2005) 5465

Martins, R.M.S., Schell, N., Silva, R.J.C., Braz Fernandes, F.M.
Structural in-situ studies of shape memory alloy (SMA) Ni-Ti thin films
Nucl. Instr. Meth. B **238** (2005) 319

Mientus, R., Grötzschel, R., Ellmer, K.
Optical and electronic properties of CrO_xN_y *films, deposited by reactive DC magnetron sputtering in* $Ar/N_2/O_2(N_2O)$ *atmospheres*
Surf. Coat. Technol. **200** (2005) 341

Mukherjee, S., Maitz, M.F., Pham, M.T., Richter, E., Prokert, F., Möller, W.
Development and biocompatibility of hard Ti-based coatings using plasma immersion ion implantation assisted deposition
Surf. Coat. Technol. **196** (2005) 312

Mukherjee, S., Prokert, F., Richter, E., Möller, W.
Comparison of TiN and $Ti_{1-x}Al_xN$ *coatings deposited on Al using plasma immersion ion implantation assisted deposition*
Surf. Coat. Technol. **200** (2005) 2459

Music, D., Kölpin, H., Atiser, A., Kreißig, U., Bobek, T., Hadam, B., Mertens, R., Schneider, J.M.
Synthesis and characterization of boron-oxygen-hydrogen thin films at low temperatures
MRS Bulletin **40** (2005) 1345

Oates, T.W.H., Ryves, L., Bilek, M.M.M., McKenzie, D.R.
Accurate determination of optical and electronic properties of ultra-thin silver films for biosensor applications
Sensors and Actuators B **109** (2005) 146

Oates, T.W.H., Ryves, L., Burgmann, F.A., Abendroth, B., Bilek, M.M.M., McKenzie, D.R., McCulloch, D.G.
Ion-implantation induced phase transformation in carbon and boron nitride thin films
Diam. Rel. Mat. **14** (2005) 1395

Pantchev, B., Danesh, P., Schmidt, B.
Hydrogen as origin of compressive intrinsic stress in hydrogenated amorphous silicon: the contribution of clustered forms
Appl. Phys. Lett. **87** (2005) 23104

Paula, A.S., Canejo, J.P.H.G., Schell, N., Braz Fernandes, F.M.
Structural evolution on thermal cycling in Ti-rich NiTi SMA
Nucl. Instr. Meth. B **238** (2005) 111

Paula, A.S., Mahesh, K.K., Braz Fernandes, F.M., Martins, R.M.S., Cardoso, A.M.A., Schell, N.

In-situ high-temperature texture characterization in NiTi shape memory alloy using synchrotron radiation
Mat. Sci. Forum **495-497** (2005) 125

Peikert, M., Wieser, E., Borany, J. von, Reuther, H., Dittmar, K., Gehre, D.
Incorporation of nitrogen in thin tantalum films using plasma immersion ion implantation
Surf. Coat. Technol. **200** (2005) 2253

Piazza, F., Grambole, D., Schneider, D., Casiraghi, C., Ferrari, A.C., Robertson, J.
Protective diamond-like carbon coatings for future optical storage disks
Diam. Rel. Mat. **14** (2005) 994

Piekoszewski, J., Kempinski, W., Andrzejewski, B., Trybula, Z., Piekara-Sady, L., Kaszynski, J., Stankowski, J., Werner, Z., Richter, E., Prokert, F., Stanislawski, J., Barlak, M.
Superconductivity of MgB_2 thin films prepared by ion implantation and pulsed plasma treatment
Vacuum **78** (2005) 123

Rosen, J., Mraz, S., Kreißig, U., Music, D., Schneider, J.M.
Effect of ion energy on structure and composition of cathodic arc deposited alumina thin films
Plasma Chem. Plasma Proc. **25** (2005) 303

Ryves, L., Bilek, M.M.M., Oates, T.W.H, Tarrant, R.N., McKenzie, D.R., Burgmann F.A., McCulloch, D.G.
Synthesis and in-situ ellipsometric monitoring of Ti/C nanostructured multilayers using a high-current, dual source pulsed cathodic arc
Thin Solid Films **482** (2005) 133

Sass, J., Mazur, K., Eichhorn, F., Strupiński, W., Turos, A., Schell, N.
Determination of In concentration in InGaAs/GaAs(001) epilayers in the early stage of anisotropic stress relaxation
J. Alloys and Comp. **401** (2005) 249

Sartowska, B., Piekoszewski, J., Wallis, L., Szymczyk, W., Stanislawski, J., Nowicki, L., Ratajczak, R., Kopcewicz, M., Kalinowska, J., Barcz, M., Prokert, F.
Modification of the near-surface layer of carbon steel with intense argon and nitrogen pulses
Vacuum **78** (2005) 181

Schell, N., Martins, R.M.S., Braz Fernandez, F.M.
Real-time and in-situ structural design of functional NiTi SMA thin films
Appl. Phys. A **81** (2005) 1441

Schell, N., Andreasen, K.P., Bøttiger, J., Chevallier, J.
On the dependence on bias voltage of the structural evolution of magnetron-sputtered nanocrystalline Cu films during thermal annealing
Thin Solid Films **476** (2005) 280

Tsyganov, I., Maitz, M.F., Wieser, E., Richter, E., Reuther, H.
Correlation between blood compatibility and physical surface properties of tinanium-based coatings
Surf. Coat. Technol. **200** (2005) 1041

Ueda, M., Berni, L.A., Castro, R.M., Reuther, H., Lepienski, C.M., Soares, P.C.
Improvements of tribological properties of CrNiMo and CrCoMo alloys by nitrogen plasma immersion ion implantation
Surf. Coat. Technol. **200** (2005) 594

Ueda, M., Leandro, C., Reuther, H., Lepienski, C.M.
Plasma immersion ion implantation of nitrogen into H13 steel under moderate temperatures
Nucl. Instr. Meth. B **240** (2005) 204

Ueda, M., Reuther, H., Lepienski, C.M.
Comparison of nitrogen ion beam and plasma immersion implantation in A15052 alloy
Nucl. Instr. Meth. B **240** (2005) 199

Nanoscale Magnetism

Blomeier, S., McGrouther, D., McVitie, S., Chapman, J.N., Weber, M.C., Hillebrands, B., Fassbender, J.
Structural analysis of ion irradiated polycrystalline NiFe/FeMn exchange bias systems
Eur. Phys. J. B **45** (2005) 213

Blomeier, S., McGrouther, D., O'Neill, R., McVitie, S., Chapman, J.N., Weber, M.C., Hillebrands, B., Fassbender, J.
Modification of the magnetic properties of exchange coupled NiFe/FeMn films by Ga^+ ion irradiation
J. Magn. Magn. Mat. **290** (2005) 731

Guseva, V.B., Zatsepin, A.F., Vazhenin, V.A., Schmidt, B., Gavrilov, N.V., Cholakh, S.O.
Magnetic resonance of metallic nanoparticles in vitreous silicon dioxide implanted with iron ions
Physics of The Solid State **47** (2005) 674

Liedke, M.O., Nembach, H., Hillebrands, B., Fassbender, J.
Analysis of the Ni81Fe19 / Fe50Mn50 exchange bias system with a varying Cu spacer thickness and position for partial decoupling
J. Magn. Magn. Mat. **290-291** (2005) 588

McCord, J., Gemming, T., Schultz, L., Fassbender, J., Liedke, M.O., Frommberger, M., Quandt, E.
Magnetic anisotropy patterning of amorphous films by He-ion irradiation
Appl. Phys. Lett. **86** (2005) 162502

Potzger, K., Bischoff, L., Liedke, M.O., Hillebrands, B., Rickart, M., Freitas, P., McCord, J., Fassbender, J.
Domain structure of magnetically micro-patterned PtMn/NiFe exchange bias bilayers
IEEE Trans. Magn. **41** (2005) 3610

Solina, D., Liedke, M.O., Tietze, U., Fassbender, J., Schreyer, A.
Reflectivity characterization of ion irradiated exchange bias FeMn-FeNi films
J. Magn. Magn. Mat. **286** (2005) 225

Turos, A., Abdul-Kader, A.M., Podsiadlo, S., Strojek, B., Strzalkowski, I., Grambole, D.
Hydrogen behaviour in novel materials for spintronic: GaFeN codoped with Mg, Si and Al
Vacuum **78** (2005) 285

Weber, M., Nembach, H., Hillebrands, B., Fassbender, J.
Modified Gilbert damping due to exchange bias in NiFe/FeMn bilayers
J. Appl. Phys. **97** (2005) 10A701

Weber, M., Nembach, H., Hillebrands, B., Fassbender, J.
Real-time temperature dynamics in exchange biased bilayers upon laser excitation
IEEE Trans. Magn. **41** (2005) 1089

Weber, M.C., Nembach, H., Blomeier, S., Kaltofen, R., Schumann, J., Carey, M., Fassbender, J.

All-optical probe of magnetization dynamics in exchange biased bilayers on the picosecond time-scale
Eur. Phys. J. B **45** (2005) 243

Nanostructures

Bischoff, L., Schmidt, B., Akhmadaliev, C., Heinig, K.-H.
Nanodrähte durch Ionenbeschuss
Dresdner Transferbrief **2** (2005) 13

Cantelli, V., Borany, J. von, Mücklich, A., Schell, N.
Investigation of the formation and phase transition of small Ge and Co nanoparticles in a SiO_2 *matrix*
Nucl. Instr. Meth. B **238** (2005) 268

Dimitrakis, P., Normand, P., Vontintseva, E., Stegemann, K.-H., Heinig, K.-H., Schmidt, B.
Memory devices obtained by Si^+ *irradiation through poly-Si/*SiO_2 *gate stack*
J. Phys.: Conf. Ser. **10** (2005) 7

Dvurechenskii, A.V., Smagina, J.V., Grötzschel, R., Zinovyev, V.A., Armbrister, V.A., Novikov, P.L., Teys, S.A., Gutakovskii, A.K.
Ge/Si quantum dot nanostructures grown with low-energy ion beam assisted epitaxy
Surf. Coat. Technol. **196** (2005) 25

Eichhorn, F., Gaca, J., Heera, V., Schell, N., Turos, A., Weishart, H., Wojcik, M.
Structural studies on ion implanted semiconductors using x-ray synchrotron radiation: strain evolution and growth of nanocrystals
Vacuum **78** (2005) 303

Grenzer, J., Bischoff, L., Pietsch, U.
Grazing-incidence diffraction strain analysis of a laterally patterned Si wafer treated by focused Ge and Au ion beam implantation
Phys. Status Solidi A **202** (2005) 1009

Johnson, S., Markwitz, A., Rudolphi, M., Baumann, H., Kuo, P.-Y., Blaikie, R., Mücklich, A.
Effect of crystal orientation on self-assembled silicon nanostructures formed by electron beam annealing
J. Appl. Phys. **97** (2005) 94301

Kurmaev, E.Z., Zatsepin, D.A., Cholakh, S.O., Schmidt, B., Harada, Y., Tokushima, T., Osawa, H., Shin, S., Takeuchi, T.
Iron nanoparticles in amorphous SiO_2*: x-ray emission and absorption spectra*
Phys. of The Solid State **47** (2005) 754

Markwitz, A., Johnson, S., Rudolphi, M., Baumann, H., Mücklich, A.
Formation of SiC surface nanocrystals by ion implantation and electron beam rapid thermal annealing
Appl. Phys. Lett. **86** (2005) 013108

Meduňa, M., Novák, J., Falub, C.V., Bauer, G., Tsujino, S., Grützmacher, D., Müller, E., Campidelli, Y., Kermarrec, O., Bensahel, D., Schell, N.
High temperature investigations of Si/SiGe based cascade structures using x-ray scattering methods
J. Phys. D: Appl. Phys. **38** (2005) A121

Oates, T.W.H., Mücklich, A.
Evolution of plasmon resonances during plasma deposition of silver nanoparticles
Nanotechnol. **16** (2005) 2606

Röntzsch, L., Heinig, K.-H., Schmidt, B., Mücklich, A., Möller, W., Thomas, J., Gemming, T.
Direct evidence of self-aligned Si nanocrystals formed by ion irradiation of Si/SiO$_2$ interfaces
Phys. Status Solidi A **202** (2005) R170

Tsvetkova, T., Takahashi, S., Zayats, A., Dawson, P., Turner, R., Bischoff, L., Angelov, O., Dimova-Malinovska, D.
Near-field optical mapping of the ion-implanted patterns fabricated in amorphous silicon carbide
Vacuum **79** (2005) 94

Tsvetkova, T., Takahashi, S., Zayats, A., Dawson, P., Turner, R., Bischoff, L., Angelov, O., Dimova-Malinovska, D.
Fabrication of nano-scale optical patterns in amorphous silicon carbide with focused ion beam writing
Vacuum **79** (2005) 100

Zeimer, U., Pietsch, U., Grenzer, J., Fricke, J., Knauer, A., Weyers, M.
Optimised two layer overgrowth of a lateral strain-modulated nanostructure
J. Alloys Comp. **401** (2005) 226

Doping and Defects in Semiconductors

Borany, J. von, Friedrich, M., Rüb, M., Deboy, G., Butschke, J., Letzkus, F.
Application of ultra-high energy boron implantation for superjunction power (CoolMOS^{TM}) devices
Nucl. Instr. Meth. B **237** (2005) 62

Brauer, G., Anwand, W., Coleman, P.G., Skorupa, W.
Slow positron annihilation spectroscopy – a tool to characterize vacancy-type damage in ion-implanted 6H-SiC
Vacuum **78** (2005) 131

Chen, X.D., Ling, C.C., Gong, M., Fung, S., Beling, C.D., Brauer, G., Anwand, W., Skorupa, W.
Anomalous behaviors of E1/E2 deep level defects in 6H silicon carbide
Appl. Phys. Lett. **86** (2005) 031903

Ferro, G., Panknin, D., Polychroniadis, E.K., Monteil, Y., Skorupa, W., Stoemenos, J.
Microstructural characterization of 3C-SiC thin films grown by flash lamp induced liquid phase epitaxy
Mat. Sci. Forum **483-487** (2005) 295

Kögler, R., Mücklich, A., Reuther, H., Krecar, D., Hutter, H., Skorupa, W.
Defect engineering in ion beam synthesis of SiC and SiO$_2$ in Si
Solid State Phenom. **108-109** (2005) 321

Kögler, R., Eichhorn, F., Mücklich, A., Skorupa, W., Serre, C., Perez-Rodriguez, A.
Effect of excess vacancies in ion beam synthesis of SiC nanoclusters
Vacuum **78** (2005) 177

Krecar, D., Fuchs, M., Kögler, R., Hutter, H.
SIMS investigation of gettering centres produced by phosphorus MeV ion implantation
Appl. Surf. Sci. **252** (2005) 278

Krecar, D., Fuchs, M., Kögler, R., Hutter, H.
Investigation of gettering effects in CZ-type silicon with SIMS
Anal. Bioanal. Chem. **381** (2005) 1526

Ling, C.C., Chen, X.D., Brauer, G., Anwand, W., Skorupa, W., Wang, H.Y., Weng, H.M.
Deep-level defects in n-type 6H silicon carbide induced by He-implantation
J. Appl. Phys. **98** (2005) 043508

Nazarov, A.N., Skorupa, W., Osiyuk, I.N., Tjagulski, I.P., Lysenko, V.S., Yankov, R.A., Gebel, T.
Comparative study of charge trapping in high-dose Si and Ge-implanted Al/SiO_2/Si structures
J. Electrochem. Soc. **152** (2005) F20

Pecz, B., Dobos, L., Panknin, D., Skorupa, W., Lioutas, C., Vouroutzis, N.
Crystallization of amorphous-Si films by flash lamp annealing
Appl. Surf. Sci. **242** (2005) 185

Pezoldt, J., Polychroniadis, E., Stauden, T., Ecke, G., Chassagne, T., Vennegues, P., Leycuras, A., Panknin, D., Stoemenos, J., Skorupa, W.
Nucleation control in FLASIC assisted short time liquid phase epitaxy by melt modification
Mat. Sci. Forum **483-487** (2005) 213

Posselt, M., Gao, F., Zwicker, D.
Atomistic study of the migration of di- and tri-interstitials in silicon
Phys. Rev. B **71** (2005) 245202

Posselt, M., Gao, F., Zwicker, D.
Migration of di- and tri-interstitials in silicon
Nucl. Instr. Meth. B **228** (2005) 212

Skorupa, W., Panknin, D., Voelskow, M., Anwand, W., Gebel, T., Yankov, R.A.
Advanced thermal processing of materials in the msec range
Vacuum **78** (2005) 673

Skorupa, W., Gebel, T., Yankov, R.A., Paul, S., Lerch, W., Downey, D.F., Arevalo, E.A.
Advanced thermal processing of ultrashallow implanted junctions using flash lamp annealing
J. Electrochem. Soc. **152** (2005) G436

Smith, M., McMahon, R., Voelskow, M., Skorupa, W., Stoemenos, J.
Regrowth mechanisms in flash lamp processing of heteroepitaxial SiC on silicon substrates
J. Cryst. Growth **277** (2005) 162

Smith, M., McMahon, R., Voelskow, M., Panknin, D., Skorupa, W.
Modelling of flash-lamp-induced crystallization of amorphous silicon thin films on glass
J. Cryst. Growth **285** (2005) 249

Smith, M., McMahon, R.A., Skorupa, W., Voelskow, M., Stoemenos, J.
A thermal model for flash lamp annealing of 3C-SiC/Si multi-layer systems (i-FLASiC)
Mat. Sci. Forum **483-487** (2005) 217

Vandervorst, W., Janssens, T., Brijs, B., Delhougne, R., Loo, R., Caymax, M., Pawlak, B. J., Posselt, M.
Athermal germanium migration in strained silicon layers during junction formation with solid-phase epitaxial regrowth
Appl. Phys. Lett. **86** (2005) 081915

Voelskow, M., Skorupa, W., Smith, M.P., McMahon, R.A.
Homogenization of the melting depth in SiC on Si structures during flash lamp irradiation
Appl. Phys. Lett. **87** (2005) 241901

Voelskow, M., Panknin, D., Polychroniadis, E.K., Ferro, G., Godignon, P., Mestres, N., Skorupa, W., Monteil, Y., Stoemenos, J.
Epitaxial SiC formation at the SiO_2/Si *interface by* C^+ *implantation into* SiO_2 *and subsequent annealing*
Mat. Sci. Forum **483-487** (2005) 233

Weih, P., Stauden, T., Ecke, G., Shokhovets, S., Zgheib, C., Voelskow, M., Skorupa, W., Ambacher, O., Pezoldt, J.
Ion beam synthesis of $3C\text{-}(Si_{1-x}C_{1-y})Ge_{x+y}$ *solid solutions*
Phys. Status Solidi A **202** (2005) 545

Weishart, H., Heera, V., Skorupa, W.
n-type conductivity in high-fluence Si-implanted diamond
J. Appl. Phys. **97** (2005) 103514

Weishart, H., Eichhorn, F., Heera, V., Pécz, B., Barna, Á., Skorupa, W.
High-fluence Si-implanted diamond: optimum implantation temperature for SiC formation
J. Appl. Phys. **98** (2005) 043503

Wiatrowski, A., Boratynski, B., Prucnal, S., Synowiec, Z., Zuk, J.
Proton implant isolation in GaN
Vacuum **78** (2005) 463

Wierzchowski, W., Wieteska, K., Graeff, W., Gawlik, G., Turos, A., Maurin, J., Mücklich, A.
Strain profiles in the insulated buried layers obtained by He implantation in AlGaAs
Acta Cryst. A **61** (2005) C449

Zolnai, Z., Ster, A., Khánh, N.Q., Kótai, E., Posselt, M., Battistig, G., Lohner, T., Gyulai, J.
Ion-beam analysis and computer simulation of damage accumulation in nitrogen implanted 6H-SiC: effects of channeling
Mat. Sci. Forum **483-485** (2005) 637

Optoelectronic Materials

Cheng, X.Q., Sun, J.M., Kögler, R., Skorupa, W., Möller, W., Prucnal, S.
Photoluminescence of Er-doped SiO_2 *layers containing Si nanoclusters using dual ion implantation and annealing*
Vacuum **78** (2005) 177

Drachenko, O., Galibert, J., Léotin, J., Tomm, J.W., Semtsiv, M.P., Ziegler, M., Dressler, S., Müller, U., Masselink, W.T.
Electron-optical-phonon interaction in the $In_{0.73}Ga_{0.27}As\text{-}AlAs$ *intersubband laser*
Appl. Phys. Lett. **87** (2005) 121114

Dreyhaupt, A.,Winnerl, S., Dekorsy, T., Helm, M.
High-intensity terahertz radiation from a microstructured large-area photoconductor
Appl. Phys. Lett. **86** (2005) 121114

Fitting, H.-J., Ziems, T., Salh, R., Charnowski, A. von, Schmidt, B.
Luminescent defect dynamics in amorphous SiO_2*:H*
Phys. Status Solidi C **2** (2005) 693

Fitting, H.-J., Ziems, T., Salh, R., Zamoryanskaya, M.V., Kolesnikova, K.V., Schmidt, B., Czarnowski, A. von
Cathodoluminescence of wet, dry, and hydrogen-implanted silica films

J. Non-Cryst. Sol. **351** (2005) 2251

Fitting, H.-J., Salh, R., Barfels, T., Schmidt, B.
Multimodal luminescence spectra of ion-implanted silica
Phys. Status Solidi A **202** (2005) R142

Gushterova, P., Sharlandjiev, P., Schmidt, B., Pham, M.T.
On the determination of the optical constants of very thin (λ/50) films
J. Optoel. Adv. Mat. **7** (2005) 305

Helm, M., Sun, J. M., Potfajova, J., Dekorsy, T., Schmidt, B., Skorupa, W.
Efficient silicon based light emitters
Microel. J. **36** (2005) 957

Helm, M., Sun, J., Potfajova, J., Winnerl, S., Dekorsy, T., Skorupa, W., Schmidt, B., Mücklich, A.
Efficient light emitting diodes based on nanoscale silicon
Phys. Status Solidi C **2** (2005) 2941

Lebedev, M.V., Misochko, O.V., Dekorsy, T., Georgiev, N.
On the nature of the coherent artifact
J. Exp. Theor. Phys. **100** (2005) 272

Misochko, O.V., Lebedev, M.V., Dekorsy, T.
Observation of longitudinal optical-transverse optical splitting for E-symmetry phonons in Te by coherent phonon spectroscopy
J. Phys. Cond. Matter **17** (2005) 3015

Nazarov, A.N., Vovk, J.N., Osiyuk, I.N., Tkachenko, A.S., Tyagulskii, I.P., Lysenko, V.S., Gebel, T., Rebohle, L., Skorupa, W., Yankov, R.A.
The effect of radio-frequency plasma treatment on the electroluminescent properties of violet light-emitting germanium implanted metal-oxide-semiconductor structures
Mat. Sci. Eng. B **124** (2005) 458

Nazarov, A.N., Sun, J.M., Skorupa, W., Yankov, R.A., Osiyuk, I.N., Tjagulski, I.P., Lysenko, V.S., Gebel, T.
Light emission and charge trapping in Er-doped silicon dioxide films containing silicon nanocrystals
Appl. Phys. Lett. **86** (2005) 151914

Prucnal, S., Cheng, X.Q., Sun, J.M., Kögler, R., Zuk, J., Skorupa, W.
Optical and microstructural properties of doubly Ge-Si implanted SiO_2 layers
Vacuum **78** (2005) 693

Rebohle, L., Gebel, T., Yankov, R.A., Trautmann, T., Skorupa, W., Sun, J.M., Gauglitz, G., Frank, R.
Microarrays of silicon-based light emitters for novel biosensor and lab-on-a-chip applications
Optical Mat. **27** (2005) 1055

Salh, R., Schmidt, B., Fitting, H.-J.
Multiplet luminescence of sulfur implanted silica – SiO_2:S
Phys. Status Solidi A **202** (2005) R53

Semtsiv, M.P., Ziegler, M., Dressler, S., Masselink, W.T., Georgiev, N., Dekorsy, T., Helm, M.
Strain-compensated AlAs/(In,Ga)As heterostructures for short wavelength intersubband absorption and laser emission
J. Crystal Growth **278** (2005) 526

Semtsiv, M., Ziegler, M., Masselink, W.T., Georgiev, N., Dekorsy, T., Helm, M.
Near-infrared intersubband transitions in InGaAs–AlAs–InAlAs double quantum wells
J. Appl. Phys. **97** (2005) 113538

Sharlandijev, P., Nazarova, D., Mednikarov, B., Pham, M.T.
On extraordinary optical transmission from periodic and random nanostructures
J. Optoelectr. Adv. Materials **7** (2005) 309

Sinning, S., Dekorsy, T., Helm, M., Mussler, G., Däweritz, L., Ploog, K.H.
Reduced sub-picosecond electron relaxation in GaNAs
Appl. Phys. Lett. **86** (2005) 161912

Skorupa, W., Sun, J.M., Prucnal, S., Rebohle, L., Gebel, T., Nazarov, A.N., Osiyuk, I.N., Helm, M.
Rare earth ion implantation for silicon based light emission
Solid State Phenom. **108-109** (2005) 755

Stehr, D., Metzner, C., Helm, M., Roch, T., Strasser, G.
Resonant impurity bands in semiconductor superlattices
Phys. Rev. Lett. **95** (2005) 257401

Sun, J.M., Skorupa, W., Dekorsy, T., Helm, M., Rebohle, L., Gebel, T.
Bright green electroluminescence from Tb^{3+} *in silicon metal-oxide-semiconductor devices*
J. Appl. Phys. **97** (2005) 123513

Sun, J.M., Dekorsy, T., Skorupa, W., Mücklich, A., Schmidt, B., Helm, M.
Efficient silicon light emitting diodes by boron implantation: The mechanism
Optical Mat. **27** (2005) 1041

Sun, J.M., Skorupa, W., Dekorsy, T., Helm, M., Nazarov, A.N.
On the mechanism of electroluminescence excitation in Er-doped SiO_2 *containing silicon nanoclusters*
Optical Mat. **27** (2005) 1050

Vandyshev, E.N., Zhuravlev, K.S., Gilinsky, A.M., Lisitsyn, V.M., Skorupa, W.
Influence of electric field on the photoluminescence of silicon nanocrystals
Thin Solid Films **493** (2005) 297

Others

Cizek, J., Prochazka, I., Smola, B., Stulikova, I., Kuzel, R., Cieslar, M., Matej, Z., Cherkaska, V., Brauer, G., Anwand, W., Islamgaliev, R.K., Kulyasova, O.
Positron annihilation studies of microstructure of ultra fine grained metals prepared by severe plastic deformation
Mat. Sci. Forum **482** (2005) 207

Cizek, J., Prochazka, I., Kuzel, R., Matej, Z., Cherkaska, V., Cieslar, M., Smola, B., Stulikova, I., Brauer, G., Anwand, W., Islamgaliev, R.K., Kulyasova, O.
Ultra fine-grained metals prepared by severe plastic deformation: a positron annihilation study
Acta Phys. Polonica A **107** (2005) 745

Cizek, J., Prochazka, I., Kuzel, R., Becvar, F., Cieslar, M., Brauer, G., Anwand, W., Kirchheim, R., Pundt, A.
Hydrogen-induced defects in niobium studied by positron annihilation spectroscopy
J. Alloys and Comp. **404-406** (2005) 580

Grynszpan, R.I., Saude, S., Anwand, W., Brauer, G.

Positron annihilation investigation and nuclear reaction analysis of helium and oxygen-implanted zirconia
Nucl. Instr. Meth. B **241** (2005) 526

Hennig, C., Reich, T., Kraus, W., Reck, G., Prokert, F., Schell, N.
Combining EXAFS and x-ray powder diffraction to solve structures containing heavy atoms
Physica Scripta T **115** (2005) 352

Kondyurin, A., Romanova, V., Begishev, V., Kondyurina, I., Günzel, R., Maitz, F.M.
Cross linking polyurethane coating on vascular stents for enhanced x-ray contrasts
J. Bioactive and Compatible Polymers **20** (2005) 77

Krause-Rehberg, R., Bondarenko, V., Thiele, E., Klemm, R., Schell, N.
Determination of absolute defect concentrations for saturated position trapping – deformed polycrystalline Ni as a case study
Nucl. Instr. Meth. B **240** (2005) 719

Oswald, S., Mazilu, I., Fahler, S., Gruner, W., Hermann, R., Loser, W., Filip, O., Wendrock, H., Schultz, L., Schmidt, B., Rodewald, W.
SIMS measurements of oxygen content in the $Nd_2Fe_{14}B$ *phase*
J. Magn. Magn. Mat. **290** (2005) 1240

Oswald, S., Schmidt, B., Heinig, K.-H.
Influence of sputtering conditions and electron energy on XPS depth profiling of Ge in SiO_2
Cryst. Res. Technol. **40** (2005) 1134

Schmidt, B., Oswald, S., Bischoff, L.
Etch rate retardation of Ga^+*-ion beam-irradiated silicon*
J. Electrochem. Soc. **152** (2005) G875

Thiele, E., Klemm, R., Hollang, L., Holste, C., Schell, N., Natter, H., Hempelmann, R.
An approach to cyclic plasticity and deformation-induced structure changes of electrodeposited nickel
Mat. Sci. Eng. A **390** (2005) 42

Tunc, S., Maitz, M.F., Steiner, G., Vázques, L., Pham, M.T., Salzer, R.
In-situ conformational analysis of fibrinogen absorbed on Si surfaces
Colloids and Surfaces: Biointerfaces **42** (2005) 219

Equipment

Bischoff, L.
Alloy liquid metal ion sources and their application in mass separated focused ion beams
Ultramicroscopy **103** (2005) 59

Bischoff, L., Mair, G.L.R., Akhmadaliev, C., Mair, A.W.R., Ganetsos, T.
The post-ionisation of Pb ions from a molten Sn host field-ion emitter
Appl. Phys. A **80** (2005) 205

Bischoff, L., Pilz, W., Ganetsos, T., Akhmadaliev, C., Aidinis, C.J., Londos, C.A.
On the temperature dependence of the mass spectra of AuGe and AuGeSi liquid metal alloy ion sources
J. Phys.: Conf. Ser. **10** (2005) 214

Kaschny, J.R., Kögler, R., Tyroff, H., Bürger, W., Eichhorn, F., Mücklich, A., Serre, C., Skorupa, W.
Facility for simultaneous dual-beam ion implantation

Nucl. Instr. Meth. A **551** (2005) 2000

Mair, G.L.R., Bischoff, L., Londos, C.A., Ganetsos, T., Akhmadaliev, C., Aidinis, C.J.
An in-depth investigation into the temperature dependence of the mass spectra of an $Au_{82}Si_{18}$ *liquid metal field emitter*
Appl. Phys. A **81** (2005) 385

Zschornack, G., Landgraf, S., Großmann, F., Kentsch, U., Ovsyannikov, V.P., Schmidt, M., Ullmann, F.
A low energy ion beam line for highly charged ions
Vacuum **78** (2005) 319

Conference Proceedings

Bonafos, C., Cherkashin, N., Carrada, M., Coffin, H., Ben Assayag, G., Schamm , S., Dimitrakis, P., Normand, P., Perego, M., Fanciulli, M., Müller, T., Heinig, K.-H., Argawal, A., Claverie, A.
Manipulation of 2D arrays of Si nanocrystals by ultra-low-energy ion beam synthesis for nonvolatile memories applications
MRS Soc. Symp. Proc. **830** (2005) D5.2

Dekorsy, T., Sun, J. M., Skorupa, W., Mücklich, A., Schmidt, B., Helm, M.
Origin of efficient light emission from si pn diodes prepared by ion implantation
AIP Conf. Proc. **772** (2005) 1539

Dekorsy, T., Sinning, S., Helm, M., Mussler, G., Däweritz, L., Ploog, K.H.
Ultrafast carrier dynamics in nitrogen containing GaAs
AIP Conf. Proc. **772** (2005) 235

Drachenko, O., Rylkov, V.V., Leotin, J.
Compact Terahertz cyclotron resonance spectrometer in high magnetic fields
IEEE Conference digest IRMMW2005/THz2005 (2005) 20

Gebel, T., Rebohle, L., Trautmann, T., Yankov, R.A., Skorupa, W., Gauglitz, G., Frank, R.
Miniaturised arrays of light-sources based on silicon technology: a promising approach for novel sensors and lab-on-a-chip systems
Sensor 2005, Conf. Proc. Vol. 1, B1.4 (2005) 125

Ling, C.C., Chen, X.D., Fung, S., Beling, C.D., Brauer, G., Anwand, W., Skorupa, W., Gong, M.
Deep level defects E1/E2 in n-type 6H silicon carbide induced by electron radiation and He implantation
AIP Conf. Proc. **772** (2005) 99

Masselink, W.T., Semtsiv, M.P., Dressler, S., Ziegler, M., Georgiev, N., Dekorsy, T., Helm, M.
High-power short-wavelength quantum cascade lasers
Proc. SPIE **5738** (2005) 13

Reuther, H., Menzel, M., Vinnichenko, M., Kolitsch, A.
Investigation of the Sn^{4+} *charge density variation in* In_2O_3 *using Mössbauer spectroscopy*
AIP Conf. Proc. **765** (2005) 132

Skorupa, W., Yankov, R.A., Voelskow, M., Anwand, W., Panknin, D., McMahon, R.A., Smith, M., Gebel, T., Rebohle, L., Fendler, R., Hentsch, W.
Advanced thermal processing of semiconductor materials in the msec range (invited)

Proc. XIII. Int. Conf. Advanced Thermal Processing of Semiconductors (RTP 2005), Oct. 4-7, 2005, Santa Barbara, USA, IEEE Cat.No.05EX1090, ISBN 0-7803-9223-X, 53-71 (2005)

Skorupa, W., Sun, J.M., Prucnal, S., Rebohle, L., Gebel, T., Nazarov, A.N., Osiyuk, I.N., Dekorsy, T., Helm, M.
Rare earth ion implantation for silicon based light emission: From infrared to ultraviolet
MRS Soc. Symp. Proc. **866** (2005) V4.1.1 / FF4.1.1

Invited Talks

Brauer, G., Anwand, W., Eichhorn, F., Skorupa, W., Hofer, C., Brandstetter, S., Teichert, C., Kuriplach, J., Cizek, J., Prochazka, I., Coleman, P.G., Nozawa, T., Kohyama, A.
Surface studies of SiC
10th Int. Workshop on Slow Positron Beam Techniques for Solids and Surfaces (SLOPOS-10), Doha, Qatar, March 19 – 25, 2005

Fassbender, J., Potzger, K., Bischoff, L., Zhou, S., Talut, G., Liedke, M.O., Reuther, H., Mücklich, A., Grötzschel, R.
Ion-driven magnetic nanostructures
14th Int. Summer School on Vacuum, Electron and Ion Technologies, Sunny Beach, Bulgaria, Sept 12 – 16, 2005

Facsko, S., Kost, D., Keller, A., Möller, W., Pesic, Z., Stolterfoht, N.
Interaction of highly-charged ions with the surface of insulators
3rd Conf. on Elementary Processes in Atomic Systems (CEPAS), Miskolc, Hungary, Aug 31 – Sept 2, 2005

Gao, F., Zhang, Y., Posselt, M., Devanathan, R., Weber, W.J.
Epitaxial recrystallization of nano-sized amorphous layers, phase nucleation and growth in 4H-SiC
MRS Fall Meeting, Boston, MA, USA, Nov 27 – Dec 1, 2005

Grenzer, J.
Grazing-incidence diffraction and small angle X-ray scattering
6th Autumn School on X-ray Scattering from Surfaces and Thin Layers, Smolenice, Slovakia, Sept 18 – 21, 2005

Grynszpan, R.I., Brauer, G., Anwand, W.
Positron annihilation investigation in ion-implanted Yttria-stabilized zirconia
MRS Fall Meeting , Boston, MA, USA, Nov 28 – Dec 2, 2005

Heinig, K.-H.
Modelling of ion-driven nanostructures
14th Int. Summer School on Vacuum, Electron and Ion Technologies, Sunny Beach, Bulgaria, Sept 12 – 16, 2005

Heinig, K.-H., Müller, T., Röntzsch, L., Möller, W.
Growth and taming of nanostructures with ion beams
Int. Symp. on Trends in Nanoscience: Structure and Functions, Irsee, Germany, Oct 8 – 12, 2005

Helm, M.
Approaches for silicon based light emitters
8th German-Vietnamese Seminar on Physics and Engineering, Erlangen, Germany, April 3 – 9, 2005

Helm, M.

Efficient silicon based light emitters
4th Workshop on Semiconductor Nanodevices and Nanostructured Materials (NANOSEMIMAT-4), Sao Pedro, SP, Brazil, March 9 – 13, 2005

Helm, M.
New concepts for short-wavelength quantum cascade lasers and few-cycle THz emitters
Japan-Germany Colloquium 2005: Semiconductor Physics and Technology, Dresden, Germany
Feb 14 – 16, 2005

Krause-Rehberg, R., Sachert, S., Brauer, G., Rogov, A., Nowak, K.
EPOS – an intense positron beam project at the Research Center Rossendorf
10th Int. Workshop on Slow Positron Beam Techniques for Solids and Surfaces (SLOPOS-10), Doha, Qatar, March 19 – 25, 2005

Masselink, W.T., Semtsiv, M.P., Dressler, S., Ziegler, M., Georgiev, N., Dekorsy, T., Helm, M.
High-power short-wavelength quantum cascade lasers
Photonics West, SPIE, San Jose, CA, USA, Jan 22 – 27, 2005

Möller, W.
Plasma surface interaction and ion bombardment
Intern. School "Nanostructuring by Ion Beams", New Delhi, India, Feb 18 – 19, 2005

Möller, W., Heinig, K.-H., Müller, T., Röntzsch, L., Schmidt, B.
Ion beam synthesis of nanostructures with keV/amu ions
Indo-German Workshop "Synthesis and Modification of Nanostructured Materials by Energetic Ion Beams", New Delhi, India, Feb 21 – 24, 2005

Möller, W., Abendroth, B., Gago, R., Kolitsch, A.
Ion bombardment for stress release in cubic boron nitride thin films
Intern. Conf. on Metallurgical Coatings and Thin Films, San Diego, USA, May 2 – 6, 2005

Möller, W.
Plasma immersion ion implantation: Process, promises and prospects
15th Intern. Colloq. on Plasma Processes, Autrans, France, June 5 – 9, 2005

Möller, W.
Ion-induced stress release in hard coatings
14th Intern. Summer School on Vacuum, Electron, and Ion Technologies, Sunny Beach, Bulgaria, Sept 12 – 16, 2005

Möller, W., Shevchenko, N., Yankov, R.A., Rogozin, A., Maitz, M.F., Richter, E., Donchev, A., Schütze, M.
Reactive ion plasma immersion implantation for surface passivation
8th Intern. Workshop on Plasma-Based Ion Implantation and Deposition, Chengdu, China,
Sept 18 – 22, 2005

Müller, T., Heinig, K.-H., Schmidt, B., Röntzsch, L., Stegemann, K.-H.
Fabrication of Si nanocrystals for nonvolatile memories using ion beams
1st Int. Workshop on Semiconductor Nanocrystals (SEMINANO), Budapest, Hungary
Sept 10 – 12, 2005

Potzger, K., Reuther, H., Zhou, S., Anwand, W., Brauer, G.
Ion implantation of 3d-metals into ZnO single crystals
Int. Topical Workshop on Heteroepitaxy of 3C-SiC on Silicon and its Application to Sensor Devices (HeT-SiC-05), Hotel Erbgericht Krippen, Germany, April 26 – May 1, 2005

Schneider, H., Maier, T., Schönbein, C., Koidl, P., Walther, M., Liu, H.C.
Optical and transport nonlinearities in quantum well infrared photodetectors
8th Int. Conf. on Intersubband Transitions in Quantum Wells, Cape Cod, MA, USA,
Sept 11 – 16, 2005

Schneider, H., Maier, T., Fleissner, J., Walther, M., Koidl, P., Weimann, G., Cabanski, W., Finck, M., Menger, P., Rode, W., Ziegler, J.
Quantum well infrared photodetectors: quantum structures for high-performance thermal imaging
Int. Symp. on Advanced Electronics for Future Generations - "Secure-Life Electronics" for Quality Life and Society, Tokyo, Japan, Oct 11 – 12, 2005

Skorupa, W., Panknin, D., Anwand, W., Voelskow, M., Yankov, R.A., Gebel, T., Paul, S., Lerch, W., Downey, D.E., Arevalo, E., Mannino, G.
Advanced thermal processing of silicon in the msec-range using flash lamps
EU-Workshop on "Non-conventional thermal processes for advanced CMOS", Rome, Italy,
Jan 21, 2005

Skorupa, W., Sun, J.M., Prucnal, S., Rebohle, L., Gebel, T., Nazarov, A.N., Osiyuk, I.N., Dekorsy, T., Helm, M.
Rare earth ion implantation for silicon based light emission: From infrared to ultraviolet
MRS Spring Meeting, San Francisco, CA, USA, March 29 – April 1, 2005

Skorupa, W.
Seltenerden-Implantation für die Si-basierte Lichtemission
Workshop "Ionenstrahlphysik und -technologie", Leipzig, Germany, April 11 – 12, 2005
Deutsches Nutzertreffen Ionenimplantation, Erlangen, Germany, May 13, 2005

Skorupa, W.
Basics and advances of ion beam synthesis
Nordic Summer School on Defects and Diffusion in Semiconductors and Heterostructures,
Sundvolden, Norway, Aug 18 – 21, 2005

Skorupa,W., Anwand, W.
Thermobehandlung von Halbleitermaterialien im msec-Bereich
Summerschool S2B Nanotronics 2005, Science to Business Center Nanotronics-DEGUSSA AG, Marl, Germany, Aug. 29 – 30, 2005

Skorupa, W., Yankov, R.A., Voelskow, M., Anwand, W., Panknin, D., McMahon, R.A., Smith, M., Gebel, T., Rebohle, L., Fendler, R., Hentsch, W.
Advanced thermal processing of semiconductor materials in the msec range
13th Annual IEEE Int. Conf. on Advanced Thermal Processing of Semiconductors (RTP2005), Santa Barbara, CA, USA, Oct 3 – 7, 2005

Skorupa, W.
USJ-related and non-related applications of flash lamp annealing
Deutsches Nutzertreffen Kurzzeit-Temperung, Reutte, Austria, Nov 10, 2005

Sun, J.M, Skorupa, W., Dekorsy, T., Schmidt, B., Helm, M.
Efficient light emission from Si pn diodes and metal-oxide-semiconductor structures
14th Int. Conf. on Luminescence (ICL05), Beijing, China, July 25 – 29, 2005

Vredenberg, A., Polman, A., Kooi, B.J., Van Dillen, T., Heinig, K.-H., Toulemonde, M.
Ion beam shaping of nanometals
MRS Fall Meeting, Boston, MA, USA, Nov 27 – Dec 1, 2005

Conference Contributions

Abrasonis, G., Gago, R., Vinnichenko, M., Kreißig, U., Mücklich, A., Kolitsch, A., Möller, W.
Deposition by ion beam sputtering of CN_x *thin films: the influence of the composition of the sputtering ion beam and temperature*
Workshop "Oberflächentechnologie mit Plasma- und Ionenstrahlprozessen", Mühlleithen, Germany, March 16 – 18, 2005

Abrasonis, G., Gago, R., Czigany, Z., Mücklich, A., Jimenez, I., Radnoczi, G., Kolitsch, A., Möller, W.
Aromatic clustering processes in C and CN_x *thin films during ion beam sputtering and ion beam assisted deposition*
7th Biennial Workshop "Fullerenes and Atomic Clusters", St. Petersburg, Russia,
June 27 – July 1, 2005

Akhmadaliev, C., Bischoff, L., Schmidt, B.
Focused ion beam synthesis of $CoSi_2$ *nanowires*
342. WE-Heraeus Seminar "Science and Technology of Inorganic Nanowires", Bad Honnef, Germany, Feb 13 – 16, 2005

Akhmadaliev, C., Schmidt, B., Bischoff, L.
Ion beam synthesis of $CoSi_2$ *nanowires using FIB*
Meeting des DFG-Schwerpunktes „Nanodrähte und Nanoröhren“, Fulda, Germany, May 2 – 4, 2005

Akhmadaliev, C., Bischoff, L., Schmidt, B.
$CoSi_2$ *nanostructures by writing FIB ion beam synthesis*
Meeting des DFG-Schwerpunktes „Nanodrähte und Nanoröhren“, Bad Honnef, Feb 14 – 17, 2005
E-MRS Spring Meeting, Strasbourg, France, May 31 – June 3, 2005

Akhmadaliev, C., Schmidt, B., Bischoff, L.
Synthesis of Cobaltdisilicide nanowires using fine focused ion beam
Meeting des DFG-Schwerpunktes 1165 „Nanodrähte und Nanoröhren“, Hirschegg, Germany,
Sept 4 – 8, 2005

Anwand, W., Skorupa, W., Rebohle, L., Trautmann, T., Tamme, S., Grass, T.
A new flash lamp apparatus for applications to millisecond heat treatments
Int. Topical Workshop on Heteroepitaxy of 3C-SiC on Silicon and its Application to Sensor Devices (HeT-SiC-05), Hotel Erbgericht Krippen, Germany, April 26 – May 1, 2005

Anwand, W., Brauer, G.
Slow positron implantation spectroscopy - a tool to characterize vacancy-type damage
1st Humboldt-Institute-Partnership Workshop, Universität Göttingen, Institut für Materialphysik, Göttingen, Germany, Oct 24 – 26, 2005

Arazi, A., Faestermann, T., Fernandez-Niello, J., Kurz, K., Korschinek, G., Poutivtsev, M., Richter, E., Wallner, A.
Stellar rates for the $^{25}Mg(p,\gamma)^{26}Al$ *reaction studied via AMS*
10th Int. Conf. Accelerator Mass Spectrometry, Sept 5 – 10, 2005

Ayache, R., Bouabellou, A., Richter, E., Kermiche, F.
Elaboration de siliciures de fer par bombardement ionique
2nd Algerian Crystallography Congress, Constantine, Algeria, April 17 – 21, 2005

Ayache, R., Boubelleou, A., Eichhorn, F., Richter, E.

Structural and optical properties of iron silicide formed ion beam mixing
E-MRS Fall Meeting, Warsaw, Poland, Sept 5 – 9, 2005

Beckers, M., Schell, N., Martins, R.M.S., Möller, W.
Texture development during growth of $Ti_{1-x}Al_xN$ *thin films studied by in-situ x-ray diffraction*
Int. Conf. on Metallurgical Coatings and Thin Films (ICMCTF 2005), San Diego, USA,
May 2 – 6, 2005

Beckers, M., Schell, N., Martins, R.M.S., Mücklich, A., Möller, W.
The growth and microstructure of magnetron sputtered Ti_2AlN *MAX phase thin films characterized by in-situ x-ray diffraction*
14th Int. Summer School on Vacuum, Electron and Ion Technologies, Sunny Beach, Bulgaria,
Sept 12 – 16, 2005

Bentzen, A., Ulyashin, A., Suphellen, A., Sauar, E., Grambole, D., Wright, D.N., Marstein, E.S., Svensson, B.G., Holt, A.
Surface passivation of silicon solar cells by amorphous silicon/silicon nitride dual layers
15th Int. Photovoltaic Science and Engineering Conference (PVSEC-15), Shanghai, China,
Oct 10 – 15, 2005

Bischoff, L. Schmidt, B., Akhmadaliev, C.
$CoSi_2$ *nanowires synthesized by FIB*
DPG-Frühjahrstagung, Berlin, Germany, March 4 – 9, 2005

Bischoff, L., Schmidt, B., Akhmadaliev, C.
Investigation of FIB assisted $CoSi_2$ *nanowire growth*
31th Int. Conf. on Micro- and Nano-Engineering (MNE2005), Vienna, Austria, Sept 19 – 22, 2005

Brauer, G., Anwand, W., Eichhorn, F., Skorupa, W., Hofer, C., Teichert, C., Kuriplach, J., Cizek, J., Prochazka, I., Coleman, P.G., Nozawa, T., Kohyama, A.
Surface characterization of a SiC/SiC composite
10th Int. Workshop on Slow Positron Beam Techniques for Solids and Surfaces (SLOPOS-10), Doha, Qatar, March 19 – 25, 2005

Brauer, G., Becvar, F., Anwand, W., Skorupa, W.
Evidence of a low quartz structure at the SiO_2/Si *interface from coincidence Doppler broadening spectroscopy*
10th Int. Workshop on Slow Positron Beam Techniques for Solids and Surfaces (SLOPOS-10), Doha, Qatar, March 19 – 25, 2005

Brauer, G., Anwand, W., Skorupa, W., Schmidt, H., Diaconu, M., Lorenz, M., Grundmann, M.
Structure and ferromagnetism of Mn^+ *ion implanted ZnO thin films on sapphire*
E-MRS Spring Meeting, Strasbourg, France May 31 – June 3, 2005

Brauer, G.
Indications for a low quartz structure at the SiO_2/Si *interface revealed by positron annihilation spectroscopies*
1st Humboldt-Institute-Partnership Workshop, Universität Göttingen, Institut für Materialphysik, Göttingen, Germany, Oct 24 – 26, 2005

Brauer, G., Anwand, W., Coleman, P.G., Skorupa, W.
Slow positron implantation spectroscopy – a tool to characterize vacancy-type damage in ion-implanted 6H-SiC
Mini-Workshop on Positron Physics and Positron Experiments / 1st User Meeting at NEPOMUC, TU München (ZWE FRM-II), Garching, Germany, Sept 1, 2005

Braurer, G., Kuriplach, J., Anwand, W., Becvar, F., Skorupa, W.
Characterisation of various crystalline structures at the SiO_2/Si interface by positrons
8th Int.Workshop on Positron and Positronium Chemistry (PPC-8), Coimbra, Portugal,
Sept 4 – 9, 2005

Braunstein, G., Hamad, O., Benndorf, G., Wenckstern, H. von, Lorenz, M., Brauer, G.
Acceptor formation by ion implantation of nitrogen into ZnO
12th Int. Workshop on Oxide Electronics (WOE-12), Cape Cod, USA, Oct 2 – 5, 2005

Braunstein, G., Muraviev, A., Saxena, H., Dhere, N., Richter, V., Kalish, R., Benndorf, G., Wenckstern, H. von, Lorenz, M., Brauer, G.
P-type doping of zinc oxide obtained by arsenic ion implantation
MRS Fall Meeting , Boston, MA, USA, Nov 28 – Dec 2, 2005

Cantelli, V., Borany, J. von, Beckers, M., Fassbender, J.
$L1_0$ ordering of magnetron sputtered FePt films at temperatures below 400°C
50th Magnetism and Magnetic Materials Conference, San Jose, CA, USA, Oct 30 – Nov 3, 2005

Cantelli, V., Borany, J. von, Grenzer, J.
X-ray investigations on NiMn films after ion beam irradiation
6th Autumn School on X-ray Scattering from Surfaces and Thin Layers, Smolenice, Slovakia,
Sept 18 – 21, 2005

Cantelli, V., Borany, J. von, Grenzer, J., Kaltofen, R., Schumann, J., Fassbender, J.
Influence of He-ion-irradiation on thin NiMn/NiFe exchange bias films
50th Magnetism and Magnetic Materials Conference, San Jose, CA, USA, Oct 30 – Nov 3, 2005

Castro, R.M., Ueda, M., Oliveira, R.M., Reuther, H., Morena, B.L.D.
Influence of the plasma density on the performance of plasma immersion íon implantation of silicon surface
8th Brazilian Meeting of Plasma Physics, Niteroi, Rio de Janeiro, Brazil, Nov 27 – 30, 2005

Cizek, J., Prochazka, I., Brauer, G., Anwand, W., Mücklich, A., Kirchheim, R., Pundt, A.
Defect studies of hydrogen-loaded thin Nb films
10th Int. Workshop on Slow Positron Beam Techniques for Solids and Surfaces (SLOPOS-10), Doha, Qatar, March 19 – 25, 2005

Cizek, J., Melikhova, O., Prochazka, I., Brauer, G., Anwand, W., Mücklich, A., Kirchheim, R., Pundt, A.
Defects in nanocrystalline Nb films: effect of sputtering temperature
10th Int. Workshop on Slow Positron Beam Techniques for Solids and Surfaces (SLOPOS-10), Doha, Qatar, March 19 – 25, 2005

Dekorsy, T., Sun, J. M., Skorupa, W., Helm, M., Rebohle, L., Gebel, T.
Traditional hot-electron MOS devices for novel optoelectronic applications
14th Int. Conf. on Nonequilibrium Carriers in Semiconductors (HCIS-14), Chiacgo, USA,
July 24 – 29, 2005

Dmitrieva, O., Rellinghaus, B., Liedke, M.O., Fassbender, J.
Structural phase transformation of FePt nanoparticles by ion irradiation
Euromat 2005, Prague, Czech Republic, Sept 5 – 8, 2005

Donchev, A., Yankov, R.A., Richter, E., Schütze, M.
Improvement of the oxidation behaviour of TiAl-alloys by halogen treatment
Euromat 2005, Prague, Czech Republic, Sept 5 – 8, 2005

Drachenko, O., Leotin, J., Galibert, J., Sirtori, C., Page, H., Semtsiv, M.P., Ziegler, M., Dreßler, S., Müller, U., Masselink, T.
Electron-phonon interaction in quantum cascade structures probed by Landau level spectroscopy
12th Int. Conf. on Narrow Gap Semiconductors, Toulouse, France, July 3 – 7, 2005

Drachenko, O., Bansal, B., Rylkov, V.V., Galibert, J., Dixit, V.K., Leotin, J.
InAsSb/GaAs hetero-epitaxial crystals studied by cyclotron resonance measurements
12th Int. Conf. on Narrow Gap Semiconductors, Toulouse, France, July 3 – 7, 2005

Drachenko, O., Leotin, J., Sirtori, C., Page, H., Semtsiv, M.P., Ziegler, M., Dreßler, S., Müller, U., Masselink, W.T.
Electron-phonon interaction in quantum cascade lasers probed by Landau level spectroscopy
8th Int. Conf. on Intersubband Transitions in Quantum Wells, Cape Cod, USA,
Sept 11 – 16, 2005

Drachenko, O., Rylkov, V.V., Leotin, J.
Compact Terahertz cyclotron resonance spectrometer in high magnetic fields
The Joint 30th Int. Conf. on Infrared and Millimeter Waves and 13th Int. Conf. on Terahertz Electronics, Williamsburg, USA, Sept 19 – 23, 2005

Facsko, S., Kost, D., Keller, A., Möller, W.
Morphology of surfaces bombarded with highly charged ions
348. Heraeus-Seminar „Ions at Surfaces: Patterns and Processes“, Bad Honnef, Germany,
June 19 – 23, 2005

Facsko, S., Rossbach, S., Keller, A., Gago, R., Möller, W.
Self-organized ordered nanostructures by ion beam sputtering
Joint Meeting of the German Vacuum Society (DVG) and the Polish Vacuum Society (PTP), Krakow, Poland, Oct 26 – 29, 2005

Fassbender, J.
Ion irradiation in exchange bias systems
EU-RTN-Meeting Nexbias, TU Kaiserslautern, Germany, Feb 17 – 18, 2005

Fassbender, J., Bischoff, J., Mattheis, R., Fischer, P.
Magnetic domains and magnetization reversal of ion-induced magnetically patterned RKKY-coupled Ni81Fe19/Ru/Co90Fe10 films
50th Conf. on Magnetism and Magnetic Materials, San Jose, CA, USA, Oct 30 – Nov 3, 2005

Fassbender, J., Borany, J. von, Potzger, K., Grötzschel, R., Mücklich, A.
Modifikation der strukturellen und magnetischen Eigenschaften von Permalloy-Schichten bei Cr-Implantation
DPG-Frühjahrstagung, Berlin, Germany, March 4 – 9, 2005

Fassbender, J., McCord, J., Mattheis, R., Potzger, K., Mücklich, A., Borany, J. von
Doping magnetic materials - tunable properties due to Cr ion implantation
348. Heraeus-Seminar "Ions at Surfaces: Patterns and Processes", Bad Honnef, Germany,
June 19 – 23, 2005

Fassbender, J., McCord, J., Mattheis, R., Potzger, K., Mücklich, A., Borany, J. von
Doping magnetic materials - tunable properties due to ion implantation
Euromat 2005, Prague, Czech Republic, Sept 5 – 8, 2005

Fassbender, J., McCord, J., Mattheis, R., Potzger, K., Mücklich, A., Borany, J. von
Tailoring magnetic properties of permalloy by means of Cr implantation

Workshop "Ionenstrahlphysik und -technologie", IOM Leipzig, Germany, April 11 – 12, 2005

Fassbender, J., McCord, J., Weisheit, M., Mattheis, R.
Modifikation der magnetischen Dämpfung in Permalloy-Schichten durch Cr-Implantation
DPG Frühjahrstagung, Berlin, Germany, March 4 – 9, 2005

Fassbender, J., McCord, J., Weisheit, M., Mattheis, R.
Increased magnetic damping of permalloy upon Cr implantation
Intermag 2005, Nagoya, Japan, April 4 – 8, 2005

Fassbender, J., Potzger, K., Bischoff, L., Zhou, S., Talut, G., Liedke, M.O., Reuther, H., Mücklich, A., Grötzschel, R.
Ion-driven magnetic nanostructures
14th Int. Summer School on Vacuum, Electron and Ion Technologies, Sunny Beach, Bulgaria, Sept 12 – 16, 2005

Friedrich, M.
A modified rf ion source with a ceramic bottle
39th Symp. of Northeastern Accelerator Personnel (SNEAP), Brookhaven, USA, Oct 16 – 20, 2005

Fromknecht, R., Linker, G., Sun, K., Zhu, S., Wang, L.M., van Veen, A., van Huis, M.A., Weimann, T., Wang, J., Niemeyer, J., Eichhorn, F., Wang, T.
Formation of Au nanocrystals in TiO_2, $SrTiO_3$ *and MgO by ion implantation*
10th Int. Symp. on Advanced Physical Fields (APF-10) "Nano-Fabrication and Nano-Characterization of Nanomaterials", Tsukuba, Japan, March 7 – 10, 2005

Gago, R., Vazquez, L., Grambole, D., Herrmann, F., Grötzschel, R., Vela, M., Amalvy, J.I., Munoz-Martin, A., Climent-Font, A.
In-depth distribution of silica nanoparticles in free-standing silica/vinyl polymer nanocomposite films
17th Int. Conf. on Ion Beam Analysis, Seville, Spain, June 26 – July 1, 2005

Gebel, T., Rebohle, L., Trautmann, T., Yankov, R.A., Skorupa, W., Gauglitz, G., Frank, R.
Miniaturised arrays of light-sources based on silicon technology: a promising approach for novel sensors and lab-on-a-chip systems
12th Int. Conf. Sensor & Test 2005, Nürnberg, Germany, May 10 – 12, 2005

Geßner, H., Posselt, M.
Atomistic study of intrinsic defects in germanium
E-MRS Spring Meeting, Strasbourg, France, May 31 – June 3, 2005

Geßner, H., Posselt, M.
Structure, energetics and migration of V and I in Ge: an atomistic study
2nd CADRES Germanium Workshop, Brussels, Belgium, Dec 1, 2005

Gomez, S., Harangus, L., Preoteasa, E.A., Iordan, A., Grambole, D., Herrmann, F., Grötzschel, R.
Micro-PIXE and histochemical studies of Zn and Ca distribution in normal bone
17th Int. Conf. on Ion Beam Analysis, Seville, Spain, June 26 – July 1, 2005

Grenzer, J., Bischoff, L., Pietsch, U.
Grazing-incidence diffraction strain analysis of a laterally patterned Si wafer treated by focused Ge and Au ion beam implantation
DPG-Frühjahrstagung, Berlin, Germany, March 4 – 9, 2005

Grenzer, J., Bischoff, L., Pietsch, U.
X-ray investigation of focused ion-beam induced semiconductor surfaces - How to make a lateral

nanostructure
348. Heraeus-Seminar “Ions at Surfaces: Patterns and Processes”, Bad Honnef, Germany, June 19 – 23, 2005

Grigorian, S., Pietsch, U., Grenzer J.
Amorphous-crystalline ripple formation in ion beam induced Si wafers
348. Heraeus-Seminar “Ions at Surfaces: Patterns and Processes”, Bad Honnef, Germany, June 19 – 23, 2005

Grötzschel, R.
High resolution analysis of ultra thin layers using light MeV ions with a magnetic spectrometer
Int. Workshop on High Resolution Depth Profiling, Bar Harbor, USA, May 23 – 26, 2005

Grynszpan, R.I., Saude, S., Thome, T., Baclet, N., Darque, A., Jolly, L., Flament, J.L., Zielinski, F., Anwand, W., Brauer, G.
Positron and deuteron depth profiling in He-implanted electrum-like alloy
10th Int. Workshop on Slow Positron Beam Techniques for Solids and Surfaces (SLOPOS-10), Doha, Qatar, March 19 – 25, 2005

Grynszpan, R.I., Saude, S., Mazerolles, L., Anwand, W., Brauer, G.
Positron depth profiling in ion-implanted zirconia stabilized with trivalent cations
8th Int. Workshop on Positron and Positronium Chemistry, Coimbra, Portugal, Sept 4 – 9, 2005

Harangus, L., Iordan, A., Preoteasa, E.A., Grambole, D., Herrmann, F., Gomez, S., Mihul, A., lonescu-Tirgoviste, C., Gutu, D.
Proton microprobe analysis of normal and osteoporosis-affected compact bone. 1. Calcium and other divalent metals
17th Int. Conf. on Ion Beam Analysis, Seville, Spain, June 26 – July 1, 2005

Harangus, L., Iordan, A., Preoteasa, E. A., Preoteasa, E., Grambole, D., Herrmann, F., Grötzschel, R.
Potential of proton microbeam in the study of dental composites. 2. Compositional heterogeneity by micro-PIXE and complementary analysis by micro-PIGE and micro-PBS
17th Int. Conf. on Ion Beam Analysis, Seville, Spain, June 26 – July 1, 2005

Heinig, K.-H.
Mechanisms of ion beam shaping of metal nanoparticles
MRS Fall Meeting, Boston, USA, MA, 27 – Dec 1, 2005

Heinig, K.-H., Bernas, H.
Ion-irradiation-induced chemical ordering of intermetallic alloys: predictions based on atomistic simulations
DPG-Frühjahrstagung, Berlin, Germany, March 4 – 9, 2005

Heinig, K.-H., Röntzsch, L.
Theoretical study on reaction paths of formation and decay of 1D nanostructures
DPG-Frühjahrstagung, Berlin, Germany, March 4 – 9, 2005

Iordan, A., Harangus, L., Preoteasa, E. A., Grambole, D., Neelmeijer, C., Herrmann, F., Grötzschel, R., Mihul, A., Noveanu, D., Batrina, D.
Proton microprobe for analysis of normal and osteoporosis-affected compact bone. 2. Low-Z elements
17th Int. Conf. on Ion Beam Analysis, Seville, Spain, June 26 – July 1, 2005

Kögler, R.
Ion implantation in silicon: limits of the +1 model
43. Arbeitstreffen “Punktdefekte” TU Dresden, Germany, March 2 – 3, 2005

Kögler, R., Mücklich, A., Reuther, H., Krecar, D., Hutter, H., Skorupa, W.
Defect engineering for ion beam synthesis of SOI structures
E-MRS Spring Meeting, Strasbourg, May 31 – June 3, 2005

Kögler, R., Mücklich, A., Reuther, H., Krecar, D., Hutter, H., Skorupa, W.
Defect engineering in ion beam synthesis of SiC and SiO_2 in Si
11th Conf. on Gettering and Defect Engineering in Semiconductor Technology (GADEST 2005), Giens, France, Sept 25 – 30, 2005

Kögler, R.
Excess vacancies in SiGe
2nd CADRES Germanium Workshop, Brussels, Belgium, Dec 1 – 2, 2005

Kolitsch, A.
Synthesis of FL-CNx films by ion beam sputtering
FULLMAT Meeting, University of Sussex, UK, Aug 31 – Sept 2, 2005

Kost, D., Facsko, S., Keller, A., Grötzschel, R., Möller, W.
Potential energy retention of slow highly charged Ar-Ions into solid surfaces - a calorimetric measurement
25th Brandt-Richie Workshop on Particle Penetration Phenomena and Excitations of Solids: Electronic Interactions at Surfaces, University of Florida, Gainesville, USA, April 10 – 13, 2005

Krause-Rehberg, R., Brauer, G.
Die intensive Positronenquelle EPOS an der Strahlungsquelle ELBE im FZ Rossendorf
Arbeitstreffen „Komitee für Forschung mit Sonden und Ionen (KFSI)“, Neubiberg, Germany, Oct 6 – 7, 2005

Krause-Rehberg, R., Brauer, G., Sachert, S., Krille, A., Bondarenko, V.
The intense positron source EPOS at Research Center Rossendorf
Scientific Workshop “The application of high intensity positron beam techniques and digital lifetime positron spectroscopy in materials science”, Bergen, Netherlands, Nov 17 – 18, 2005

Krille, A., Krause-Rehberg, R., Becvar, F., Brauer, G.
The (upcoming) digital real-time positron lifetime measurement of EPOS
Scientific Workshop “The application of high intensity positron beam techniques and digital lifetime positron spectroscopy in materials science”, Bergen, Netherlands, Nov 17 – 18, 2005

Kuepper, K., Fassbender, J., Bischoff, L., Mattheis, R., Fischer, P.
Magnetic domains and magnetization reversal of ion-induced magnetically patterned RKKY-coupled Ni81Fe19/Ru/Co90Fe10 films
ALS Users' Meeting 2005, Advanced Light Souce, Lawrence Berkeley Lab, Berkeley, USA, Oct 20 – 22, 2005

Kuriplach, J., Melikhova, O., Brauer, G.
Basic positron properties of oxides: a computational study
8th Int. Workshop on Positron and Positronium Chemistry, Coimbra, Portugal, Sept 4 – 9, 2005

Kuriplach, J., Melikhova, O., Anwand, W., Brauer, G.
Positron annihilation at SiO_2/Si interface
8th Int. Workshop on Positron and Positronium Chemistry, Coimbra, Portugal, Sept 4 – 9, 2005

Lehnert, U., Michel, P., Teichert, J., Seidel, W., Stehr, D., Wohlfarth, D., Wünsch, R.
Optical beam properties and performance of the MID-IR FEL at ELBE
27th Int. Free Electron Laser Conference, Stanford University, Arrillaga Alumni Center, Stanford,

USA, Aug 21 – 26, 2005

Liedke, M.O., Potzger, K., Bischoff, L., Bothmer, A.H., Hillebrands, B., Rickart, M., Freitas, P.P., Fassbender, J.
Domain structure during magnetization reversal of PtMn/CoFe exchange bias micro-pattered lines
50th Conf. on Magnetism and Magnetic Materials, San Jose, CA, USA, Oct 30 – Nov 3, 2005

Liedke, M.O., Potzger, K., Hillebrands, B., McCord, J., Rickart, M., Freitas, P., Fassbender, J.
Magnetic domain structure of micro-patterned PtMn/CoFe exchange bias bilayers
The European Conference on Physics of Magnetism, Poznan, Poland, June 24 – 27, 2005

Liedke, M.O., Potzger, K., Hillebrands, B., Rickart, M., Freitas, P., Fassbender, J.
Magnetic domain structure of micro-patterned PtMn/CoFe exchange bias bilayers
DPG-Frühjahrstagung, Berlin, Germany, March 4 – 9, 2005

Manova, D., Hirsch, D., Richter, E., Mändl, S., Neumann, H., Rauschenbach, B.
Microstructure of nitrogen implanted stainless steelafter wear experiments
14th Int. Conf. Surface Modification of Materials by Ion Beams, Kusadasi,Turkey, Sept 5 – 9, 2005

Martins, R.M.S., Schell, N., Beckers, M., Silva, R.J.C., Braz Fernandes, F.M.
Structural in-situ investigations of Shape Memory Alloy (SMA) Ni-Ti thin films
ESRF User's Meeting 2005, Grenoble, France, Feb 8 – 9, 2005

Martins, R.M.S., Braz Fernandes, F.M., Silva, R.J.C., Beckers, M., Schell, N.
In-situ observation of Ni-Ti thin film growth by synchrotron radiation scattering
III. Int. Materials Symposium (MATERIAIS 2005), Aveiro, Portugal, March 20 – 23, 2005

Martins, R.M.S., Beckers, M., Mücklich, A., Schell, N., Silva, R.J.C., Braz Fernandes, F.M.
Characterization of magnetron Sputtered Ni-Ti thin films by in-situ x-ray diffraction and complementary ex-situ techniques
EUROMAT 2005, Prague, Czech Republic, Sept 5 – 8, 2005

Martins, R.M.S., Beckers, M., Mücklich, A., Schell, N., Silva, R.J.C., Braz Fernandes, F.M.
Comparing the growth of magnetron sputter deposited Ti-Al-N and Ni-Ti thin layers by in-situ x-ray diffraction
EUROMAT 2005, Prague, Czech Republic, Sept 5 – 8, 2005

Martins, R.M.S., Beckers, M., Mücklich, A., Schell, N., Silva, R.J.C., Mahesh, K.K., Braz Fernandes, F.M.
HR-TEM observation of the interfacial diffusion zone in magnetron sputtered Ni-Ti thin films deposited on different Si substrates
40th Meeting of the Portuguese Society for Microscopy and Cell Biology, Lisbon, Portugal, Dec 8 – 10, 2005

McCord, J., Fassbender, J., Frommberger, M., Liedke, M.O., Quandt, E., Schultz, L.
Anisotropy patterning of amorphous CoFeSiB films by Heion irradiation
DPG-Frühjahrstagung, Berlin, Germany, March 4 – 9, 2005

McCord, J., Fassbender, J., Frommberger, M., Liedke, M.O., Quandt, E., Schultz, L.
Magnetic anisotropy and domain pattering of amorphous films by He-ion irradiation
Workshop "Ionenstrahlphysik und -technologie", IOM Leipzig, Germany, April 11 – 12, 2005

McCord, J., Fassbender, J., Frommberger, M., Liedke, M.O., Quandt, E., Schultz, L.
Magnetic anisotropy and domain patterning by means of ion irradiation
348. Heraeus-Seminar "Ions at Surfaces: Patterns and Processes", Bad Honnef, Germany,

June 19 – 23, 2005

Mücklich, A., Kögler, R., Eichhorn, F.
TEM-investigation of Si(001) modified by Pr implantation
Microscopy Conf., Davos, Switzerland, Aug 28 – Sept 2, 2005

Müller, T., Heinig, K.-H., Röntzsch, L., Schmidt, B., Stegemann, K.-H., Votintseva, E.
Fabrication of semiconductor nanocrystals for non-volatile memories using ion beams
1st Int. Workshop on Semiconductor Nanocrystals (SEMINANO), Budapest, Hungary,
Sept 10 – 12, 2005

Nazarov, A.N., Vovk, J.N., Osiyuk, I.N., Tkachenko, A.S., Tyagulskii, I.P., Lysenko, V.S., Skorupa, W., Yankov, R.A.
The effect of plasma treatment on the properties of Ge-implanted MOS structures
E-MRS Spring Meeting, Strasbourg, France, May 31 – June 3, 2005

Nembach, H., Martin-Pimentell, P., Weber, M., Fassbender, J., Hillebrands, B.
Damping in thin ferromagnetic films
DPG Frühjahrstagung, Berlin, Germany, March 4 – 9, 2005

Oates, T.W.H., Ryves, L., Mücklich, A., Bilek, M.M.M., McKenzie, D.R.
Ultrathin metal film physical properties determined by in-situ spectroscopic ellipsometry
DPG-Frühjahrstagung, Berlin, Germany, March 4 – 9, 2005

Oates, T.W.H., Mücklich, A., Ryves, L., Bilek, M.M.M., McKenzie, D.R., McCulloch, D.G., Burgmann, F.A.
In-situ spectroscopic ellipsometric determination of morphological and electronic properties of plasma deposited ultra-thin metal films
Int. Conf. on Metallurgical Coatings and Thin Films, San Diego, CA, USA, May 2005

Oates, T.W.H., Mücklich, A.
Optical properties of silver nanoparticles on polymer film
2nd Int. Workshop on Polymer/Metal nanocomposites, GKSS Geesthacht, Germany, Sept 11, 2005

Oates, T.W.H.
Analysing the growth of metal nanoparticles by in-situ ellipsometry
J.A. Woollam Spectroscopic Ellipsometry Application Seminar, Darmstadt, Germany,
Oct 11 – 12, 2005

Pecz, B., Barna, Á., Heera, V., W. Skorupa
Magic matching in semiconductor heterojunctions
14th Int. Conf. on Microscopy of Semiconducting Materials (MSMXIV), Oxford, UK,
April 11 – 14, 2005

Pereira, L., Águas, H., Beckers, M., Martins, R.M.S., Fortunato, E., Martins, R.
Spectroscopic ellipsometry study of the role of the annealing time on nickel induced crystallization of a-Si
21th Int. Conf. on Amorphous and Nanocrystalline Semiconductors (ICANS 21), Lisbon, Portugal,
Sept 4 – 9, 2005

Pereira, L., Beckers, M., Martins, R.M.S., Fortunato, E., Martins, R.
Optimization of the metal/silicon ratio on nickel assisted crystallization of amorphous silicon
MRS Spring Meeting, San Francisco, USA, April 28 – May 1, 2005

Pietsch, U., Grenzer, J., Hazra, S., Chini, T.K., Sanyal, M.K.

Ripple structure of ion beam induced Si wafers
20th Congress of the International Union of Crystallography (IUCr 2005), Florence, Italy, Aug 23 – 31, 2005

Posselt, M.
Atomistic simulation of defects in Si: migration of di- and tri-interstitials
43. Arbeitskreis Punktdefekte, Dresden, Germany, March 2 – 3, 2005

Posselt, M.
Formation of highly mobile di-interstitials during ion implantation
E-MRS Spring Meeting, Strasbourg, France, May 31 – June 3, 2005

Posselt, M., Gao, F.
A modified concerted exchange mechanism for antisite pair recombination in cubic and hexagonal silicon carbide
11th Int. Autumn Meeting on Gettering and Defect Engineering in Semiconductor Technology (GADEST), Giens, France, Sept 25 – 30, 2005

Posselt, M., Gao, F.
Atomistic study of the mobility of small interstitial clusters in silicon
11th Int. Autumn Meeting on Gettering and Defect Engineering in Semiconductor Technology (GADEST), Giens, France, Sept 25 – 30, 2005

Potfajova, J., Sun, J.M., Dekorsy, T., Skorupa, W., Schmidt, B., Wiemer, M., Helm, M.
Silicon microcavity light emitting diodes with buried cobalt silicide metallic mirrors
E-MRS Spring Meeting, Strasbourg, France, May 31 – June 3, 2005

Potzger, K., Bischoff, L., Liedke, M.O., Hillebrands, B., Rickart, M., Freitas, P. P., McCord, J., Fassbender, J.
Magnetic domain structure of micro-patterned PtMn/NiFe exchange bias bilayers
DPG-Frühjahrstagung, Berlin, Germany, March 4 – 9, 2005

Potzger, K., Bischoff, L., Liedke, M.O., Hillebrands, B., Rickart, M., Freitas, P. P., McCord, J., Fassbender, J.
Domain structure of magnetically micro-patterned PtMn/NiFe exchange bias bilayers
50th Conf. on Magnetism and Magnetic Materials, San Jose, CA, USA, Oct 30 – Nov 3, 2005

Potzger, K., Bischoff, L., Liedke, M.O., Hillebrands, B., Rickart, M., Freitas, P., McCord, J., Fassbender, J.
Magnetic domain structure of micro-patterned PtMn/NiFe exchange bias bilayers
Intermag 2005, Nagoya, Japan, April 4 – 8, 2005

Potzger, K., Reuther, H., Zhou, S., Mücklich, A., Grötzschel, R., Eichhorn, F., Liedke, M.O., Fassbender, J.
Ion beam synthesis of Fe nanoparticles in MgO and Y:ZrO_2
50th Magnetism and Magnetic Materials Conference, San Jose, CA, USA, Oct 30 – Nov 3, 2005

Potzger, K., Zhou, S., Reuther, H., Brauer, G., Anwand, W., Eichhorn, F., Bischoff, L., Herrmann, F., Grambole, D., Grötzschel, R., Fassbender, J.
Effects of implantation of magnetic ions into ZnO
Int. Topical Workshop on Heteroepitaxy of 3C-SiC on Silicon and its Application to Sensor Devices (HeT-SiC-05), Hotel Erbgericht Krippen, Germany, April 26 – May 1, 2005

Potzger, K., Zhou, S., Reuther, H., Mücklich, F., Talut, G., Fassbender, J., Herrmannsdörfer, T., Bianchi, A.

Doping ZnO with Fe far from thermal equilibrium
50th Magnetism and Magnetic Materials Conference, San Jose, CA, USA, Oct 30 – Nov 3, 2005

Preoteasa, E.A., Preoteasa, E., Harangus, L., Iordan, A., Grambole, D., Herrmann, F., Neelmeijer, C.
Potential of proton microbeam in the study of dental composites. 1. Micro-PIXE mapping of Ca, Zr, Ba and Yb
17th Int. Conf. on Ion Beam Analysis, Seville, Spain, June 26 – July 1, 2005

Prucnal, S., Sun, J.M., Cheng, X.Q., Skorupa, W.
Charge trapping in SiO_2 layers implanted with rare earths and Ge ions
DPG-Frühjahrstagung, Berlin, Germany, March 4 – 9, 2005

Prucnal, S., Sun, J.M., Skorupa, W., Nazarov, A.N., Osiyuk, I.N., Tyagulski, I.P., Lysenko, V.S.
Charge trapping in SiO_2 layers implanted with rare earth and Ge ions
E-MRS Spring Meeting, Strasbourg, France, May 31 – June 3, 2005

Rellinghaus, B., Dmitrieva, O., Liedke, M.O., Fassbender, J.
Structural phase transformation of FePt nanoparticles by ion irradiation
Intermag 2005, Nagoya, Japan, April 4 – 8, 2005

Rellinghaus, B., Dmitrieva, O., Liedke, M.O., Schultz, L., Fassbender, J.
Ionenstrahlinduzierte Strukturänderungen in FePt Nanopartikeln
DPG-Frühjahrstagung, Berlin, Germany, March 4 – 9, 2005

Renger, J., Seidel, J., Olk, P., Grafström, S., Eng, L., Schmidt, B., Bischoff, L., Akhmadaliev, C.
Excitation and propagation of surface plasmon polaritons at grooves and gratings
Int. Conf. Surface Plasmon Photonics 2, SSP2, Graz, Austria, May 21 – 26, 2005

Reuther, H., Potzger, K., Zhou, S., Mücklich, A., Eichhorn, F.
Investigation of the creation of Fe nanoparticles in MgO by ion beam synthesis
Int. Conf. on the Applications of the Mössbauer Effect, Universität Montpellier, Montpellier, France, Sept 5 – 9, 2005

Reuther, H., Ulrich, K.-U.
Quantification of iron minerals formed during aging of iron-containing colloids
Int. Conf. on the Applications of the Mössbauer Effect, Universität Montpellier, Montpellier, France, Sept 5 – 9, 2005

Reviere, J.P., Templier, C., Declermy, A., Redjal, O., Chumlyakov, Y., Abrasonis, G.
Microstructure of expanded austenite in ion-nitrided AISI 316L single crystals
14th Int. Conf. Surface Modification of Materials by Ion Beams, Kusadasi, Turkey, Sept 5 – 9, 2005

Richter, E., Yankov, R.A., Möller, W., Donchev, A., Schütze, M.
Halogen PIII for high-temperature oxidation protection of γ-TiAl
8th Int. Workshop on Plasma-Based Ion Implantation and Deposition, Chengdu, China, Sept 20 – 25, 2005

Rogozin, A., Shevchenko, N., Vinnichenko, M., Seidel, M., Kolitsch, A., Möller, W.
Annealing of the indium tin oxide films with an electrical current
13th Int. Congress on Thin Films / 8th Int. Conf. on Atomically Controlled Surfaces, Interfaces and Nanostructures, Stockholm, Sweden, June 19 – 23, 2005

Röntzsch, L., Heinig, K.-H.
Predictive atomistic computer simulations on synthesis and stability of $CoSi_2$ nanowires
348. Heraeus-Seminar “Ions at Surfaces: Patterns and Processes”, Bad Honnef, Germany,

June 19 – 23, 2005

Röntzsch, L., Heinig, K.-H., Schmidt, B.
Ion irradiation through SiO_2*-Si interfaces: TEM study of self-organized Si nanocrystals applicable in nonvolatile memories*
DPG-Frühjahrstagung, Berlin, Germany, March 4 – 9, 2005

Röntzsch, L., Heinig, K.-H.
Atomistic computer simulations on ion beam synthesis and decay of single-crystalline nanowires
DPG-Frühjahrstagung, Berlin, Germany, March 4 – 9, 2005

Röntzsch, L., Heinig, K.-H.
Atomistic computer simulations on synthesis and stability of single-crystalline nanowires
Treffen DFG-Schwerpunkt Nanodrähte und Nanoröhren, Fulda, Germany, May 2 – 4, 2005

Röntzsch, L., Heinig, K.-H.
Ion beam synthesis of $CoSi_2$ *nanowires in Si and their stability - predictions of atomistic computer simulations*
E-MRS Spring Meeting, Strasbourg, France, May 31 – June 3, 2005

Röntzsch, L., Heinig, K.-H.
Ion beam synthesis of single-crystalline nanowires and their stability – predictions of atomistic computer simulations
25th GIF Conference, Dresden, Germany, June 20 – 23, 2005

Röntzsch, L., Heinig, K.-H.
Predictions on ion-assisted synthesis of functional 1D-nanostructures using atomistic computer simulations
14th Int. Summer School on Vacuum, Electron and Ion Technologies, Sunny Beach, Bulgaria, Sept 12 – 16, 2005

Röntzsch, L., Heinig, K.-H.
Reaction pathways of ion beam synthesis and stability of monocrystalline nanowires
1st Int. Workshop on Semiconductor Nanocrystals (SEMINANO), Budapest, Hungary, Sept 10 – 12, 2005

Rossi, J.O., Ueda, M., Reuther, H.
Plasma immersion íon implantation with high-energy íons for use in surface treatments
8th Brazilian Meeting of Plasma Physics, Niteroi, Rio de Janeiro, Brazil, Nov 27 – 30, 2005

Rossi, J.O., Ueda, M., Silva, G., Reuther, H.
A solid-state compact pulser of 5 kV / 2 A / 5 kHz for surface treatment by plasma immersion ion implantation
8th Brazilian Meeting of Plasma Physics, Niteroi, Rio de Janeiro, Brazil, Nov 27 – 30, 2005

Schell, N., Beckers, M., Martins, R.M.S., Mücklich, A, Möller, W.
Observation of the growth and microstructural development of MAX Phase Ti_2AlN *thin films during magnetron sputtering using synchrotron radiation*
AVS 52nd Int. Symposium & Exhibition, Boston, USA, Oct 30 – Nov 4, 2005

Schmidt, B., Heinig, K-.H., Röntzsch, L., Mücklich, A., Stegemann, K.-H., Votintseva, E., Klimenkov, M.
Fabrication of Si nanocrystals for memory application by ion irradiation through SiO_2*/Si-interfaces*
DPG-Frühjahrstagung, Berlin, Germany, March 4 – 9, 2005

Schreiner, M., Mäder, M., Bidaud, E., Zich, W., Uhlir, K., Grambole, D., Herrmann, F., Alram, M.
The Becin hoard – Analysis of the ancient silver coins
17th Int. Conf. on Ion Beam Analysis, Seville, Spain, June 26 – July 1, 2005

Schütze, M., Donchev, A., Yankov, A., Richter, E.
Improvement of high temperature oxidation resistance of TiAl
14th Int. Conf. Surface Modification of Materials by Ion Beams, Kusadasi, Turkey, Sept 5 – 9, 2005

Semtsiv, M.P., Masselink, W.T., Georgiev, N., Dekorsy, T., Helm, M.
Intersubband absorption in GaP-AlP multiple quantum wells
8th Int. Conf. on Intersubband Transitions in Quantum Wells (ITQW 2005), Cape Cod, USA,
Sept 11 – 16, 2005

Semtsiv, M. P., Masselink, W.T., Georgiev, N., Dekorsy, T., Helm, M.
Intersubband transitions in GaP-AlP heterostructures for infrared applications
12th Int. Conf. on Narrow Gap Semiconductors (NGS-12), Toulouse, France, July 3 – 7, 2005

Shevchenko, N., Mücklich, A., Richter, E., Maitz, M.F.
Porous surface of NiTi alloy produced by plasma ion implantation
E-MRS Spring Meeting, Strasbourg, France, May 31 – June 3, 2005

Shevchenko, N., Rogozin, A., Vinnichenko, M., Cantelli, V., Kolitsch, A., Möller, W.
Real-time investigations of ITO film structure evolution during annealing
13th Int. Congress on Thin Films / 8th International Conference on Atomically Controlled Surfaces,
Interfaces and Nanostructures, Stockholm, Sweden, June 19 – 23, 2005

Shevchenko, N., Richter, E., Pham, M.T., Maitz, M.F.
Structure and properties of oxygen implanted NiTi surfaces
13th Int. Congress on Thin Films / 8th International Conference on Atomically Controlled Surfaces,
Interfaces and Nanostructures, Stockholm, Sweden, June 19 – 23, 2005

Shevchenko, N., Richter, E., Maitz, M.F., Möller, W.
Oxygen implanted NiTi surfaces for biomedical application
8th Int. Workshop on Plasma Based Ion Implantation and Deposition, Chengdu, China,
Sept 18 – 22, 2005

Skorupa, W., Sun, J.M., Dekorsy, T., Helm, M., Rebohle, L., Gebel, T., Nazarov, A.N., Tjagulski, I.P.,
Osiyuk, I.N., Prucnal, S., Zuk, J.
Silicon-based light emission from rare earth ion-implanted silicon dioxide
E-MRS Spring Meeting, Strasbourg, France, May 31 – June 3, 2005

Skorupa, W., Panknin, D., Voelskow, M., Smith, M., McMahon, R.A.
Rapid thermal processing using flash lamps for the crystallisation of amorphous silicon layers
21st Int. Conf. on Amorphous and Nanocrystalline Semiconductors (ICANS21), Lisbon, Portugal,
Sept 3 – 9, 2005

Skorupa, W., Sun, J.M., Prucnal, S., Rebohle, L., Gebel, T., Nazarov, A.N., Osiyuk, I.N., Helm, M.
Rare earth ion implantation for silicon based light emission
11th Conf. on Gettering and Defect Engineering in Semiconductor Technology (GADEST 2005),
Giens, France, Sept 25 – 30, 2005

Silva, M.M., Ueda, M., Lepienski, C.M., Soares Jr., P.C., Gonçalves, J.A.N., Reuther, H.
Nitrogen plasma immersion ion implantation in Ti6Al4V with treatment temperatures ranging from 400 to 800°C
5th Asian-European Int. Conf. on Plasma Surface Engineering, Qingdao City, China,

Sept 12 – 16, 2005

Silva, M.M., Ueda, M., Otani, C., Reuther, H., Lepienski, C.M., Soares Jr., P.C.
Surface modification of Ti6Al4V alloy by duplex plasma processing
18th Int. Congress of Mechanical Engineering, Cobem 2005, Ouro Preto, Minas Gerais, Brazil, Nov 6 – 11, 2005

Smith, M., McMahon, R.A., Voelskow, M., Skorupa, W.
Modelling of flash lamp processing of SiC-on-silicon heterostructures
Int. Topical Workshop on Heteroepitaxy of 3C-SiC on Silicon and its Application to Sensor Devices (HeT-SiC-05,), Hotel Erbgericht Krippen, Germany, April 26 – May 1, 2005

Solina, D., Lott, D., Kaltofen, R., Schumann, J., Fassbender, J., Tietze, U., Schreyer, A.
X-ray and Neutron Scattering studies of NiMn-CoFe exchange bias systems
DPG Frühjahrstagung, Berlin, Germany, March 4 – 9, 2005

Stehr, D., Metzner, C., Helm, M., Roch, T., Strasser, G.
Impurity states in quantum wells and superlattices and their influence in the intersubband absorption spectra
8th Int. Conf. on Intersubband Transitions in Quantum Wells (ITQW 2005), Cape Cod, MA, USA, Sept 11 – 16, 2005

Sun, J.M., Skorupa, W., Dekorsy, T., Helm, M., Rebohle, L., Gebel, T.
Modulation of the 1535 nm photoluminescence from Er-doped Si-rich silicon dioxide by field-induced quenching
E-MRS Spring Meeting, Strasbourg, France, May 31 – June 3, 2005

Sun, J.M., Skorupa, W., Dekorsy, T., Helm, M., Rebohle, L., Gebel, T.
Efficent electroluminescence from Tb-implanted silicon metal-oxide-semiconductor devices
E-MRS Spring Meeting, Strasbourg, France, May 31 – June 3, 2005

Sun, J.M., Skorupa, W., Dekorsy, T., Helm, M.
Efficient electroluminescence from rare-earth implanted SiO_2 metal-oxide-semiconductor structures
2nd Int. Conf. on Group IV Photonics, Antwerp, Belgium, Sep 21, 2005

Tan, I.H., Ueda, M., Dallaqua, R.S., Abramof, E., Reuther, H.
Effects of low magnetic fields on nitrogen implantation in silicon by plasma immersion
8th Brazilian Meeting of Plasma Physics, Niteroi, Rio de Janeiro, Brazil, Nov 27 – 30, 2005

Tsvetkova, T., Takahashi, S., Zayats, A., Dawson, P., Turner, R., Bischoff, L., Angelov, O., Dimova-Malinovska, D.
Nano-scale optical pattering in amorphous silicon carbide
Opto Ireland, SPIE Europe, Dublin, Ireland, April 4 – 6, 2005

Tsyganov, I., Richter, E.
Phase formation, corrosion behaviour and mechanical properties of boron implanted near-alpha titanium alloy
14th Int. Conf. Surface Modification of Materials by Ion Beams, Kusadasi, Turkey, Sept 5 – 9, 2005

Turos, A., Abdul-Kader, A. M., Grambole, D., Jagielski, J., Piątkowska, A.
The effects of ion bombardments of polymers: hydrogen release and oxidation
17th Int. Conf. on Ion Beam Analysis, Seville, Spain, June 26 – July 1, 2005

Ueda, M., Silva, M.M., Lepienski, C.M., Soares Jr., P.C., Gonçalves, J.A., Reuther, H.
High temperature plasma immersion ion implantation of Ti6Al4V

8th Int. Workshop on Plasma-Based Ion Implantation and Deposition, SouthWest Jiaotong University, Chengdu, China, Sept 18 – 22, 2005

Vinnichenko, M., Poperenko, L., Lebyedyeva, T., Shpylovyy, P., Shevchenko, N., Rogozin, A., Sudovtsova, V., Kolitsch, A., Möller, W.
Control of properties and structure of ZnO thin films by a wide variation of oxygenpressure during reactive magnetron deposition and by post-deposition annealing
EMRS Spring Meeting, Strasbourg, France, May 31 – June 3, 2005

Vinnichenko, M., Rogozin, A., Shevchenko, N., Kolitsch, A., Kreißig, U., Möller, W.
Spectroscopic ellipsometry monitoring of ITO thin film properties evolution during amorphous-to-crystalline transition
Int. Conf. on Metallurgical Coatings and Thin Films, San Diego, CA, USA, May 2 – 6, 2005

Vinnichenko, M., Rogozin, A., Shevchenko, N., Kolitsch, A., Möller, W.
Spectroscopic ellipsometry of tin-doped indium oxide at elevated temperatures: properties evolution during film growth and annealing
J.A. Woollam Spectroscopic Ellipsometry Application Seminar, Darmstadt, Germany, Oct 11 – 12, 2005

Voelskow, M., Mücklich, A., Stoemenos, J., Skorupa, W.
Two recipes to stabilize the surface melting in FLASiC structures
Int. Topical Workshop on Heteroepitaxy of 3C-SiC on Silicon and its Application to Sensor Devices (HeT-SiC-05,), Hotel Erbgericht Krippen, Germany, April 26 – May 1, 2005

Vredenberg, A., Polman, A., Kooi, B.J., Van Dillen, T., Heinig, K.-H., Toulemonde, M.
Ion beam shaping of nanometals
6th Int. Symp. on Swift Heavy Ions in Matter, Aschaffenburg, Germany, May 28 – 31, 2005

Weber, M.C., Nembach, H., Carey, Matt J., Hillebrands, B., Fassbender, J.
Real time evidence of two-magnon scattering in exchange coupled bilayers
50th Magnetism and Magnetic Materials Conference, San Jose, CA, USA, Oct 30 – Nov 3, 2005

Weber, M., Nembach, H., Hillebrands, B., Fassbender, J.
Small and large angle precession in exchange biased bilayers
DPG-Frühjahrstagung, Berlin, Germany, March 4 – 9, 2005

Weber, M., Nembach, H., Hillebrands, B., Fassbender, J.
Small and large angle precession in exchange biased bilayers
Intermag 2005, Nagoya, Japan, April 4 – 8, 2005

Weber, M., Nembach, H., Schultheiss, H., Bayer, C., Blomeier, S., Kaltofen, R., Schumann, J., Carey, M., Hillebrands, B., Fassbender, J.
All-optical probe of magnetization dynamics in exchange bias systems
DPG-Frühjahrstagung, Berlin, Germany, March 4 – 9, 2005

Wierzchowski, W., Wieteska, K., Graeff, W., Gawlik, G., Turos, A., Maurin, J., Mücklich, A.
Strain profiles in the insulated buried layers obtained by He implantation in AlGaAs
20th Congress of the International Union of Crystallography, IUCr 2005, Florence, Italy, Aug 23 – 31, 2005

Wierzchowski, W., Wieteska, K., Graeff, W., Gawlik, G., Turos, A., Mücklich, A.
Investigation of insulated buried layers obtained by ion implantation in AlGaAs with various Al concentration
E-MRS Fall Meeting, Warsaw, Poland, Sept 5 – 9, 2005

Winnerl, S., Dreyhaupt, A., Krenz, M., Stehr, D., Dekorsy, T., Helm, M.
High-intensity THz radiation pulses from a scalable photoconductive device
DPG Frühjahrstagung, Berlin, Germany, March 4 – 9, 2005

Winnerl, S., Krenz, M., Dreyhaupt, A., Stehr, D., Dekorsy, T., Helm, M.
High-intensity THz radiation pulses from a scalable large-aperture emitter
Conf. on Lasers and Opto-Electronics/Quantum Electronics and Laser Science Conference (CLEO/QELS), Baltimore, USA, May 22 – 27, 2005

Winnerl, S., Dreyhaupt, A., Peter, F., Stehr, D., Helm, M., Dekorsy, T.
High-intensity THz radiation from a large-aperture photoconductive emitter
14th Int. Conf. on Nonequilibrium Carrier Dynamics in Semiconductors (HCIS-14), Chicago, USA, July 24 – 29, 2005

Yankov, R.A., Richter, E., Donchev, A. Schütze, M.
Efficient oxidation protection of γ-TiA.l alloys by ion implantation of halogens
Int. Conf. on Novel Applications for Surface Modification, Chester, UK,
Sept 18 – 21, 2005

Zen, A., Saphiannikova, M., Neher, D., Grenzer, J., Pietsch, U, Asawapirom, U., Scherf, U.
Molecular structure and electronic properties of poly(3-hexylthiophene)
DPG Frühjahrstagung, Berlin, Germany, March 4 – 9, 2005

Lectures

Abrasonis, G.
Synthesis of CN_x *films by ion beam sputtering: the influence of the sputtering beam composition and substrate temperature*
RWTH Aachen, Germany, May 31, 2005

Bischoff, L.
The application of FIB from mass separated alloy LMIS
NanoFIB Meeting, University of Oxford, UK, April 15, 2005

Bischoff, L.
Nanofabrication with a mass-separated FIB
FAHL Academica, University Leipzig, Wörlitz , Sept 26 – 27, 2005

Brauer, G., Anwand, W., Coleman, P.G., Skorupa, W.
The positron as an antiparticle – from a poetic to a physical view
University of Qatar, Physics Dept., Doha, Qatar, March 29, 2005

Fassbender, J.
Magnetization dynamics
Evaluierung von Beschichtungs- und Oxidationsverfahren für Tunnel-Schichtsysteme, Singulus Technologies AG, Kahl, Germany, April 19, 2005

Fassbender, J.
The potential of ion irradiation for the creation of artificial magnetic structures
Argonne National Laboratories, Argonne, USA, June 1, 2005

Fassbender, J.
Tuning magnetic properties locally by ion irradiation and implantation
Center for X-ray Optics, Lawrence Berkeley National Laboratory, Berkeley, USA, May 26, 2005

Fassbender, J.
Ion induced modifications of magnetic thin films and multilayers
Universität Konstanz, Germany, Dec 2, 2005

Grenzer, J.
Depth resolved strain analysis of lateral nanostructures by x-ray grazing incidence diffraction
Warsaw University, Faculty of Physics, Warszawa, Poland, May 11, 2005

Grötzschel, R.
Ionenstrahlanalytik ultradünner Schichten
TU Dresden, Germany, Sept 27, 2005

Grötzschel, R., Grambole, D., Güttler, D., Herrmann, F., Kreißig, U., Neelmeijer, C.
Ionenstrahlanalytik an den Rossendorfer Beschleunigern
Zukunftsperspektiven und Anwendungen von Ionenstrahlen, Bundesanstalt für Materialforschung und -prüfung (BAM), Berlin, Germany, Oct 17, 2005

Heinig, K.-H.
Ion beam synthesis and processing of nanostructures
GSI Darmstadt, Germany, Nov 15, 2005

Helm, M.
From short-wavelength quantum cascade lasers to impulsive THz emitters
THALES Research & Technology, Orsay, France, Feb 24, 2005

Helm, M.
Silizium-basierte Lichtemitter: auf dem Weg zur Silizium-Photonik?
Universität Kaiserslautern, Germany, Jan 17, 2005

Krause-Rehberg, R., Brauer, G.
Die intensive Positronenquelle EPOS am Forschungszentrum Rossendorf
FSU Jena, Institut für Festkörperphysik, Jena, Germany, Dec 2, 2005

Möller, W.
Ion-based materials research at FZR
Laborat. of Ion Beam Physics and Materials Research, University of Lanzhou, China, Sept 23, 2005

Möller, W.
Fast ions for nano technology
Fraunhofer Center of Nanoelectronic Technologies, Dresden, Germany, Oct 13, 2005

Möller, W., Beckers, M., Schell, N., Mücklich, A.
Deposition and characterization of nitride MAX phase thin films
CSIC-ICMM, Madrid, Spain, Dec 13, 2005

Neelmeijer, C.
Ionen als Agenten und Detektive
Berufliches Schulzentrum Dresden, Wissenschaftstag 12. Klassen, Dresden, Germany, Sept 29, 2005

Oates, T.W.H.
In situ spectroscopic ellipsometric determination of morpholoigal and electronic properties of plasma deposited ultra-thin metal films
RWTH Aachen, Germany, May 31, 2005

Oates, T.W.H.

Analysing the growth of metal nanoparticles by in-situ ellipsometry
Institut für Experimentalphysik, Universität Leipzig, Germany, Sept 2005

Oates, T.W.H.
Analysing the growth of metal nanoparticles by in-situ ellipsometry
Institut für Festkörperphysik, Technische Universität Berlin, Germany, Nov 2005

Posselt, M.
Atomistic simulation of ion irradiation, ion-beam-induced defect formation and defect migration
Physikalisches Institut der Universität Bern, Switzerland, April 20, 2005

Posselt, M.
Atomistische Computersimulation ionenstrahlinduzierter Prozesse: Implantation, Defektbildung, Defektmigration
Leibniz-Institut für Oberflächenmodifizierung, Leipzig, Germany, May 19, 2005

Posselt, M.
Atomistic computer simulation of ion implantation, ion-beam-induced defect formation and defect migration
CEA-LETI, Grenoble, France, Oct 11, 2005

Posselt, M.
Atomistische Simulation von Defekten in Festkörpern
Institut für Sicherheitsforschung des FZR, Dresden, Germany, Nov 17, 2005

Prucnal, S.
Investigation of electroluminescence mechanisms in SiO_2 *layers implanted with rare earth ions*
Maria Curie-Sklodowska University, Lublin, Poland, Jan 12, 2005

Reuther, H.
Oberflächenmodifizierung durch Ionenstrahlbehandlung – Charakterisierung mittels Elektronen
Institut für Festkörperanalytik und Strukturforschung, IFW Dresden, Germany, April 20, 2005

Richter, E.
Hitzebeständige TiAl-Legierungen
Werkstoff-Forum, Hannover Messe, Germany, April 11-15, 2005

Rogozin, A., Vinnichenko, M., Shevchenko, N., Kolitsch, A., Möller, W.
Properties and structure tailoring of ITO films grown by pulsed reactive magnetron sputtering
RWTH Aachen, Germany, May 31, 2005

Schmidt, B.
Nano-Technologie
Lehrerfortbildungsseminar, FZ Rossendorf, Germany, Feb 12, 2005

Schmidt, B.
Präparation und Charakterisierung von Strukturen für die Nanotechnologie
Institut für Physik, Universität Rostock, Germany, June 27, 2005

Schmidt, B.
Nano-Technologie – Materialien für die Zukunft
Lange Nacht der Wissenschaften, Dresden, Germany, July 1, 2005

Schmidt, B.
Was können Ionenstrahlen in der Nanotechnologie bewirken?

Universität der Bundeswehr, München-Neubiberg, Germany, Oct 6, 2005

Schmidt, B.
Ion beam synthesis of $CoSi_2$ *for nanoscale interconnects*
FhG Center of Nanotechnology, Dresden, Germany, Oct 13, 2005
Infineon Technologies, Dresden, Germany, Dec 16, 2005

Schmidt, B.
Ionenstrahltechnik und Nano-Technologie
URANIA Vortragszentrum e.V. Dresden, Germany, Oct 14, 2005

Skorupa, W.
Advanced thermal processing of silicon in the msec-range using flash lamps
Heraeus GmbH, Hanau, Germany, April 6, 2005

Skorupa, W.
Ion beam processing for Si-based light emission: From IR to UV
Inst. of Electronic Materials Technology, Warsaw, Poland, June 20, 2005

Skorupa, W.
Ion beam processing for Si-based light emission: From IR to UV
Inst. Fiz. Jądr. im. H. Niewodniczańskiego Polsk. Ak. Nauk, Krakow, Poland, June 24, 2005

Skorupa, W.
Advanced ion beam processing of semiconductor materials
Depto. de Física, Universidade de Coimbra, Portugal, Sept 9, 2005

Winnerl, S.
Die Lichtrevolution durch Leuchtdioden
Licht-Licht-Licht, Interdisziplinärer Studientag an der TU Dresden, Germany, Dec 15, 2005

Winnerl, S.
Die Lichtrevolution durch Leuchtdioden
Lange Nacht der Wissenschaften, Dresden, Germany, July 1, 2005

Reports

Brauer, G., Skorupa, W. (Editors)
HeT-SiC-05, International Topical Workshop on Heteroepitaxy of 3C-SiC on Silicon and its Application to Sensor Devices, Hotel Erbgericht Krippen / Germany, April 26 – May 1, 2005 – Selected Contributions –
Wissenschaftlich-Technische Berichte FZR-433, Aug 2005, ISSN 1437-322x

Scheinost, A.C., Schell, N. (Editors)
Rossendorf Beamline at ESRF: Biannual Report 2003/2004
Wissenschaftlich-Technische Berichte, FZR-418, Jan 2005

Rogozin, A., Shevchenko, N., Vinnichenko, M., Prokert, F., Cantelli, V., Kolitsch, A., Möller, W.
Real-time evolution of the ITO film properties and structure during annealing in vacuum
ESRF Highlights 2004, Feb 2005

Patents

Dekorsy, T., Neuhaus, J., Helm, M.
Sättigbarer Absorber
Patentanmeldung 10 2005 022 436.9

Pilz, W., Bischoff, L.
Needleless emitter for liquid metal (alloy) ion source
European patent application 05016351.8
Applicant: ICT GmbH 27.07.2005

Voelskow, M., Skorupa, W., Anwand, W.
Verfahren zur Behandlung von Halbleiter-Substratoberflächen, die mittels intensiven Lichtimpulsen kurzzeitig aufgeschmolzen werden
Deutsche Patentanmeldung DE 10 2005 036 669.4 (2005)

PhD Thesis

Müller, T.
Low energy ion beam synthesis of Si nanocrystals for nonvolatile memories – modeling and process simulation
TU Dresden, Oct 19, 2005
Wissenschaftlich-Technische Berichte, FZR-439, 2005

Master/Diploma Theses

Heller, R.
Optimierung der Ionenextraktion aus der EBIT der Rossendorfer Zweiquellenionenstrahlanlage
TU Dresden 2005

Keller, A.
Komparative Studie des Energieeintrags langsamer hochgeladener Ionen in Halbleiter und Isolatoroberflächen
FH Coburg, May 2005

Kreller, M.
Studium der Ionisationseigenschaften hochdichter Elektronenstrahlen mit röntgenspektroskopischen und elektrischen Analysemethoden
TU Dresden 2005

Roßbach, S.
Nanostrukturierung von Silizium-Oberflächen durch atomare Erosion
FH Zwickau, Dec 2005

Awards

Anwand, W., Panknin, D., Skorupa, W., Schumann, T., Voelskow, M.
Blitzlampentemperung im ms-Bereich für modernste Halbleiterprozessierung
Technologiepreis 2005 des FZR

Workshops (organized by IIM)

Brauer, G., Skorupa, W.
Heteroepitaxy of 3C-SiC on silicon and its application to sensor devices-HeT-SiC-05
Int. Topical Workshop, Hotel Erbgericht Krippen, Germany, April 26 – May 1, 2005

Facsko, S. (Co-Organizer)
Workshop "Ions at Surfaces: Patterns and Processes"
Bad Honnef, Germany, June 19 – 23, 2005

Helm, M., Mathis, Y.-L., Schade, U. (jointly with ANKA and BESSY)
International Workshop on Infrared Microscopy and Spectroscopy with Accelerator Based Sources
Rathen, Germany, June 26 – 30, 2005

Laboratory Visits

Beckers, M.
ESRF Grenoble, ROBL-Beamline, France, Jan 25 – 31, June 27 – July 4, Aug 31 – Sept 3, 2005

Borany, J. von
ESRF Grenoble, ROBL-Beamline, France, Feb 24 – March 1, Dec 8 – 13, 2005

Brauer, G.
Universität Halle-Wittenberg, Fachbereich Physik, Halle/Saale, Germany, Feb 9 – 11, 2005
University of Qatar, Physics Department, Doha, Qatar, March 28 – 30, 2005
Universität Göttingen, Institut für Materialphysik, Göttingen, Germany, Oct 24 – 26,2005

Cantelli, V.
ESRF Grenoble, ROBL-Beamline, France, Dec 6 – 13, 2005

Drachenko, O.
LNCMP Toulouse, France, May 9 – 17, June 27 – July 11, 2005

Eichhorn, F.
ESRF Grenoble, ROBL-Beamline, France, April 19 – 24, Aug 24 – 31, Nov 20 – 25, 2005
Institute of Electronic Materials Technology, Warsaw, Poland, Sept 19 – 24, 2005

Facsko S.
ESRF, Grenoble, France, Feb 23 – 26, Nov 23 – 28, 2005
Ciril, Caen, France, Oct 9 – 11, 2005

Fassbender, J.
Advanced Light Source, Berkeley, USA, May 23 – June 2, Sept 26 – Oct 3, 2005

Friedrich, M.
Universidad Autónoma de Madrid, Centro de Microanálisys de Materiales (CMAM), Madrid/Spain, Sept 12 – 15, 2005

Grambole, D.
Universität Bochum, Germany, Sept 28 – Oct 2, 2005

Grenzer, J.

Institute of Electronic Materials Technology, Warsaw, Poland, May 9 – 13, 2005
ESRF Grenoble, ROBL-Beamline, France, Feb 10 – 15, July 13 – 18, Nov 2 – 8, Nov 16 – 21, 2005

Heinig, K.-H.
CNRS Orsay/University Paris South, France, April 27 – 29, 2005

Helm, M.
Université Paris VII, Paris, France und Thales Research & Technology, Orsay, France,
Feb 20 – 25, July 8 – 22, 2005

Kögler, R.
University of Oslo, Oslo, Norway, June 20 – 30, 2005

Kolitsch, A.
Centro de Micro-Análisis de Materiales, Universidad Autónoma de Madrid, Spain, Dec 12 – 14, 2005

Kost, D.
Hahn-Meitner Institut, Berlin, Gemany, June 13 – 24, July 25 – 29, Dec 5 – 9, 2005

Küpper, K.
Swiss Light Source, Paul Scherrer Institute, Switzerland, Aug 13 – 16, Nov 26 – 29, 2005
Advanced Light Source, Berkeley, USA, Sept 26 – Oct 31, 2005

Rogozin, A.
ESRF Grenoble, ROBL-Beamline, France, May 14 – 15, Sept 20 – 26, 2005

Schneider, H.
Institute for Microstruct. Sciences, National Research Council, Ottawa, Canada, Sept 19 – 30, 2005

Shevchenko, N.
ESRF Grenoble, ROBL-Beamline, France, May 14 – 15, Sept 20 – 26, 2005
Siberian Physical and Technical Institute, Tomsk, Russia, July 18 – 22, 2005

Skorupa, W.
University of Oslo, Norway, Aug 14 – 21, 2005

Guests

Abdul-Kader, A.M.
Institute of Electronic Materials Technology, Warsaw, Poland, Jan 30 – Febr 2, 2005

Aidinis, C.J.
University of Athens, Greece, July 19 – 30, 2005

Andersson, J.
Linköping University, Linköping, Sweden, Sept 6 – 9, 2005

Arazi, A.
University of Buenos Aires, Argentinia, July 18 – 23, 2005

Ayache, R.
University of Batna, Algeria, June 1 – Aug 31, 2005

Bernas, H.

CSNSM Orsay, Paris, France, Oct 18 – 21, 2005

Bhattacharjee, K.
Institute of Physics Bhubaneswar, India, Dec 11 – 31, 2005

Bilek, M.M.
University of Sydney, Australia, June 27 – July 8, 2005

Blomqvist, M.
University of Milano, Milano, Italy, July 26 – Aug 10, 2005

Brongersma, H.
TU Eindhoven, The Netherlands, Dec 6 – 9, 2005

Carpenter, B.A.
University of Sheffield, UK, Nov 7 – 11, 2005

Cenger, Y.
University of Ankara, Turkey, July 4 – Sept 8, 2005

Chini, T.
Surface Physics Division, Saha Instit. of Nuclear Phys., Bidhannagar, Kolkata, India, Dec 1 – 31, 2005

Cizek, J.
Charles University, Prague, Czech Republic, Oct 7 – Nov 5, 2005

Dagkaldiran, Ü.
Universität Bochum, Germany, April 21 – 22, Aug 1 – 9, Nov 1 – 3, 2005

Dev, B.
Institute of Physics Bhubaneswar, India, April 1 – Dec 31, 2005

Emmerlich, J.
Linköping University, Linköping, Sweden, Aug 16 – 19, 2005

Gago, R.
Universidad Autonoma de Madrid, Spain, Feb 27 – March 3, 2005

Ganetsos, T.
T.E.I. of Lamia- Athens, Greece, Oct 4 – 12, 2005

Gracia, J.A.
Universidad Autonoma de Madrid, Spain, Oct 17 – Nov 4, 2005

Guarino, A.
ETH Zürich, Switzerland, June 27 – 29, Sept 21 – 23, Dec 6 – 9, 2005

Kondyurin, A.
University of Perm, Russia, Jan 1 – March 31, Aug 1 – 31, 2005

Korschinek, G.
TU München, Germany, July 17 – 20, 2005

Krasilnikova, O.
University of Lipezk, Russia, Nov 25 – Dec 24, 2005

Kuriplach, J.
Charles University, Prague, Czech Republic,
May 11 – 25, June 22 – July 6, Nov 16 – 30, Dec 6 – 20, 2005

Levin, J.
Applied Materials Israel Ltd., Israel, Dec 5 – 8, 2005

Mackova, A.
NPI Rez, Czech Republic, March 23 – 25, Dec 7 – 9, 2005

Mäder, M.
Akademie der Bildenden Künste Wien, Austria,
Feb 2 – 4, March 22 – 24, June 24 – 27, July 8 – 12, 2005

Markov, A.
Institute for High Current Electronics, Tomsk, Russia, May 9 – July 3, 2005

McMahon, R.
University of Cambridge, Engineering Dept., UK, July 18 – 19, Sept 13 – 15, Dec 12 – 14, 2005

Murdin, B.N.
University of Surrey, UK, July 25 – 29, 2005

Nazarov, A.N.
Ukraine Academy of Sciences, Kyiv, Ukraine, July 19 – Aug 17, 2005

Osiyuk, I.N.
Ukraine Academy of Sciences, Kyiv, Ukraine, June 17 – Aug 17, 2005

Ozerov, M.
Kyiv National Taras Shevchenko University, Ukraine, Oct 17 – Dec 16, 2005

Pecheva, E.
University of Sofia, Bulgaria, Feb 14 – April 8, 2005

Peeva, A.
Academy of Sciences of Bulgaria, Sofia, Bulgaria, July 1 – Aug 28, Nov 1 – Dec 23, 2005

Poberaj, G.
ETH Zürich, Switzerland, June 27 – 29, Aug 15 – 17, 2005

Poutivtev, M.,
Kurchatov Institute Moskau, Russia, July 18 – 20, 2005

Prochazka, I.
Charles University, Prague, Czech Republic, Sep 15 – Oct 14, 2005

Prucnal, S.
Marie Curie-Sklodowska University Lublin, Poland,
Feb 1 – March 31, May 1 – June 30, Aug 15 – Dec 15, 2005

Rugel, G.
TU München, Germany, July 20 – 23, 2005

Sass, J.

Institute of Electronic Materials Technology, Warsaw, Poland, Oct 5 – 9, 2005

Schrey, F.F.
TU Wien, Austria, June 19 – 24, 2005

Siketic, Z.
Ruder Boskovic Institute, Zagreb, Croatia, Sept 5 – Oct 5, 2005

Singkarat, S.
Chiang Mai University, Thailand, Aug 8 – 12, 2005

Som, T.
Institute of Physics Bhubaneswar, India, June 1 – July 31, 2005

Ster, A.
Research Institute for Technical and Materials Science, Budapest, Hungary, Sept 4 – 17, 2005

Stonert, A.
Institute of Electronic Materials Technology, Warsaw, Poland, Dec 6 – 12, 2005

Tsyganov, I.
University of Lipezk, Russia, Jan 16 – March 24, Nov 25 – Dec 19, 2005

Turos, A.
Institute of Electronic Materials Technology, Warsaw, Poland,
Jan 30 – Feb 3, Feb 13 – 15, April 24 – 30, Sept 10 – 15, Dec 6 – 12, 2005

Zibik, E.A.
University of Sheffield, UK, Nov 4 – 11, 2005

ROBL-MRH Visitors

Almtoft, K.P.
Dept. of Physics and Astronomy, University of Aarhus, Aarhus, Denmark, June 22 – 28, 2005

Bjeoumikhov, A.
Institut for Scientific Instruments, Berlin, Germany, 26, 2005

Bøttiger, J.
Dept. of Physics and Astronomy, University of Aarhus, Aarhus, Denmark, June 22 – 28, 2005

Braz-Fernandes, F.M.
CENIMAT F.C.T., Universidade Nova de Lisboa, Lisbon, Portugal, Feb 16 – 22, April 12 – 19, 2005

Cieslak, J.
Institute for Optics and Quantumelectronics, FSU Jena, Germany, May 11 – 15, 2005

Cordeiro Silva, R.J.
CENIMAT F.C.T., Universidade Nova de Lisboa, Lisbon, Portugal, Feb 16 – 22, April 12 – 19, 2005

Dev, B.N.
Institute of Physics Bhubaneswar, India, Nov 16 – 21, 2005

Ejsing, M.

Dept. of Physics and Astronomy, University of Aarhus, Aarhus, Denmark, June 22 – 28, 2005

Fuhse, C.
Institute for X-Ray Physics, University Göttingen, Germany, March 23 – 27, Sept 3 – 6, 2005

Gaca, J.
ITME Warsaw, Poland, April 20 – 27, Aug 27 – 31, 2005

Hahn, T.
Institute for Optics and Quantum Electronics, FSU Jena, Germany, May 11 – 15, 2005

Juricic, C.
Institut für Werkstoffkunde, TU Wien, Vienna, Austria, July 20 – 27, 2005

Kräußlich, J.
Institute for Optics and Quantum Electronics, FSU Jena, Germany, May 11 – 15, 2005

Mahesh, K.
CENIMAT F.C.T., Universidade Nova de Lisboa, Lisbon, Portugal, Feb 16 – 22, April 12 – 19, 2005

Mazur, K.
ITME Warsaw, Poland, April 20 – 27, Aug 27 – 31, 2005

Ollinger, C.
Institute for X-Ray Physics, University Göttingen, Germany, March 23 – 27, Sept 3 – 6, 2005

Prinz, H.
AMD Saxony, Dresden, Germany, March 16 – 21, Nov 9 – 15, 2005

Pyzalla, A.
Institut für Werkstoffkunde, TU Wien, Vienna, Austria, July 20 – 27, 2005

Rinderknecht, J.
AMD Saxony, Dresden, Germany, March 16 – 21, Nov 9 – 15, 2005

Salditt, T.
Institute for X-Ray Physics, University Göttingen, Germany, March 22 – 27, 2005

Sass, J.
ITME Warsaw, Poland, April 20 – 27, 2005

Silva da, P.
Institut für Werkstoffkunde, TU Wien, Vienna, Austria, July 20 – 27, 2005

Walther, K.
GeoForschungszentrum Potsdam, Germany, Dec 14 – 17, 2005

Weiss, A.
Institut for Scientific Instruments, Berlin, Germany, Aug 24 – 26, 2005

Wojcik, M.
ITME Warsaw, Poland, April 20 – 27, Aug 27 – 31, 2005

Zienert, I.
AMD Saxony, Dresden, Germany, March 16 – 21, Nov 9 – 15, 2005

Colloquium of the Institute

D.K. Avashti – Nuclear Science Center New Delhi, India
Nanostructuring with ion beams at Nuclear Science Center
June 2, 2005

H. Biederman – Dept. of Macromolecular Physics, Charles University Prague, Czech Republic
Plasma polymer coatings prepared by rf sputtering
Feb 3, 2005

H. Brongersma – Calipso B.V., Eindhoven, Netherlands
LEIS: A new tool for the analysis of the outer surface, ultra-thin layers and contacts
Dec 8, 2005

F. Cristiano – LAAS/CNRS Toulouse, France
Extended defects, boron diffusion and activation anomalies in ultra-shallow junctions
Jan 27, 2005

G. Deboy – Infineon Technologies, Villach, Austria
Power semiconductor devices - trends and trade offs
Dec 1, 2005

T. Dietl – Laboratory for Cryogenic and Spintronic Research, Institute of Physics, Polish Academy of Sciences, Warszawa and Institute of Theoretical Physics, Warsaw University, Poland
Wide-band-gap ferromagnetic semiconductors
May 12, 2005

O. Hahn – BAM Berlin, AG "Emission aus Materialien", Germany
Röntgenfluoreszenz- und Röntgenabsorptionsuntersuchungen an historischen Eisengallustinten
Oct 20, 2005

J. Keinonen – Accelerator Laboratory, University of Helsinki, Finland
Materials research in the Accelerator Laboratory of the University of Helsinki
Jan 13, 2005

P. Kücher – Center Nanoelectronic Technologies, Infineon Technologies Dresden GmbH, Germany
Center Nanoelectronic Technologies - Scaling for future production
May 20, 2005

Y. Lifshitz – Technion, Israel Institute of Technology, Haifa, Israel
Nanostructuring materials - from witchcraft to science
June 23, 2005

S. Müller – Institut für Angewandte Physik, Universität Erlangen, Nürnberg, Germany
Modellierung mesoskopischer Systeme auf quantenmechanischer Basis
Oct 10, 2005

K. Nielsch – MPI für Mikrostrukturphysik, Halle, Germany
Magnetic nanowires and nanotubes based on aluminium oxide membranes
April 28, 2005

U. Pietsch – Universität Potsdam, Institut für Physik, Germany
Ripple structure in ion beam implanted silicon wafers
May 27, 2005

E. Schultheiß – FhI für Elektronenstrahl- und Plasmatechnik, Dresden, Germany
Dünne Schichten - große Flächen (Aktivitäten am Fraunhofer FEP Dresden)
Jan 20, 2005

Ch. Treutler – Robert Bosch GmbH, Stuttgart, Germany
Industrieller Einsatz der Plasmabeschichtungstechnik zum Schutz von Bauteilen der Kraftfahrzeugtechnik gegen Reibung und Verschleiß
Oct 27, 2005

W. Vandervorst – IMEC Leuven, Belgium
Basics, properties and limitations of SIMS in nanometer scale semiconductor technologies
Nov 3, 2005

A. Vantomme – Nuclear and Radiation Physics Section, Katholieke Universiteit Leuven, Belgium
Rare earth implanted GaN: defect accumulation and lattice site
March 31, 2005

J. Vlcek – Faculty of Applied Sciences University of West Bohemia, Plzen, Czech Republic
Reactive magnetron sputtering of new quaternary Si-B-C-N films and their properties
Nov 17, 2005

W. Windl – Ohio State University, USA
Ab-initio assisted atomic-resolution characterization and process modeling for nanoelectronic devices
July 7, 2005

Other Seminars

I. Bakony – Research Institute for Solid State Physics and Optics, Budapest, Hungary
Recent progress on electrodeposited multilayer films with giant magnetoresistance (GMR) behaviour
Nov 24, 2005

U. Birkenheuer – MPI für Physik Komplexer Systeme, Dresden, Germany
Ab initio investigations in surface and material science
Sept 2, 2005

A. Deac – CEA Grenoble, France
Current induced magnetisation switching in spin-valve pillars for CPP-GMR heads
Feb 2, 2005

M.A. Djouadi – Institut des Matériaux, Nantes, France
BN, CNx and carbon thin films synthesis by plasma methods
March 14, 2005
S. Gemming – Institut für Physikalische Chemie und Elektrochemie, TU Dresden, Germany
DF investigations of Ti-Si interfaces
Aug 23, 2005

C. Ichihara – Kobe Steel, Ltd., Japan
Presentation of high-resolution RBS system
July 8, 2005

M. Johnston – Clarendon Laboratory, Oxford University, UK
Polarisation resolved terahertz time domain spectroscopy
Sept 5, 2005

R. Kalish – Solid State Institute, Technion Haifa, Israel
Electron Emmission from Diamond - what is so special about it?
Aug 8, 2005

F. Kolb – MPI für Mikrostrukturphysik, Halle
SiO-VLS growth of silicon nanowires
May 25, 2005

D. Kovalev – Physik Dept., TU München, Germany
Nanosilicon: new properties - new functionality
June 3, 2005

J. K. Le – Fudan University of Shanghai, China
The influence of stoichometry on the growth of cBN thin films
Oct 17, 2005

J. Levin – Applied Materials, Rehovot, Israel
FIB applications - Pecularities of applied materials new FIB Tool
Dec 7, 2005

O. Liepack – Jet Propulsion Laboratory, Pasadena, USA
First results and details of the Huygens landing at Titan
June 1, 2005

H. Ohno – Tohoku University, Sendai, Japan
Electrical magnetization manipulation in semiconductors
May 12, 2005

F.M. Peeters – Physics Dept., University Antwerpen, Belgium
Excitons in single and vertically coupled type II quantum dots in the presence of high magnetic fields
Oct 20, 2005

D. Tsoukalas – Institute of Microelectronics, RC Demokritos, Athens, Greece
Nanocrystals and their application in nonvolatile memories
Oct 19, 2005

T. Winkelmann – HMI Berlin, Germany
Die Injektoren des ISL Berlin: Aufbau, Leistungsparameter und spezielle Anwendungen
Dec 9, 2005

Projects based on External Funds

04/2002 – 06/2005 European Union EU
FLASiC - Flash lamp supported deposition of 3C-SiC films
Dr. W. Skorupa Tel.: 0351 260 3612 w.skorupa@fz-rossendorf.de

09/2002 – 08/2005 WTZ with Russia WTZ
Dynamische Bestrahlungseffekte in metastabilen Legierungen unter Ionenbeschuss
Dr. E. Richter Tel.: 0351 260 3326 e.richter@fz-rossendorf.de

10/2002 – 09/2005 WTZ with Poland WTZ
Strukturelle Charakterisierung von Heterostrukturen für Opto- und Mikroelektronik
Dr. F. Eichhorn Tel.: 0351 260 3534 f.eichhorn@fz-rossendorf.de

10/2002 – 09/2006 European Union EU
New Fullerene - Synthesis, structure and properties of new fullerene like materials
Dr. A. Kolitsch Tel.: 0351 260 3348 a.kolitsch@fz-rossendorf.de

11/2002 – 01/2006 Deutsche Forschungsgemeinschaft DFG
Phasen- und Strukturdesign von Ti-Al-N-Schichten durch
Echtzeit-in-situ-Röntgendiffraktion
Dr. N. Schell Tel.: +33 (0)4.76.88.23.67 schell@esrf.fr

01/2003 – 12/2005 WTZ with Russia WTZ
Substituted hydroxyapatite for improved adsorption of osteoinductive factors
Dr. E. Richter Tel.: 0351 260 3326 e.richter@fz-rossendorf.de

04/2003 – 03/2005 Arbeitsgemeinschaft industrieller Forschungsvereinigungen AiF
Oxidationsschutz für neuartige Hochtemperatur-Leichtbauwerkstoffe
durch Ionenimplantation (II)
Dr. E. Richter Tel.: 0351 260 3326 e.richter@fz-rossendorf.de

08/2003 – 12/2005 Applied Materials, ICT GmbH Auftrag
Fabrication and investigation of the parameters of LMIS emitters
Dr. L. Bischoff Tel.: 0351 260 2963 l.bischoff@fz-rossendorf.de

01/2004 – 12/2005 DAAD-Norwegen DAAD
Ion implantation induced defects in Si-SiGe-based heterostructures
Dr. R. Kögler Tel.: 0351 260 3613 r.koegler@fz-rossendorf.de

01/2004 – 12/2005 DAAD-Acciones Integradas Hispano-Alemanas DAAD
Preparation and characterization of Boron-Carbon-Nitrogen compounds:
functional materials for biocompatibility
Prof. W. Möller Tel.: 0351 260 2245 w.moeller@fz-rossendorf.de

03/2004 – 02/2009 European Union EU
IA-SFS - Integrating activity on synchrotron and free electron laser science
Prof. M. Helm Tel.: 0351 260-2260 m.helm@fz-rossendorf.de

07/2004 – 06/2006 Deutsche Forschungsgemeinschaft DFG
Theoretische Untersuchungen zu Wachstum, Stabilität und Funktionalität
von Nanodrähten
Dr. K.-H. Heinig Tel.: 0351 260-3288 k.h.heinig@fz-rossendorf.de

07/2004 – 06/2006 Deutsche Forschungsgemeinschaft DFG
Synthese von Nanodrähten und Nanoketten mit feinfokussierten Ionenstrahlen
Dr. B. Schmidt Tel.: 0351 260 2726 bernd.schmidt@fz-rossendorf.de

08/2004 – 07/2006 European Union, Marie-Curie-Program EU
POLYION - Polymer surface modification by ion implantation
Dr. E. Richter Tel.: 0351 260-3326 e.richter@fz-rossendorf.de

09/2004 – 06/2006 Bundesministerium für Bildung und Forschung BMBF
Funktionalisierung der Oberflächen von Polyurethan als Basiswerkstoff für flexible und im Blutkontakt stehende medizinische Implantate und Devices
Dr. E. Richter Tel.: 0351 260 3326 e.richter@fz-rossendorf.de

09/2004 – 08/2006 WTZ with Russia WTZ
Titan im Blutkontakt
Dr. E. Richter Tel.: 0351 260 3326 e.richter@fz-rossendorf.de

10/2004 – 12/2005 AMD Saxony Auftrag
Strukturuntersuchungen an BEOL-Komponenten
Dr. N. Schell Tel.: +33 (0)4.76.88.23.67 schell@esrf.fr

01/2005 – 12/2006 DAAD-Poland DAAD
Ionenstrahlmodifizierung mit Polymeren
Dr. D. Grambole Tel.: 0351 260 3050 d.grambole@fz-rossendorf.de

01/2005 – 12/2008 European Union EU
EuroMagNET – A coordinated approach to access, experimental development and scientific exploitation of European large infrastructures for high magnetic fields
Prof. M. Helm Tel.: 0351 260 2260 m.helm@fz-rossendorf.de

02/2005 – 03/2006 European Union EU
NANOMULTI – Nanostructured nonmagnetic and magnetic multilayers
Dr. R. Grötzschel Tel.: 0351 260 3294 r.groetzschel@fz-rossendorf.de

04/2005 – 12/2006 DEGUSSA AG Auftrag
Untersuchungen zur Blitzlampentemperung beschichteter Substrate
Dr. W. Skorupa Tel.: 0351 260 3612 w.skorupa@fz-rossendorf.de

04/2005 – 03/2007 Arbeitsgemeinschaft industrieller Forschungsvereinigungen AiF
Oxidationsschutz für neuartige Hochtemperatur-Leichtbauwerkstoffe durch Ionenimplantation (III)
Dr. E. Richter Tel.: 0351 260 3326 e.richter@fz-rossendorf.de

04/2005 – 03/2010 European Union EU
PRONANO – Technology for the production of massively parallel intelligent cantilever-probe platforms for nanoscale analysis and synthesis
Dr. B. Schmidt Tel.: 0351 260 2726 Bernd.Schmidt@fz-rossendorf.de

06/2005 – 12/2006 AMD Saxony Auftrag
Röntgen-Mikrofokus an ROBL
Dr. N. Schell Tel.: +33 (0)4.76.88.23.67 schell@esrf.fr

06/2005 – 05/2007 Deutsche Forschungsgemeinschaft DFG
Mössbauerspektroskopie an ionenimplantierten magnetischen Halbleitern
Dr. H. Reuther Tel.: 0351 260 2898 h.reuther@fz-rossendorf.de

07/2005 – 06/2007 Robert Bosch GmbH Auftrag
NanoHoch - Nanostrukturierte Hochtemperatur-Halbleiter für integrierte Abgassensoren in Dieselmotor- und Magermotorapplikationen
Dr. V. Heera Tel.: 0351 260 3343 v.heera@fz-rossendorf.de

09/2005 – 02/2010 European Union EU
FOREMOST – Fullerene-based opportunities for robust engineering: Making optimised surfaces for tribology
Dr. A. Kolitsch Tel.: 0351 260 3348 a.kolitsch@fz-rossendorf.de

11/2005 – 10/2007 Eifeler GmbH Auftrag
Technologietransfer cBN
Dr. A. Kolitsch Tel.: 0351 260 3348 a.kolitsch@fz-rossendorf.de

01/2005 – 12/2005 Boston Scientific Scimed Auftrag
Nitinol
Dr. E. Richter Tel.: 0351 260 3326 e.richter@fz-rossendorf.de

04/2005 – 12/2005 Boston Scientific Scimed Auftrag
Polymer Ballons
Dr. E. Richter Tel.: 0351 260 3326 e.richter@fz-rossendorf.de

07/2003 – 06/2005 ISE Integrated Systems Engineering AG Auftrag
Weiterentwicklung eines Implantationsmoduls
Dr. M. Posselt Tel.: 0351 260 3279 m.posselt@fz-rossendorf.de

Experimental Equipment

1. Accelerators, Ion Implanters and Ion-Assisted-Deposition

⇒	Van de Graaff accelerator	(VdG)	1,8 MV	*TuR Dresden, D*
⇒	Tandem accelerator	(Td)	5 MV	*NIIEFA, RU*
⇒	Tandetron accelerator	(Tdtr)	3 MV	*HVEE, NL*
⇒	Ion implanter		80 kV	Own construction
⇒	Low energy ion implanter		0.5 - 50 keV	*Danfysik, DK*
⇒	High current ion implanter		200 kV, high current	*Danfysik, DK*
⇒	High energy ion implanter		500 kV	*HVEE, NL*
⇒	Plasma-immersion ion implantation		5 - 60 keV	Own construction
⇒	Fine focused ion beam		30 keV, 15 nm, 10 A/cm^2	*Orsay Physics, F*
⇒	Dual beam magnetron sputter deposition			*Roth & Rau, D*
⇒	Ion beam assisted deposition			
⇒	UHV He-irradiation		0 - 5 keV, Scan 10 × 10 mm^2	*VG, USA*

2. Ion Beam Analysis (IBA)

A wide variety of advanced IBA techniques are available at the MeV accelerators of the Ion Beam Centre Rossendorf.

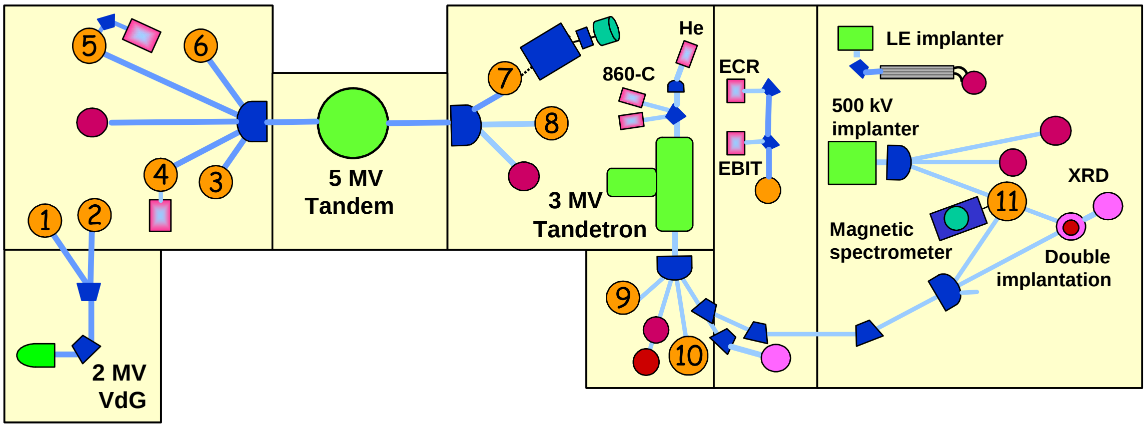

⇒	RBS	Rutherford backscattering	(1), (2), (3), (9)	VdG, Td, Tdtr
⇒	RBS/C	RBS + channelling	(1), (2), (3), (9)	VdG, Td, Tdtr
		High-resolution RBS/C	(11)	Tdtr
⇒	ERDA	Elastic recoil detection analysis	(2), (4), (5)	VdG, Td
⇒		High-resolution ERDA	(7), (8)	Td
⇒	PIXE	Proton induced X-ray emission	(3)	Td
⇒	PIGE	Proton induced γ emission	(3)	Td
⇒	NRA	Nuclear reaction analysis	(4)	Td
⇒	NRRA	Nuclear resonance reaction analysis	(6)	Td
⇒		Nuclear microprobe	(10)	Tdtr

Some stations are equipped with additional process facilities which enable *in-situ* IBA investigations during ion irradiation, sputtering, deposition, annealing etc.

3. Other Particle Based Analytical Techniques

⇒	SEM	Scanning electron microscope	<1 - 30 keV, EDX	*Hitachi, JP*
⇒	TEM	Transmission electron microscope	300 kV	*Philips, NL*
⇒	AES	Auger electron spectroscopy	+ XPS-option	*Fisions, GB*
⇒	CEMS	Mössbauer spectroscopy	^{57}Fe source	

4. Photon Based Analytical Techniques

⇒	XRD/XRR	X-ray diffraction / X-ray reflection	8.04 keV (Cu-K_α)	*Bruker axs, D*
	HR-XRD	High-resolution XRD	8.04 keV (Cu-K_α)	*GE Inspection Techn., D*
	XRD/XRR	with Synchrotron radiation	5 – 35 keV	*ROBL-CRG at ESRF, F*
⇒	SE	Spectroscopic ellipsometry	250 - 1700 nm	*Woollam, USA*
⇒	FTIR	Fourier transform infrared spectrometry	600 - 7000 cm^{-1}	*Nicolet, USA*
⇒	FTIR	Fourier transform infrared spectrometry with infrared microscope	50 - 15000 cm^{-1}	*Bruker, D*
⇒		Ti:Sapphire femtosecond laser		*Spectra Physics, USA*
⇒		Femtosecond optical parametric oscillator		*APE, D*
⇒		Ti:Sapphire femtosecond amplifier		*Femto Laser, A*
⇒		Femtosecond optical parametric amplifier		*Light Conversion, LT*
⇒	Raman	Raman spectroscopy (532 nm, 633 nm)	> 45 cm^{-1} shift	*Jobin-Yvon-Horiba, F*
⇒	PL	Photoluminescence	300 - 1500 nm	*Jobin-Yvon-Horiba, F*
⇒	EL	Electroluminescence (10-300 K)	300 - 1500 nm	*Jobin-Yvon-Horiba, F*
⇒		Optical split-coil supercond. magnet	7 T	*Oxford Instrum., UK*
⇒	PR	Photomodulated reflectivity	300 - 1500 nm	*Jobin-Yvon-Horiba, F*
⇒	PLE	Photoluminescence Excitation	300 - 1500 nm	*Jobin-Yvon-Horiba, F F*
⇒	TRPL	Time resolved PL	$\tau > 5$ ns	*Stanford Research, USA*

5. Magnetic Properties Analysis

⇒	MOKE	Magneto-Optic Kerr Effect	± 200 Oe	Home-built
			± 3.5 kOe	Home-built
⇒	MFM	Magnetic Force Microscope	~ 50 nm resol.	*Veeco/DI, USA*

6. Other Analytical and Measuring Techniques

⇒	Scanning tunneling microscope (with AFM-option)		*DME, DK*
⇒	Dektak surface profilometer		*Veeco, USA*
⇒	Micro indenter		*Shimatsu, J*
⇒	Scratch tester		*Shimatsu, J*
⇒	Spreading resistance profiling		*Sentech, D*
⇒	Hall-effect equipment	(2 – 400 K, ≤ 9 T)	*LakeShore, USA*
⇒	*I-V* and *C-V* analyzer		*Keithley, USA*
⇒	Wear tester (pin-on-disc)		Own construction

7. Preparation Techniques

⇒	Wet chemical etching and cleaning	including anisotropic selective KOH-etching	
⇒	Photolithographic patterning	5 µm-level	
⇒	Thermal treatment	Room Temperature - 2000°C	
		• Furnace	*Innotherm, D*
		• Rapid thermal annealing	*Addax, F*
		• Flash lamp unit (0.5 – 20 ms)	
		• RF-Heating (Vacuum)	*Nordico, GB*
⇒	Physical deposition	Sputtering DC / RF, Evaporation	
		Electron beam evaporation system	*Leybold Optics, D*
⇒	Dry etching	Plasma and RIE mode	*Sentech, D*
⇒	Bonding techniques	Anodic, Si-Si and Wire Bonding	
⇒	Cutting, grinding, polishing		*Bühler, D*
⇒	TEM sample preparation	plan-view and cross-section	
		including ion milling equipment	*Gatan, USA*

Services

The institute serves as a user center and technology transfer point in connection with its many years of experience in the application of ion beams for modification and analysis of solid surfaces and thin films of arbitrary materials.

Ion beam treatment of metallic materials (e.g. light metals like Al, Ti; stainless steel) can be advantageously applied for the improvement of the tribological properties (hardness, wear, corrosion resistance etc.). Using ion beam assisted deposition, hard coatings with special properties are obtained, such as a high adhesive strength and low internal stress. New technologies of high energy ion implantation or focused ion beam techniques result in new applications of electronic devices or microintegrated circuits.

Ion beams are an excellent instrument for the analysis of solid state surfaces. The interaction of the incident ion beam with the surface layer of a material leads to a specific radiation response, which yields information on the elemental composition as function of depth in a quantitative and essentially non-destructive way.

Additional means of preparation and diagnostics are available to fulfill the needs of users from different industrial branches. Do not hesitate to contact our experienced team.

Main areas of competence:

- Development and fabrication of sensors and detectors for charged particle spectroscopy
- Deposition of functional coatings using ion-assisted physical vapor deposition
- Fabrication of wear protection layers on metallic materials or alloys
- Deposition of blood compatible layers (i.e. TiO_x) on different materials
- Ion implantation in a broad range of ion energy (~ 200 eV to ~ 50 MeV) and substrate temperature
- Advanced ion beam technologies (high energy ion implantation, focused ion beam) for microelectronic applications
- Application of high energy ion implantation for power devices and laser structures
- Doping of semiconductors, in particular wide bandgap semiconductors
- Surface analysis of solid materials with high energy ion beams
- Computer simulation of ion beam interaction with materials
- Optical characterization of materials (luminescence, FTIR, Raman)

Offers:

- Consultation and problem evaluation for ion beam applications
- Process development for ion beam treatment of different materials (metals, ceramics, semiconductors)
- Process development in ion-assisted deposition of thin films
- Preparation and treatment of material samples, tools or complex parts of devices
- Ion implantation and ion beam analysis services
- Ion implantation into semiconductor materials for applications in microsystems and micro- and power electronics,
- Preparation / fabrication of semiconductors or silicon radiation sensors under clean room conditions
- Structural diagnostics of materials surfaces including e-beam- (SEM, TEM, AES) and X-ray techniques (XRD, XRR with both Cu-K and Synchrotron (5-35 keV) radiation).

Examples:

- Improvement of wear resistance of austenitic stainless steels using plasma immersion ion implantation
- High energy ion implantation for power semiconductor devices,
- Micro- and nanoengineering with focused ion beams
- Non-destructive quantitative hydrogen analysis in materials

- Non-destructive ion beam analysis of art objects
- Doping of wide-bandgap-semiconductors (SiC, diamond)
- Nuclear microprobe for ion beam analysis with high spatial resolution
- Synchrotron radiation analysis of materials at the ROBL Beamline in Grenoble.

Contact:

Please direct your inquiry about the application of ion beams for modification and analysis of materials to one of the following experts:

Field of application	**Name**	**Phone / Fax**	**E-mail**
Ion implantation (metals, ceramics, polymers, biomaterials)	Dr. Edgar Richter	3326 / 2703	e.richter @fz-rossendorf.de
Ion implantation (semiconductors, in particular high energy)	Dr. Johannes von Borany	3378 / 3438	j.v.borany @fz-rossendorf.de
Thin film deposition	Dr. Andreas Kolitsch	3348 / 2703	a.kolitsch @fz-rossendorf.de
High energy ion beam analysis	Dr. Rainer Grötzschel	3294 / 2870	r.groetzschel @fz-rossendorf.de
Semiconductor preparation Detector / Sensor fabrication	Dr. Bernd Schmidt	2726 / 3285	bernd.schmidt @fz-rossendorf.de
Focused ion beams	Dr. Lothar Bischoff	2963 / 3285	l.bischoff @fz-rossendorf.de
Structural diagnostics	Dr. Johannes von Borany	3378 / 3438	j.v.borany@ fz-rossendorf.de
Materials research with synchrotron radiation at ROBL (ESRF)	Dr. Norbert Schell	2367 / 2371	schell @esrf.fr
Optical materials characterization	Dr. Stephan Winnerl	2880 / 3285	s.winnerl @fz-rossendorf.de

For all phone/ fax-numbers choose the country / local code:	++ 49 351 260 - xxxx (for FZR)
	++ 33 47 688 - xxxx (for ROBL)

The abbreviations are explained in the Glossary (see page 81).

The institute also recommends to visit the homepages of its spin-off companies

“GeSiM mbH”	www.gesim.de
“APT Dresden”	www.apt-dresden.de
“nanoparc GmbH”	www.nanoparc.de

Forschungszentrum Rossendorf e.V.

Institute of Ion Beam Physics and
Materials Research (IIM)

Postfach 51 01 19
D-01314 Dresden

Tel.: 0351 260 2245
Fax: 0351 260 3285
www.fz-rossendorf.de

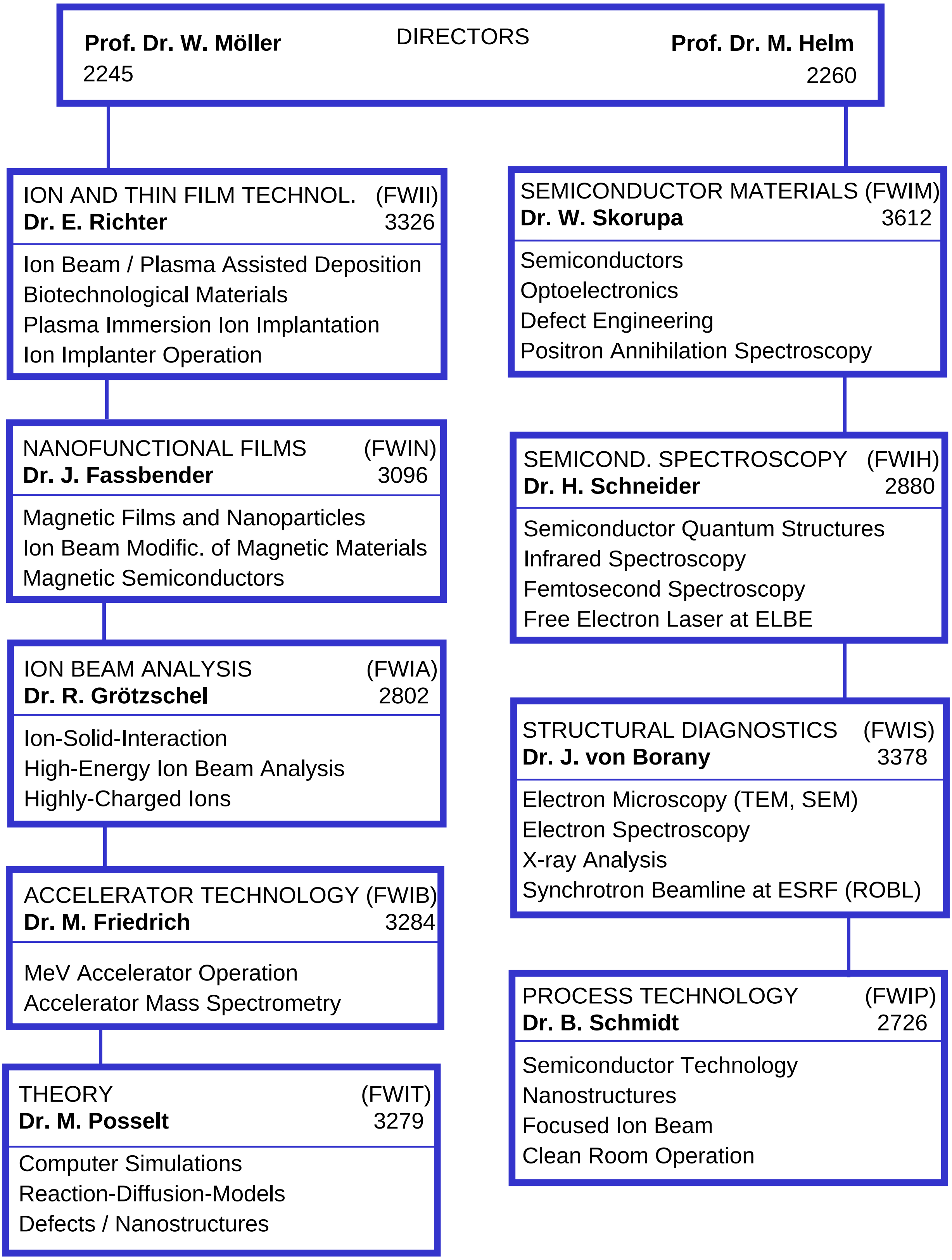

DIRECTORS

Prof. Dr. W. Möller 2245

Prof. Dr. M. Helm 2260

ION AND THIN FILM TECHNOL. (FWII)
Dr. E. Richter 3326

- Ion Beam / Plasma Assisted Deposition
- Biotechnological Materials
- Plasma Immersion Ion Implantation
- Ion Implanter Operation

NANOFUNCTIONAL FILMS (FWIN)
Dr. J. Fassbender 3096

- Magnetic Films and Nanoparticles
- Ion Beam Modific. of Magnetic Materials
- Magnetic Semiconductors

ION BEAM ANALYSIS (FWIA)
Dr. R. Grötzschel 2802

- Ion-Solid-Interaction
- High-Energy Ion Beam Analysis
- Highly-Charged Ions

ACCELERATOR TECHNOLOGY (FWIB)
Dr. M. Friedrich 3284

- MeV Accelerator Operation
- Accelerator Mass Spectrometry

THEORY (FWIT)
Dr. M. Posselt 3279

- Computer Simulations
- Reaction-Diffusion-Models
- Defects / Nanostructures

SEMICONDUCTOR MATERIALS (FWIM)
Dr. W. Skorupa 3612

- Semiconductors
- Optoelectronics
- Defect Engineering
- Positron Annihilation Spectroscopy

SEMICOND. SPECTROSCOPY (FWIH)
Dr. H. Schneider 2880

- Semiconductor Quantum Structures
- Infrared Spectroscopy
- Femtosecond Spectroscopy
- Free Electron Laser at ELBE

STRUCTURAL DIAGNOSTICS (FWIS)
Dr. J. von Borany 3378

- Electron Microscopy (TEM, SEM)
- Electron Spectroscopy
- X-ray Analysis
- Synchrotron Beamline at ESRF (ROBL)

PROCESS TECHNOLOGY (FWIP)
Dr. B. Schmidt 2726

- Semiconductor Technology
- Nanostructures
- Focused Ion Beam
- Clean Room Operation

List of Personnel

Directors: Prof. M. Helm, Prof. W. Möller
Office: I. Heidel, S. Kirch

Scientific Staff:

Permanent:

Dr. G. Abrasonis
Dr. L. Bischoff
Dr. J. von Borany
Dr. W. Bürger
Dr. F. Eichhorn
Dr. S. Facsko
Dr. J. Faßbender
Dr. M. Friedrich
Dr. D. Grambole
Dr. J. Grenzer
Dr. R. Grötzschel
Dr. V. Heera
F. Herrmann
Dr. K.-H. Heinig
Dr. H.-U. Jäger
Dr. R. Kögler
Dr. A. Kolitsch
Dr. U. Kreißig
Dr. A. Mücklich
Dr. C. Neelmeijer
Dr. M. Posselt
Dr. H. Reuther
Dr. E. Richter
Dr. N. Schell
Dr. B. Schmidt
Dr. H. Schneider
Dr. W. Skorupa
Dr. M. Voelskow
Dr. S. Winnerl

Post Docs:

Dr. K. Küpper
Dr. K. Potzger
Dr. J. Sun
Dr. M. Vinnichenko

Projects:

Dr. B. Abendroth
Dr. C. Akhmadaliev
W. Anwand
Dr. G. Brauer
N. Bulatovic
Dr. O. Drachenko
Dr. A. Lebedev
R. Martins
Dr. T. Oates
Dr. W. Pilz
Dr. A. Rogozin
Dr. M. Seidel
Dr. N. Shevchenko
Dr. C. V.-B. Tribuzy
Dr. H. Weishart
Dr. R. Yankov
Dr. M. Zier

PhD Students:

M. Beckers
M. Berndt
V. Cantelli
A. Dreyhaupt
H. Geßner
D. Güttler
A. Keller
D. Kost
M. O. Liedke
J. Potfajova
L. Röntzsch
S. Sinning
D. Stehr
S. Zhou

Diploma Students:

S. Friebel
R. Heller
M. Kreller
H. Lange
S. Ohser
F. Peter
S. Roßbach
G. Talut
M. Wagner
S. Walther

Technical Staff:

Permanent:

R. Aniol
G. Anwand
W. Boede
K.-D. Butter
E. Christalle
H. Felsmann
K. Fukarek
B. Gebauer
H.-J. Grahl
G. Grunert
P. Hartmann
J. Haufe
G. Hofmann
S. Klare
J. Kreher
A. Kunz
U. Lucchesi
M. Mißbach
C. Neisser
E. Quaritsch
A. Reichel
B. Richter
M. Roch
B. Scheumann
G. Schnabel
A. Schneider
J. Schneider
A. Scholz
T. Schumann
H. Seifert
K. Thiemig
S. Turuc
A. Vetter
R. Weidauer
A. Weise
J. Winkelmann
G. Winkler
I. Winkler

Projects:

F. Ludewig
M. Steinert
I. Skorupa
J. Zscharschuch